

NAVAL POSTGRADUATE SCHOOL

Monterey, California



FINAL TECHNICAL REPORT OF NSF
GRANT ATM 79-24010

"LARGE-SCALE ATMOSPHERE-OCEAN COUPLING"

by

Chih-Pei Chang and K. M. Lau

May 1984

Final Report
for Period

May 1980 - April 1983

Approved for public release; distribution unlimited.

Prepared for: National Science Foundation
Washington, D.C. 20550

FedDocs
D 208.14/2
NPS-63-84-004

Fed 6000

[2003 4/2. NPS-63-84-004

NAVAL POSTGRADUATE SCHOOL
Monterey, California

Commodore R. H. Shumaker
Superintendent

D. A. Schraday
Provost

The work reported herein was supported by the National Science Foundation, Atmospheric Research Section, under Grant ATM 79-24010.

This report was prepared by:

REPORT DOCUMENTATION PAGE		READ INSTRUCTIONS BEFORE COMPLETING FORM
1. REPORT NUMBER NPS 63-84-004	2. GOVT ACCESSION NO.	3. RECIPIENT'S CATALOG NUMBER
4. TITLE (and Subtitle) Final Technical Report of NSF Grant ATM 7924010. "Large-scale Atmosphere-ocean Coupling"		5. TYPE OF REPORT & PERIOD COVERED Final Report for May 1980 - Apr 1981
7. AUTHOR(s) C.-P. Chang and K. M. Lau		6. PERFORMING ORG. REPORT NUMBER
9. PERFORMING ORGANIZATION NAME AND ADDRESS Naval Postgraduate School Monterey, California 93943		8. CONTRACT OR GRANT NUMBER(s) NSF ATM 79-24010
11. CONTROLLING OFFICE NAME AND ADDRESS National Science Foundation Washington, D.C. 20550		10. PROGRAM ELEMENT, PROJECT, TASK AREA & WORK UNIT NUMBERS
14. MONITORING AGENCY NAME & ADDRESS (if different from Controlling Office)		12. REPORT DATE May 1984
		13. NUMBER OF PAGES 99
		15. SECURITY CLASS. (of this report) UNCLASSIFIED
		15a. DECLASSIFICATION/DOWNGRADING SCHEDULE
16. DISTRIBUTION STATEMENT (of this Report) Approved for public release; distribution unlimited.		
17. DISTRIBUTION STATEMENT (of the abstract entered in Block 20, if different from Report)		
18. SUPPLEMENTARY NOTES		
19. KEY WORDS (Continue on reverse side if necessary and identify by block number) El Nino Atmosphere-Ocean Interaction Tropical Meteorology		
20. ABSTRACT (Continue on reverse side if necessary and identify by block number) Large-scale coupling between the tropical atmosphere and ocean in relation to the El Nino/Southern Oscillation (ENSO) phenomenon is studied using both observational and theoretical/modeling approaches.		

(i) Observational studies

We have successfully identified from satellite observations a connection between Pacific tropical diabatic heating anomalies and extratropical circulation system over the North Pacific from East Asia to the continental North America. This teleconnection is strongly correlated with tropical Pacific sea surface temperature anomalies during ENSO. Shorter period fluctuation (40-50 day period) in the atmosphere also shows some signature of the above teleconnection pattern suggesting the presence of a multi-equilibrium climate state realizable both in the intraseasonal and interannual time scale. The above observations have led to the development of a stochastic-dynamical theory of ENSO, now being pursued by one of the Co-PI's (KML).

(ii) Theoretical/Modeling studies

Based on the results of an earlier theoretical investigation showing the presence of unstable coupled air-sea interaction in the tropics, a coupled atmosphere-ocean model has been developed. Various versions of this model and parameterization of air-sea coupling have been tested, and experiments performed. Results show that the sea surface temperature (or thermocline) anomalies have profound effects on the air-sea system producing both stable and unstable coupled modes. The temporal evolution of ENSO anomalies, in particular the 82/83 ENSO, appear to be the fairly well described by the presence of the unstable coupled modes. These results will be reported in a series of forthcoming papers.

Final Technical Report for Grant ATM-7924010

- a. Abstracts of publication (attached).
- b. Publication citations. (see References)
- c. Scientific Collaborators

P.I. W. K.-M. Lau:

Adjunct Assistant Professor, Naval Postgraduate School,
Monterey CA (1978-81).

Research Meteorologist, NASA/Goddard Space Flight
Center, MD (1981-present).

C.-P. Chang: Professor of Meteorologist, Naval Postgraduate School,
Monterey CA, 93940.

Other Collaborators

M. A. Rennick: Adjunct Assistant Professor, Naval Postgraduate
School, Monterey CA.

J. S. Boyle: NRC Postdoctoral fellow, NPS.

P. H. Chan: Research Scientist, Applied Research Corporation.

- d. Information on Inventions: None
- e. Technical description of Projects and results: (see attach reprints)
- f. References

1981

Lau, K.-M.: Oscillations in a simple equational climate system, J. Atmos. Sci., 38, 248-261.

Lau, K.-M.: Large-Scale atmosphere-ocean feedback mechanisms in relation to short-term climate fluctuations. Proceeding of the First Conference on climate variations, San Diego, CA.

1982

Lau, K.-M.: Thermally driven circulation in an equational β - plane: Hadley and Walker circulation during the winter monsoon. Mon. Wea. Rev., 110, 336-353.

Lau, K.-M.: Equatorial responses to northeasterly cold surges during winter monsoon as inferred from satellite cloud imageries. Mon. Wea. Rev., 110, 1306-1313.

C.-P. Chang and K.-M. Lau: Short-term planetary scale interactions over the tropics and midlatitudes, Part I: Contrast between active and inactive periods. Mon. Wea. Rev., 110, 933-946.

Lau, K.-M.: A simple model of atmosphere-ocean interaction during El Nino. Tropical Ocean-Atmosphere Newsletter, vol. 13, September.

Lau, K.-M.: Atmosphere-ocean feedback during El Nino/Southern Oscillation. Proceeding of the 4th Conference on Air-sea Interaction.

1983

Lau, K.-M and P. H. Chan: Short-term climate variability and atmospheric teleconnection from satellite observed outgoing longwave radiation. I: Simultaneous relationships J. Atmos. Sci. 40, 2735-2750.

Lau, K.-M and P. H. Chan: Short-term climate variability and atmospheric teleconnection from satellite-observed outgoing longwave radiation II. Lagged correlations. J. Atmos. Sci. 40, 2751-2767.

Rennick, M. A.: A model of atmosphere-ocean coupling in El Nino. Tropical Ocean-Atmosphere Newsletter, January issue.

Lau, K.-M.: Climate variability from cloud fluctuation statistics Proceeding of the fifth Conference on Atmospheric Radiation, Baltimore, Maryland.

1984

Lau, K.-M., J. S. Boyle and C. P. Chang: Anomalous diabatic heating and large scale circulation during the 1976-77 and the 1982-83 ENSO's: Tropical Ocean-Atmosphere Newsletter, March issue.

Lau, K.-M.: Subseasonal scale oscillation, bimodal climatic state and ENSO. Elsevier Oceanographic Series, Ed. J. Nihoul. (to be published).

Lau, K.-M.: A stochastic-dynamical theory of the long-term variability of ENSO. (submitted to JAS).

Oscillations in a Simple Equatorial Climate System

KA-MING LAU

Department of Meteorology, Naval Postgraduate School, Monterey, CA 93940

(Manuscript received 4 September 1979, in final form 14 October 1980)

ABSTRACT

Coupling between large-scale atmospheric and oceanic equatorial Kelvin waves is shown to be relevant in the climatic time scale related to equatorial ocean/atmosphere processes. The present analyses show that the inclusion of air-sea coupling into the linearized shallow-water equations can result in two types of dispersion relations for the Kelvin waves. The first type (Mode I) has fast phase speed and is mostly manifest in the atmospheric response. This mode is relatively unaffected by air-sea coupling. The second type (Mode II) has slow phase speed and is the predominant mode in the time-scale of the ocean. A resonant stationary wave is shown to exist as an intrinsic mode in the coupled system, the length scale of which is determined by the strength of the coupling and the magnitude of the damping. The positive feedback mechanism shown to exist between these coupled Kelvin waves in the Mode II regime is suggested to play an important role in relation to observed low-latitude teleconnections.

Results of the numerical experiments using the coupled model show that an El Niño-type oscillation can occur in a baroclinic ocean-atmosphere system as a result of a prolonged period of strengthening and subsequent weakening in the barotropic component of the wind. The weakening and the eastward shift of the rising branch of the Walker cell, identified as the atmospheric component of a coupled quasi-stationary Kelvin wave, during El Niño provide a positive feedback favoring warm water formation in the eastern Pacific and contribute to the large amplitude of the oscillation.

1. Introduction

In the study of the interannual fluctuations in the ocean-atmosphere system, the El Niño and associated events have attracted growing interests and concern among meteorologists and oceanographers largely because of the scientific importance as well as the far-reaching economic ramifications that have been attached to the phenomenon. Accompanying the El Niño anomalous SST changes are numerous observed changes such as the weakening of the trade winds, intensification of the equatorial countercurrents, rapid rising sea level in the eastern Pacific and falling sea level to the west (Ramage, 1975; Wyrtki, 1975, 1977). The interrelationships between these various parameters and the causes of their changes are widely debated (Barnett, 1977). At present the leading contender of the various theories regarding the origin of El Niño is perhaps the one due to Wyrtki (1975). He maintained that the sudden onset of El Niño is only a signal of the dynamical response of the entire equatorial Pacific Ocean to atmospheric forcings. Because of the observation that a prolonged period of increased surface easterlies always occurs in the central and western Pacific prior to the onset of each major El Niño, he proposed that these increased easterlies increase the strength of the westward flowing South Equatorial Current which tends to pile up water in the warmer western

Pacific and increases the east-west sea level slope. Following the relaxation of the surface easterlies, the pressure gradient from the enhanced sea slope will drive back water toward the east leading to a rise in sea level and deepening of the warm surface layer along the eastern border of the Pacific.

In equatorial oceans, Godfrey (1975), Hurlbert *et al.* (1976) and McCreary (1976) showed that the eastward movement of the water mass as a result of a relaxed surface easterly wind stress is likely to occur in the form of an eastward propagating equatorial Kelvin wave originating from the western boundary. The phase speed of this wave is $\sim 2 \text{ m s}^{-1}$ which means a time of approximately two months for the wave to travel across the span of the equatorial Pacific Ocean. Such a time scale is consistent with the time lag between the relaxation of wind in the west and first occurrence of warm water in the east observed during El Niño. Study of the baroclinic response of the ocean by Cane and Sarachik (1976) also confirmed that the internal Kelvin mode plays a decisive role in determining the initial response of a disturbance originating from the western part of a meridionally bounded ocean as a result of a symmetric weakening of zonal winds. They showed that as a Kelvin wave moves from west to east along the equator, water mass is continually built up ahead of the wave and an equal amount depleted behind it. At the coastal boundaries the reflection of the waves

produces, among others, equatorial-trapped Rossby waves whose phase speeds are about three times smaller than that of the Kelvin wave. In the absence of other external forcings, a relaxation in wind stress will result in an oversimplified manner, in a seiche-like oscillation across the ocean basin made up of fast eastward traveling Kelvin waves and slower westward propagating Rossby waves.

On the other hand, in the equatorial troposphere Webster (1973) showed that the Walker circulation may be viewed as a stationary wave set up by resonant excitation forced by the semi-permanent heat sources in the tropics, and this east-west overturning favors the largest zonal scale. Chang (1977) further demonstrated the importance of viscous damping to produce the correct phase speed and vertical scales in the observed low-frequency Kelvin-like oscillations of the forced equatorial waves. The variabilities in the amplitude and positions of the Walker circulation are then manifest in the response of stationary waves to slow variations in heat sources and sinks controlled, in part, by the change in surface conditions over the ocean.

There are many El Niño-like events in the ocean-atmosphere system which exhibit dynamic similarities to the above but with different intensities and time scales (Wyrtki *et al.*, 1976). In particular, the time scale of the theoretically predicted equatorial oceanic waves is of the order of months, while the observed time scale of the fluctuations is of the order of years. It is reasonable to suggest that the coupling of the ocean-atmosphere system may introduce additional important time scales. In view of the largely independent observations and hypotheses described above, there is a great need for studies to bring together these different hypotheses so that a coherent picture may hopefully emerge. This paper represents a first step toward this goal by using a simple coupled two-component (ocean/atmosphere) model which includes most of the elements of the physical processes discussed above including the interaction between the two components. The study is aimed at the large-scale spatial and temporal response of the coupled system to free and forced conditions, with emphasis on seeking closed cycles, if any exist, under certain given causal sequences.

In Section 2 the model equations are developed and in Sections 3 and 4 some properties of the analytical solutions, in particular those related to the mechanisms of the coupling are discussed. Sections 5 and 6 are devoted to the results of several numerical experiments designed to further elucidate, in terms of the results of the previous sections, the role of the air-sea coupling, in particular those related to El Niño, including the effect of diabatic heating. This study parallels a recent paper by Lau (1979) in which the changes in Hadley-type circulations in relation to local changes of wind stress and oceanic

upwelling were studied using a domain-averaged air-sea interactive model.

2. The model

For the purpose of elucidating the basic mechanism involved in the coupling of large scale oceanic and atmospheric Kelvin waves, we use the following simple model.

a. The atmosphere

Since the equatorial Kelvin waves are characterized by a vanishing meridional velocity component, we may write the linearized equations governing the Kelvin mode for a layer of incompressible fluid of homogeneous density with a free surface under hydrostatic balance, as

$$\frac{\partial u_a}{\partial t} + \frac{\partial \phi}{\partial x} + D_a u_a = F_a, \quad (1)$$

$$\frac{\partial \phi}{\partial t} + g H_a \frac{\partial u_a}{\partial x} + D_a \phi = Q_a, \quad (2)$$

where u_a and ϕ are the perturbation zonal velocity and geopotential; H_a the equivalent depth, D_a the linear damping coefficients and F_a , Q_a the coupling and forcing functions to be specified. Although (1)–(2) represent the so-called barotropic equations, they can be interpreted as the baroclinic component of a two-layer system in which u_a and ϕ are defined by

$$u_a = u_{a2} - u_{a1}, \quad \phi = \phi_2 - \phi_1, \quad (3)$$

where subscripts 2 and 1 refer to the upper and lower layer, respectively. The phase speed of the internal gravity wave in such case is given by $c_a = (g H_a)^{1/2} = [S(\Delta p)^2/2]^{1/2}$, depending on the static stability S and thickness Δp between the two levels. Therefore, (1) and (2) are also valid for internal mode of motions provided the velocity is taken as a wind shear and the geopotential replaced by the thickness or the mean temperature of the layers (Matsuno, 1966). In fact, (1)–(2) can have a more general interpretation applicable to continuous, stratified fluid. In such a case the equivalent depth H_a would have arisen as the separation constant or eigenvalue of the vertical structure equation in equatorial β -plane theory. However, because the emphasis of this paper is on the ocean-atmosphere coupling mechanism, the study of the vertical structure is not pursued.

b. The ocean

The governing equations for an ocean compatible with our simplistic atmosphere model are the linear shallow water equations (e.g., Lighthill, 1969). The one-dimensional form of these equations linearized about a state of rest and uniform stratification are

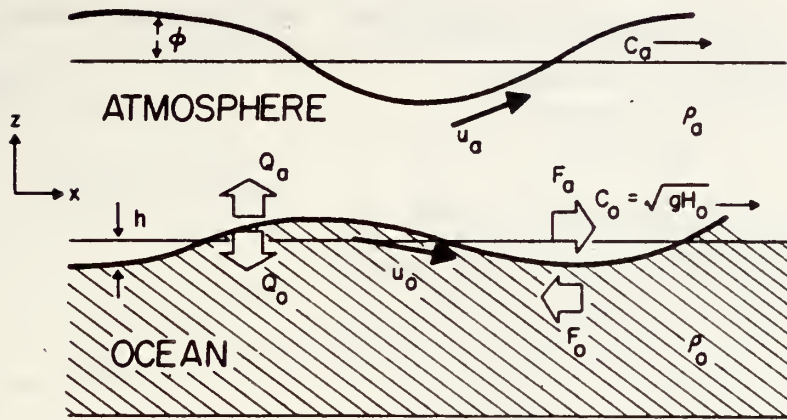


FIG. 1. Schematic diagram showing the structure of the coupled ocean-atmosphere system. See text for definitions of symbols.

given by

$$\frac{\partial u_0}{\partial t} + g \frac{\partial h}{\partial x} + D_0 u_0 = F_0, \quad (4)$$

$$\frac{\partial h}{\partial t} + H_0 \frac{\partial u_0}{\partial x} + D_0 h = Q_0, \quad (5)$$

where u_0 denotes the zonal current, h the deviation of the thermocline depth from its mean value, g the acceleration of gravity, D_0 the linear damping coefficients. The forcing functions F_0 and Q_0 which appear on the right-hand sides of (4)–(5) are the projections of the atmospheric forcing into the baroclinic mode of the ocean with equivalent depth H_0 which is of the order of 0.5 m or less in the equatorial regions (Moore and Philander, 1977). Eqs. (4) and (5) describe the time dependence of the Kelvin wave mode with a nondispersive phase speed given by $c_0 = (gH_0)^{1/2}$. In a two-layer formulation the variables u and h can be identified with a baroclinic zonal current and a depth-averaged temperature, respectively (Godfrey, 1975), i.e.,

$$u_0 = u_{01} - u_{02}; \quad h = \alpha(D_1\theta_1 + D_2\theta_2), \quad (6)$$

where subscripts 1, 2 refer to the top and bottom layers, respectively, θ is the departure of the layer temperature from some mean value, α the coefficient of thermal expansion of water and D the depth of the oceanic layer. The dual nature of the thermocline depth h as a measure of pressure (gh) and depth-averaged temperature [by (6)] allows a simple physical interpretation of the response of the model in relation to the real ocean. In this paper we shall refer to h as the thermocline depth, sea level or SST where appropriate. The schematic structure of the coupled model is shown in Fig. 1.

3. Solution of the coupled equations

In order to solve the coupled shallow-water equations (1), (2), (4) and (5), the first task is to specify

the forcing functions and coupling terms. We assume the following simple forms, i.e.,

$$\left. \begin{aligned} F_a &= 0, & Q_a &= \sigma' \mathcal{P}_a^0 h + Q_c' \\ F_0 &= \frac{\rho_a C_D |V_s|}{\rho_0 D_1} \mathcal{P}_0^a u_s, & Q_0 &= 0 \end{aligned} \right\} \quad (7)$$

where $|V_s|$ is a typical wind speed at the ocean surface; ρ_a , ρ_0 the density of surface air and water, respectively; C_D the drag coefficient, u_s the zonal wind at the surface. The symbol \mathcal{P}_a^0 represents the projection of the oceanic Kelvin mode onto the atmosphere Kelvin mode and \mathcal{P}_0^a vice versa. Here, we have neglected the direct effect of the oceanic drag on the wind field ($F_a = 0$) as frictional effects are included in the internal linear drag term. Also, because the effect of the atmospheric heat flux on the ocean cannot be properly represented without some kind of explicit oceanic mixed-layer dynamics, we have assumed $Q_0 = 0$ and concentrate only on the wind stress effect. If we assume that the barotropic component or the external mode of the wind in a two-layer model is given by

$$\langle u_a \rangle = u_{a2} + u_{a1} \quad (8)$$

and that the wind at the surface is taken to be that of the lower layer, then by (3) and (8) we have

$$u_s = \frac{1}{2}(\langle u_a \rangle - u_a). \quad (9)$$

The form of the forcing F_0 in (7) implies that the effect of the surface wind stress is to act as a body force uniformly distributed over the upper layer of depth D_1 . Assuming the change in temperature of the ocean is much larger in the upper than in the lower layer, the first term in the right-hand side of the heating function Q_a represents a measure of the heat flux from the ocean surface. We further assume that the perturbation heat flux H_s from the ocean is given by the form

$$H_s = \rho_a C_D C_p |V_s| \theta_1, \quad (10)$$

where C_p is the specific heat of air. Using (6) and (10) and the hydrostatic relation, the coupling constant σ' will be given approximately by

$$\sigma' = \frac{2gR\rho_a C_D |\mathbf{V}_s|}{p_s \alpha D_1}, \quad (11)$$

where p_s is the surface pressure and R the gas constant. The second term Q_c' in the heating function Q_a represents the effect of diabatic heating from cumulus convection. Thus the form of the forcing functions (7) gives a system where the ocean is driven by the wind stress and the atmosphere by heat flux from the ocean and heating from cumulus convection.

Next, we determine the projection coefficients \mathcal{P}_a^0 and \mathcal{P}_0^a which arise as a result of the different meridional scales of motions in the ocean and in the atmosphere. The meridional structure of the uncoupled Kelvin waves in an equatorial β plane has the form

$$\left. \begin{aligned} (u_a, \phi) &\sim \exp(-1/2 y_a^2) \\ (u_0, h) &\sim \exp(-1/2 y_0^2) \end{aligned} \right\}, \quad (12)$$

where $y_a = \beta^{1/2}(gH_a)^{-1/4}y$, $y_0 = \beta^{1/2}(gH_0)^{-1/4}y$.

When the ocean forces the atmosphere, the appropriate projection is

$$\begin{aligned} \mathcal{P}_a^0 &= \pi^{-1/2} \int_{-\infty}^{+\infty} \exp(-1/2 y^2) \exp(-y^2/2\gamma) dy \\ &= \left(\frac{2\gamma}{1+\gamma} \right)^{1/2}, \end{aligned} \quad (13)$$

where $\gamma = (H_0/H_a)^{1/2}$ is the ratio of the uncoupled phase speeds of the oceanic to the atmospheric Kelvin waves.

Similarly, when the atmosphere forces the ocean, the coefficient is

$$\begin{aligned} \mathcal{P}_0^a &= \pi^{-1/2} \int_{-\infty}^{+\infty} \exp(-1/2 \gamma y^2) \exp(-1/2 y^2) dy \\ &= \left(\frac{2}{1+\gamma} \right)^{1/2}. \end{aligned} \quad (14)$$

In the following we seek the solution of the basic equations for some simple cases. Eliminating ϕ and u_0 from (1)–(5) yields

$$\left\{ \begin{aligned} \left[\left(\frac{\partial}{\partial t} + D_a \right)^2 - c_a^2 \frac{\partial^2}{\partial x^2} \right] u_a + \sigma \frac{\partial \eta}{\partial x} \\ = - \frac{\partial Q_c'}{\partial x} \\ \left[\left(\frac{\partial}{\partial t} + D_0 \right)^2 - c_0^2 \frac{\partial^2}{\partial x^2} \right] \eta - \kappa c_0^2 \frac{\partial u_a}{\partial x} \\ = - c_0^2 \frac{\partial F_0'}{\partial x} \end{aligned} \right\}, \quad (15)$$

where we have defined $\eta \equiv gh$, $c_0 \equiv (gH_0)^{1/2}$, $\sigma \equiv \sigma' \mathcal{P}_a^0/g$,

$$\kappa \equiv \frac{\rho_a C_D |\mathbf{V}_s|}{2\rho_0 D_1} \mathcal{P}_0^a$$

and $F_0' \equiv \kappa \langle u_a \rangle$.

Fourier transform of (12), (13) in space and time yields

$$\mathbf{A}\mathbf{X} = \mathbf{Y}, \quad (16)$$

where

$$\mathbf{A} = \begin{pmatrix} (-i\omega + D_a)^2 + c_a^2 k^2 & ik\sigma \\ -ik\kappa c_0^2 & (-i\omega + D_0)^2 + c_0^2 k^2 \end{pmatrix},$$

$$\mathbf{X} = \begin{pmatrix} u_a(\omega, k) \\ \eta(\omega, k) \end{pmatrix}, \quad \mathbf{Y} = \begin{pmatrix} -kQ_c'(\omega, k) \\ -ic_0^2 k F_0'(\omega, k) \end{pmatrix}.$$

Solution to the homogeneous part of (14) is given by a vanishing determinant of the matrix \mathbf{A} , which gives a quartic equation in the frequency ω of the free modes

$$[(-i\omega + D_a)^2 + c_a^2 k^2][(-i\omega + D_0)^2 + c_0^2 k^2] = \omega_c^2 k^2 c_0^2, \quad (17)$$

where the coupling frequency ω_c is defined by $\omega_c = (\kappa\sigma)^{1/2}$.

To illustrate the change of the dispersion relation with variation in the strength of the coupling we consider two separate cases—with dissipation and without dissipation.

a. Zero dissipation

By putting $D_0 = D_a = 0$, the homogeneous solution to (16) can be obtained analytically. The frequency equation (17) yields two solutions for the phase speed of the coupled modes:

$$(c^{I,II})^2 = 1/2(c_0^2 + c_a^2) \pm 1/2[(c_a^2 - c_0^2)^2 + 4c_0^2 \omega_c^2 k^{-2}]^{1/2}. \quad (18)$$

The superscripts I and II are used to denote the plus and minus roots which correspond to a fast mode and a slow mode, respectively, with eigenfrequencies given by $\omega^{I,II} = kc^{I,II}$. As the phase speeds c_0, c_a are both real and provided $\omega_c \leq kc_a$ the phase speeds of the coupled modes c^I and c^{II} must also be real. The coupling frequency ω_c is nonzero only if κ, σ are both nonzero. From (18) we see that the coupling favors the large scale and approaches zero as the zonal wavenumber increases. When $\omega_c = 0$, the phase speeds reduce to those of the uncoupled modes with $c^I = c_a, c^{II} = c_0$. Using the values $\rho_a = 1.25 \text{ kg m}^{-3}$, $\gamma = 10^{-1}$, $\rho_0 = 10^3 \text{ kg m}^{-3}$, $|\mathbf{V}_s| = 5 \text{ m s}^{-1}$, $C_D = 1.25 \times 10^{-3} \text{ s}^{-1}$, $D_1 = 500 \text{ m}$ and $\alpha = 2 \times 10^{-4} \text{ }^\circ\text{C}^{-1}$, we obtain $\kappa = 2.16 \times 10^{-8}$ and $\sigma = 1.91 \times 10^{-4} \text{ s}^{-1}$. This results in a typical value of $\omega_c \equiv (\kappa\sigma)^{1/2} = 2 \times 10^{-6} \text{ s}^{-1}$. From the typical values of $c_a \sim 15 \text{ m s}^{-1}$ (Madden and Julian, 1972) and $c_0 \sim 2$

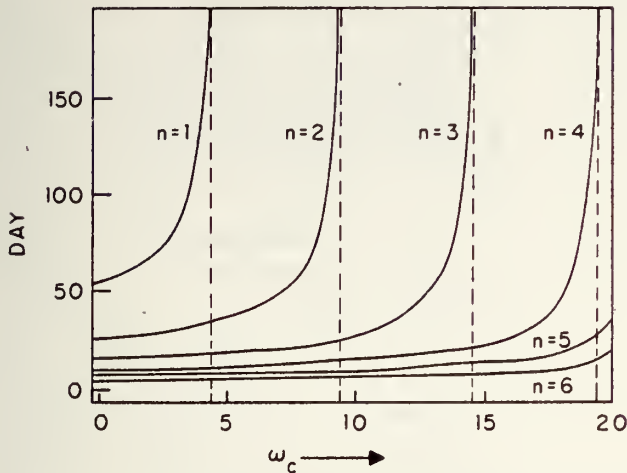


FIG. 2. Transit time for the slow (Mode II) coupled waves to cross an ocean basin of width $L = 10\,000$ km for different wavenumbers $k_n = n\pi/L$ as a function of the coupling frequency ω_c (10^{-6} s^{-1}). The dashed vertical lines represent the values of the critical frequency $\omega_c = k_n c_a$ on the abscissa.

m s^{-1} (McWilliams and Gent, 1978), and a horizontal scale of the width of the equatorial Pacific, the phase speed of the coupled modes are $c^I = 15.04 \text{ m s}^{-1}$ and $c^{II} = 1.6 \text{ m s}^{-1}$. The phase speed of the fast mode c^I , therefore, is not very different from those of the uncoupled atmospheric mode, whereas that of the slow mode c^{II} is significantly reduced from the uncoupled values. For different zonal wavenumbers n , Fig. 2 shows the times $T^{II} = L/c^{II}$ required for the slower of these coupled waves to cross an oceanic basin of width $L = 10\,000$ km. It can be seen that these transit times are substantially prolonged by increasing coupling especially at low wavenumbers. The effect becomes increasingly prominent as $\omega_c \rightarrow \omega_{cr} = k_n c_a$ [$k_n = n(\pi/L)$] for which cases the coupling is unrealistically large and T^{II} tends to infinity. The frequency ω_{cr} at which $c^{II} = 0$ has yet another interpretation. For fixed κ and σ the condition occurs when $k = (\kappa\sigma)^{1/2}/c_a$ wherein the free-traveling waves become stationary with respect to the earth. In the real system the presence of such modes are likely to be important in determining the character of the resonant response with respect to stationary forcings from topography and differential heating. From the values of κ , σ and c_a given above, the length scale of the stationary mode is 8000 km, which is of the same order of scale ($\sim 10^4$ km) found in some observed low-latitude zonal pressure oscillations. However, this scale is modified by the presence of friction as we shall see in the next section. Further increase of ω_c beyond $k_n c_a$ will render the system unstable with respect to that particular mode. The detailed stability properties of the solution will be discussed in the next section.

b. Nonzero dissipation

As we have seen in (i), stationary condition ($c^{II} = 0$) occurs at $\omega_c = \omega_{cr}$ in the inviscid case and we shall see in Section 4 later, when this occurs the Mode II amplitude becomes infinitely large. In our linear analysis finite amplitude at resonance is possible only in the presence of frictional dissipation. To see the effect of frictional damping on the growth rates and frequencies of the eigenmodes of the system (16), we consider the complete solution to (17) with nonzero dissipation terms. The values of the dissipation coefficients used are $D_a = 2.3 \times 10^{-6} \text{ s}^{-1}$ and $D_0 = 2 \times 10^{-7} \text{ s}^{-1}$ corresponding to dissipation time scales of 5 and 60 days for the atmosphere and ocean, respectively. The large value of D_a can be justified in terms of the effect of cumulus friction (e.g., Chang, 1977). However the value of D_0 appropriate for the baroclinic modes in the ocean is less certain. As shown below, within specific ranges, the behavior of the solution will have the same qualitative features. By introducing a new variable $\lambda \equiv i\omega$, Eq. (17) can be transformed into a quartic equation with real coefficients, where the complete set of roots can be obtained by numerical methods. Thus the real part λ_r of the eigenvalue λ gives the growth or decay rate and the imaginary part λ_i the oscillation frequency of the coupled mode.

The graphs of $\lambda_r = \lambda_r(\omega_c)$, $\lambda_i = \lambda_i(\omega_c)$ for different wavenumbers are shown in Figs. 3a and 3b. The most interesting results are seen in the Mode II response (see Fig. 3b). As in the inviscid case the eigenfrequencies λ_i decrease from an uncoupled value at $\omega_c = 0$ to zero (stationary condition) as ω_c approaches a critical frequency ω_{cr} and as long as $\omega_c \leq \omega_{cr}$ for a fixed wavenumber n , the damping time scale λ_r is independent of ω_c . As ω_c increases beyond ω_{cr} , the solution first bifurcates into two stable non-oscillatory modes ($\lambda_r < 0$). One of these modes, with λ_r increasing, soon becomes unstable ($\lambda_r > 0$) as ω_c further increases. Comparison of Figs. 2 and 3b shows that the stable region ($\omega < \omega_{cr}$) is increased as a result of the stabilizing effect of frictional damping. For a coupling time scale of 4–6 days ($\omega_c \sim 3 - 2 \times 10^{-6} \text{ s}^{-1}$) the frequency of the largest ($n = 1$) coupled waves is in the range which corresponds to a transit time of 75–90 days across a longitudinal span of $L = 10\,000$ km. At this coupling frequency, the effect on the frequencies of the waves with $n < 3$ becomes negligible. For Mode I (Fig. 3a) the eigenvalues indicate damped oscillations ($\lambda_i \neq 0$ and $\lambda_r < 0$) with damping time scale and oscillations frequency virtually independent of the strength of the coupling.

In the stationary limit $\omega = 0$, the frequency equation (17) can be solved for the stationary wavelength k_n , yielding

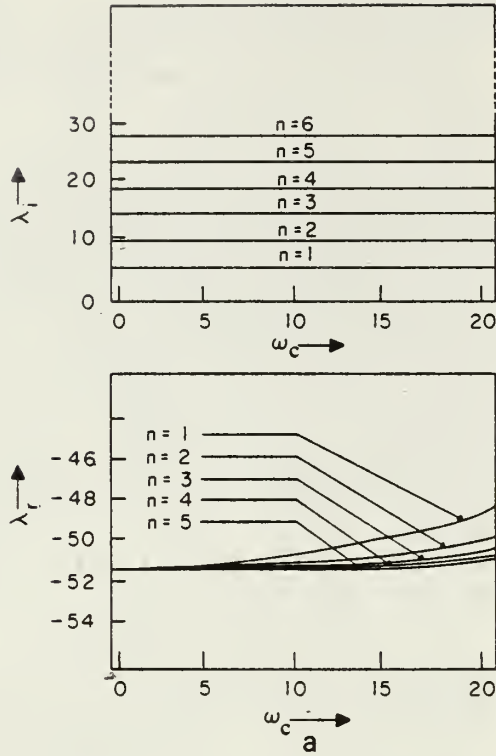


FIG. 3a. Graphs of the real $[\lambda_r(\omega_c)]$ and imaginary $[\lambda_i(\omega_c)]$ parts of eigenvalues for Mode I. Units are 10^{-6} s^{-1} .

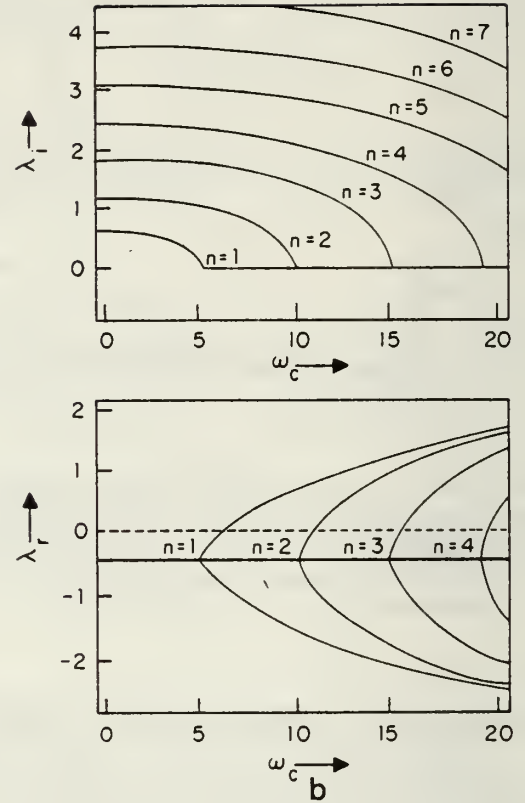


FIG. 3b. As in Fig. 3a except for Mode II.

$$k_s^2 = \frac{1}{2} \left(- \left[\left(\frac{D_a}{c_a} \right)^2 + \left(\frac{D_0}{c_0} \right)^2 - \left(\frac{\omega_c}{c_a} \right)^2 \right] \right. \\ \left. \pm \left[\left[\left(\frac{D_a}{c_a} \right)^2 + \left(\frac{D_0}{c_0} \right)^2 - \left(\frac{\omega_c}{c_a} \right)^2 \right]^2 - 4 \left(\frac{D_a}{c_a} \right)^2 \left(\frac{D_0}{c_0} \right)^2 \right]^{1/2} \right). \quad (19)$$

It can be shown from (19) that k_s is imaginary, complex or real depending on the magnitude of the coupling. Fig. 4 shows the variation of $k_r \equiv \text{Re}(k_s)$ and $k_i \equiv \text{Im}(k_s)$ in Mode II as a function of the coupling strength ω_c . Three functional regimes are immediately obvious. They are [also from Eq. (19)] given by the following:

Regime I: $\omega_c/c_a < D_a/c_a - D_0/c_0$. Here $k_r = 0$ and $k_i > 0$. The solution represents pure damping of a Kelvin wave toward the east (positive x direction) as a result of the relatively overwhelming effect of dissipation.

Regime II: $D_a/c_a - D_0/c_0 < \omega_c/c_a < D_a/c_a + D_0/c_0$. In this range, $k_r > 0$, $k_i > 0$. The solution consists of a wave part with an exponentially damped component toward the east. As the coupling increases, the relative effect of the damping diminishes reflecting the increasing importance of the positive feedback (see Section 4) effect of the coupling.

Regime III: $\omega_c/c_a > D_a/c_a + D_0/c_0$. This regime is dominated by the positive feedback effect of the coupling with $k_i = 0$ and $k_i > 0$. As the coupling increases the stationary wave is undamped and its magnitude is given asymptotically at large values of ω_c by the nondissipative limit $k_r = \omega_c/c_a$.

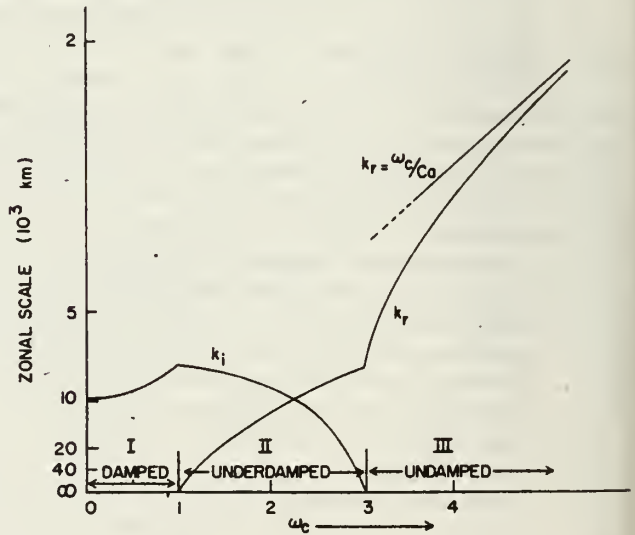


FIG. 4. Zonal scales of the stationary wave as a function of the coupling strength. Abscissa is in units of 10^{-6} s^{-1} .

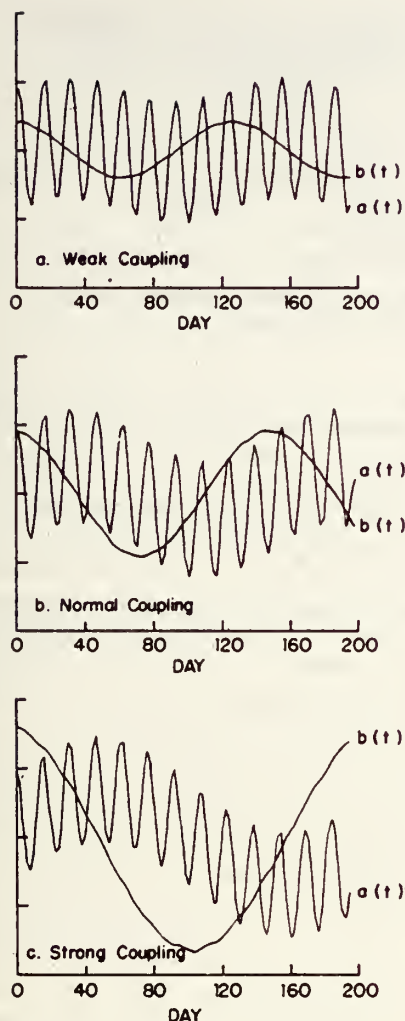


FIG. 5. Time variation of the Fourier coefficients $a(t)$ for the zonal wind and $b(t)$ for the sea level of the longest wave ($n = 1$). (a) Weak coupling ($\omega_c = 10^{-6} \text{ s}^{-1}$); (b) normal coupling ($\omega_c = 2 \times 10^{-6} \text{ s}^{-1}$); and (c) strong coupling ($\omega_c = 4 \times 10^{-6} \text{ s}^{-1}$). Ordinate is in arbitrary units.

The zonal scale of the wave and its decay length, for typical values of the parameters used previously are approximately 15 000 and 8000 km, respectively. These length scales are in accordance with some observed zonal teleconnections in the equatorial oceans and atmospheres (Julian and Chervin, 1978).

4. Initial value problem

To illustrate some basic properties of the coupled system, we consider a simple initial value problem.

$$\begin{aligned} a(t) &= \left[a(0) - \frac{ik\sigma b(0)}{k^2 c_a^2} \gamma (1 - \xi^2)^{1/2} \right] \exp(-i\omega^I t) + \left[-a(0) \gamma \frac{\xi^2}{(1 - \xi^2)^{1/2}} + \frac{ik\sigma b(0)}{k^2 c_a^2} \right] \exp(-i\omega^{II} t) \\ b(t) &= \left[b(0) \xi^2 (1 - \xi^2)^{1/2} \gamma^3 - ia(0) \frac{\kappa}{k} \gamma^2 \right] \exp(-i\omega^I t) + \left[b(0) + ia(0) \frac{\kappa}{k} \frac{\gamma}{(1 - \xi^2)^{1/2}} \right] \exp(-i\omega^{II} t) \end{aligned} \quad (25)$$

Because the case with nonzero friction does not admit simple analytic solution, we consider the problem only for the inviscid case. The case with nonzero friction will be dealt with numerically in the next section. The eigenvectors corresponding to the eigenvalues ω^I and ω^{II} in the inviscid case are

$$Z^I = \begin{pmatrix} ik\sigma \\ S^I \end{pmatrix} \quad \text{and} \quad Z^{II} = \begin{pmatrix} ik\sigma \\ S^{II} \end{pmatrix},$$

where

$$S^{I,II} = \frac{1}{2}(c_a^2 - c_0^2)k^2 \mp \frac{1}{2}[(c_a^2 - c_0^2)^2 k^4 + 4c_0^2 k^2 \omega_c^2]^{1/2}. \quad (20)$$

The general solution to the free mode of (16) in terms of a truncated Fourier series have the form

$$\begin{pmatrix} u_a(x, t) \\ \eta(x, t) \end{pmatrix} = \sum_n \begin{pmatrix} a_n(t) \\ b_n(t) \end{pmatrix} e^{ik_n x}, \quad (21)$$

where

$$k_n = n\pi/L,$$

$$\begin{pmatrix} a_n(t) \\ b_n(t) \end{pmatrix} = C_n^I \times Z_n^I \exp(-i\omega_n^I t) + C_n^{II} \times Z_n^{II} \exp(-i\omega_n^{II} t). \quad (22)$$

In (22), C_n^I and C_n^{II} are complex constants which can be determined from initial conditions. To see the relative amplitudes of the two modes and their temporal variations, we consider the simple case in which the coupled system is initially in steady state, i.e.,

$$\dot{b}_n(0) = \dot{a}_n(0) = 0 \quad (23)$$

Fig. 5 shows the time variations of the Fourier coefficients $a(t)$, $b(t)$ of the longest wave ($n = 1$) for different values of ω_c . The most noticeable features are the two-time scale variation in the surface wind, $a(t)$ and the Mode II dominated slower variation of the sea level $b(t)$. Comparing the three cases in Fig. 5 it can be seen that as the coupling is increased the period of the Mode II response is prolonged and its amplitude becomes larger.

Next, we consider the structure of the coupled waves at the stationary limit. This occurs for strong coupling or small wavenumbers. Defining $\xi = \omega_c(kc_a)^{-1}$, we have from (18) and (20)

$$\left. \begin{aligned} \omega^I &\rightarrow kc_a, & \omega^{II} &\rightarrow kc_0(1 - \xi^2)^{1/2} \\ S^I &\rightarrow -c_0^2 k^2 \xi^2, & S^{II} &\rightarrow k^2 c_a^2 \end{aligned} \right\} \quad (24)$$

The solution remains stable provided $\xi < 1$. In the stationary wave limit ($\xi \rightarrow 1$) $\omega^{II} \rightarrow 0$, it can be shown that (22) can be written in the form

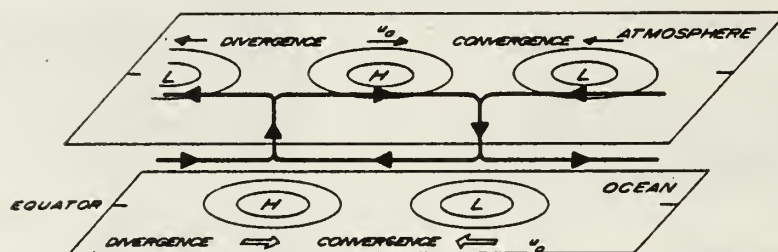


FIG. 6. Schematic of the coupling mechanism between the atmospheric and oceanic Kelvin waves in the Mode II regime.

It is clear from (25) that the most important effect of the increasing coupling on the ocean is to increase the time scale of the purely oceanic mode and to enhance the amplitude of the Mode II response by a factor of $(1 - \xi^2)^{-1/2}$. Resonance conditions occur at the Mode II response both in the wind field $a(t)$ and the sea level $b(t)$ at $\xi = 1$. Since the fast mode (Mode I) in the oceanic response $b(t)$ is of the order ≤ 0 (γ^2), they only provide a negligible contribution of not more than 1% of the total variation. Physically, this is reasonable to expect because the large inertia of the ocean compared with that of the atmosphere ($\gamma^{-1} \gg 1$) makes it unlikely for the fast mode to develop there.

To see the dependence of the coupling on the scale of the disturbance in the limit $\xi \rightarrow 1$ it can be shown using the definition of ξ and (25) that

$$\begin{pmatrix} a(t) \\ b(t) \end{pmatrix} \sim \begin{pmatrix} (k^2 c_a^2 - \omega_c^2)^{-1/2} k^{-1} \\ i(k^2 c_a^2 - \omega_c^2)^{-1/2} \end{pmatrix} \exp(-\omega'' t), \quad (26)$$

which means that for a fixed coupling frequency ω_c ($< k c_a$) stronger amplitude is favored for smaller values of wavenumber.

A further result of the coupling is to introduce an additional phase factor in the Mode II time variation of $b(t)$ given by

$$\varphi_b = \tan^{-1} \left[\frac{a(0) \kappa \gamma}{b(0) k (1 - \xi^2)^{1/2}} \right]. \quad (27)$$

On the other hand, the phase of the Mode II response of $a(t)$ is given by

$$\varphi_a = \tan^{-1} \left[\frac{k \sigma}{k^2 c_a^2} \frac{b(0) (1 - \xi^2)^{1/2}}{a(0) \gamma \xi^2} \right]. \quad (28)$$

It is interesting to note using (27), (28) and the definitions of ξ and ω_c that the phase difference between the dominant waves in the two media is a constant given by

$$\varphi_a - \varphi_b = \pi/2, \quad (29)$$

i.e., in the Mode II regime the oceanic thermocline response always lags that of the surface wind by one-fourth of a wavelength.

This condition for the phase difference of the Mode II waves can be shown to be a very good approxi-

mation for all ranges of ω_c and k which give stable solutions. The positive feedback between the oceanic and atmosphere Kelvin waves implied by (29) can be illustrated as follows. Fig. 6 shows the structure of the coupled waves in the Mode II regime. In the ocean a high (H) will denote a high sea level (baroclinic pressure) or high SST. Since these are Kelvin waves the pressure gradient perpendicular to the equator are in geostrophic balance. The upper layer flow therefore is eastward as a result of which warm water is removed from the west of the high and built up east of it, causing the wave to move eastward. Since the dominant mode has the atmospheric wave $1/4$ wavelength ahead of its oceanic counterpart it is always in a position to assist in the building up of the oceanic high which provides increased heat input into the atmosphere thus reinforcing its circulation. Apparently, the larger amplitude of the reinforced oceanic wave makes it more difficult for the wave to be displaced eastward thus increasing the transit time of the wave. For a given suitable coupling these Kelvin waves in the two media can become locked in with the correct phase in a stationary mode.

5. Numerical experiments

In this and the following sections we study the behavior of the coupled system, i.e., the variations of the amplitudes and phase of the coupled waves, and see how a model El Niño can evolve given certain external forcings. As the coupled response of the model is biased toward ultralong waves and long time scales, the spatial domains of the model for numerical experimentations are designed along the same bias. The large longitudinal extent of the response requires that the variables change slowly over large east-west distances. As a result they should be adequately described by the so-called low-resolution models (e.g., McWilliams and Gent, 1978). Here we choose the model domains so as to coincide with the bulk regions of the western, central and eastern Pacific Ocean (see Fig. 7). Using a domain-averaging technique similar to that of Webster and Lau (1977), the momentum equations in (1)–(5) are averaged over each domain and the spatial derivatives in the height equations are approxi-

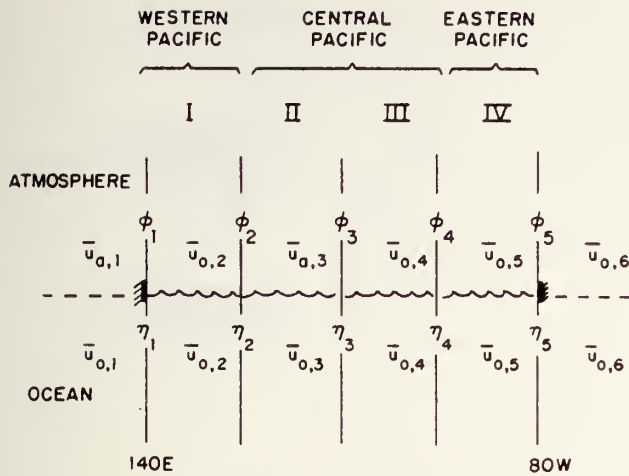


FIG. 7. Schematic representation of model configurations for the numerical experiments.

mated in terms of the domain-averaged quantities. The basic equations become

$$\left. \begin{aligned} \frac{\partial \bar{u}_{a,i}}{\partial t} + (\phi_i - \phi_{i-1})(\Delta x)^{-1} + D_a \bar{u}_{a,i} &= 0 \\ \frac{\partial \phi_i}{\partial t} + c_a^2 (\bar{u}_{a,i+1} - \bar{u}_{a,i})(\Delta x)^{-1} \\ &+ D_a \phi_i - \sigma \eta_i = Q_{c,i} \\ \frac{\partial \bar{u}_{o,i}}{\partial t} + (\eta_i - \eta_{i+1})(\Delta x)^{-1} \\ &+ D_o \bar{u}_{o,i} + \kappa \bar{u}_{a,i} = \bar{F}_{o,i} \\ \frac{\partial \eta_i}{\partial t} + c_0^2 (\bar{u}_{o,i+1} - \bar{u}_{o,i})(\Delta x)^{-1} + D_o \eta_i &= 0 \end{aligned} \right\}, \quad (30)$$

where the overbars denote domain-averaged quantities, Δx is the longitudinal extent of each domain and the i index for η and ϕ are staggered with respect to the domain index denoted by Roman numerals. We have taken into account the conditions $u_a = u_o = 0$ at the boundary by setting $\bar{u}_{a,1}$ to be $-\bar{u}_{a,2}$, $\bar{u}_{a,6} = -\bar{u}_{a,5}$, $\bar{u}_{o,1} = -\bar{u}_{o,2}$ and $\bar{u}_{o,6} = -\bar{u}_{o,5}$ on two imaginary domains outside the boundary. Although the coupled equations cannot model explicitly the reflection of the equatorially trapped waves at the boundaries, we can still mimic the time scales of such process by including the following conditions on the phase speed such that

$$c_0 = \begin{cases} c_K (=2 \text{ m s}^{-1}) & \text{if } \frac{\partial \eta_1}{\partial t} < 0 \\ & \text{and } \frac{\partial \eta_5}{\partial t} > 0 \\ \frac{1}{3}c_K & \text{otherwise} \end{cases} \quad (31)$$

in accordance with the observation that the oceanic Kelvin waves are associated with eastward propagation, rising and falling sea level in the East and West Pacific, respectively, and that the phase speed of the gravest Rossby modes is approximately one-third of that of the Kelvin waves (Cane and Sarachik, 1976).

In the tropical atmosphere, an important source of energy that maintains the east-west overturning is in the diabatic heating from latent heat release in cumulus convections. Therefore, the interaction picture will not be complete without including this important effect. Here we assume the following simple form of condensation heating, *viz.*,

$$Q_{c,i} = \begin{cases} \epsilon \delta_i, & \delta_i \geq 0 \\ 0, & \delta_i \leq 0 \end{cases} \quad i = 1, 5 \quad (32)$$

where $\delta_i = (\bar{u}_{a,i+1} - \bar{u}_{a,i})$ is a measure of the upper level divergence between adjacent domains and ϵ a scaling constant, chosen to be $3 \times 10^{-5} \text{ m s}^{-2}$ which gives a heating rate comparable to that due to adiabatic effects. The parameterization in (32) will crudely take into account the convective heating in the rising branch (positive divergence aloft) of the overturning motions.

Experiments were performed by numerical integration of the coupled ordinary differential equations (30) with a time step of 1 day for the atmosphere and 10 days for the ocean. In the following sections we present results for two experiments to study 1) the response of the model to sudden relaxation of imposed surface wind stress, 2) sensitivity of the model to changes in various parameters.

6. Results

In the past, a number of ocean spin down experiments (e.g., Godfrey, 1975; Hurlbert *et al.*, 1976) have been done using *fixed* atmospheric boundary conditions. The following experiments, however, are designed to elucidate the role of the coupling mechanism in the light of the development of the previous sections. They are not aiming at any realistic simulation. Such effort will require more sophisticated model structure and physics. For our purpose on El Niño will mean an anomalously high SST or equivalently a high sea level in the eastern Pacific (domain IV).

a. Wind relaxation

In this experiment the coupled model is first spun up with constant mean easterly surface wind $\langle \bar{u}_a \rangle = -6.4 \text{ m s}^{-1}$ in the western domains (I and II) and $\langle \bar{u}_a \rangle = -4 \text{ m s}^{-1}$ in the eastern domains (III and IV). These values are obtained as averages from the 25-year surface wind stress of Wyrtki (1975). After the steady state is reached the spindown phase for

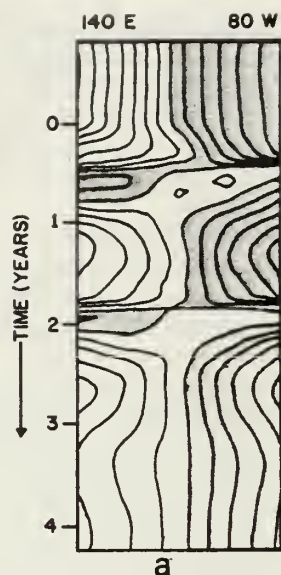


FIG. 8a. Longitude-time section of the sea level during spin-down for INT. The time axis is in units of years with year 0 denoting the start of the wind relaxation. Contours are in 5 cm intervals with negative deviations shaded.

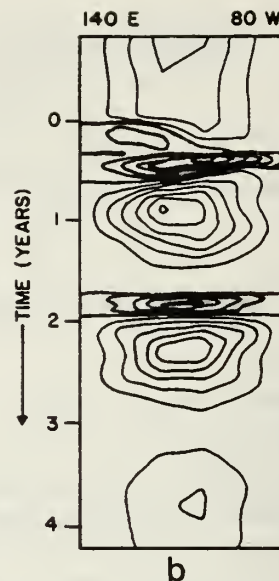


FIG. 8b. As in Fig. 8a except for the surface current. Contour interval is 10 cm s^{-1} with the eastward flow shaded.

the interactive ocean-atmosphere system (INT) is initiated from the steady-state conditions by suddenly turning down the mean wind over the western portions of the Pacific (domains I and II) to -2 m s^{-1} . The same procedure is then repeated with a non-interactive atmosphere (NINT) kept fixed at the steady-state conditions. At the end of three simulated years in the spinup phase a steady state is reached with a strong westward equatorial current ($\sim 30 \text{ cm s}^{-1}$) in the central Pacific and generally increasing thermocline depth toward the west. The atmosphere is dominated by a single Walker cell with strong upper level westerlies in the central Pacific, rising motion in the west and sinking motion to the east. Figs. 8a and 8b show the longitude-time section of the sea level and surface current during the spin-down phase. Immediately following the wind relaxation in INT (Fig. 8a) a rapid equalization of the east-west pressure gradient occurs as a Kelvin wave progresses toward the east and eventually causes the sea level gradient and the current to reverse (Fig. 8b). A seiche-like oscillation follows and becomes strongly damped at the end of the third year after spin-down. The model El Niño is marked by a rapid rise (fall) in sea level in the east (west) followed by a less rapid reversal reflecting the larger phase speed of the Kelvin waves compared to those of the Rossby waves. Here the triggering of oceanic Kelvin waves causes rapid reversal of pressure gradient and velocity field in about 2–3 months. Hurlbert *et al.* (1976), however, found in a similar oceanic spindown experiment that current reversal near the equator occurred in only ~ 50 days. The difference is most likely due to the interactive role of the at-

mospheric Walker-type circulations whereby the wave speed is reduced. The times for the coupled waves to be effective in the basin are approximately 3.5 and 10.5 months, respectively, for the Kelvin and the Rossby waves giving a periodicity of ~ 14 months for the coupled sloshing motion. Observations in a number of El Niño's in the past (Wyrtki, 1975) showed that anomalous conditions were repeated in succession ~ 12 – 15 months apart, and that the onset of SST and sea level anomalies, in general, occurred faster than its decay over a large extent of the equatorial Pacific. Also, of interest is the response of the interactive atmosphere (Fig. 8c). Dur-

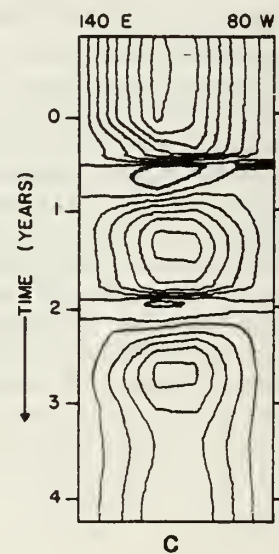


FIG. 8c. As in Fig. 8a except for the upper level wind. Contour interval is 1 m s^{-1} . Region of easterlies is shaded.

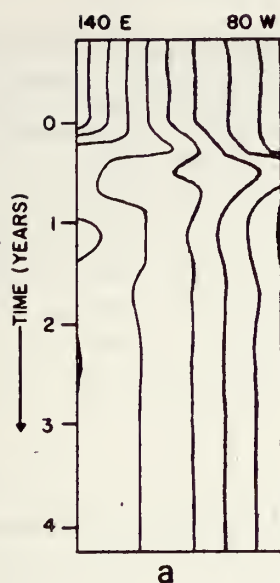


FIG. 9a. As in Fig. 8a except for a non-interacting atmosphere NINT.

ing the spin-down the atmosphere is coupled closely to the sloshing motions of the underlying oceans — an essentially Mode II response superimposed on which is a fast (Mode I) response characteristic of the atmosphere. In a matter of less than a month or so after the maximum thermocline depth in the east (El Niño) has been attained, the upper level zonal winds are all reversed to easterlies, signaling a weakening or even a reversal of the Walker cell. The change in wind over domain II is $\sim 4 \text{ m s}^{-1}$ which agrees somewhat with the observed averaged 200 mb wind change of $\sim 6 \text{ m s}^{-1}$ over Canton Island during periodic anomalous warm waters in the eastern Pacific (Julian and Chervin, 1978). At the end of the integration period, the ocean/atmosphere settles down to a steady state with much weakened wind and current fields. An important difference between the final and the initial steady state in the atmosphere is in the extent and the apparent eastward displacement of the upper level westerlies. This displacement will imply an eastward shift of the ascending branch of the Walker cell whose weakened intensity is then consistent with the reduced large-scale east-west gradient of SST. The effect of the Walker circulation to accentuate the initial perturbation in INT is evident by its much larger response amplitudes compared to NINT (Figs. 9a and 9b). Here the model El Niño does not produce the second peak in sea level and surface current as in INT. By comparing Figs. 8 and 9 it can also be seen that larger spatial scales, in addition to longer time-scale oscillations are preferred by the interactive mode. In the present coupled system positive feedback between the large-scale atmospheric and the oceanic waves is made possible by the exchange of heat and momentum

at the air-sea interface. A slackening of surface easterlies in the west will cause h to decrease (increase) in the west (east), decreasing the zonal SST contrast which in turn weakens the Walker cell. As the SST continues to increase in the central and eastern domains, the zonally oriented overturning motions become centered over the central and eastern Pacific, thus further diminish the surface easterlies in the west.

It can be seen in this experiment, the large-scale zonal SST gradient is the primary driving force of the Walker cell which in turn enhances the oceanic response and prolongs its time scales. The key point to note here is that in this coupled system an oceanic Kelvin wave has to be first triggered before the positive air-sea feedback can enhance its amplitude. In our model the triggering is achieved by relaxation from a period of sustained easterlies in the barotropic component of the wind. While this suggests that the ocean anomaly is caused by the atmosphere, it does not contradict the fact that the Walker cell is controlled by the large-scale SST gradient. What is manifest in this experiment is the strong baroclinic response of the coupled system in the presence of positive feedback as a result of a change of its barotropic wind component. The reversal of the zonal wind after the maximum sea level in the east also agrees with the observational study of Newell and Weare (1976) which showed that in some cases atmospheric changes are preceded by SST changes in the equatorial region.

b. Parameter tendencies

There are eight important parameters used in the model *viz.*, c_a , c_0 , D_a , D_0 , C_D , κ , σ and ϵ . Typical

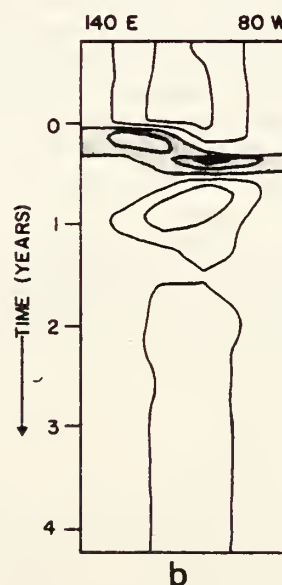


FIG. 9b. As in Fig. 8b except for NINT.

values of the first five of these parameters can be obtained from the literature and have been listed in Section 3. Only the last three are new parameters. The largest uncertainties in κ and σ according to their definitions (Section 3) are in the uncertainty of determining the depth of the wind-driven upper layer of the ocean. However, their values are restricted to within 20% of the values used to give a realistic coupling time scale of the order of months. The parameter ϵ governing the convective heating in (32) is the only free parameter in the model. It is therefore desirable to determine the sensitivity of the model with respect to this parameter. A series of nine separate model runs are made each similar to that described in Section 6a. In each of these runs the coupled model is spun up from rest with the same wind forcing as in Section 6a and then relaxed after steady state is reached with the condensation heating parameter $\epsilon = 0, \epsilon_0, 2\epsilon_0$ ($\epsilon_0 = 3 \times 10^{-5} \text{ m s}^{-2}$) under conditions of zero ($\omega_c = 0$), normal ($\omega_c = 2 \times 10^{-6} \text{ s}^{-1}$) and strong ($\omega_c = 4 \times 10^{-6} \text{ s}^{-1}$) coupling. The sensitivity of the model with respect to this parameter is evaluated in terms of the amplitudes of the sea level changes and atmospheric wind changes between each generated model El Niño and its corresponding initial steady state. Given that the coupling mechanisms and the convective heating parameterization are valid approximations, the result of these experiments will provide further insight into the relative importance of these processes in the real system.

Tables 1a and 1b show the amplitude of the changes in sea level Δh and zonal wind $\Delta \bar{u}_a$ during the Model El Niño. For the wind changes, it should be remembered that $\Delta \bar{u}_a$ is the change only of the baroclinic component. The total change is obtained as the average of $\Delta \bar{u}_a$ and the change in the barotropic component $\Delta \langle \bar{u}_a \rangle$, i.e., -4.4 m s^{-1} in domains I and II and zero in domains III and IV. In all cases the distribution shows that the sea level drops in the west and rises in the east and that $\Delta \bar{u}_a$ is everywhere

TABLE 1a. Anomalous sea level changes (cm) at different east-west locations of the model El Niño for different convective heating parameters ϵ and different degrees of air-sea coupling, with $\epsilon_0 = 3 \times 10^{-5} \text{ m s}^{-2}$ and $\omega_c^{(0)} = 2 \times 10^{-6} \text{ s}^{-1}$.

ϵ	Δh_1	Δh_2	Δh_3	Δh_4	Δh_5	
0	-10	-5	2	2	6	$(\omega_c = \kappa = \sigma = 0)$
ϵ_0	-10	-5	2	2	6	
$2\epsilon_0$	-10	-5	2	2	6	
0	-21	-15	2	8	10	$(\omega_c = \omega_c^{(0)})$
ϵ_0	-40	-22	5	23	30	
$2\epsilon_0$	-55	-48	8	30	38	
0	-43	-21	9	21	25	$(\omega_c = 2\omega_c^{(0)})$
ϵ_0	-55	-28	11	28	33	
$2\epsilon_0$	—	—	—	—	—	

TABLE 1b. Same as in Table 1a except for the zonal wind (m s^{-1}).

ϵ	$\Delta \bar{u}_a^{(I)}$	$\Delta \bar{u}_a^{(II)}$	$\Delta \bar{u}_a^{(III)}$	$\Delta \bar{u}_a^{(IV)}$	
0	0	0	0	0	$(\omega_c = \kappa = \sigma = 0)$
ϵ_0	0	0	0	0	
$2\epsilon_0$	0	0	0	0	
0	-1	-1.6	-1.1	-0.4	$(\omega_c = \omega_c^{(0)})$
ϵ_0	-1.1	-5.0	-3.6	-1.4	
$2\epsilon_0$	-4.7	-7.0	-5.6	-1.8	
0	-2.6	-5.1	-3.8	-1.4	$(\omega_c = 2\omega_c^{(0)})$
ϵ_0	-4.5	-8.1	-5.8	-2.1	
$2\epsilon_0$	—	—	—	—	

negative, indicating a weakening or reversal of the Walker circulation with decreased (increased) easterlies below (aloft). The maximum sea level drop is in the west as a result of coupled oceanic Kelvin waves leaving the western boundary and the maximum wind change is over the western central Pacific. This pattern is not changed by a $\pm 100\%$ change of ϵ from its reference values ϵ_0 . It is clear that the amplitudes of the oscillations are enhanced by increased coupling and by increased condensation heating. The blanks in the tables for the case of strong coupling [$\omega_c = 2\omega_c^{(0)}$] and strong heating ($\epsilon = 2\epsilon_0$) correspond to an unstable situation and suggest that the model is more sensitive at these limits. As shown in Section 6a, the convective heating also causes wind fluctuations in the fast time scale. Thus the heating contributes both to the amplitudes of Modes I and II. The Mode II contribution, however, is only possible in the presence of coupling. For the case of zero coupling, there is no change in the baroclinic component of the atmosphere and the amplitude of the sea level oscillation is much smaller. The case with normal coupling and heating gives a realistic change of $\Delta \bar{u}_a = -5 \text{ m s}^{-1}$ in the western central Pacific (domain II) and $\Delta \bar{h} = -40 \text{ cm}$ in the extreme west. The latter will correspond to a SST change of approximately -4.5°C over upper layer ocean depth of 400 m—a typical amplitude of the anomalous SST change in El Niño.

It is important to note that in this model there are two sources contributing to the diabatic heating of the atmosphere, viz., the condensation heating given by (32) and the heat input directly from the ocean which is proportional to the SST. The foregoing analyses show that the former contributes both to the fast and slow responses whereas the latter affects essentially only the slow time scale because it is related to an oceanic variable. However, physically the distinction of the two forms of heating is not mutually exclusive, as the heat input from ocean to atmosphere has to be realized in some type of condensation processes.

7. Summary and concluding remarks

In this paper we have studied the response of a simple two-component ocean/atmosphere system applicable in the equatorial regions to free and forced conditions. The heuristic model employs four basic equations, governing the zonal momentum and the temperature variation for the atmosphere and the ocean, respectively. Within each component, the equations are the shallow-water equations with simplifying assumptions based on the observed properties of large-scale equatorially trapped waves in relation to short-term climatic time scales. In practice the model can be compared to the internal mode of a two-level baroclinic system of equations within each component. The equivalent depths are chosen to correspond to the dominant baroclinic modes in the atmosphere and ocean respectively. In the ocean, provided the lower layer has large stability, the solutions can be regarded as vertical standing modes (Philander, 1978). In the atmosphere Chang (1976) showed that tropospheric forced wave has no vertical propagation within the troposphere. In the presence of frictional damping a mode exists with large vertical wavelength and strong vertical trapping (Chang, 1977). Therefore, the present atmospheric solution can be identified with this viscous mode. The energy exchange between these oceanic and atmospheric modes are then effected by the coupling in surface wind stress and heat flux.

Our analyses show that the inclusion of air-sea coupling into the linearized shallow-water equations can result in two types of dispersion relations for the Kelvin waves. The first type (Mode I) has fast phase speed and is mostly manifest in the atmospheric response, being relatively unaffected by air-sea coupling. The second type (Mode II) has slower phase speed and is the predominant mode in the equatorial climatic time-scale. The time-scale and the amplitude of the latter mode is substantially increased by increasing air-sea interaction. Because of the widely differing response time of the ocean and the atmosphere the effect of the coupling is to superimpose on the fast variation of the latter, a variation of a longer time scale relevant to oceanic processes. Most important is the existence of a positive feedback between the atmospheric zonal circulation and the large-scale ocean circulation in the equatorial plane, leading to the resonant excitation of a stationary mode within the coupled system. It is plausible that this mode is related to the quasi-stationarity of low-latitude teleconnections in the real system.

The results of the numerical experiments using the simple coupled model show that an El Niño type of oscillation can occur in a baroclinic ocean-atmosphere system in the form of trapped equatorial waves as a result of a prolonged period of weakening

in the barotropic component of the wind stress. Specifically, the antecedent strengthening and ensuing relaxation of surface easterlies in the central and western Pacific and the subsequent triggering of a coupled Kelvin wave lead to a rapid onset of El Niño conditions in the equatorial Pacific. This is a simple verification of Wyrtki's (1975) hypothesis. The large amplitude in the oscillation is a result of the coupling through exchanges of heat and momentum from the ocean surface. The weakening and eastward shift of the rising branch of the atmospheric Walker cell during El Niño provides a positive feedback favoring warm water formation in the eastern Pacific. In the experiment, the warm SST development is checked by the reflection at the eastern boundary of westward propagating equatorial trapped Rossby waves. In practice, the warm water likely will be dispersed poleward as well as westward along the equator by a combination of Rossby and Yanai wave modes (Godfrey, 1975; Cane and Sarachik, 1976).

Results also showed that the basic driving force of the equatorial Walker cell is the differential diabatic heating which is derived mostly from the largescale SST contrast. The recent theoretical study of the zonally symmetric circulation in a coupled air-sea system by Lau (1979) and the observational study by Cornejo-Garrido and Stone (1977) showed that indeed there is a high correlation between condensation heating and SST. However, the present findings differ significantly from those of Cornejo-Garrido and Stone (1977, hereafter referred to as CGS) to warrant a more careful discussion. CGS indicated that while SST may be important in determining the initial response of the Walker circulation, it only plays a minor role in maintaining the circulation. They suggested that the release of latent heat is the primary driving force of the Walker cell, but the source of the heating is derived not directly from evaporation from the ocean, but largely from dynamical moisture convergence. As indicated above, evaporation and dynamical convergence are included in our model. Both are found to be driving forces for the Walker cell. Yet in the time scale of interest, i.e., the oceanic time scale, our model shows that the circulation is controlled strongly by the heat contribution directly from the surface evaporation which is proportional to SST. The two apparently contradictory views can be resolved by the fact that the mechanisms discussed in this paper allow transient structure to exist such that the forcing functions, i.e., the wind stress and the oceanic heat flux are functions of the phenomenon itself and not merely boundary conditions. The heat budget study of CGS assumed time-averaged conditions and therefore is expected to give only steady-state results. In the time scale of our study the oceanic time scale becomes important and the stationarity assumption

is no longer valid. However, as stated by CGS, due to the presence of cloud cover, the evaporation over regions of high SST can be significantly reduced, thereby reducing the effectiveness of the coupling and our result may be significantly changed by including this effect. Nevertheless, such inclusion requires a more detailed radiation calculation in order that the effect of solar and infrared radiations can be handled properly. In such a case a compatible ocean model should also consist of more detailed mixed-layer dynamics. The inclusion of these physical processes into a coupled model can perhaps shed light on some features *not* predicted by the present model, e.g., the observation that heat storage and evaporation in the eastern equatorial Pacific did not increase during the 1972 El Niño (e.g., Wyrtki *et al.*, 1977). Another obvious weakness in this model is the absence of an explicit moisture budget thus neglecting the important effect of dynamic moisture convergence.

While the results of the analyses described in this paper illustrate the causal sequence involved in the purely equatorial and zonal processes of the ocean/atmosphere in a very simple manner, because of the limited model physics, the ability of the model to simulate the real system is seriously deficient. Nevertheless, the simple model may provide some useful backgrounds for data interpretation and for developing more sophisticated models of the ocean-atmosphere system.

Acknowledgments. I wish to thank Professors R. L. Haney and C. P. Chang for reading and suggesting useful comments on the earlier version of this paper. Also acknowledged is the effort of an anonymous reviewer whose critical review leads to an improved interpretation of the results of this work. All the computations of this work were done at the W. R. Church Computer Center of the Naval Postgraduate School, Monterey. This research was supported by the Climate Dynamic Research Section, National Science Foundation under Grants ATM77-14820 and ATM79-24010. Partial support was obtained from the Foundation Research Program of the Naval Postgraduate School.

REFERENCES

- Barnett, T. P., 1977: An attempt to verify some theories of El Niño. *J. Phys. Oceanogr.*, **7**, 633–647.
- Cane, M. A., and E. S. Sarachik, 1976: Forced baroclinic ocean motions II. The linear equatorial bounded case. *J. Mar. Res.*, **35**, 395–432.
- Chang, C.-P., 1977: Viscous internal gravity waves and low frequency oscillations in the tropics. *J. Atmos. Sci.*, **34**, 901–910.
- , 1976: Vertical structure of tropical waves maintained by internally-induced cumulus heating. *J. Atmos. Sci.*, **33**, 729–739.
- Cornejo-Garrido, A. G., and P. H. Stone, 1977: On the heat balance of the Walker circulation. *J. Atmos. Sci.*, **34**, 1155–1162.
- Godfrey, J. S., 1975: On ocean spindown I: A linear experiment. *J. Phys. Oceanogr.*, **5**, 399–409.
- Hurlbert, H. E., J. C. Kindle and J. J. O'Brien, 1976: A numerical simulation of the onset of El Niño. *J. Phys. Oceanogr.*, **6**, 621–631.
- Julian, P. R., and R. M. Chervin, 1978: A study of the Southern Oscillation and Walker circulation phenomenon. *Mon. Wea. Rev.*, **106**, 1433–1451.
- Lau, K. M. W., 1979: A numerical study of tropical large-scale air-sea interaction. *J. Atmos. Sci.*, **36**, 1467–1489.
- Lighthill, M. J., 1969: Dynamic response of the Indian Ocean to onset of Southwest Monsoon. *Phil. Trans. Roy. Soc. London*, **265**, 45–92.
- Madden, R. A., and P. R. Julian, 1972: Description of a global scale circulation cell in the tropics with a 40–50 day period. *J. Atmos. Sci.*, **29**, 1109–1123.
- Matsuno, T., 1966: Quasi-geostrophic motions in the equatorial area. *J. Meteor. Soc. Japan*, **44**, 25–42.
- McCreary, J., 1976: Eastern tropical ocean response to changing wind systems with application to El Niño. *J. Phys. Oceanogr.*, **6**, 632–645.
- McWilliams, J. C., and P. R. Gent, 1978: A coupled air-sea model for the tropical Pacific. *J. Atmos. Sci.*, **35**, 962–989.
- Moore, D. W., and S. G. H. Philander, 1977: Modeling the tropical oceanic circulation. *The Sea*, Vol. 6, Wiley, 319–361.
- Newell, R. E., and B. C. Weare, 1976: Ocean surface temperature and large-scale atmospheric variations. *Nature*, **262**, 40–41.
- Philander, S. G., 1978: Forced oceanic waves. *Rev. Geophys. Space Phys.*, **16**, 15–46.
- Ramage, C. S., 1975: Preliminary discussion of the meteorology of the 1972–73 El Niño. *Bull. Amer. Meteor. Soc.*, **56**, 234–242.
- Webster, P. J., 1973: Temporal variation of low-latitude zonal circulation. *Mon. Wea. Rev.*, **101**, 803–916.
- Wyrtki, K., 1977: Sea level changes during the 1972 El Niño. *J. Phys. Oceanogr.*, **7**, 779–787.
- , E. Stroup, W. Patzert, R. Williams and W. Quinn, 1976: Predicting and observing El Niño. *Science*, **191**, 343–346.
- , 1975: El Niño—the dynamic response of the equatorial Pacific Ocean to atmospheric forcing. *J. Phys. Oceanogr.*, **5**, 572–584.

Thermally Driven Motions in an Equatorial β -Plane: Hadley and Walker Circulations During the Winter Monsoon

KA-MING LAU

Goddard Laboratory for Atmospheric Sciences, NASA/Goddard Space Flight Center, Greenbelt, MD 20771

HOCK LIM¹

Department of Meteorology, Naval Postgraduate School, Monterey, CA 93940

(Manuscript received 27 April 1981, in final form 8 February 1982)

ABSTRACT

The linearized shallow-water equatorial β -plane equation was solved for a subset of approximate solutions applicable to thermally driven large-scale tropical circulation. In particular, the heat-induced monsoon circulations during Southeast Asian northeasterly cold surges are investigated. It was demonstrated that the response of the tropical atmosphere to a localized heat source consists of forced Rossby waves propagating westward and Kelvin waves eastward along the equator away from the region of forcing. In general, for any source/sink distribution, the heat-induced motion can have the characteristics of a Walker-type ($v = 0$ at the equator) or a Hadley-type ($u = 0$ at the equator) response or a combination of both, depending on the latitudinal location of the forcing. Away from the equator, a forcing corresponding to the sudden imposition of mass at the lower layer, or equivalently in our model a rapid cooling of the lower troposphere, produces a sudden local surface pressure rise and strong anticyclonic flow to the west of the forcing. Strong NE-SW tilt in the axis of the anticyclone is observed and can be understood in terms of the dispersion of the various wave modes excited. The low-latitude response is, as expected, dominated by Kelvin and the gravest Rossby wave modes.

Coupled with an equatorial heat source, the sudden cooling of the lower troposphere over a localized area in the subtropics gives rise to a northeasterly wind surge and large-scale Walker and Hadley circulations reminiscent of periods of strong cold surges over East Asia. Finally, the effect of the presence of a mean wind is shown to modify the spatial extent of the equatorial circulation with a mean *easterly* wind favoring the formation of equatorially trapped Walker cells.

1. Introduction

It has long been known that a large part of the tropical circulation is thermally driven. The observed large-scale quasi-stationary zonally asymmetric motions derive most of their energy from diabatic heating processes within the tropics (Ramage, 1968; Webster, 1972). Major condensation heat sources within the tropics are found to be over the three continents straddling the equator, i.e., South America, equatorial Africa and the "maritime continent" of Borneo and Indonesia (Krishnamurti *et al.*, 1973; Krueger and Winston, 1973, 1975). Although these heat sources are relatively confined spatially, the motions that they drive are of planetary scale. Longitudinally localized meridional circulations (local Hadley cells) extending to midlatitudes and equatorially trapped east-west oriented circulations (Walker cells) covering half of the globe emanate from these source regions and constitute a major part of the tropical general circulation. Since the zonal

asymmetries of these circulations arise as a result of land-sea thermal contrasts which determine the heat source/sink distribution, these heat-induced motions can essentially be regarded as part of the planetary-scale monsoon circulation. In particular, during the Northern Hemisphere winter, the diabatic heat source over the Borneo-Indonesia region is by far the strongest of the three tropical heat sources (Ramage, 1968). The large thermal contrast between this equatorial heat source and the immense cold source over northern China and Siberia provides the major driving force for the East Asia winter monsoon, which is one of the most energetic wintertime circulation systems in the tropics. The understanding of the dynamics of this circulation is crucial to forecasting the weather in this part of the world.

Although observational work on tropical large-scale circulations is abundant (e.g., Krishnamurti *et al.*, 1973; Krueger and Winston, 1973, 1975; Murakami and Unninayar, 1977; Murakami, 1980a,b; and many others), theoretical studies aiming at dynamical interpretation of these circulations are relatively few. The pioneer work of Webster (1972)

¹ On leave from Singapore Meteorological Services.

suggested that the Walker circulation may be regarded as rotationally trapped Kelvin waves in response to diabatic heating. However, Webster did not provide an explanation for the observed east-west asymmetry in his results. Further, the vertical structure of his Kelvin wave did not agree well with observation. Chang (1977) showed that in the presence of frictional damping and Newtonian cooling, the forced Kelvin wave indeed has the correct phase speed and vertical wavelength. In a recent study Gill (1980) addressed the zonal asymmetry problem by pointing out that the steady state response of the tropical atmosphere to an isolated heating function concentrated at the equator consists of planetary Rossby waves to the west and Kelvin waves to the east of the forcing. All these studies point to the fact that at least to a first approximation, the tropical large-scale circulation, including the monsoons, can be regarded as being driven by local heat sinks and sources, provided they are related realistically to the actual land-sea distribution. However, for more detailed and accurate descriptions the effects of orography and lateral coupling with midlatitudes will have to be included.

In this paper we seek simple solutions appropriate to thermally-forced long waves in a divergent barotropic equation in an equatorial β -plane. Here, we stress the planetary-scale aspect of the heat-induced motions with a particular solution relevant to thermal forcings during the winter monsoon period. As the model is highly idealized, we do not attempt to make detailed simulation of every nuance of the monsoon circulation, but rather we aim at the physical interpretation of the large-scale dynamical processes involved. In Sections 2 and 3 the model is developed and general solutions applicable to all heating functions are obtained. Section 4 focuses on the characteristics of the response in the Hadley and the Walker regimes. In Sections 5 and 6, we start with a brief discussion of the East Asian monsoon and its relevance to thermally-forced circulations. Solutions using specific forcing functions are then obtained and results analyzed. In Section 7 we examine the crucial effect of a mean zonal wind on the structure and intensity of the Walker circulation.

2. The model

The basic equations are the shallow-water equations in an equatorial β -plane:

$$\frac{\partial u}{\partial t} + U \frac{\partial u}{\partial x} - \beta y v + \frac{\partial \phi}{\partial x} + \epsilon u = 0, \quad (1)$$

$$\frac{\partial v}{\partial t} + U \frac{\partial v}{\partial x} + \beta y u + \frac{\partial \phi}{\partial y} + \epsilon v = 0, \quad (2)$$

$$\frac{\partial \phi}{\partial t} + U \frac{\partial \phi}{\partial x} + gh \left(\frac{\partial u}{\partial x} + \frac{\partial v}{\partial y} \right) + \epsilon' \phi = Q, \quad (3)$$

where u, v are the zonal and meridional velocity linearized from a basic state with constant zonal wind U ; ϕ is the geopotential, ϵ, ϵ' the Rayleigh friction and Newtonian cooling coefficient, respectively; $\beta = 2\Omega/a$, where Ω is the angular frequency and a the radius of the earth; Q the forcing (mass sink or source) term, and h an equivalent depth for the tropical atmosphere. Although (1)–(3) are the so-called divergent barotropic equations, their validity as representing a particular baroclinic mode corresponding to a specific structure in a continuous stratified atmosphere or as a two-layer atmospheric system has been demonstrated by Matsuno (1966) and Gill (1980). Here we prefer the two-layer interpretation, whereby heating means increasing the mass of high potential temperature fluids or equivalently transferring mass from a lower to an upper layer, and the reverse situation occurs for cooling. Because of the limited degree of freedom in the shallow-water system, the implied upper and lower flows have to be exactly opposite in order to maintain continuity. We should point out that, in the subsequent discussion, when a mass source is referred to in the surface layer, cooling of the troposphere is implied, and when it is referred to in the upper layer, heating is implied.

The eigenfrequencies ω of the free modes of the system (1)–(3) are given by the dispersion relation for

$$\omega = (\omega_r - Uk) + i\omega_i, \quad (4)$$

as

$$\frac{(\omega_r - Uk)^2}{\beta \sqrt{gh}} - \frac{k^2 \sqrt{gh}}{\beta} + \frac{k}{(\omega_r - Uk)} \sqrt{gh} = (2n + 1) \quad (5)$$

and

$$\omega_i = -\epsilon,$$

where k is a wavenumber.

The dispersion relation (5) for the Doppler-shifted frequency $(\omega_r - Uk)$ depicted in Fig. 1 shows that for large-scale waves (small k) only the Kelvin wave and the Rossby waves have small frequencies. For an equivalent depth of 40 m the fundamental phase speed of $c = \sqrt{gh}$ is 20 m s⁻¹, close to that observed for Kelvin wave-like oscillations in the tropical troposphere (Chang, 1977). At length scale greater than 4000 km, the gravity waves and the mixed Rossby-gravity wave all have frequencies corresponding to a time scale of less than 1/2 day, which is too short to be of significance for planetary-scale motions of the monsoonal time scale. Therefore if we emphasize the slow and large-scale waves (stippled region in Fig. 1), the dispersion relation (5) for these waves,

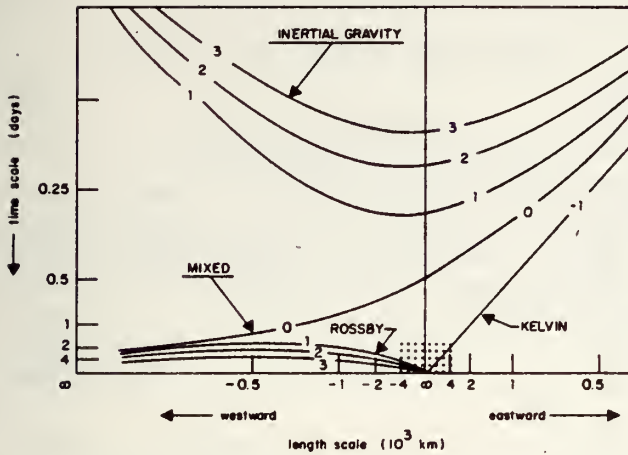


FIG. 1. Dispersion relation for the real part of the eigenfrequency and the wavelengths in an equatorial β -plane. The region within which the longwave approximation remains valid is indicated by stippling.

to a very good approximation becomes

$$\frac{k}{\omega_r - Uk} \sqrt{gh} = (2n + 1). \quad (6)$$

The "long wave" approximation expressed by (6) had been shown (Lighthill, 1969) to be equivalent to assuming geostrophic balance in the zonal direction, which is a fairly accurate assumption for large-scale Rossby- and Kelvin-type waves. We shall show in the following that such balance does lead to the dispersion relation (6). Following a procedure similar to Gill (1980), we non-dimensionalize (1)–(3) in terms of the basic equatorial length, time and velocity scales

$$L = (2\beta)^{-1/2}(gh)^{1/4}, \quad T = (2\beta)^{-1/2}(gh)^{-1/4}$$

$$\text{and } C = \sqrt{gh},$$

and define two new non-dimensional quantities,

$$\psi = \phi + u, \quad \chi = \phi - u. \quad (7)$$

For large-scale waves and small friction parameter, the non-dimensional equivalence of (1)–(3) is the following set

$$\frac{\partial \psi}{\partial t} + \epsilon \psi + (U + 1) \frac{\partial \psi}{\partial x} + \frac{\partial v}{\partial y} - \frac{1}{2} y v = Q, \quad (8)$$

$$\frac{\partial \chi}{\partial t} + \epsilon \chi + (U - 1) \frac{\partial \chi}{\partial x} + \frac{\partial v}{\partial y} + \frac{1}{2} y v = Q, \quad (9)$$

$$\frac{\partial \psi}{\partial y} + \frac{1}{2} y \psi + \frac{\partial \chi}{\partial y} - \frac{1}{2} y \chi = 0, \quad (10)$$

where (10) represents the zonal geostrophic condition. The non-dimensional frictional parameters for wind and geopotential are assumed to be the same in (8) and (9).

To solve (8)–(10), consider the following expansions:

$$(\psi, \chi, v, Q) = \sum_n (\psi_n, \chi_n, v_n, Q_n) D_n(y), \quad (11)$$

where $D_n(y)$ are parabolic functions of order n . For small values of ϵ , these functions are approximate eigenfunctions to the system (8)–(10) and have the following properties

$$D_n(y) = (-1)^n \exp(1/4 y^2) \frac{d^n}{dy^n} \exp(-1/2 y^2), \quad (12)$$

$$\int_{-\infty}^{\infty} D_n(y) D_m(y) dy = \sqrt{2\pi n!} \delta_{mn} \quad (13)$$

and

$$\frac{dD_n}{dy} + \frac{1}{2} y D_n = n D_{n-1}, \quad (14)$$

$$\frac{dD_n}{dy} - \frac{1}{2} y D_n = -D_{n+1}. \quad (15)$$

Using (11), (14) and (15), after solving for ψ_n , v_n and χ_n (8)–(10) can be written as

$$\frac{\partial \psi_0}{\partial t} + (U + 1) \frac{\partial \psi_0}{\partial x} + \epsilon \psi_0 = Q_0, \quad (16)$$

$$\left. \begin{aligned} \frac{\partial \psi_{n+1}}{\partial t} + \left(U - \frac{1}{2n+1} \right) \frac{\partial \psi_{n+1}}{\partial x} + \epsilon \psi_{n+1} \\ = \frac{n Q_{n+1} + Q_{n-1}}{(2n+1)} \end{aligned} \right\}, \quad (17)$$

$$\psi_1 = 0$$

$$\left. \begin{aligned} v_n = \frac{2(n+1)}{2n+1} \frac{\partial \psi_{n+1}}{\partial x} - \frac{[(n+1)Q_{n+1} - Q_{n-1}]}{2n+1} \\ v_0 = -Q_1 \end{aligned} \right\} \quad (18)$$

and

$$\chi_{n-1} = (n+1)\psi_{n+1}, \quad \text{for } n \geq 1. \quad (19)$$

It is readily seen that (16) represents a Kelvin wave moving eastward with unit phase speed and (17) represents Rossby waves moving westward with phase speed $(2n+1)^{-1}$ both relative to the mean wind U . Notice that in this approximation the Rossby wave speeds are independent of the east-west wavenumber as predicted by (6) and that the high-frequency gravity modes are completely filtered making possible the separation of the large-scale Kelvin and Rossby modes in a very simple manner. Given the space- and time-dependence of the forcing Q , the functions ψ , χ and v can be determined from (16)–(19) and the velocity and geopotential fields can then be obtained from (7).

3. The initial value problem

In this section we consider the general solution to a simple switch-on forcing. The solution for arbitrary

time-dependence can then be obtained by convolution. While the choice of the switch-on time dependence may not be entirely consistent with our assumption of slowly varying modes, because of the high frequencies contained in such function, we note that the "long wave" approximation we used filtered all these fast modes or transients in our problem. The solutions obtained are only a subset of the total solution. Nevertheless, this is an important subset, because in reality we expect that the largest uncertainty in the response of the tropical atmosphere to heat-induced forcing is due to the large variability of these fast, gravity-like modes arising from even slight variations in the temporal and spatial distribution of the forcing. The degree of sophistication in our present model does not warrant a detailed description of the these rather complex variations. However, all these responses share common characteristics which are most likely carried by the slowly-varying modes. If we look at the average response over a large number of cases with similar but slightly different forcings, as in composite methods used in observational studies, these fast modes would be expected to cancel out as "background noise." Therefore, for the purpose of this work, the use of the simple time-dependence in the forcing is not in conflict with our simplifying approximation used for the solutions. Consider a forcing of the form

$$Q_n(x, t) = q_n \exp(-\alpha^2 x^2) H(t), \quad (20)$$

where $H(t)$ is the Heaviside step-function given by

$$H(t) = \begin{cases} 1 & \text{for } t > 0 \\ 0 & \text{for } t < 0 \end{cases}, \quad (21)$$

and α^{-1} is the east-west scale of the heating function. Eqs. (16)–(18) are then easily solved by transform methods. The solutions are given by, for the Kelvin wave

$$\begin{aligned} \psi_0(x, t) = q_0 \exp\left\{-\frac{\epsilon x}{(U+1)}\right\} \\ \times \{G_0(x) - G_0[x - (U+1)t]\} \end{aligned} \quad (22)$$

and for the Rossby waves

$$\begin{aligned} \psi_{n+1}(x, t) = (nq_{n+1} + q_{n-1}) \exp\left\{-\frac{\epsilon x}{(U-c_n)}\right\} \\ \times \{G_n(x) - G_n[x - (U-c_n)t]\}, \end{aligned} \quad (23)$$

where

$$\begin{aligned} G_0(x) = \frac{\sqrt{\pi} \exp\left\{\frac{\epsilon}{2\alpha(U+1)}\right\}^2}{2\alpha(U+1)} \\ \times \sigma_0 \operatorname{Erfc}\left\{\sigma_0 \left[\frac{\epsilon}{2\alpha(U+1)} - \alpha x\right]\right\} \end{aligned} \quad (24)$$

and

$$\begin{aligned} G_n(x) = \frac{\sqrt{\pi} \exp\left\{\frac{\epsilon}{2\alpha(U-c_n)}\right\}^2}{2(2n+1)\alpha(U-c_n)} \sigma_n \\ \times \operatorname{Erfc}\left\{\sigma_n \left[\alpha x - \frac{\epsilon}{2\alpha(U-c_n)}\right]\right\}, \text{ for } n \geq 1, \end{aligned} \quad (25)$$

where

$$\sigma_0 = \operatorname{sgn}(U+1), \quad \sigma_n = \operatorname{sgn}(U-c_n)$$

and

$$c_n = \frac{1}{2n+1},$$

and $\operatorname{Erfc}(z)$ is the complimentary error function defined by

$$\operatorname{Erfc}(z) = \frac{2}{\sqrt{\pi}} \int_z^\infty \exp(-t^2) dt. \quad (26)$$

The cases of $(U+1) = 0$ and $(U-c_n) = 0$ represent stationary resonant situations and require special treatment. They are considered in a later section. It is clear that for non-resonance the solutions (22) and (23) have a stationary component and a transient component which move away from the source region with non-dimensional phase speed 1 and c_n to the east and west, respectively. The magnitude of the damping depends on the friction coefficient and the propagation speed. For the case of no mean wind ($U = 0$), the ratio of decay distances to the east and west for the strongly trapped or the lowest-order mode is 3 to 1, implying strong zonal asymmetry in the east-west direction.

To solve the complete problem for a specific horizontal heating distribution, the next step is to determine the expansion coefficients q_n in (20). These coefficients are most simply obtained for the case when the forcing distribution is also Gaussian in the y -direction. Consider a general forcing function of the form

$$\begin{aligned} Q(x, y, t) \\ = \exp[-(y-y_c)^2 \lambda^2] \exp(-\alpha^2 x^2) H(t), \end{aligned} \quad (27)$$

where y_c is the center and λ^{-1} is a measure of the width of the Gaussian function in y . The coefficients of the heating function in (20) are given by

$$q_n = \frac{1}{n! \sqrt{2\pi}} \int_{-\infty}^{+\infty} \exp[-(y-y_c)^2 \lambda^2] D_n(y) dy, \quad (28)$$

which has a recurrence relationship of the form

$$\begin{aligned} (n+1)(1+4\lambda^2)q_{n+1} \\ = 4\lambda^2 y_c q_n + (1-4\lambda^2)q_{n-1}, \end{aligned} \quad (29)$$

with

$$q_0 = 2^{1/2}(1 + 4\lambda^2) \exp[-y_c^2 \lambda^2 / (4\lambda^2 + 1)]$$

and

$$q_1 = 2^{1/2}(1 + 4\lambda^2)^{-3/2} y_c 4\lambda^2 \exp[-y_c^2 \lambda^2 / (4\lambda^2 + 1)].$$

Given a general forcing function of the form (27), or a combination of several of these functions with different geometric shape factors y_c , λ , α , the initial value problem is completely solved using (22)–(25), (28)–(29). In the latter case, the solutions for multiple mass sources and sinks can be obtained by linear superposition.

4. Special solutions

a. Symmetric heating

The properties of the solutions (22)–(25) are best examined by considering a heating function of the following form

$$Q(x, y, t) = \exp[-1/4(x^2 + y^2)]H(t), \quad (30)$$

which corresponds to a circular heat source concentrated at the equator with radius equal to one equatorial Rossby radius of deformation ($y_c = 0$, $\lambda = \alpha = 1/2$). From (29)–(30), we see that all q_n 's except $q_0 (=1)$ are zero. The only non-zero components from (22)–(25) and (18) are ψ_0 , χ_0 , v_1 , ψ_2 . The geopotential and velocity fields are given by

$$\begin{pmatrix} \phi \\ u \\ v \end{pmatrix} = \begin{pmatrix} \frac{\psi_0}{2} D_0(y) \\ \frac{\psi_0}{2} D_0(y) \\ 0 \end{pmatrix}$$

Kelvin mode

$$+ \begin{pmatrix} 1/2(\psi_2 D_2(y) + \chi_0 D_0(y)) \\ 1/2(\psi_2 D_2(y) - \chi_0 D_0(y)) \\ v_1 D_1(y) \end{pmatrix}. \quad (31)$$

Rossby mode ($n = 1$)

Fig. 2 shows the *upper level* response to the heating at the end of two, five, and nine simulated days. The solution approaches the steady state at the end of nine days. It is clear from Fig. 2 that the imposed heating generates Kelvin and Rossby ($n = 1$) waves which emanate to the east and west with different phase speeds and markedly different horizontal structures. Most noticeable is the strong zonal out-

flow trapped about the equator with $u \gg v$. The u and ϕ fields are symmetric and the v field antisymmetric with respect to the equator. Close to the equator the flow is dominated by a Walker-type circulation. The amplitude of the Hadley-type component is relatively small in this case. A different perspective of the response of the system can be obtained from an examination of the vorticity equation appropriate to the system (1)–(3) for $U = 0$

$$\left(\frac{\partial}{\partial t} + \epsilon \right) \left(\zeta - \frac{\beta y \phi}{gh} \right) + v\beta = S \equiv -\frac{\beta y Q}{gh}, \quad (32)$$

where ζ is the relative vorticity. It is readily seen that for a symmetric heating function with positive Q at the upper level (heating), a vorticity sink/source pair is produced on opposite sides of the equator. For the function (30), these sink and source maxima, obtained by differentiating the function S with respect to y , are at a distance of $\sqrt{2}$ times a Rossby radius of deformation away from the equator. At the equator, however, vorticity generation is zero and the flow becomes strongly divergent. These features are represented very well in Fig. 2.

b. Asymmetric heating

Here we consider the solution for the case in which the heating function is of the form

$$Q(x, y, t) = y \exp[-1/4(y^2 + x^2)]H(t). \quad (33)$$

In (33), the y -dependence is just that of $D_1(y)$ from (12). By the orthogonality relation (13), the only non-zero coefficient is $q_1 (=1)$. Using (22), (23), and (17), the pressure and velocity fields can be shown to have the following form

$$\begin{pmatrix} \phi \\ u \\ v \end{pmatrix} = \begin{pmatrix} 1/2[\psi_3 D_3(y) + \chi_1 D_1(y)] \\ 1/2[\psi_3 D_3(y) - \chi_1 D_1(y)] \\ v_2 D_2(y) \end{pmatrix}$$

Rossby mode ($n = 2$)

$$\times \begin{pmatrix} \psi_1 D_1(y) \\ \psi_1 D_1(y) \\ v_0 D_0(y) \end{pmatrix}. \quad (34)$$

mixed Rossby-gravity mode ($n = 0$)

As $v_0 D_0 = -\exp[1/4(y^2 + x^2)]$ from (18), the $n = 0$ mixed mode in this case represents a purely local response. The pressure and zonal wind fluctuation of the mixed mode are in fact zero because $\psi_1 = 0$ by (17).

Fig. 3 shows the evolution of model response at the upper level for days 2, 5, and 9 respectively. Here no Kelvin waves are excited and the response consists of a local component plus a slowly westward-propagating component with phase speed $c_2 = 0.2$ (~ 4

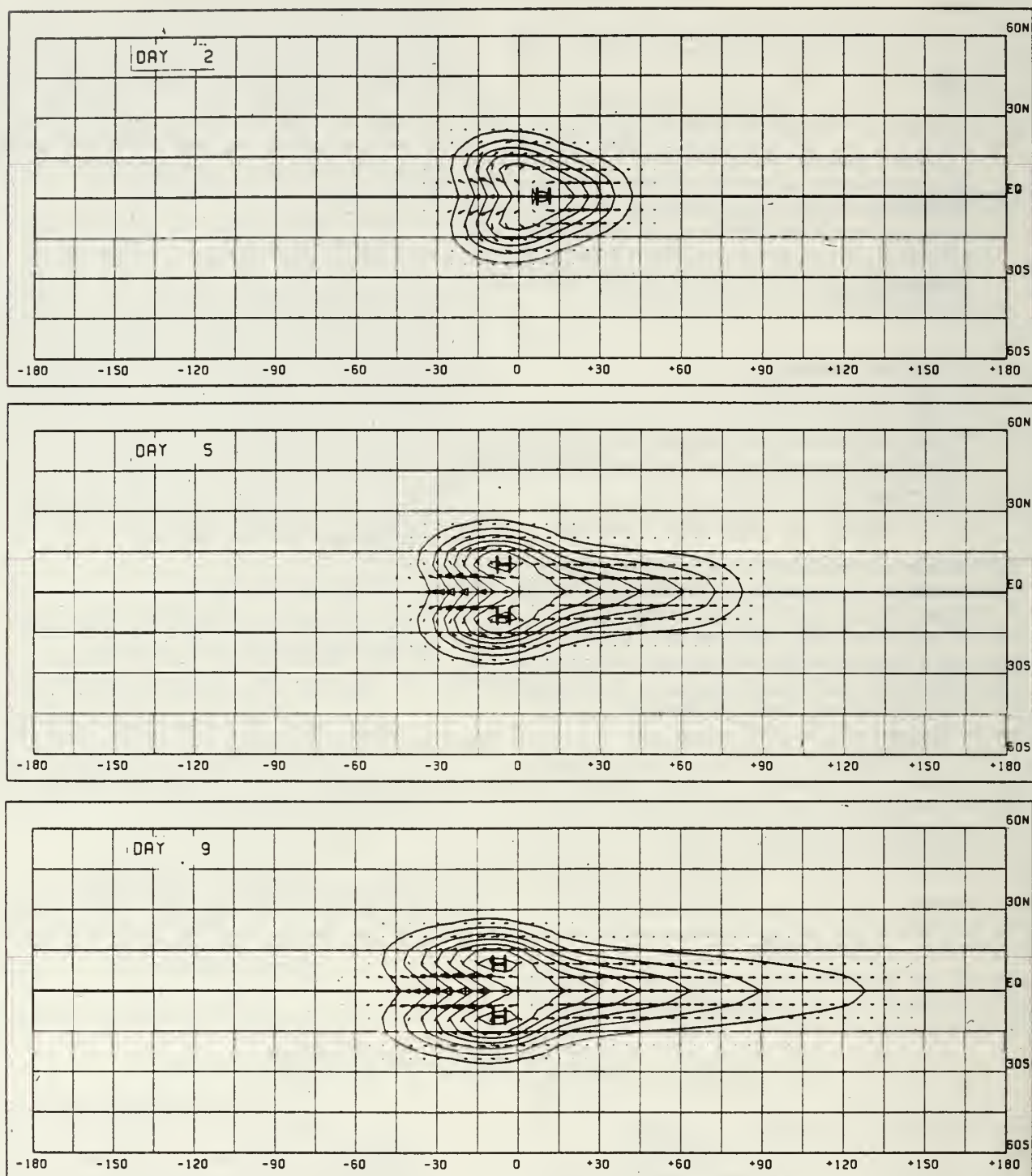


FIG. 2. Upper-level wind and geopotential response to a heating function of the form $Q = \exp[-(x^2 + y^2)/4]$ at days 2, 5, 9 with the friction coefficient $\alpha = 0.5$.

m s^{-1}). The presence of strong cross-equatorial flow with anticyclonic centers on the opposite side of the equator is evident of the antisymmetric nature (with respect to u and ϕ) of the response. Such features are characteristics of strong Hadley-type circula-

tions. In this case from (32), two upper-level vorticity sinks are produced at a distance of twice the Rossby radius of deformation on opposite sides of the equator, and as the zonal pressure gradient vanishes at the equator the zonal flow is zero there.

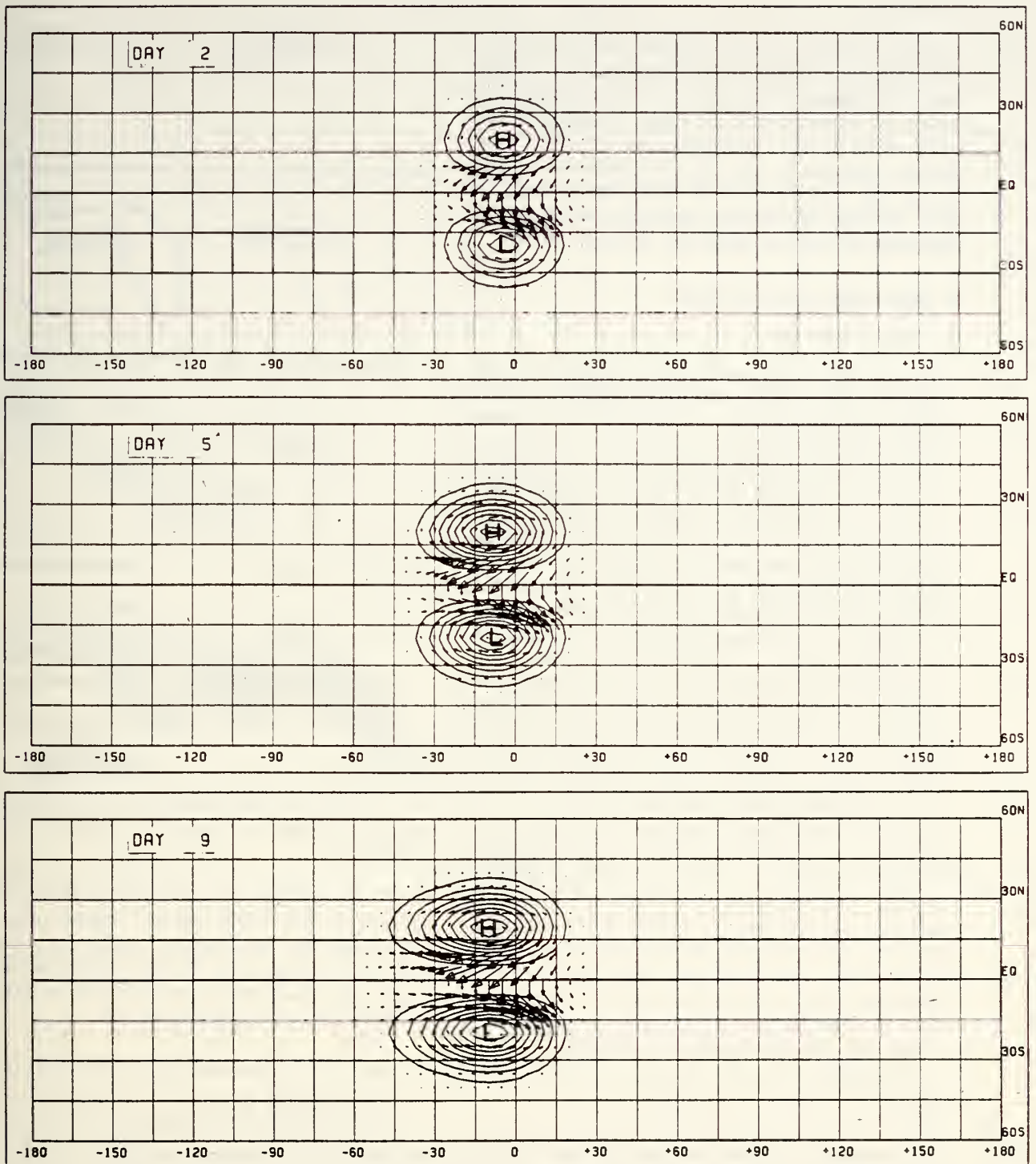


FIG. 3. Same as in Fig. 2 except for a heating function of the form $Q = y \exp[-\frac{1}{4}(x^2 + y^2)]H(t)$.

Summing up the two cases, it is clear that a symmetric forcing concentrated at the equator will produce a symmetric (Walker-type) response. (Kelvin waves are excited only if $q_0 \neq 0$.) Likewise, an antisymmetric forcing will produce only an antisymmetric (Hadley-type) response. For the Walker re-

gime, symmetric mode Rossby and Kelvin waves are responsible for propagating disturbances to the west and east of the source region, respectively. Conversely, in the Hadley regime, only the antisymmetric Rossby modes are important and an implied north-south overturning to the west is set up con-

necting the mass source and sink on opposite sides of the equator. In the real atmosphere, the distribution of diabatic heating is rarely perfectly symmetric or antisymmetric, so that a response is generally made up of a combination of the Hadley and Walker regimes. In the next two sections we shall discuss the relative roles of these two regimes for some heating distributions generally believed to be important during the northeast monsoon season.

5. East-Asian monsoon surges

a. The phenomenon

During the winter season of the Northern Hemisphere, an intense high pressure system develops over central Asia and Siberia. The build-up of this huge Siberian High is known to result from excessive radiative heat loss over the Asiatic land masses, reinforced by the blocking effect of the Himalayan massif to the west. Although the Siberian High appears as a quasi-permanent feature during the winter monsoon season, it is subject to large fluctuations in intensity and variations in structure. Migratory anticyclonic cells often break away and move eastward or southeastward, causing widespread outbreaks of cold continental air. As the cold air spreads southward, strong subsidence occurs in the lower atmosphere and surface pressure over southeast China rises rapidly (Danielsen and Ho, 1969; Ramage, 1975). When the cold air reaches over the southeast China coast, northeasterly winds strengthen rapidly over an extensive area downstream. Chang and Lau (1980, 1982) showed that a monsoon surge can sometimes lead to an intensification of convective activity in the maritime continent area of Borneo and Indonesia. This increased convection, in turn, causes planetary-scale divergent outflow in the upper troposphere, enhancing the Walker and Hadley circulations. Fig. 4 (adopted from Chang and Lau 1980) illustrates schematically the sequence of events believed to take place in a typical surge cycle.

To make possible comparison of the model solution with observations we concentrate only on the following specific large-scale features:

- 1) A large influx of surface cold air from the very cold region of Siberia into central and southeast China, causing a rapid cooling of the lower troposphere and a rapid rise in surface pressure there. This is followed by a rapid establishment of northeasterly to northerly surface flow over the South China Sea.

- 2) A strong local Hadley circulation with sinking motion over the cold continent and rising motion just south of the equator over the maritime continent.

- 3) Intense Walker-type circulations with ascending motion over the maritime continent and subsiding motions eastward over the central Pacific and westward over the Indian Ocean and Africa.

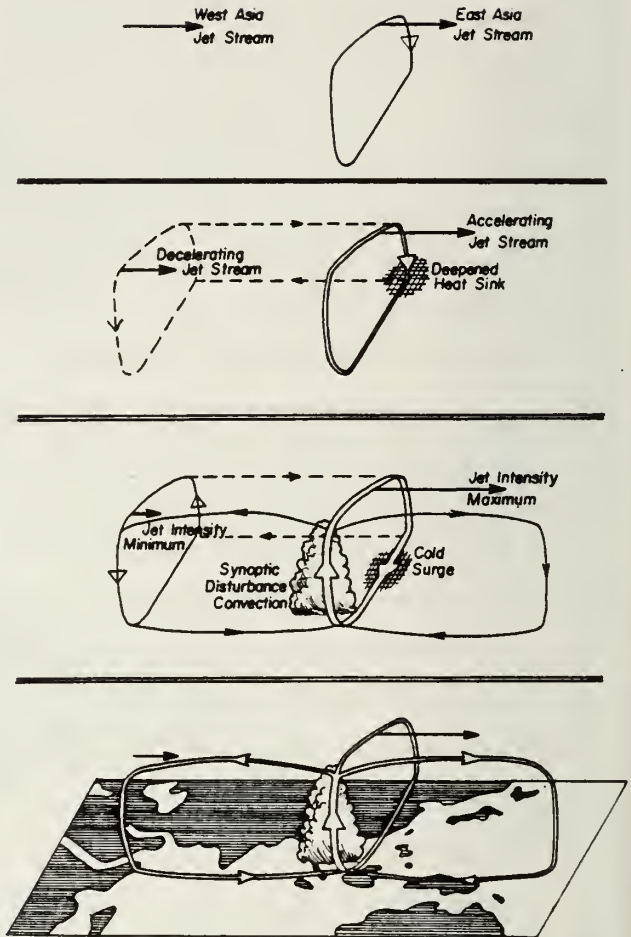


FIG. 4. Schematic diagram showing a plausible sequence of events during a typical cold surge cycle (adopted from Chang and Lau, 1980).

- 4) The confinement of the Hadley cell to the longitudes of the "cold source" region over central China and the "heat source" region over south Borneo; the trapping of the Walker cells in the equatorial region and the marked asymmetry on the eastern and western sides of the source region.

b. Response to forcings during monsoon surges

In this section we present two solutions which isolate the effect of the latitudinal location of the forcing on the large-scale response of the model. To simulate the sudden influx of cold air from polar into subtropical latitudes during monsoon surges, we use a forcing function of the form

$$Q(x, y, t)$$

$$= \exp[-(y - y_c)^2 \lambda^2] \exp(-\alpha^2 x^2) H(t), \quad (35)$$

representing a mass source at the surface layer (cooling) with $\alpha = \lambda = 1/2$ and y_c corresponding to forcing centered at (a) 35°N and (b) 27°N . The two cases are chosen to correspond to the rapid rise in surface

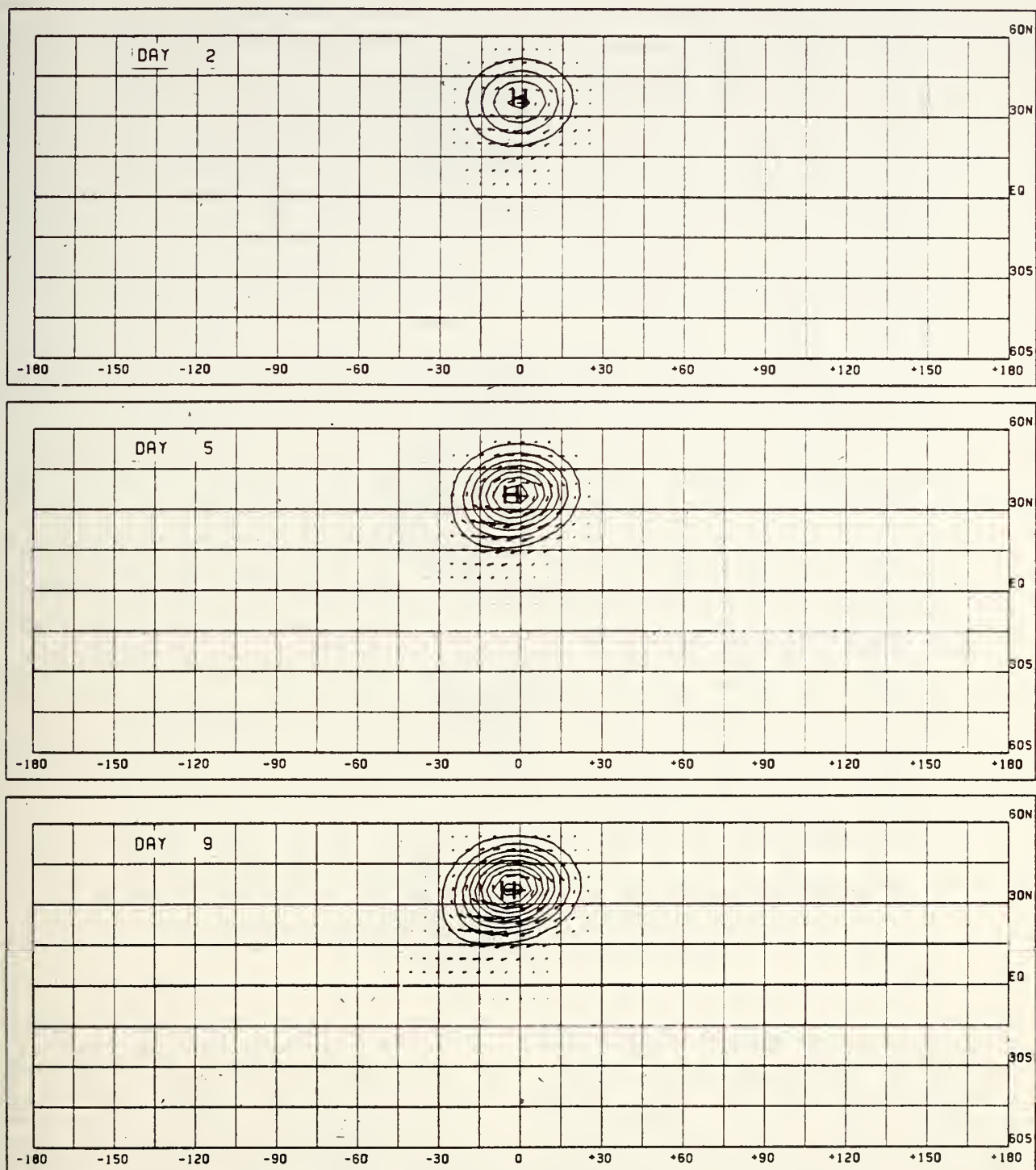


FIG. 5. Lower-level wind and geopotential response for a low-level mass source placed at 35°N, at days 2, 5, 9 for $\lambda = \alpha = 0.5$.

pressure often observed between these latitudes during the winter monsoon cold outbreaks over the Asian continent. Figs. 5 and 6 show the time sequence of the low-level response for days 2, 5, and 9 after the switch-on of the pressure perturbation for cases (a) and (b), respectively. In both cases, the flow adjusts

to the pressure perturbation rapidly with strong anticyclonic outflow from a gradually-developing high pressure center. At the end of day 9, a steady state is attained with the anticyclone well developed on the western margin of the cooling center. Such a feature is commonly observed for quasi-stationary

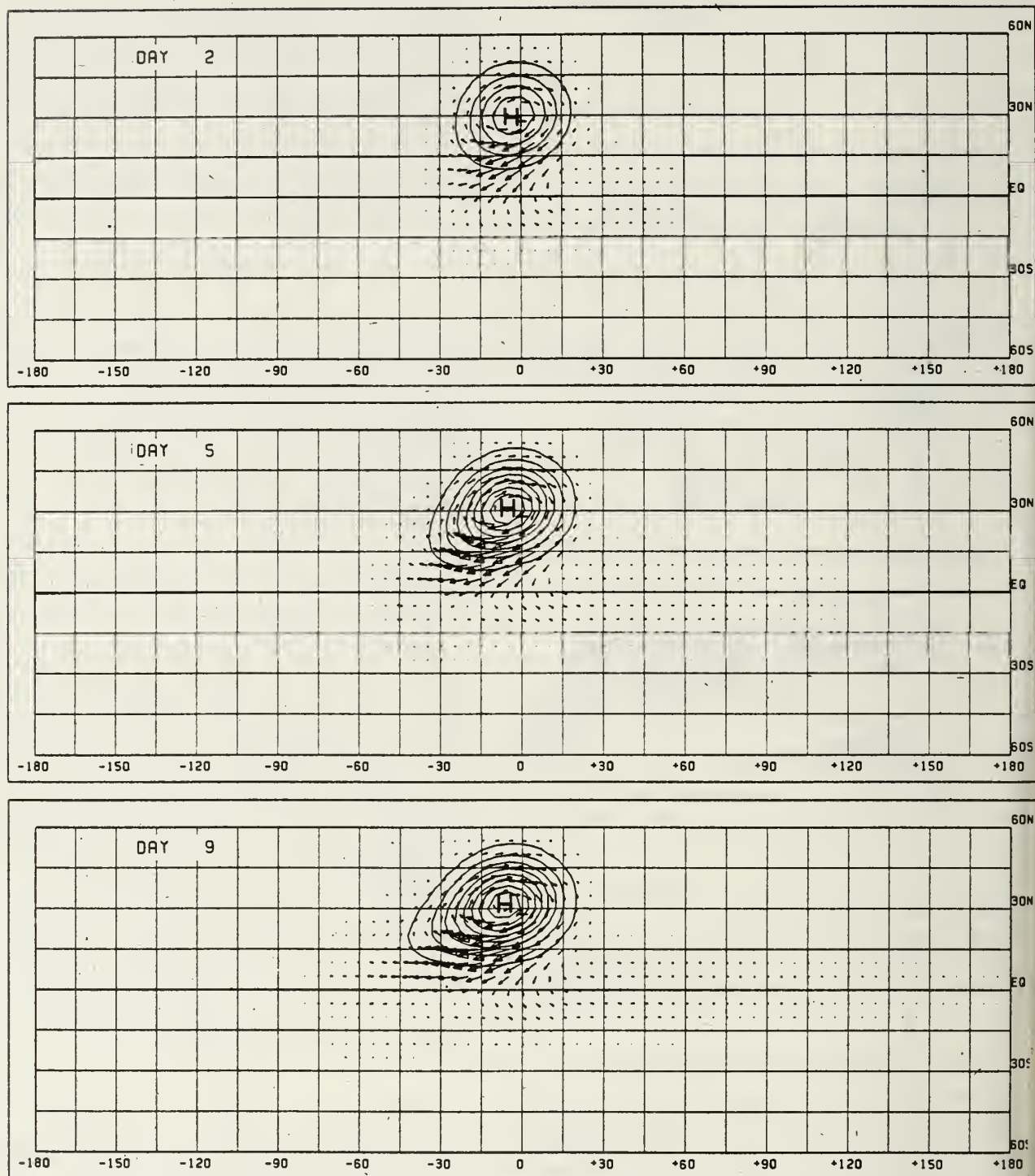


FIG. 6. As in Fig. 5 except for a mass source at 27°N.

anticyclones (Wexler, 1951; Ramage, 1975). An outstanding feature in the time evolution is the appearance of a northeast-southwest tilt in the wind and pressure fields. In the steady state, the phase tilt becomes very pronounced, especially for case (b) where the forcing is located at the lower latitude. This is

not surprising because the higher Rossby waves which account for most of the amplitude of the response away from the equator, have smaller westward phase speed. Therefore, they tend to remain in the vicinity but to the west of the source region. Conversely, the lower-order modes ($n = 1, 2$), which

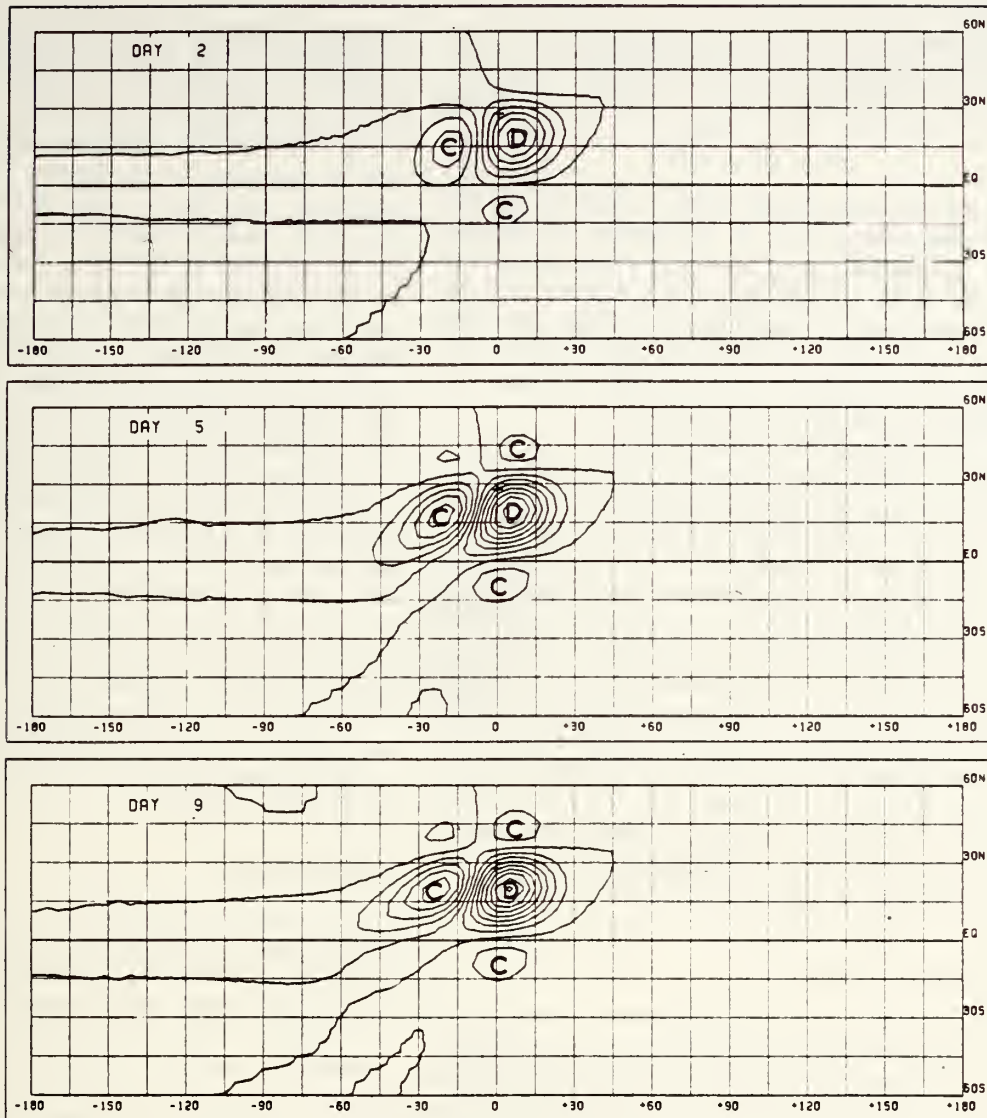


FIG. 7. Divergence of the lower-level wind field as a result of the mass source at 27°N . The letters C, D denotes convergence and divergence respectively.

have large amplitude close to the equator, propagate with relatively fast phase speed toward the west. In other words, the dispersion of the various modes excited creates the appearance of the northeast-southwest phase tilt. The same tilt was noticed in the numerical simulation of heat-induced tropical motion by Webster (1972, 1981) and also in the observational study of Krishnamurti *et al.* (1973). Although there are certain similarities in the responses for the two cases there are important differences. In case (b) (Fig. 6), the gravest equatorial modes have larger amplitudes and propagate further downstream, thus giving the appearance of a more pronounced northeast-southwest tilt. Also obvious in case (b) is the presence of an eastward-propagating Kelvin mode which becomes strongly developed at day 9.

In reality, the duration of a monsoon surge period is highly variable. Typically, a surge can last for 3 or 4 days, although the occurrence of sub-stained surge periods made up of two or more successive or overlapping surges are not uncommon. Therefore, in Fig. 6, while the flow field at day 2 which depicts a strong northerly component is typical of the initial development for a single surge case, the flow at days 5–9 can be compared to that during a sustained surge period.

Also of interest is the low-level horizontal divergence associated with these flow fields (Fig. 7). As expected, an intense positive divergence area indicating subsidence is found near the source region. The divergence center is, however, on the southeast quadrant of the source region. This can be under-

stood by the following vorticity consideration. In the approach to steady state, the principal balance in the vorticity of the flow away from the equator is given by

$$\beta v + f \nabla \cdot \mathbf{v} = 0. \quad (36)$$

Because the anticyclonic center is displaced to the west of the mass source, βv is negative on the east side of the center. As a result the local vortex line has to shrink ($\nabla \cdot \mathbf{v} > 0$) in order to achieve the balance. Equatorwards, since f decreases, the same balance has to be achieved by a stronger low-level divergence, thus creating a divergence maximum on the southeast side of the mass source.

The same arguments explain the presence of low-level convergence areas found to the west and the south in the near-equatorial regions of the Southern Hemisphere. Further experiments (not shown) with different latitudinal locations of the forcing indicate that the equatorial responses have significant amplitudes only when the forcing is placed at sufficiently low latitudes ($\leq 27^\circ$). This is consistent with the observation by Riehl and Somervell (1967) that rapid surges in the northeast trade winds over the South China Sea are often preceded by a high-pressure system moving out to sea along the southeast China coast at $20\text{--}30^\circ\text{N}$. The low-level convergence induced at the equatorial region implies rising motion ahead of the subsiding monsoon outflow air and thus could favor the development of convection there.

6. Equatorial response

While there is increasing evidence to suggest that near-equatorial disturbances intensify as a result of the incursion of monsoon air into equatorial latitudes, the mechanism(s) leading to the intensification is not apparent. At this stage, it is not unreasonable to speculate that the induced low-level convergence in the equatorial regions may provide an environment conducive to the enhancement of convective activity.

Given the connection between the increased convection at equatorial latitudes and the occurrence of a monsoon surge, we can study the equatorial response by specifying the following forcing functions:

$$Q(x, y, t) = H(t) \exp[-(y - y_c)^2 \lambda^2 - \alpha^2 x^2] - bH(t - \tau) \exp[-(y - y_c)^2 \lambda^2 - \alpha^2 x^2], \quad (37)$$

where we use $\lambda = \alpha = 1/2$, $b = 1/2$, $y_c = 2.7$ and $y_c = -0.6$, corresponding to a low-level mass source (cooling) at 27°N and a mass sink (heating) at 6°S . The lag time τ is set at 36 h for the switch-on of the equatorial heat source to simulate a delayed equatorial response after the abrupt pressure rise at 27°N . The time lag is chosen to agree with the following observations. Chang and Lau (1980) showed that the equatorial response followed immediately (≤ 1 day)

after a cold surge as defined by a surface temperature minimum in Hong Kong. A surface pressure rise at $\sim 25\text{--}30^\circ\text{N}$, however, preceded the Hong Kong temperature minimum by $1\frac{1}{2}\text{--}2$ days.

Fig. 8 shows the time sequence of the low-level flow in response to the forcing (37). It should be compared with Fig. 6 where the equatorial forcing is omitted. At day 2, where the equatorial heat source has been turned on for 12 h, the inflow into the low center joins with the northeast winds from the monsoon surge, thus extending the northerly flow into the Southern Hemisphere convergence region. As the equatorial disturbance becomes fully developed at day 9, the equatorial inflow becomes more zonal and more extensive in the east-west direction, as a result of the excitation of Kelvin modes with surface easterlies to the east and Rossby modes with surface westerlies to the west. Because of the proximity of the heating to the equator, the equatorial response shows the characteristics of a Walker-type circulation. The steady-state situation agrees well with the observed mean winter low-level circulation over the Borneo-Indonesia region (Newell *et al.*, 1972).

The extent and horizontal structure of the Walker and Hadley circulations and the associated vertical motion is best visualized by considering the total low-level divergence field.

a. Hadley cells

The strongest Hadley-type overturning is concentrated about the longitude of the forcing (Fig. 9). In contrast to the southeastward displacement of the divergence center with respect to the forcing, the convergence center is almost coincident with the equatorial heat source. This is expected because of the decreasing effect of rotation with decreasing latitude. In the equatorial regions, the main balance is between the diabatic heating and the adiabatic cooling generated by the upward motion expressed here by

$$\nabla \cdot \mathbf{v} = Q(gh). \quad (38)$$

As a result of this latitude difference in dynamical balance, the axis of the Hadley cell has a slight northeast-southwest tilt.

Compared with Fig. 7, the divergence centered at $\sim 18^\circ\text{N}$ is enhanced by the inclusion of the equatorial heat source. Within the tropics the induced Hadley circulation also leads to the enhancement of the northerly wind component (Fig. 8). However, this feedback does not extend far enough poleward to have any significant influence in higher latitudes. This, however, may not be true in reality because at higher latitudes the equatorial β -plane is no longer a valid approximation. The numerical experiments of Webster (1981) using a spherical model showed that the effect of a diabatic heat source in the tropics

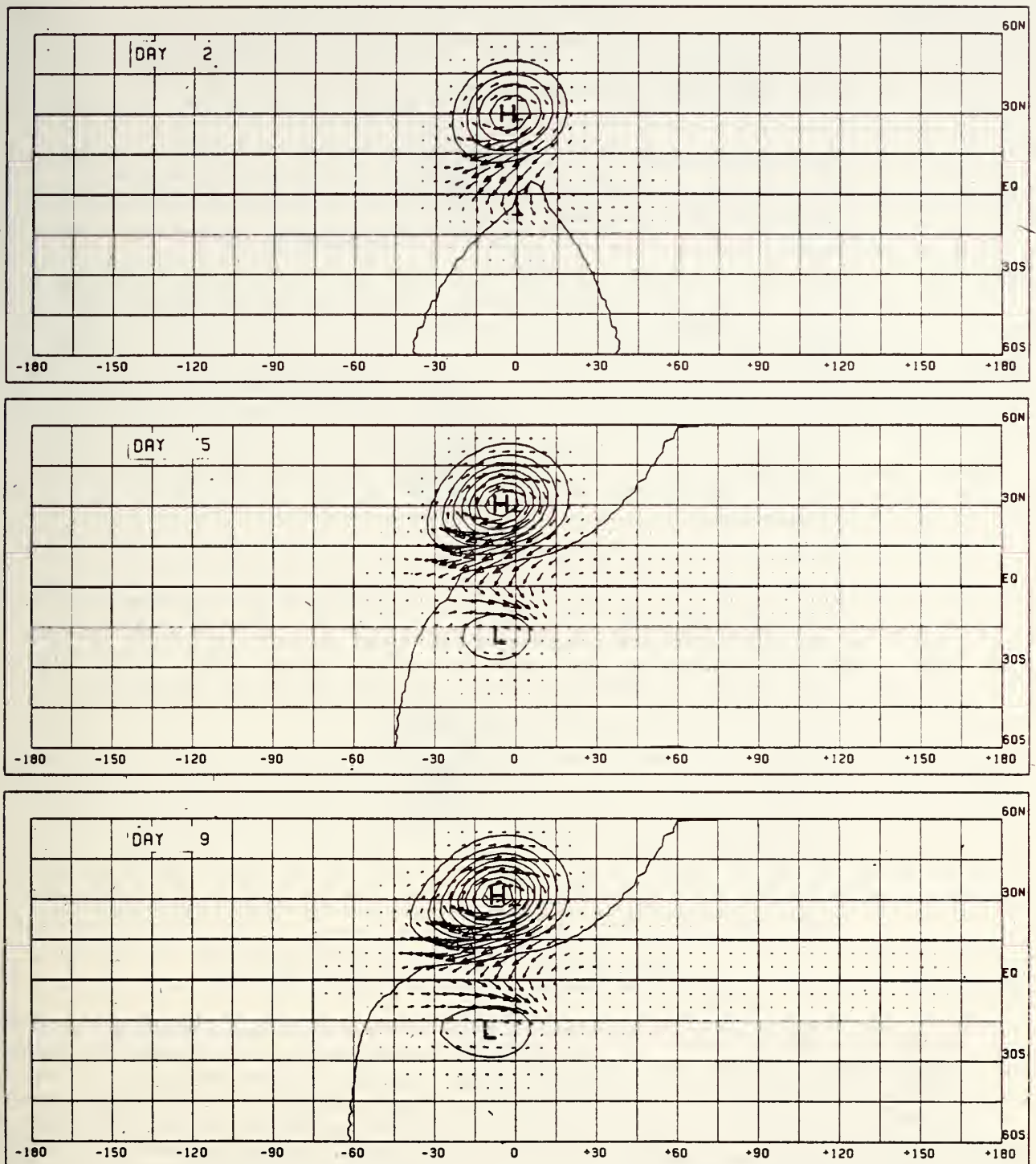


FIG. 8. Low-level wind and geopotential response for heating corresponding to a sudden turn-on of a mass source at 27°N and an equatorial heat source of 5°S, 36 h later with $\alpha = 0.5$.

can indeed cause wave energy to propagate into higher latitudes, given suitable mean zonal wind distributions.

An interesting and somewhat surprising feature in the time evolution of the divergence field (Fig. 9) is the generation of a secondary Hadley-type cir-

ulation $\sim 30^\circ$ west of the longitude of the forcings. This secondary cell has a reverse polarity compared with the primary cell and a pronounced northeast-southwest tilt, evidence of forcing by Rossby waves emanating from the source regions. The presence of a similar "reverse local Hadley cell" had been sug-

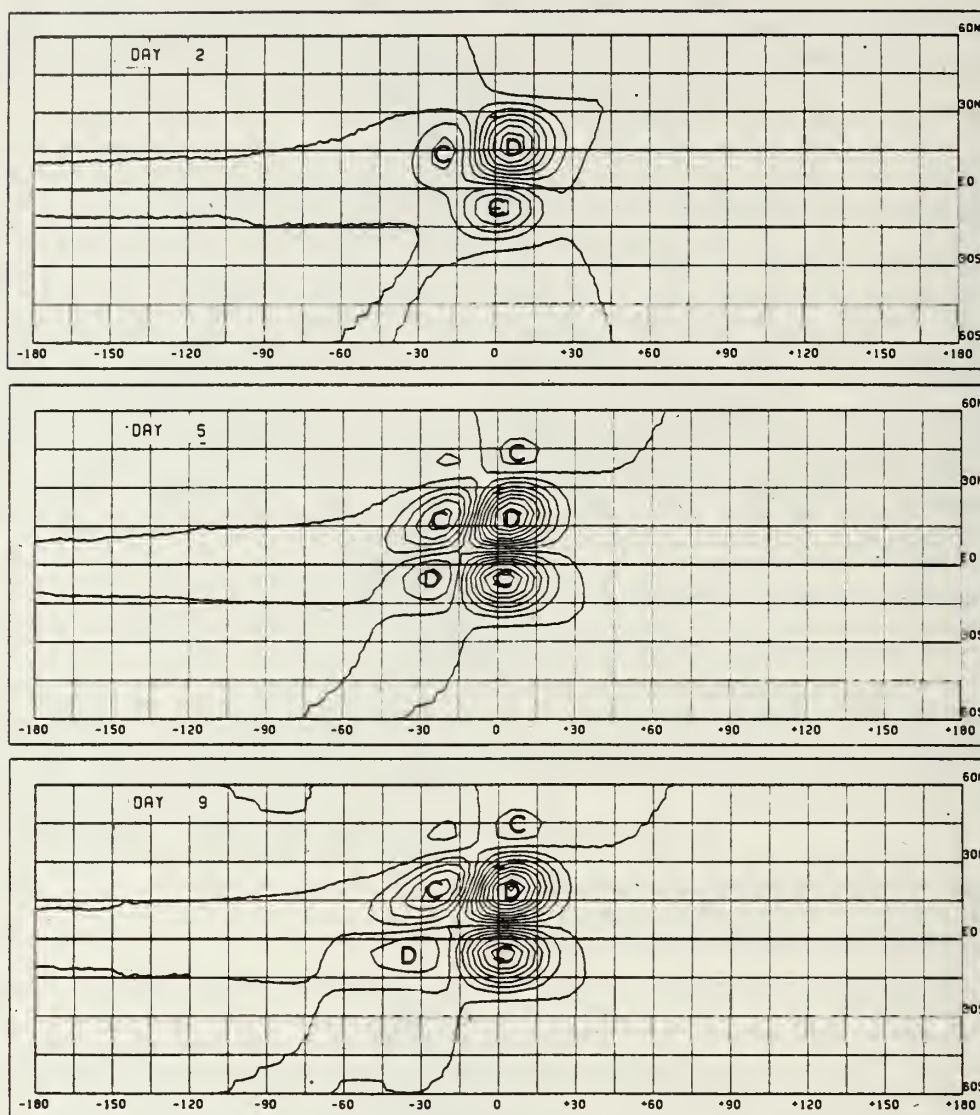


FIG. 9. As in Fig. 8 except for the low-level divergence field. C and D denotes convergence and divergence, respectively.

gested by Chang and Lau (1980), although their reverse cell is found $\sim 60^\circ$ west of the forcing region. Because of this discrepancy, even if the reverse cell arises by the mechanism suggested here, other factors such as the effect of the mean zonal wind and/or effects of midlatitude origin may be necessary to account for its observed locations.

b. Walker cells

The presence of divergent/convergent centers to the west of the source regions imply the presence of two east-west cells at the latitudes of the sources. For the equatorial branch, widespread subsidence is also induced to the east (see also Fig. 8) by Kelvin waves. It is clear that judging from the strength of the divergent/convergent centers that while the east-

ward branch of the cell possesses a larger horizontal extent, the total low-level mass inflow is considerably less than the westward branch. In other words, a steady equatorial forcing will exert more influence to the west than to the east. This agrees with the findings of Krueger and Winston (1973) that a large part of the mass outflow from the Indonesia-Borneo convections is carried off towards the west over the Indian Ocean. However, observations (Krishnamurti *et al.*, 1973) showed that the two east-west cells on each side of the Indonesia-Borneo region are approximately equal in extent, with the westward branch crossing Africa into the eastern Atlantic and the eastern branch ending near the mid-Pacific region.

A clue to the possible cause of the discrepancy may be found in the effect of the zonal mean wind

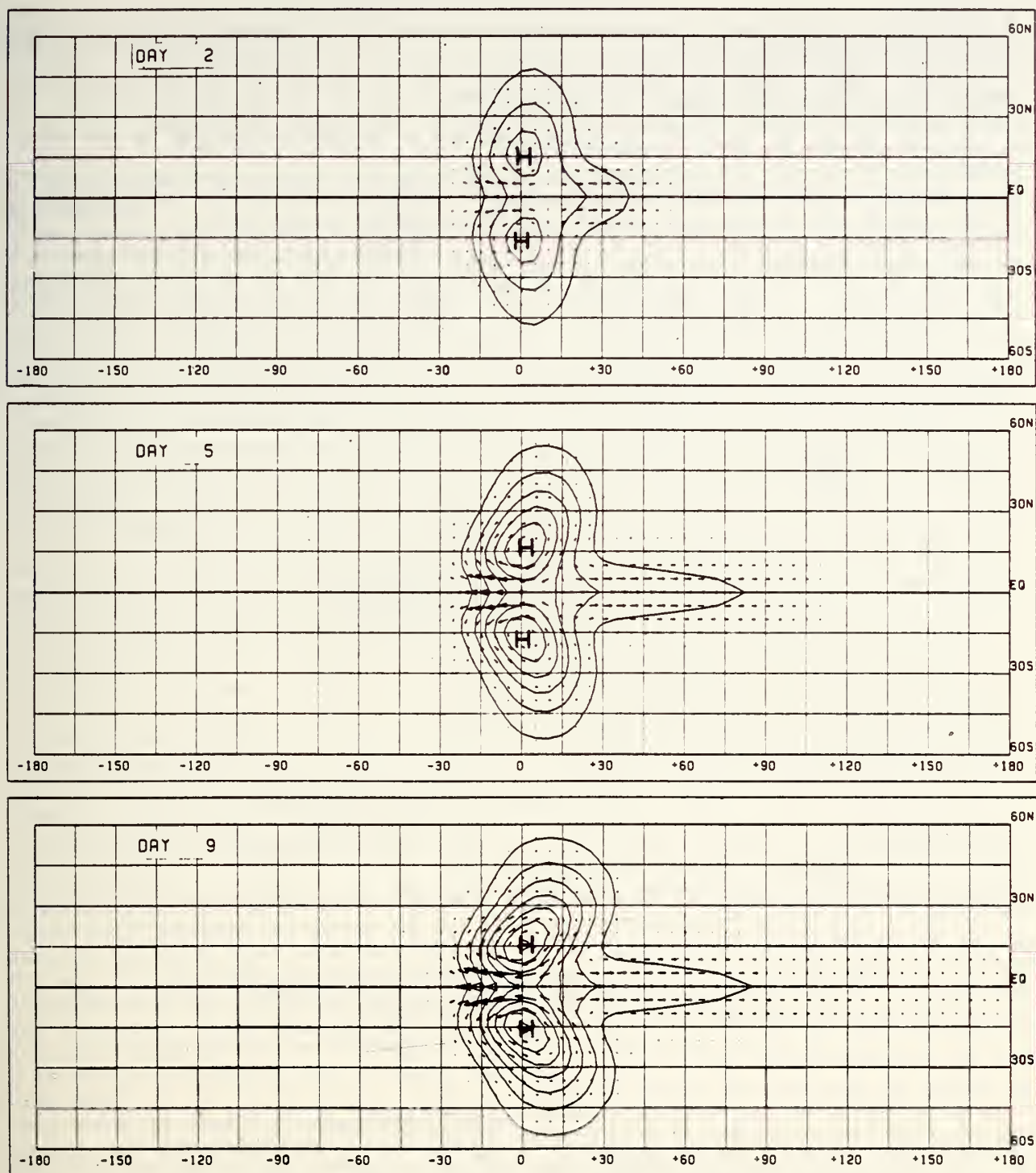
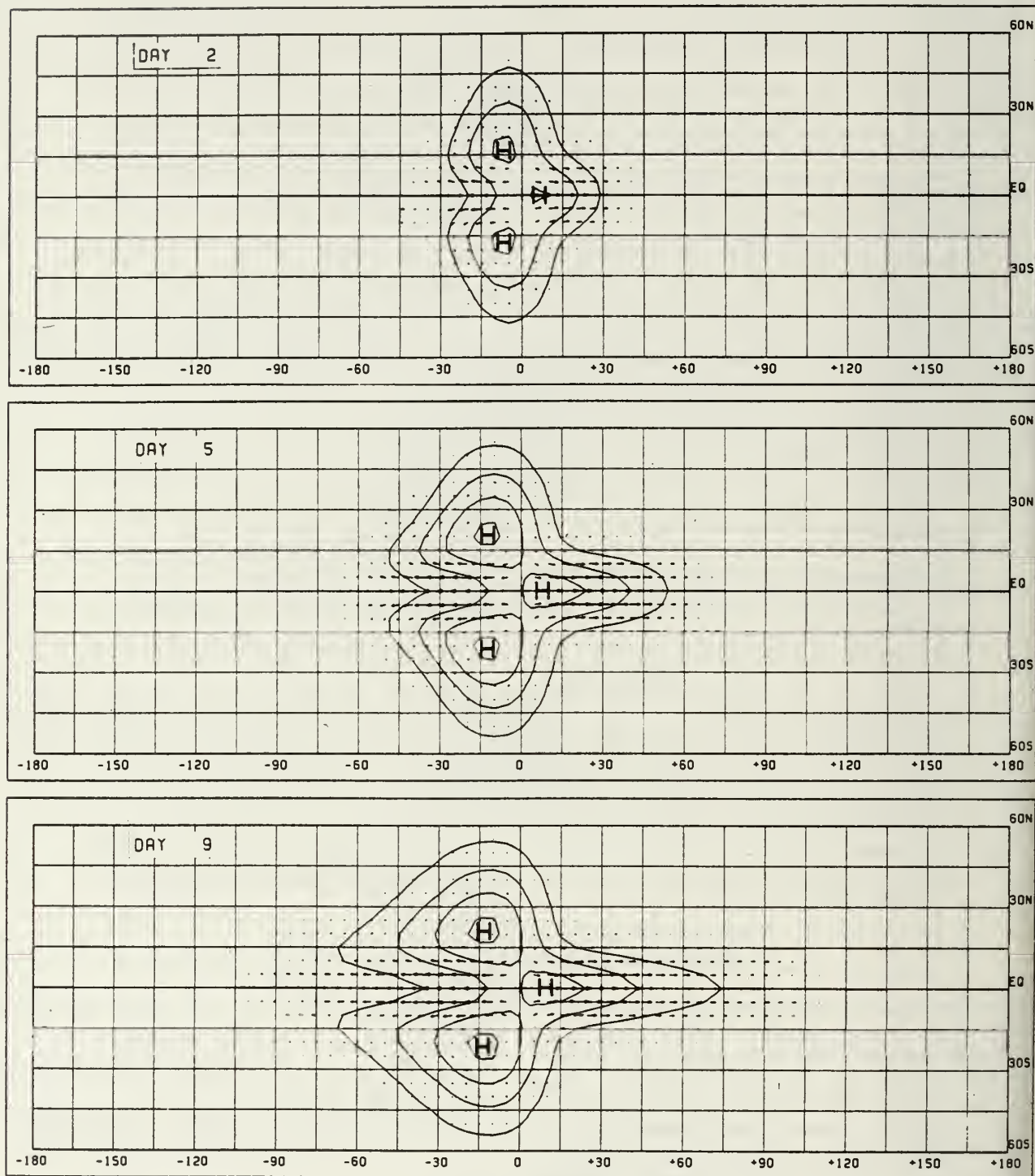


FIG. 10. As in Fig. 3, except for a heating function of the form $Q = \exp[-\frac{1}{4}x^2 + (y^2/9)]H(t)$, in the presence of a mean wind $U = 0.3$.

on these circulations because the Indonesia-Borneo region is dominated in the wintertime by a broad region of upper level easterlies of 5-10 m s^{-1} strength, covering a large part of the east-west extent of these zonal circulations. This leads us to the subject of the next section.

7. Effect of zonal mean wind

Going back to the solutions (22)–(25), it is apparent that they become indeterminate at the stationary resonant condition, i.e., $U + 1 = 0$ or $U = c_n$. Using the asymptotic expansion

FIG. 11. As in Fig. 10 except the mean wind is $U = -0.3$.

$$\text{Erfc}(z) \sim (\sqrt{\pi}z)^{-1} \exp(-z^2), \quad (39) \quad \psi_{n+1}(x, t) = \frac{1}{\epsilon} [1 - \exp(-\epsilon t)] \frac{nq_{n+1} + q_{n-1}}{2n+1}$$

the resonant solutions of (22)–(25) are given by

$$\psi_0(x, t) = \frac{1}{\epsilon} [1 - \exp(-\epsilon t)] q_0 \exp(-\alpha^2 x^2), \quad (40)$$

$$\times \exp(-\alpha^2 x^2), \quad n \geq 1. \quad (41)$$

As expected, the resonant responses become completely localized since they no longer propagate. For

small ϵ , (40) and (41) become

$$\psi_0 \approx tq_0 \exp(-\alpha^2 x^2), \quad (42)$$

$$\psi_{n+1} \approx t \frac{nq_{n+1} + q_{n-1}}{2n+1} \exp(-\alpha^2 x^2), \quad (43)$$

i.e., the amplitude of the resonant mode grows linearly with time.

Figs. 10 and 11 show the effect of the mean wind on the upper level flow for $U = +0.3$ and $U = -0.3$, respectively. To illustrate the effect on the various modes, we use a forcing centered at the equator but with a y -scale of 1.5 times the equatorial Rossby radius. At day 2, when the response is still somewhat localized, the effect of the mean wind is not very prominent, but further developments at days 5 and 9 show large differences in the structure and amplitude of the response between the two cases. In the westerly regime (Fig. 10), the local response is very strong, because the gravest resonant mode, which has westward phase speed of $1/3$, is close to resonance at $U = +0.3$. While there is no disturbance to the west, the Kelvin wave to the east propagates further downstream, giving the appearance of an elongated but much weakened circulation. Some indication of eastward propagation of the higher-order Rossby modes can also be envisaged.

In contrast, in the easterly regime ($U = -0.3$), the wind becomes increasingly zonal ($u \gg v$) on both sides of the source regime, with the "Pacific Walker cell" appearing more concentrated and more intense than in the westerly regime. The longitudinal extents of the two branches are now approximately equal. The above results therefore suggest that for a given equatorial forcing, the establishment of equatorially-trapped circulation is favored by the presence of a mean easterly wind. Bennet and Young (1972) showed that a basic zonal flow moving westward relative to a midlatitude wave disturbance will inhibit the wave from penetrating the tropics because of energy absorption due to resonance. Our result shows that a reciprocal relation may also hold, i.e., an equatorially-forced disturbance will remain trapped more readily in an easterly than a westerly zonal mean wind.

In reality, the effect of the mean zonal wind on the east-west circulation is expected to be more complicated because of the presence of horizontal wind-shear which would alter the properties of the basic equatorial modes (e.g., Boyd, 1978). But if we focus on the large-scale circulation close to the equator where the local mean wind shear is small, the above analysis may provide a clue to the observed extent of these low-latitude circulations.

8. Conclusions

Many large-scale features of the thermally driven calculations in the tropical atmosphere have been

reproduced using a "long-wave," shallow-water β -plane model with time-dependent forcings. These features can be interpreted in terms of basic characteristics of equatorial Rossby and Kelvin modes. Responses to the west of the source regions are forced Rossby waves and to the east at low latitudes, Kelvin waves. Results show that there are two basic regimes in which the tropical atmosphere can respond to specific diabatic heat sources. The Walker regime, which is excited by heating symmetric about the equator, is identified with the Kelvin and the gravest symmetric Rossby mode ($n = 1$) and is characterized by a strong equatorially-trapped response with $u \gg v$. In contrast, the Hadley regime, which is excited by antisymmetric heating, shows strong cross-equatorial flow and is a manifestation of antisymmetric Rossby modes. In reality, the geography of the Asiatic continent including India and the adjacent oceanic regions provide heat sources and sinks somewhat antisymmetric about the equator and therefore can support a strong local Hadley-type circulation. In the winter monsoon season, when the equatorial heat source is located at $\sim 6^\circ\text{S}$ over the Borneo-Indonesia area, substantial energy also goes into the Walker-type of symmetric mode, so that the Hadley and the Walker circulations both appear strong. The eastward propagation of a Kelvin wave mode in our solution is particularly interesting in view of the recent findings by Williams (1979) which showed the possibility of an eastward-propagating disturbance trapped near the equator originating from an enhanced equatorial heat source following a cold surge event.

An important result from this study is that a *steady* heat source near the equator exerts considerably more influence to the west than to the east. However, while this result agrees with the observation of Krueger and Winston (1975), it does not belie the importance of the eastward branch or the Pacific Walker circulation. The earlier works on equatorial planetary-scale circulation (e.g., Krueger and Winston, 1973, 1975; Krishnamurti, *et al.*, 1973) showed that alternate heat sources and sinks exist along the entire equatorial belt. The much stronger and more extensive oceanic heat sink over the central and eastern Pacific than that over the Indian Ocean will contribute to a stronger Pacific Walker cell than predicted here. Further, our results demonstrate that the presence of a mean *easterly* wind favors the formation of equatorially-trapped Walker-type circulations.

Finally, it should be pointed out that the use of a shallow-water system to study tropical motions may be criticized as being overly simplified, because most tropical systems are not barotropic in nature and generally involve complex diabatic processes such as cumulus convection. However, to some extent this problem has been alleviated by taking the view of a two-layer baroclinic system for the shallow-

water equations (Matsuno, 1966). This approximation is justified because it had been shown that in a tropical baroclinic atmosphere, the effect of cumulus friction tends to alter equatorial wave behavior such that the vertical scales of the low-frequency modes is comparable to the depth of the troposphere (Chang, 1977). The next logical step is to extend this study to truly baroclinic models. Such work will provide useful guidance for the analysis and interpretation of the Winter-MONEX data.

Acknowledgments. Thanks are due to Professor C. P. Chang for discussions related to the paper. Part of this work was performed while one of the authors (KML) was at the Department of Meteorology, Naval Postgraduate School, Monterey, CA. This research was supported by the Climate Dynamics Section, National Science Foundation under Grant ATM 79-24010, and the Global Atmospheric Research Program under Grant ATM 80-13153.

REFERENCES

- Bennet, J. R., and J. A. Young, 1972: The influence of latitudinal shear upon large-scale wave propagation into the tropics. *Mon. Wea. Rev.*, **99**, 202-214.
- Boyd, J. P., 1978: The effects of latitudinal shear on equatorial waves, Part II: Application to the atmosphere. *J. Atmos. Sci.*, **35**, 2295-2267.
- Chang, C. P., 1977: Viscous internal gravity waves and low frequency oscillation in the tropics. *J. Atmos. Sci.*, **34**, 901-910.
- , and K. M. Lau, 1980: Northeasterly cold surges and near-equatorial disturbances, Part II: Planetary-scale aspects. *Mon. Wea. Rev.*, **108**, 298-312.
- , and —, 1982: Short-term planetary scale interactions over the tropics and midlatitudes. Part I: Contrast between active and inactive periods. *Mon. Wea. Rev.*, **110** (in press).
- Danielson, E. F., and F. P. Ho, 1969: An isentropic trajectory study of a strong northeast monsoon surge. Sci. Rep. No. 2, AFCRL-69-0036, Hawaii Institute of Geophysics, 13 pp. [Available from Dept. Meteor., University of Hawaii, Honolulu 96822.]
- Gill, A. E., 1980: Some simple solutions for heat-induced tropical circulation. *Quart. J. Roy. Meteor. Soc.*, **106**, 447-462.
- Krishnamurti, T. N., N. Kanamitsu, W. J. Koss and J. D. Lee, 1973: Tropical east-west circulations during the northern winter. *J. Atmos. Sci.*, **30**, 780-787.
- Krueger, A. F., and J. S. Winston, 1973: A comparison of the flow over the tropics during the contrasting circulation regimes. *Mon. Wea. Rev.*, **31**, 358-370.
- , 1975: Large-scale circulation anomalies over the tropics during 1971-72. *Mon. Wea. Rev.*, **103**, 465-473.
- Lighthill, M. J., 1969: Dynamic response of the Indian Ocean to onset of the southwest monsoon. *Phil. Trans. Roy. Soc. London*, **265**, 45-92.
- Matsuno, T., 1966: Quasi-geostrophic motions in the equatorial area. *J. Meteor. Soc. Japan*, **44**, 25-43.
- Murakami, T., 1980a: Temporal variation of satellite-observed outgoing longwave radiation over the winter monsoon region. Part I: Long-period (15-30 day) oscillations. *Mon. Wea. Rev.*, **108**, 408-426.
- , 1980b: Temporal variation of satellite-observed outgoing longwave radiation over the winter monsoon region. Part II: Short period (4-6 day) oscillations. *Mon. Wea. Rev.*, **108**, 427-444.
- , and M. S. Unninayar, 1977: Atmospheric circulation during December 1970 through February 1971. *Mon. Wea. Rev.*, **105**, 1024-1038.
- Newell, R. E., J. W. Kidson, D. G. Vincent and G. J. Boer, 1972: *The General Circulation of the Tropical Atmosphere and Interaction with Extratropical Latitudes*. Vol. 1, MIT Press, 258 pp.
- Ramage, C. S., 1975: *Monsoon Meteorology*. Academic Press, 296 pp.
- , 1968: Role of a tropical maritime continent on the atmospheric circulation. *Mon. Wea. Rev.*, **96**, 365-370.
- Riehl, H., and W. J. Somervell, 1967: Weather sequence during the northeast monsoon. Navy Weather Research Facility, Tech. Rep. No. 7-67, 78 pp. [Available from Naval Environmental Prediction Research Facility, Monterey, CA 93940.]
- Webster, P. J., 1972: Response of the tropical atmosphere to local steady forcing. *Mon. Wea. Rev.*, **100**, 803-816.
- , 1981: Mechanisms determining the atmospheric response to sea surface temperature anomalies. *J. Atmos. Sci.*, **38**, 554-571.
- Wexler, H., 1951: Anticyclones. *Compendium of Meteorology*, T. F. Malone, Ed., Amer. Meteor. Soc., 621-629.
- Williams, M., 1979: Inter-hemispheric interaction during winter-MONEX. GARP Spec. Rep. 34, Rep. Sixth Planning Meeting for the Monsoon Experiment, pp. 16. [Available from WMO, Case postale No. 5, CH-1211 Geneva 20, Switzerland.]

Short-Term Planetary-Scale Interactions over the Tropics and Midlatitudes during Northern Winter. Part I: Contrasts between Active and Inactive Periods

C.-P. CHANG

Department of Meteorology, Naval Postgraduate School, Monterey, CA 93940

K. M. LAU

Goddard Space Flight Center, NASA, Greenbelt, MD 20771

(Manuscript received 22 October 1981, in final form 12 April 1982)

ABSTRACT

Objectively analyzed 200 mb winds of four winters are used to study the short-term (several days) teleconnections between planetary-scale circulation components over the monsoon region. The composited structures suggest that during very active northeasterly monsoon (surge) periods, the midlatitude and tropical circulation components vary in a coherent way. The jet streak and local Hadley circulation over East Asia, the divergent flow over the maritime continent, and the equatorial Walker circulations over the Pacific and Indian Oceans all strengthen steadily, while the secondary jet streak over West Asia weakens. During inactive (break) periods the midlatitude circulation components all exhibit reversed changes, while the variations in the tropics are less coherent, although still showing reversed tendencies. The results basically verify the short-term teleconnection model proposed by Chang and Lau (1980), but more complex processes in the acceleration of the midlatitude jet streaks are indicated. In addition, the contrast between the very active and break monsoon periods suggests the relative importance of tropical versus midlatitudinal forcings in different regions of the monsoon circulation.

1. Introduction

Ramage (1971) suggested that the occurrence of cold surges off the South China coast is related to an intensification of the local Hadley circulation over East Asia. Motivated by his observations, in a previous case study (Chang and Lau, 1980; hereafter referred to as CL) we carried out and presented preliminary results which suggest that several components of the planetary-scale circulations over the winter monsoon region may vary coherently on a time scale of several days to about two weeks. The variations encompass a vast area of both the tropical and midlatitude parts of Asia, as well as the equatorial Pacific and Indian Oceans and may be described by the following sequence of events:

- 1) The East Asia local Hadley circulation strengthens prior to a cold surge on the South China coast. This strengthening is accompanied by an intensified jet stream maximum centered over Japan, which is apparently a result of the upstream acceleration by the Coriolis torque of the upper-level poleward flow.

- 2) The jet stream maximum over Afghanistan-Pakistan varies inversely with the eastern jet maximum and appears to be related to a West Asia meridional circulation which becomes thermally indirect prior to the surge.

- 3) Immediately after a cold surge the convection associated with pre-existing synoptic-scale disturbances in the equatorial South China Sea intensifies, causing the East Asia local Hadley circulation to reach its maximum intensity and also strengthens two east-west (Walker) cells along the equator.

- 4) Shortly (≤ 1 day) after the surge the increased large-scale ascending motion over the equatorial South China Sea, due to the continued strong convective activity, contributes mainly to a further increase in the intensity of the two Walker cells.

The purpose of the present work is to extend the previous study by using a much larger data base. In this paper (Part I) a composite study of the strongest circulation variations in four winters is carried out. The variations include eight abnormally active periods of the northeast monsoon winds over Southeast Asia and five abnormally inactive periods, each period lasting 5–8 days. The active periods are manifested by occurrences of very strong cold air surges off the South China coast in the lowest 1–2 km of the atmosphere, while the inactive periods are characterized by unusual occurrences of sustained southerly surface winds over the South China Sea. The former will also be referred to as the surge periods and the latter as the break periods of the monsoon. A contrasting comparison of the planetary-scale circulation in the two periods brings out the salient

TABLE 1. Area-averaged parameters

Parameter	Data and area	Circulation component represented
U_J	200 mb zonal wind over Japan and vicinity	East Asia jet streak
U_I	200 mb zonal wind over India-Afghanistan	West Asia jet streak
U_W	200 mb zonal wind over equatorial Indian Ocean	Western Walker circulation
U_E	200 mb zonal wind over equatorial Pacific	Eastern Walker circulation
V_N	200 mb meridional wind over East Asian coastal region and western Pacific	Southerly flow south of the East Asia jet streak
D	200 mb divergence over maritime continent or equatorial Pacific	Large-scale deep convection in the major heat source region
V_S	Surface meridional wind over northern South China Sea	Surge and break index

features of the coherent interrelationships between the various components of the circulations as well as some important questions. In a subsequent paper under preparation (Part II), data from the 1978-79 Winter Monsoon Experiment (Winter MONEX) will be composited to study the cold surge cases in detail. The surges during the Winter MONEX are mostly of only weak to moderate intensities, but apparently due to interannual changes the circulation regime is somewhat different in 1978-79 compared to 1973-76. This difference plus the much improved data available during MONEX sheds additional light on the short-term planetary scale teleconnections during winter.

2. Data and procedure

The periods of study are the four winters (November-February) of 1973-74, 1974-75, 1975-76 and 1978-79 (Winter MONEX). The winters of 1976-77 and 1977-78 are excluded because of the relative weakness of their northeast monsoons resulting in the absence of any strong cold surges. The 1978-79 winter monsoon was also weaker than normal but it was slightly more developed than 1976-78 according to our surge criteria.

The data used are the surface and 200 mb winds obtained from the global band objective analysis produced by the Fleet Numerical Oceanographic Center (FNOC). These winds are available twice daily on a 49×144 Mercator grid between 40°S and 60°N around the tropical belt. The zonal (u) and meridi-

onal (v) velocity components at 200 mb are also used to compute the vorticity, divergence, streamfunction (ψ) and velocity potential (χ) according to the following equations:

$$\nabla^2\psi = \zeta = \left(\frac{\partial v}{\partial x} - \frac{\partial u \cos\phi}{\cos\phi \partial y} \right) \sec\phi, \quad (1)$$

$$\nabla^2\chi = -\delta = -\left(\frac{\partial u}{\partial x} + \frac{\partial v \cos\phi}{\cos\phi \partial y} \right) \sec\phi. \quad (2)$$

where the horizontal coordinates in the Mercator projection are

$$x = a\lambda, \quad y = a \ln \left(\frac{1 + \sin\phi}{\cos\phi} \right).$$

Here a is the radius of the earth, and λ and ϕ are longitude and latitude, respectively. To solve (1) and (2), we use a method similar to that proposed by Hawkins and Rosenthal (1965) by assuming $\chi = 0$ at the lateral boundaries (40°S and 60°N) and deriving the boundary values of ψ after compositing the χ field.

Time series of seven area-averaged motion parameters are constructed to study the time variation of the various circulation components. Table 1 lists these parameters and the circulation components they are used to represent, and Fig. 1 shows their respective areas. Because a considerable change in the mean position of the upper tropospheric outflow is observed between the early and late winter, the area over which the divergence parameter is averaged is changed from D for November-December to D' for January-February in accordance with the seasonal patterns. Moreover, for the 1978-79 winter the area further shifts eastward into the equatorial Pacific area of D_x apparently signifying interannual planetary-scale changes in the tropics.

The area-averaged northerly component of the surface winds over an area just off the southern China coast ($18^\circ\text{--}20^\circ\text{N}$, $110^\circ\text{--}120^\circ\text{E}$), V_S , is used as an index to determine the timing of the major circulation changes, both for the active monsoon surge periods and for the break periods. Due to the highly aperiodic and variable nature of the cold surges (Chin, 1969; Murakami, 1979), the choice of a time reference with respect to a cold surge occurrence for the purpose of compositing can be difficult. Compounding this problem is the generally marginal quality of the upper air data over tropical Southeast

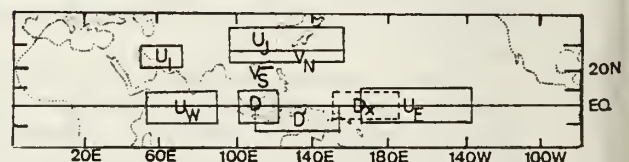


FIG. 1. Map showing different areas over which the parameters indicated are averaged. (See text and Table 1 for details.)

Asia and the adjacent oceans. Therefore our composites of the active periods include only the surge cases which are both strong and sustained. Since CL suggests that the FNOC objective analysis is capable of revealing physically meaningful large-scale fluctuations, selection of these strong cases assures that the equatorial responses will give the most identifiable signals that can be clearly distinguished from the inherent noise levels in the data.

Using the time series of our index V_S , an active surge period in this paper is defined by the following: 1) an increase in the area-averaged northerly surface wind of $>5 \text{ m s}^{-1}$ over 12–24 hours, and 2) a period of three or more days over which the increased northerly wind speed attained in 1) is $\geq 7 \text{ m s}^{-1}$. A break period is defined by: a) a decrease of the northerly wind to $\leq 2 \text{ m s}^{-1}$ (often leading to southerly winds), and b) a period of six or more days over which the change in a) is sustained. The criteria for the surge are more stringent than those defined by the First GARP Global Experiment (FGGE) Implementation Operation Plans (World Meteorological Organization, 1978).

With the above criteria for surges and breaks, respectively, eight strong surge cases (two in 1973–74, four in 1974–75, one in 1975–76 and one in 1978–79) and five break cases (one in each winter except for two in 1974–75) over the four winter seasons are chosen. A time series of each parameter (i.e., U_J , U_I , U_E , U_W , V_N , D) is then constructed for each case starting from 48 h prior to the occurrence of a surge or break, until the end of the particular period. The composited series are then obtained by simple averaging of all surge cases and break cases, respectively. Also prepared are the composited charts of the 200 mb velocity potential and streamfunction for different stages of the surge and break periods.

3. Results

a. Active (surge) periods

Fig. 2 shows the composite time series for the index V_S over the eight active or surge periods. As in all time series to be shown later, all quantities shown are deviations from their values at day 0, the onset of the surge. The averaged actual value for the period from day 0 to day 8 is also indicated beside each time series. Note that from our definition, the northerly wind speed can be small at the start of a surge provided the acceleration is large. This may differ considerably from some other surge criteria which are based on pressure rises or temperature falls (Chin, 1969). The sharp initial increase in northerly wind speed of $\sim 7.5 \text{ m s}^{-1}$ over two days is therefore a result of the choice of our surge criteria.

In Fig. 3, a coherent change in the time series of all the composited 200 mb parameters with respect

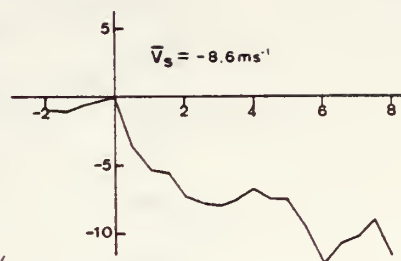
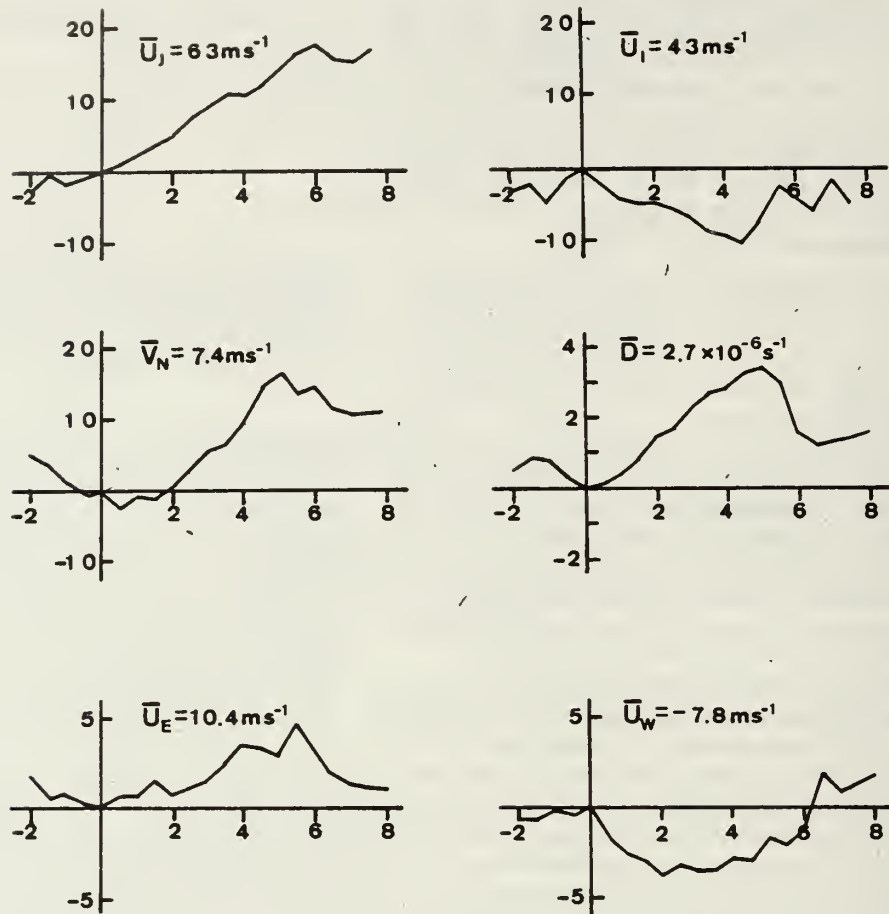


FIG. 2. Time series of composited V_S for the active (surge) cases. All quantities shown are deviations from their values at day 0. The overbar denotes time-averaged value within the period day 0–8. The abscissa is time (days). The unit for the ordinate is same as the unit of the averaged value.

to the onset of the surge is exhibited. From day 0 on, both the East Asia jet streak (U_J) and the tropical convective-area divergence (D) intensify steadily, the former by 18 m s^{-1} lasting over six days and the latter by $3 \times 10^{-6} \text{ s}^{-1}$ over five days, respectively. The West Asia jet streak (U_2), on the other hand, weakens by 10 m s^{-1} over four days. The upper level southerly wind south of the East Asia jet streak (V_N) also increases steadily by $\sim 15 \text{ m s}^{-1}$, but the starting time lags the onset of the surge by approximately one day. The two Walker cells also both show strengthening tendencies beginning from the surge onset, as indicated by a westerly acceleration of U_E (Pacific cell) and an easterly acceleration of U_W (Indian Ocean cell). The total speed increase is $\sim 4 \text{ m s}^{-1}$ for both cells, but the rates of acceleration are different, with the former at a more gradual rate lasting over five days, and the latter at a faster rate lasting only two days.

The foregoing results during the active periods are, in general, consistent with the model of a short-term teleconnection suggested by CL, with one exception—the slightly delayed increase of V_N . A possible explanation for this is that the southerly winds may increase due to the meridional circulation-inducing mechanism in the entrance region of the jet streak (Uccellini and Johnson, 1979). This mechanism may become important after the jet strengthens, thus causing a slight time lag in the increase of V_N . To investigate this possibility, we examined the 200 mb meridional wind changes south of the East Asia jet streak region by constructing composite v series averaged over five 5° -latitude bands between 0 – 25°N and 100 – 140°E . The results are shown in Fig. 4. Here it is seen that the slightly delayed southerly acceleration is well correlated down to 10°N , covering a much larger latitudinal span than just the immediate vicinity of the jet entrance. Thus the increase of the 200 mb southerlies is unlikely to be just a result of the jet entrance region mechanism. Fig. 4 also shows that the increase of the upper-level southerly flow in the equatorial latitudes starts almost immediately with the onset of the surge, co-

FIG. 3. As in Fig. 2 except for U_I , U_E , V_N , D , U_E and U_W .

inciding with the increase of the divergence over the tropical convective area (D). This equatorial increase therefore is likely a manifestation of the intensifying local Hadley circulation. The magnitude of this increase is on the order of 5 m s^{-1} , in good agreement with the $\sim 5 \text{ m s}^{-1}$ increase in the divergent component of V_N (not shown). Thus only about one-third of the total increase in V_N over the composited active period can be attributed to the strengthened local Hadley cell, and there is no time lag between this strengthening and the onset of the active period. The other two-thirds of the increase in V_N is in the rotational component and is of midlatitude origin. This also implies that it is the decrease in this midlatitude rotational component prior to and at the beginning of the active periods that causes the delayed increase of V_N .

To provide a horizontal perspective of the upper-tropospheric flow changes, we composited the 200 mb streamfunction and velocity potential fields for all surge cases except the one during Winter MONEX. The latter is excluded because the inter-annual change of the tropical divergence pattern, i.e., the shift from D to D_X , makes its inclusion in the

composite inappropriate. The seven surge cases included are divided into three periods by averaging the winds over five synoptic times centered at days 0, 2.5 and 5, respectively, in order to reduce noisy fluctuations especially over the tropics. The resultant composite ψ and χ fields for the three sequential periods are shown in Figs. 5 and 6. In Fig. 5 the composite zonal wind isotachs of 45, 55 and 65 m s^{-1} are also indicated. It is evident from this figure that after the surge onset there is a continued acceleration and an eastward extension of the jet core over East Asia and the western Pacific. A slight southward movement is also indicated.

Composites of the geopotential height field produced by FNOC's Northern Hemispheric analysis at 500 and 200 mb are shown in Figs. 7 and 8, respectively. At both levels, the existence of a fairly broad trough northwest of the East Asia jet streak causes the jet core to orient from west-southwest to east-northeast. This geometry results in a significant southerly rotational component which is part of the V_N parameter at 200 mb. The trough remains north of 40°N without any apparent movement at 200 mb even though the accelerating jet streak extends east-

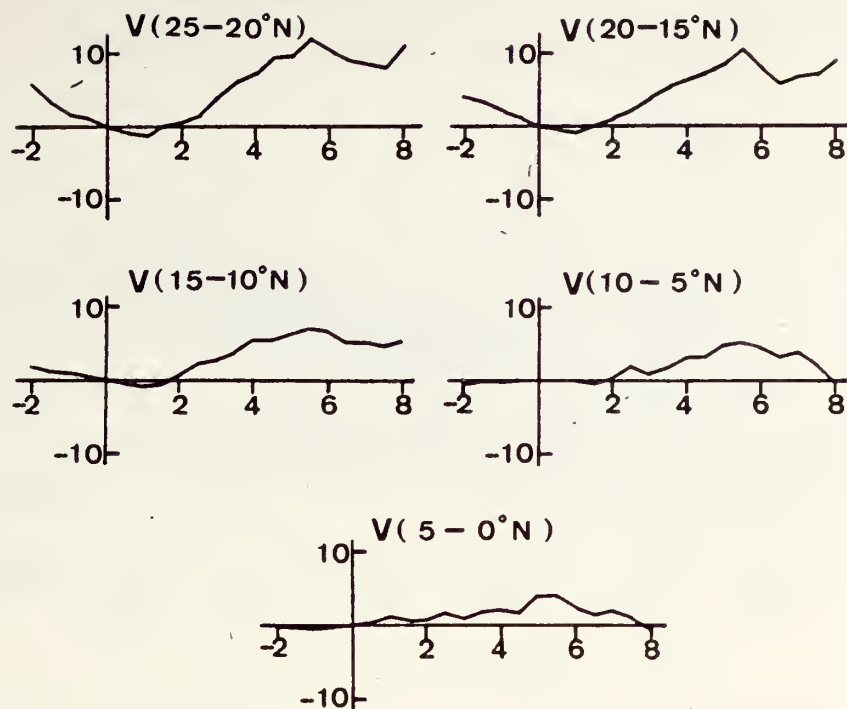


FIG. 4. As in Fig. 2 except for composited 200 mb v component averaged over five 5° latitudinal sections between $0\text{--}25^\circ\text{N}$ and $100\text{--}140^\circ\text{E}$.

ward (Fig. 5). On the other hand, at 500 mb the trough extends deeply into the subtropics and moves eastward with time.

In the tropics, the main anticyclonic ψ center over Southeast Asia (Fig. 5) also moves eastward by $\sim 20^\circ$ from the Indochina Peninsula to northern Philippines, signifying an eastward movement of the motion systems encompassing a large tropical and midlatitude area of East Asia.

The West Asia jet streak, which is the secondary (and much weaker) local jet maximum in the seasonal mean field, is not apparent in Fig. 5 because the jet over Pakistan–Afghanistan is weaker than its mean throughout the active monsoon periods. Nevertheless, a slackening of the zonal flow over this area from period 1 to 2 can be seen, in agreement with the U_7 time series shown in Fig. 3.

Fig. 6 gives a two-dimensional view of the increased intensity and organization of the upper-level divergence over the maritime continent from period 1 to 3 during the surges. Also, from the positive and negative centers of χ , one may infer the areas of upward and downward motions, respectively, and therefore the location and intensity of the local Hadley and Walker cells. The strengthening of the East Asia local Hadley circulation and the two Walker circulations on either side of the maritime continent is indicated by the increased gradient of χ . The local Hadley cell changes its orientation from southeast–northwest to south–north due to the eastward move-

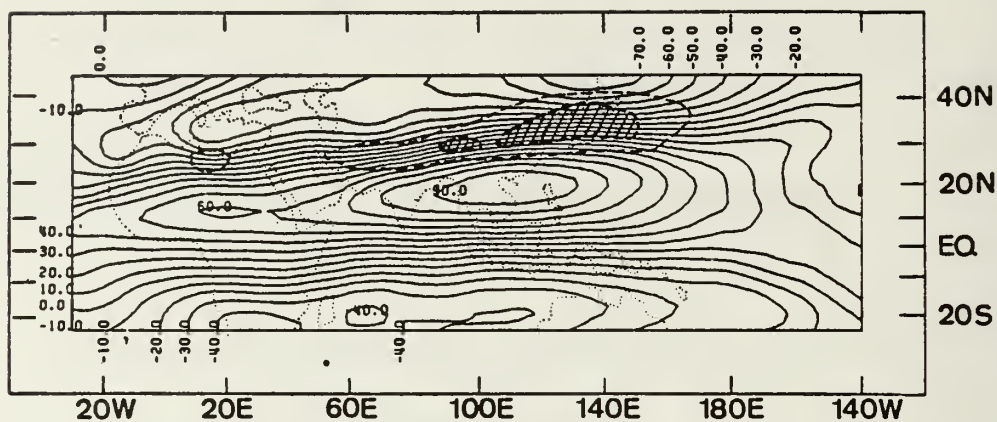
ment of the convergence center near 30°N and the relative stationarity of the tropical divergence center. The latter causes the local Hadley cell to remain upstream of the East Asia jet core. In the vicinity of the West Asia jet streak, no discernible systematic change of the divergent wind is detected.

The eastward movement of the East Asia jet core suggests that there should be an eastward progression of the acceleration of the 200 mb southerly winds if the jet entrance region mechanism is important in increasing the meridional circulation. We therefore separated the V_N parameter into five equal-area longitudinal sections and composited the five section-averaged v series with respect to the onset of the surges. The result (not shown) indicates a well correlated variation of the v series with largest coherent fluctuation in the central three sections, and there is no discernible time lag between the different longitudinal sections. This again indicates that the increased southerly V_N is not due to the jet entrance region mechanism.

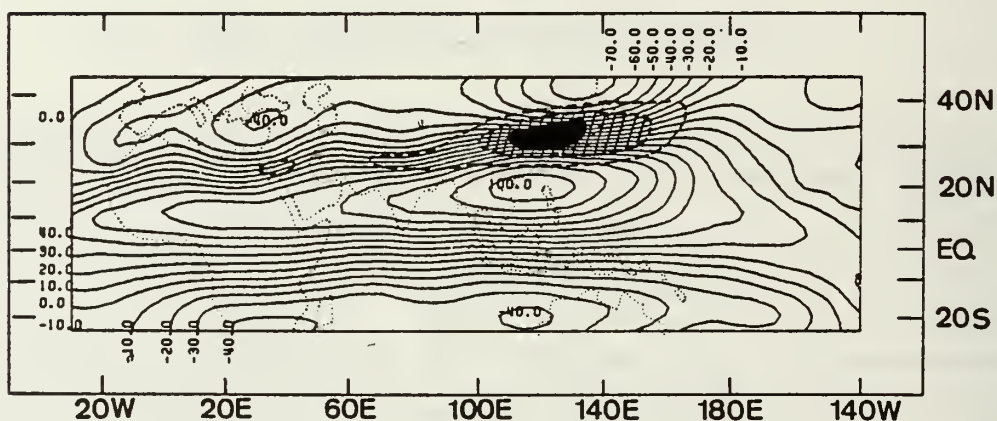
b. Inactive (break) periods

The composite time series for V_S over the five break periods are shown in Fig. 9. In contrast to the surge cases, our choice of the “onset” of the break (day 0) is not the exact time of the beginning of changes. The relaxation of the northerly surface wind over the northern South China Sea actually starts

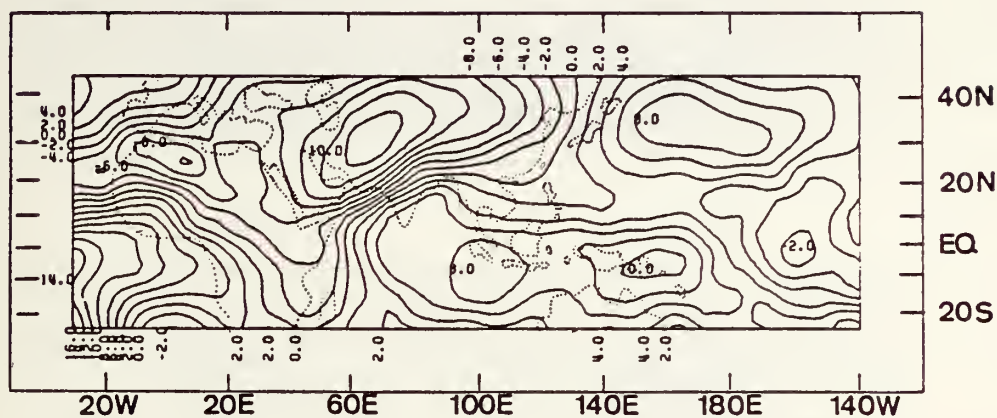
STREAM FUNCTION AT 200 MB SURGE PERIOD 1



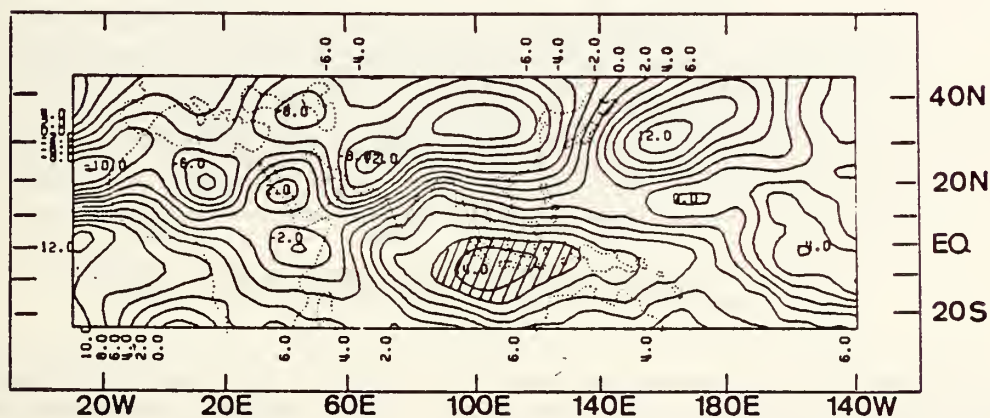
SURGE PERIOD 2



VELOCITY POTENTIAL AT 200 MB SURGE PERIOD 1



SURGE PERIOD 2



SURGE PERIOD 3

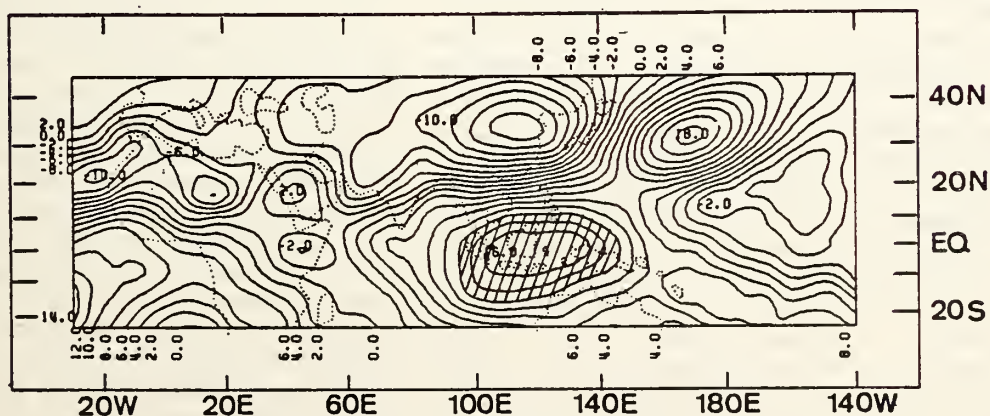


FIG. 6. As in Fig. 4 except for the composited 200 mb velocity potential.
Hatched area indicates $\chi > 12 \times 10^6 \text{ m}^2 \text{ s}^{-1}$.

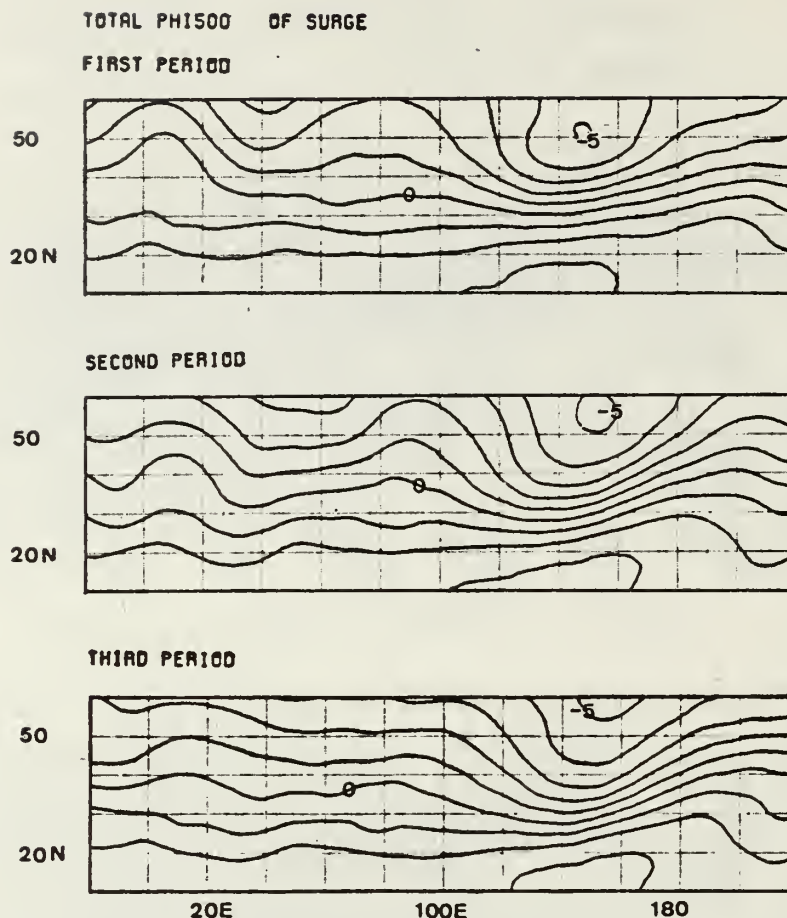


FIG. 7. As in Fig. 5 except for the 500 mb geopotential height. Values shown are departures from the standard atmosphere (5574 m). Intervals are 100 m.

about 36 h prior to day 0. The average decrease from day -1.5 to day 2.5 (the time of minimum northerly, or maximum southerly, wind) is $\sim 6 \text{ m s}^{-1}$. After day 2.5 the decrease does not continue, but the composite surface wind remains southerly through day 8.

The time series for the six 200 mb parameters for the break cases are shown in Fig. 10. The three midlatitude parameters (U_J , U_I and V_N) all show reversed trends compared to the surge cases. The slackening of the East Asia jet streak and the upper return flow of the local Hadley cell both appear to begin at least 36 h prior to day 0, in phase with the southerly acceleration of the surface wind over the northern South China Sea. In general, the changes of the midlatitude parameters during breaks are not as steady as during surges. The decreases of U_I and V_N pause at day 0.5 for 3 and 1.5 days, respectively. The parameter U_I increases from day 0 to day 1.5, then decreases for three days before resuming the increase. Nevertheless, the changes through day 8 of the break periods for all three parameters are comparable to (but opposite of) the changes during the surge periods.

The changes in the three equatorial parameters

(D , U_E and U_W), on the other hand, are more noisy and less suggestive of a trend. Moreover, the distribution of the individual cases is also more scattered than that during the active periods. Nevertheless, both D and U_W exhibit an out-of-phase relationship with the surge cases (Fig. 3). The tropical convective-area divergence weakens from day 0.5 to day 3, and the Indian Ocean Walker cell weakens from day -2 to day 1.5. Afterwards both reverse their tendencies in a way similar to that during the surge periods. For D the decrease during the break period is less than half the increase during the surge period, but for U_W they are comparable. Overall, however, the changes in the tropics are much less systematic than the changes in the midlatitudes.

Figs. 11–12 show the time-averaged distributions of the composite 200 mb streamfunction and velocity potential, respectively, for the three sequential periods centered at day 0, 2.5 and 5 for the break cases. The Winter MONEX case is again excluded. The zonal wind isotachs of 45, 55 and 65 m s^{-1} are again superimposed in the streamfunction diagrams. Compared to Figs. 5 and 6, a reversed change in the midlatitude motion components can be seen even

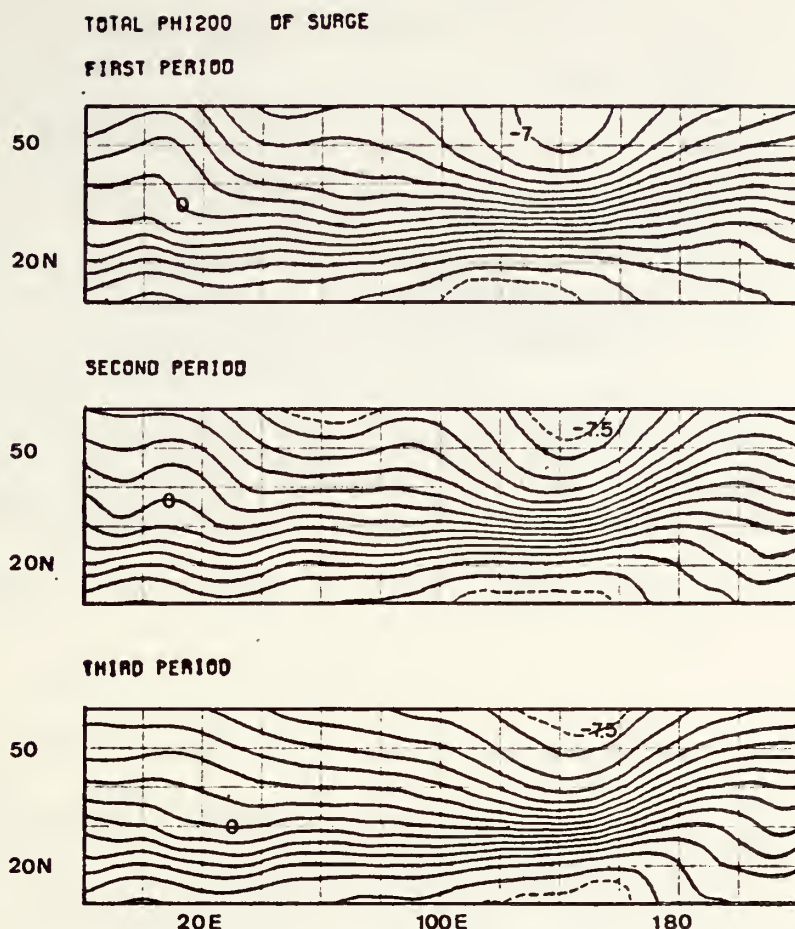


FIG. 8. As in Fig. 5 except for the 200 mb geopotential height. Values shown are departures from the standard atmosphere (11 784 m). Intervals are 100 m.

though the changes are less well defined. The East Asia jet core shows a dramatic weakening throughout the periods. The area enclosed by the 55 m s^{-1} isotach (hatched) retreats westward from period 1 to 2 and breaks up in period 3. In contrast to this is a continued intensification and eastward progression of the West Asia jet streak.

In Fig. 12 the midlatitude convergence center over northern China diminishes from period 1 to 2, while a convergence center near 40°N , 60°E increases through period 3, becoming the main midlatitude convergence center. The equatorial divergence center, on the other hand, decreases from period 1 to 2, then increases afterwards, as can be expected from the D series in Fig. 10. In addition, a divergence center appears in the equatorial Indian Ocean, almost exactly south of the tip of the Indian subcontinent. This divergence center is not evident during the active monsoon periods (Fig. 6). In East Asia these changes indicate a weakening local Hadley circulation and cause the southerly divergent wind component in the tropics and subtropics to decrease steadily from period 1 to 3. In West Asia, a convergence center situated near 20°N over Pakistan-Af-

ghanistan disappears after period 1, causing the southerly divergent wind exiting the divergence center in the equatorial Indian Ocean to extend into the main break-period convergence center near 40°N . This southerly divergent wind further increases from period 2 to 3, making the local Hadley circulation stronger throughout the break period over West Asia.

4. Discussion and concluding remarks

Our composite result for the surge cases basically reaffirms the schematic model of CL during the active periods of the northern winter monsoon, with some modifications. In the beginning of an active

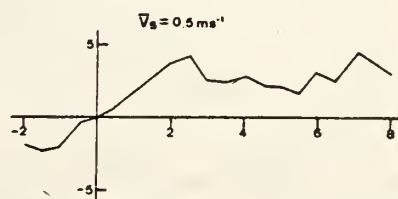


FIG. 9. As in Fig. 2 except for the inactive (break) cases.

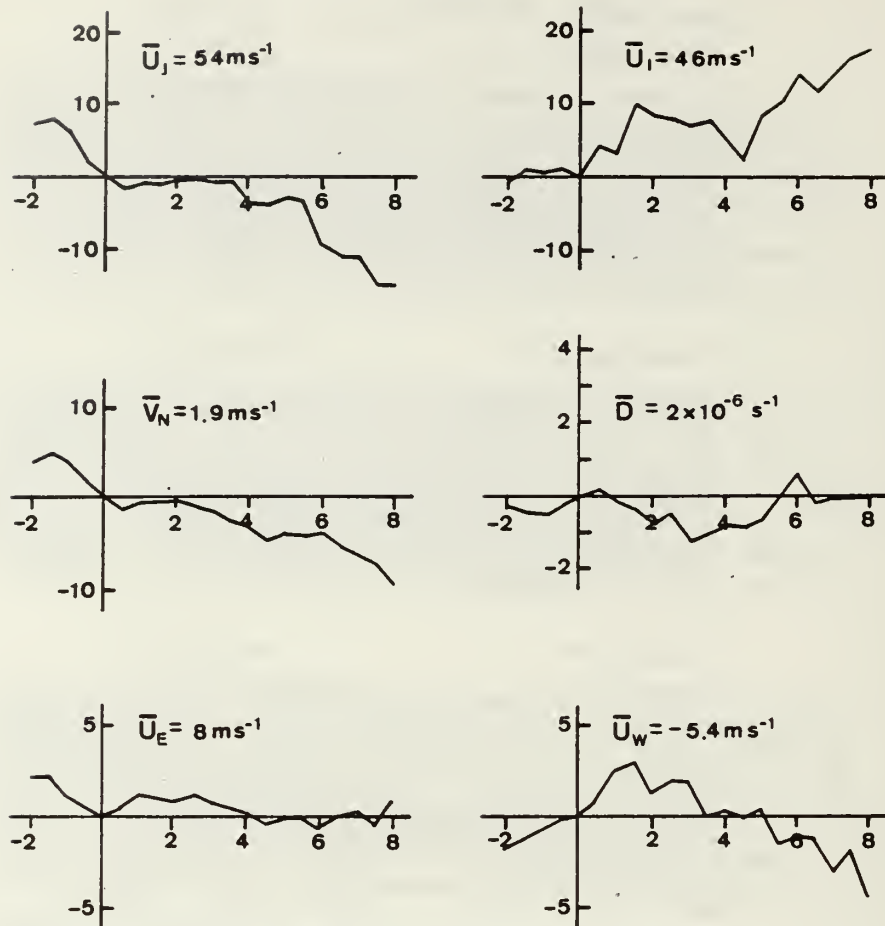


FIG. 10. As in Fig. 3 except for the inactive (break) cases.

period, many components of the planetary-scale motion complex "spin up" almost simultaneously, including the eastward movement of an upper level trough, the onset of a cold surge off the South China coast, the enhanced divergent outflow over the tropical convective area, and the strengthening of the Pacific and Indian Ocean Walker cells. The upper tropospheric southerly winds that form the return flow of the local Hadley cell over East Asia also strengthen, but the increase of the meridional velocity is evident only in the equatorial latitudes where the meridional velocity is mainly in the divergent component. The primary jet streak over East Asia and the much weaker jet streak over West Asia vary inversely, with the former intensifying and the latter weakening as the active period develops.

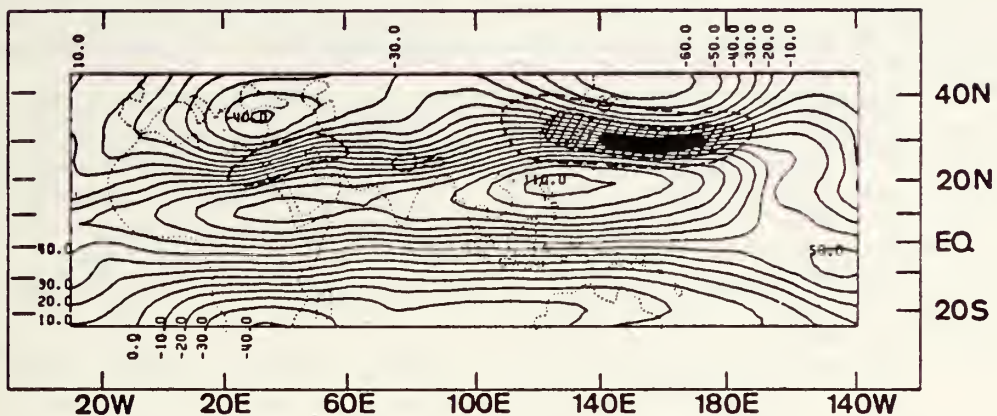
The upper-level southerly acceleration in the jet streak area occurs about one day after an active period begins. From that time on, the enhanced southerly winds over a broad latitudinal span appear very likely to contribute to a continuous acceleration of the jet streak throughout the active period, as hypothesized by CL. The mechanism for the initial acceleration, however, is not as obvious. Before the

onset of the surge, cold air advection over the northern latitudes is very intense throughout most of the troposphere. The increased baroclinicity is accompanied by the eastward passage of a wave trough, northwest of the jet streak in the middle troposphere. This may cause an acceleration of the westerly wind at 500 mb by the residual Coriolis torque, due to the southerly wind ahead of the trough, if the pressure gradient associated with the trough is insufficient to balance the Coriolis force. In addition, the wave passage will cause a coupled anticyclogenesis-cyclogenesis at the surface that appears to trigger the cold air surge.

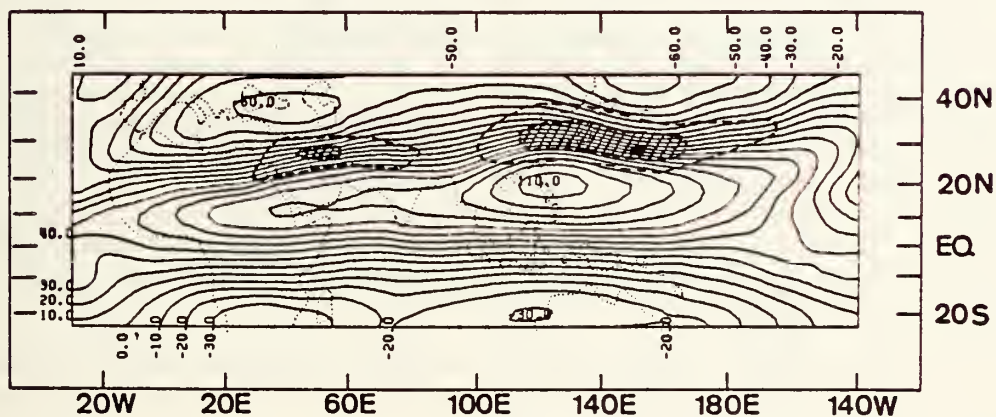
At 200 mb, the southerly wind in the vicinity of the East Asia jet streak actually starts to decrease about one day prior to the surge onset, when the jet streak starts a westerly acceleration. This decrease is due to a decrease in the rotational v component which overshadows the increase in the divergent component. Assuming that the rotational component is largely balanced by the pressure gradient, the increased divergent v which represents a strengthening of the meridional circulation should contribute to the acceleration of the jet streak. This strengthening of

STREAM FUNCTION AT 200 MB

BREAK PERIOD 1



BREAK PERIOD 2



BREAK PERIOD 3

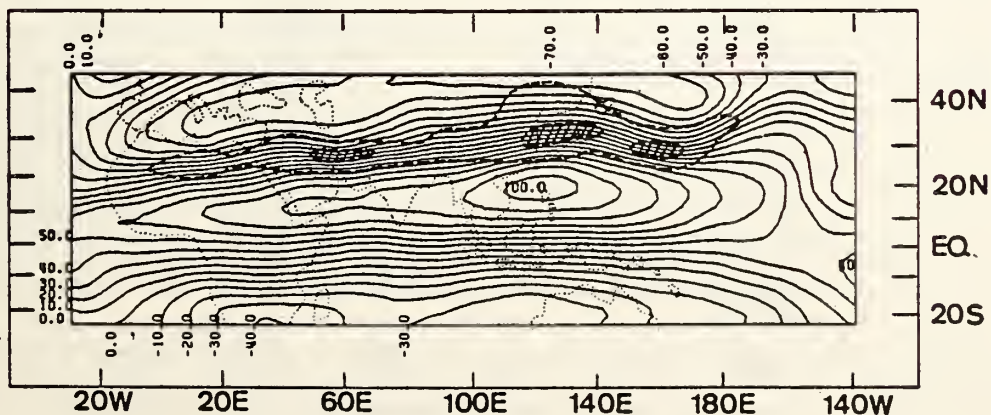
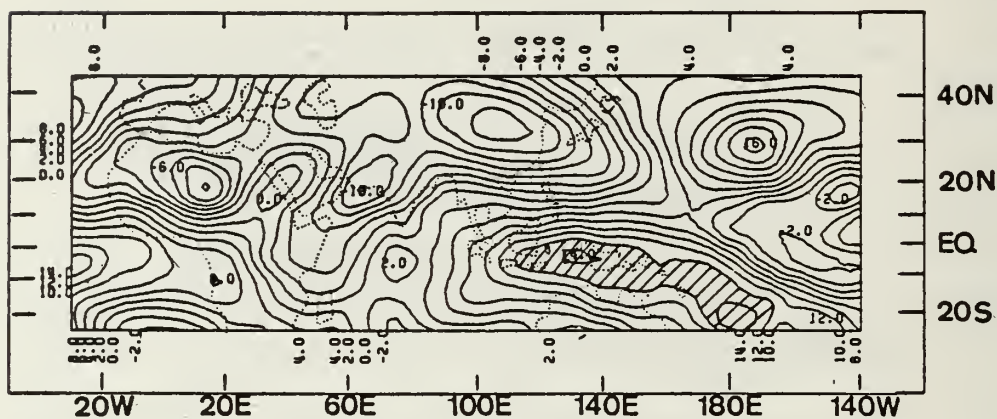
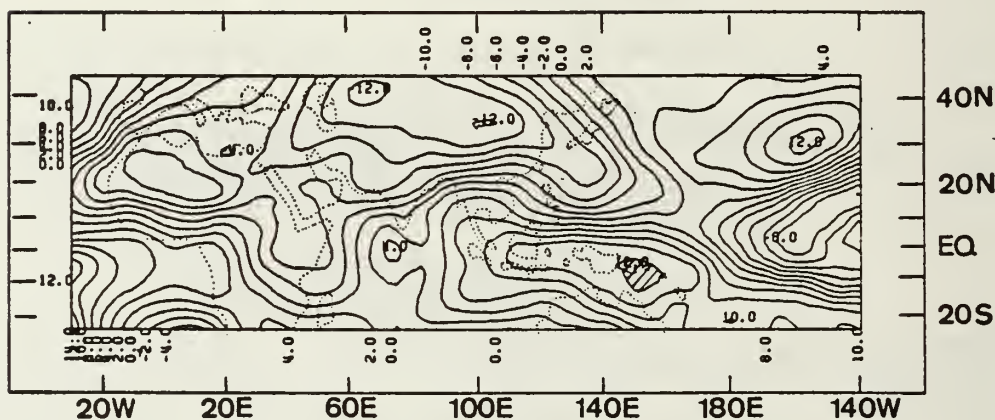


FIG. 11. As in Fig. 5 except for the inactive (break) cases.

VELOCITY POTENTIAL AT 200 MB
BREAK PERIOD 1



BREAK PERIOD 2



BREAK PERIOD 3

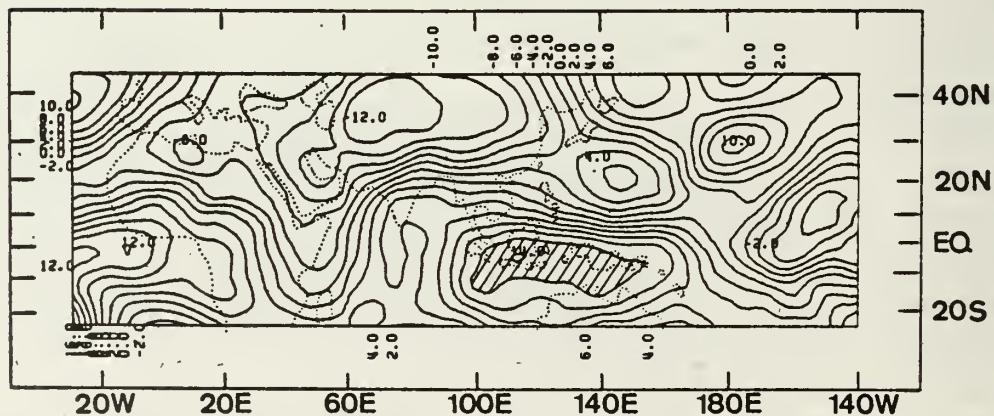


FIG. 12. As in Fig. 6 except for the inactive (break) cases.

the local Hadley circulation may be due to either an enhancement of the midlatitude baroclinicity or an increase in the tropical convection and condensation heating, or both. As the former is a process mainly occurring in the region near and north of the jet core, the simultaneous increase of the divergent v across a broad latitude band, from the equator to the jet latitude, suggests that the latter plays an important role.

In addition to the strengthening of the local Hadley circulation, a convergence of eddy momentum fluxes at the 200 mb level will also accelerate the jet. In fact, this mechanism, if operating on a zonally symmetric jet, will induce an indirect circulation across the jet (Holton, 1979) and cause a decrease of the southerly wind. However, the strong and primarily zonal cold advection northwest of the jet, can alone increase the temperature gradient normal to the jet to maintain a thermal wind balance without requiring an indirect circulation. Thus the secondary circulations due to the cold advection and the eddy momentum flux convergence, whose influences are both limited to the immediate neighborhood of the jet streak, will tend to offset each other. Therefore the time variation of the divergent v component may not reveal the relative importance of these two mechanisms at all. Quantitative calculations will be needed to resolve this problem.

The hypothesis of sustained jet streak acceleration due to the enhanced local Hadley circulation is indirectly supported by the jet behavior during the break periods. Over East Asia the tropical and subtropical southerly divergent wind at 200 mb weakens in consonance with a deceleration of the jet streak there, while over West Asia the reverse is observed. This is further evidence that the Coriolis torque of the broad-scale tropical-to-midlatitude meridional circulation provides the changes of the zonal momentum. Since the East Asia local Hadley circulation is immediately related to the tropical convective activity, a short-term teleconnection between the tropical and midlatitude circulations is established. This teleconnection covers a particularly broad longitudinal span in the equatorial latitudes where the Pacific and Indian Ocean Walker cells respond directly to the tropical convective activity.

The contrasts between the active and break periods point to the existence of distinctively different planetary-scale circulation regimes during the two periods. The difference exists both in the mean basic state as well as the short-term variations of the circulations within each period, the latter of which are almost totally reversed. The largest contrast is in midlatitudes, where the variation tendencies are clearly opposite and the magnitudes are comparable. It is generally believed that cold air surges are probably a result of the enhanced higher-latitude baro-

clinity which is due to strong cold advection; thus tropical forcing is not required to initiate the surges. The fact that the oscillations of the equatorial parameters are more prominent and coherent with midlatitude events during the active periods than during the break periods, therefore, seems to suggest that the tropics are initially forced by the midlatitudes, rather than vice versa, at least over East Asia and the Pacific. The feedback of the intensified tropical convection via a strengthened local Hadley circulation seems to be a subsequent development. On the other hand, the development of an upper-level divergence center in the equatorial Indian Ocean during break periods, which is apparently the main cause for the strengthening of a local Hadley cell and the jet streak over West Asia, seems to indicate a tropical forcing of the midlatitudes over West Asia and the Indian Ocean. There is no obvious indication of any initial triggering mechanism from the midlatitudes in this region.

In summary, this study provides strong evidence of the short-term planetary scale teleconnections in the midlatitude and tropical monsoon region during winter. However, several important questions remain unanswered. The most intriguing one is, why does the equatorial convective activity increase simultaneously with the onset of the surge. CL suggested that the surge causes low-level convergence which, in turn, enhances tropical convection. In a theoretical study of the surge motions in the tropics, Lim and Chang (1981) also showed that cyclogenesis occurs in the equatorial trough region downstream of the surge forcing, due to a Rossby-wave group response, and due to the equatorial beta-effect the time scale is given by a modified gravity wave phase speed rather than by an advective speed. In the real atmosphere this cyclogenesis will be associated with enhanced convective activity. However, the near-zero time lag between the equatorial and midlatitude developments is still difficult to explain adequately, even in view of the short time-scale implied in the modified gravity-wave speed. Another question is the relative importance of baroclinic secondary circulation due to cold advection and that of the eddy processes in the acceleration of the jet streak. A third question is the significance of the apparent out-of-phase relationship between the oscillations of the East and West Asia jet-streaks, which are quite remote from each other. These questions and several other aspects of the present results, such as the variation of the rotational component of the meridional wind which is related to the upper-level trough, the development of the 200 mb divergence center in the Indian Ocean during break periods, as well as the overall cause and effect, if any, of the various components of the planetary scale oscillations, must be studied further with more detailed data analysis.

Acknowledgments. We wish to thank Profs. P. J. Webster and R. H. Johnson for discussion, Prof. R. Haney for reading the manuscript, and Mr. L. C. Chou for assistance in data processing. Data used in this study were provided by the Fleet Numerical Oceanographic Center, Monterey, California. This research was supported in parts by the National Oceanic and Atmospheric Administration under Contract NA81AAG00885, and by the National Science Foundation under Grants ATM 80-13153 and ATM 79-24010.

REFERENCES

- Chang, C.-P., and K. M. Lau, 1980: Northeasterly cold surges and near-equatorial disturbances over the Winter MONEX area during December 1974. Part II: Planetary-scale aspects. *Mon. Wea. Rev.*, **108**, 298-312.
- Chin, P. C., 1969: Cold surges over South China. *Roy. Observ. Hong Kong Tech. Note*, No. 28, 19 pp.
- Hawkins, H. F., and S. L. Rosenthal, 1965: On the computation of stream-function from the wind field. *Mon. Wea. Rev.*, **93**, 245-252.
- Holton, J. R., 1979: *An Introduction to Dynamic Meteorology*. Academic Press, 391 pp.
- Lim, H., and C.-P. Chang, 1981: A theory for midlatitude forcing of tropical motions during winter monsoons. *J. Atmos. Sci.*, **38**, 2377-2392.
- Murakami, T., 1979: Winter monsoon surges over East and South-east Asia. *J. Meteor. Soc. Japan*, **57**, 133-158.
- Ramage, C. S., 1971: *Monsoon Meteorology*. Academic Press, 296 pp.
- Uccellini, L. W., and D. R. Johnson, 1979: The coupling of upper and lower tropospheric jet streaks and implications for the development of severe convective storms. *Mon. Wea. Rev.*, **107**, 682-703.
- World Meteorological Organization, 1978: FGGE implementation/operations plans, Vol. 6A: The Winter Monsoon Experiment.

A Simple Model of Atmosphere-Ocean Interaction during El Niño-Southern Oscillation

Recently McCreary (1982) showed that the time scale in the occurrence of El Niño-Southern Oscillation (ENSO) can be explained by including the effect of air-sea interaction in the closed ocean basin. In this note we present a formulation of a simple coupled model of the ocean and atmosphere, and use it to illustrate the role of atmospheric interaction in generating El Niño events.

In the atmosphere, the distribution of the vertically averaged zonal wind induced by the heating was computed analytically and represented by a streamfunction representation in the zonal-vertical plane (Gill, 1980; Lau, 1982). To obtain the solution shown in Figure 1, a linear vertical dependence was assumed for the zonal wind. The most striking

feature is the east-west asymmetry. As a consequence of the 3-to-1 ratio in the theoretical phase speed between the Kelvin wave and the lowest order Rossby wave, the eastern branch of the Walker cells spans a longitudinal extent about three times larger than its western counterpart.

For the ocean, we used a nonlinear system of shallow water equations (Busalacchi and O'Brien, 1980) driven by wind stress of the form

$$\tau = \tau_s + \tau_i + \tau_e \quad (1)$$

where τ_s is the observed annual and semi-annual component of the surface wind stress, τ_i is the interactive component as obtained from the atmospheric model and is a function of the thermocline depth, and τ_e denotes all other stresses external to the coupled systems and effects not explicitly represented by τ_s or τ_i .

Observational studies (e.g., Rasmusson and Carpenter, 1982; Lau and Chan, in preparation) indicate that the tropical atmosphere-ocean circulation system exhibits a bimodal climatic state corresponding to the two extreme phases of ENSO. The two modes are represented schematically in Figure 2. Referring to the sea surface temperature (SST) in the eastern Pacific, the two modes correspond to the cold SST for pre-El Niño and warm SST for El Niño. In the coupled model the two situations are represented by an atmospheric heating distribution (Q) in the zonal (x , positive eastward) and meridional (y , positive northward) directions of the form

$$Q(x, y, \sigma) = Q_- [1 + \sigma H(\sigma)] \exp [-\alpha^2(y^2 + (x - H(\sigma)x_c)^2)] \quad (2)$$

where $Q_- = \kappa(\bar{h}_w - \bar{h}_e)$,
 $Q_+ = \kappa(\bar{h}_w + \bar{h}_e - \bar{h}_o)$,
 and $\sigma = (Q_+ - Q_-)/Q_-$

with $\bar{h}_w = \frac{1}{\Delta_w} \int_{\Delta_w} h \, dx \, dy$

and $\bar{h}_e = \frac{1}{\Delta_e} \int_{\Delta_e} h \, dx \, dy$.

The areas of the western and eastern regions of the ocean are denoted by Δ_w and Δ_e , respectively. κ is a coupling constant, h_0 is a reference thermocline depth at midlatitudes, x_c is a longitude corresponding to the dateline, and $H(\sigma)$ is the Heaviside step function. We have made the heating function $Q_-(Q_+)$ a linear function of the large-scale sea surface temperature anomaly (SSTA) longitudinal (meridional) gradient. Equation (2) shows that the surface wind stress on the ocean switches from the cold to warm SST regime and *vice versa* whenever σ changes sign.

In a preliminary experiment with no seasonal effects ($\tau_s = 0$), the ocean-atmosphere system was spun up with a uniform external surface wind ($\tau_e = -5 \, \text{m s}^{-1}$) for 80 days and then the wind was abruptly relaxed over the western part of the ocean basin to set the coupled system in the pre-El Niño mode. Two cases were run: one with a non-interactive atmosphere (NINT, $\tau_i = 0$) and one with an interactive atmosphere (INT, $\tau_i \neq 0$). In the latter case, τ_i , which was assumed uniform across the meridional width of the ocean basin,

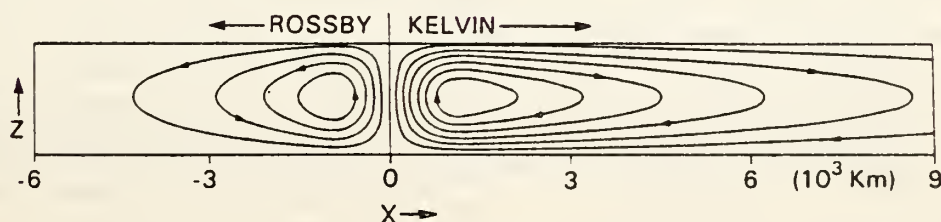


FIGURE 1 (Lau)

The model Walker Circulation in the x-z (zonal-vertical) plane arising from a heat source localized at $x = 0$.

CONTENTS

—A simple model of atmosphere-ocean interaction during El Niño-Southern Oscillation

—AGE—Observations of surface wind speed in the ocean climate data set

—GUY—A climatic scenario in the western Pacific associated with El Niño events

—NER—More accurate estimates of El Niño rainfall anomalies in the central Pacific

—EY AND VAN LEER—Observations and simulation of a bottom Ekman layer off the coast of Peru

—INS AND SAUNDERS—Physical oceanographic observations in the northwest tropical Atlantic

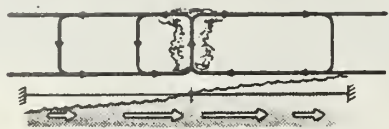
—R, BEAN, HANSON AND KRAUS—Preliminary report on factors contributing to the maintenance of the California stratus clouds

—TINGS
—CE

(a) PRE-EL NIÑO



(b) EL NIÑO



MARITIME CONTINENT DATELINE SOUTH AMERICA

FIGURE 2 (Lau)

Schematic diagram showing the different tropical atmospheric-oceanic circulation regimes during two extreme phases of ENSO.

sin, was obtained from the steady state zonal wind distribution induced by the heating function $Q(x, y, \sigma)$ defined in equation (2). Figure 3 shows the time-longitude sections of the thermocline depth at the equator for the NINT and INT cases. Comparison of the two cases shows that during the early period of the spin down, the east-west thermocline gradient is larger in INT than in NINT due to positive feedback from the enhanced Walker circulation arising from convection concentrated near the extreme western Pacific during the spin up phase ($\sigma \leq 0$). As a result, the intensity of the El Niño measured by the rate of thermocline deepening at the eastern boundary following the arrival of the oceanic Kelvin wave is much larger in INT than in NINT. For INT, by about three months after the initial wind relaxation, the surface wind switches to the warm SST ($\sigma > 0$) regime. In this circulation regime, the central Pacific convection produces increasingly strong surface westerly (easterly) winds to the west (east) of the forcing as the zonally averaged thermocline depth ($\bar{h}_w + \bar{h}_e$) increases. Thus, the decrease in the surface easterly wind in the western Pacific due to the initially weakened Walker cell is further enhanced. In contrast, over the eastern Pacific, the increase in surface easterly wind due to

$Q(\sigma > 0)$ actually opposes a similar initial decrease in easterly wind there. This east-west asymmetry arising from the central Pacific heating $Q(\sigma > 0)$ may provide a clue to the observed continual easterly wind slackening in the western and central Pacific during the course of ENSO and the lack of such observation over the eastern Pacific.

In the NINT case, the reflected Rossby wave from the eastern ocean boundary propagates westward across the basin, reaching the western boundary about eight months after the onset. While in INT, the westward movement of the Rossby wave appears to be arrested near the central Pacific, with warm water continually being drained away from the western Pacific due to the increased overlying westerlies. The warm SSTA condition over the eastern

Pacific is, however, more rapidly annihilated in INT than in NINT because the enhanced easterly increases local upwelling, causing the thermocline to rise. As a result of these interactions, a large pool of warm SSTA (or positive thermocline depth deviation) appears to separate from the eastern boundary and to persist over the central Pacific. This is in good agreement with recent observations (e.g., Rasmusson and Carpenter, 1982). In NINT, the model shows only a weak tendency for such an anomaly to develop in the central Pacific.

References

- Busalacchi, A. J. and J. J. O'Brien (1980) The seasonal variability in a model of the tropical Pacific. *Journal of Physical Oceanography*, 10, 1929-1951.
- Gill, A. E. (1980) Some simple solutions for heat-induced tropical circulation. *Quarterly Journal of the Royal Meteorological Society*, 106, 447-462.
- Lau, K. M. (1980) Oscillation in a simple equatorial climate system. *Journal of Atmospheric Sciences*, 38, 246-261.
- Lau, K. M. and H. Lim (1982) Thermally driven motions in an equatorial β -plane: Hadley and Walker circulations during winter monsoon. *Monthly Weather Review*, 110, 336-353.
- McCreary, J. P. (1982) A model of tropical ocean-atmosphere interaction. *Monthly Weather Review*, submitted. (Also, *Tropical Ocean-Atmosphere Newsletter*, No. 9, 6-7).
- Rasmusson, E. M. and T. H. Carpenter (1982) Variation in tropical sea surface temperature and surface wind fields associated with the Southern Oscillation/El Niño. *Monthly Weather Review*, 110, 354-384.

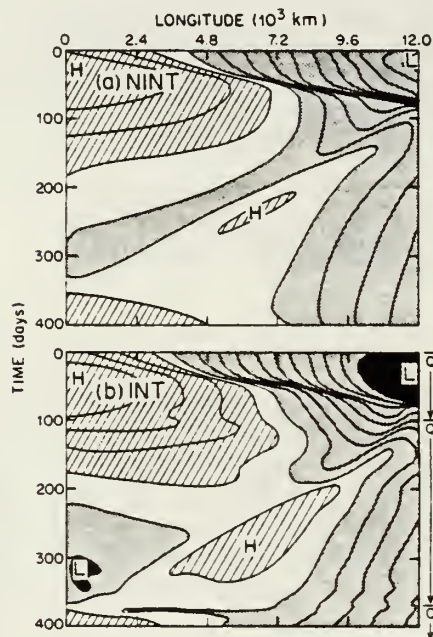


FIGURE 3 (Lau)

Time-longitude sections of the variation of the upper layer thickness of the model ocean at the equator after an abrupt relaxation of surface easterly wind in the western Pacific with (a) a non-interactive atmosphere (NINT) and (b) an interactive atmosphere (INT).

Ka-Ming Lau
Goddard Laboratory for
Atmospheric Sciences
NASA/Goddard Space Flight Center
Greenbelt, MD 20771

Observations of Surface Wind Speed in the Ocean Climate Data Set

Since 1861, the first year of the Ocean Climate Data Set (Fletcher *et al.*, 1982), three overlapping methods of determining surface winds have primarily been used: (a) the Beaufort Scale defined in terms of sailing ship performance, (b) the Beaufort Scale redefined in terms of local sea state, and (c) shipboard anemometry. Before climatic anomalies in the 105-year record can be identified with confidence, we must first assess the effects of inaccuracies in each method and of discontinuities

introduced during the prolonged transitions between the methods (a-b: 35 years, b-c: > 30 years).

In 1806 Admiral Beaufort developed a scale for recording wind force at sea based on the effect of the wind on a full-rigged frigate. The values were determined by the speed the ship could travel with all sails set (force 2-4), the sails the ship could carry "in chase full and by" (force 5-9), the ship being able to carry few or no sails (force 10-12). The scale was

modified in 1874 (Garrett, 1926) consequent to the introduction of double topsails about 1850. Then it was discovered that the sailing ship "anemometer" indicated a higher force when a ship was sailing against the wind as compared to sailing with the wind (Harding, 1885; Köppen, 1885, 1897). As far as I can discover, no adjustments were ever made to compensate for this difference, which averaged about half a Beaufort Scale division.

Scott (1886) drew attention to another

Equatorial Response to Northeasterly Cold Surges as Inferred from Satellite Cloud Imagery

KA-MING LAU

Goddard Laboratory for Atmospheric Sciences, NASA/Goddard Space Flight Center, Greenbelt, MD 20771

(Manuscript received 5 January 1982, in final form 24 May 1982)

ABSTRACT

Day-to-day convective activity in the equatorial regions (10°N – 10°S and 90° – 180°E) during December 1974 and January 1975 was estimated from NOAA satellite visible imageries using simple visual techniques. The daily convective estimates were composited with respect to the phase of individual cold surge episodes occurring during the two-month period. By decomposing the data into symmetric and anti-symmetric components with respect to the equator, it was shown that eastward and westward propagating cloud clusters had phase speeds $\sim 10 \text{ m s}^{-1}$ and $\sim 5 \text{ m s}^{-1}$, respectively, and were generated near southwestern Borneo following a cold surge onset. The strong equatorially trapped character of the eastward moving components suggested the possibility of Kelvin wave responses. The eastward moving convective clusters interacted strongly with westward moving disturbances which may be identified with low-order symmetric Rossby waves originating from the western Pacific. The predominantly larger response amplitude of the symmetric compared with that of the antisymmetric component, especially near the equator, suggested that the most strongly trapped of these waves were likely generated from heat sources concentrated near the equator.

1. Introduction

The low-level monsoon cold air surge off the south-east coast of China is known to have a strong influence on the development of near-equatorial convection over the maritime continent region of Malaysia, Borneo and Indonesia. Chang *et al.* (1979) showed that convection associated with transient westward propagating disturbances in the South China Sea and stationary disturbances over the western part of Borneo were significantly intensified following a cold surge. Houze *et al.* (1981) and Johnson and Priegnitz (1981) observed that during Phase I of the Winter Monsoon Experiment (Winter-MONEX), 1 December 1978 to 3 January 1979, convective activity over Borneo increased during the occurrence of cold air surges. Often the influence of the monsoon surges can be more far-reaching. It has been observed that the penetrating low-level northeasterlies during a cold surge may lead to enhanced convection over the Java Sea and may be linked to the Southern Hemisphere summer monsoon of Australia (Williams, 1979). However, the subsequent development of the enhanced convective activity and possibly the generation and propagation of cloud clusters associated with them still remain largely unknown. The identification of such features will be an important step toward understanding the vagaries of the weather over the maritime continent of monsoon Southeast Asia. Yet, to detect signals in tropical convection as a direct response to the monsoon surge is a difficult task due to the complex nature of the convection over the

maritime continent and its large variability associated with strong interactions with wave features in the equatorial western Pacific, compounded with the lack of observational network in this part of the tropics.

Information derived from satellite data has played a major role in observational studies of large-scale tropical disturbances. Chang (1970) and Wallace and Chang (1972) used time-longitude sections of satellite-observed brightness data to demonstrate westward propagation of tropical disturbances in the central and eastern Pacific. Murakami and Ho (1972), Gruber (1974) and Zangvil (1975) studied tropical disturbances by applying spectral analyses to satellite data. Recently, Murakami (1980a,b) used empirical orthogonal functions of the outgoing longwave radiative flux at the top of the atmosphere to study the temporal variability of the large-scale winter circulation. While these studies provided valuable information on the time and length scales of the most dominant tropical disturbances, they did not clarify the relationships of these disturbances with specific changes in the large-scale circulation. This study is an attempt to identify from routinely available satellite information, possible tropical wave disturbances associated with the northeasterly monsoon surges. This work is a prelude to a more detailed study now being undertaken by the author using a combination of satellite and wind data from FGGE/MONEX to deduce the propagation properties as well as spatial structure of equatorial disturbances during Winter-MONEX.

2. Data and analyses

Numerical estimates of the strength of convective activity (α) associated with large-scale equatorial disturbances were obtained from daily NOAA-3 mosaic of visible brightness covering a two-month period from 1 December 1974 to 31 January 1975. Attention was focused on the area between 90–180°E and 10°N–10°S. Using a method similar to that of Payne and McGarry (1977), the above area was divided into $2.5 \times 2.5^\circ$ grid squares and each was assigned a value for α of 1, 0, -1 according to the following scheme. A value of 1 was assigned to squares which appeared over 80% white in the images, indicating organized deep convection or the resulting cirrus canopy. Squares assigned a value of -1 appeared very dark in the imagery, indicating clear sky. For squares which appeared uniformly grey or which did not fit any of the two above categories a value of 0 was assigned. These numerical values can also be viewed as a crude indicator of large-scale vertical motion with updraft in the organized deep convection ($\alpha = 1$) and subsidence in the clear areas ($\alpha = -1$). The cloud images we used were of sufficiently high quality for our purpose. Despite its subjectivity, the use of visual techniques, which depends essentially on pattern recognition, has been shown to be a useful tool for identifying convective disturbances in the tropics (Wallace and Chang, 1972).

Using the above scheme, daily values of α for each grid square over the area of interest were obtained for the two-month period. For the purpose of identifying disturbances that were related to the cold surges, we composited the daily maps with respect to the phase of each surge event. Here, the occurrence of a surge event was determined from time series of the area-averaged northerly surface wind component over the

northern part of the South China Sea (15–20°N, 110–120°E) and the pressure difference between a location at 30°N, 115°E and Hong Kong (22°N, 116°E). Data required to construct the above time series were obtained from the Fleet Numerical Oceanographic Center (FNOC). Although the term “cold surge” is suggestive of the use of temperature as a criterion for determining the occurrence of such an event, the use of surface wind and pressure difference as a “surge index” in this case is far better than the use of surface temperature. This is because of the difficulty in tracing the effect of cold air advection over the open ocean as a result of air-mass modification by strong air-sea interaction that takes place as soon as the cold continental air enters the South China Sea (Chang *et al.*, 1979). Fig. 1 shows that there is generally a good correlation between the sudden increase in the northerly wind component and the maxima in the pressure difference between the two locations. In all, there are seven distinct surge episodes occurring during this period, as shown subjectively by the shaded regions in Fig. 1. Each episode lasted from two to seven days. The time of onset, denoted by day 0 in the subsequent discussion, was determined by a sudden increase in surface wind (10 kt in 1–2 days) coupled with a large drop in the surface pressure difference between the two chosen locations. The end of each episode was marked by a recovery of the area-averaged surface wind to <80% of its maximum value.

Although there is generally large variability during the time in which individual northeasterly surges last, a feature that appears to be common to all surges is the rather abrupt increase in surface northerly wind over a large part of the South China Sea within one to two days after the surge onset. Chang and Lau (1980) showed that convection near Borneo began to

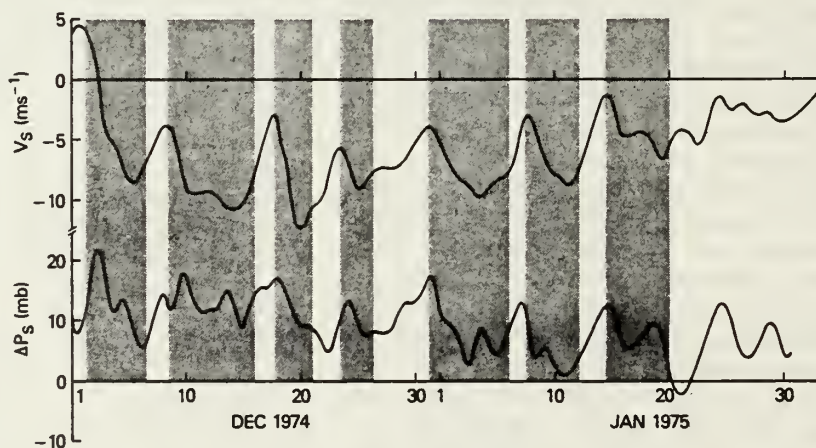


FIG. 1. Time series of (top) area-averaged northerly component of surface wind over the northern part of the South China Sea (15–20°N, 110–120°E) and (bottom) surface pressure difference between Hong Kong (22°N, 116°E) and a location at 30°N, 115°E. Shaded regions denote “cold surge” periods as defined in the text.

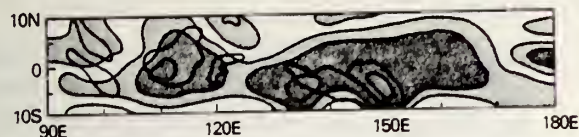


FIG. 2. Averaged convective estimates $\bar{\alpha}$ over all the surge periods. In a scale from -1 to 1 , $\bar{\alpha}$ indicates conditions ranging from clear sky to highly organized convection. Contour intervals are in units of 0.2 . Areas where $\bar{\alpha}$ exceeds 0.4 are shaded.

intensify typically within two days after the cold surge onset. This suggests that the triggering of increased equatorial convection occurs shortly after the onset, perhaps associated with fast gravity wave-like response to midlatitude forcing (Lim and Chang, 1981). What determines whether a surge will sustain, appears to depend on the degree of subsequent feedback between the midlatitude wave disturbance that instigates the cold surge and the surge-induced tropical convection. Such feedback process is, however, highly variable and is influenced strongly by the large-scale circulation. As a result, the time for the northeasterly wind over the South China Sea to attain its maximum and the time during which an individual surge lasts vary considerably from case to case. Because of these variations, the use of the so-called superposed-epoch method for compositing (where different phases of an event are identified and the same phase averaged for different cases) is not expected to yield the best results. Here, we adopt the following simple procedure. A composite picture of convective activity associated with the northeasterly surges was obtained by averaging the value of α for each grid square starting from Day 0 to Day 6 for each event. When a surge did not last over the specified day, the averaging was done only for those which only lasted up to or longer than the specified day. Thus all seven surges contributed to the Day-0 average, but only three cases comprised the Day-6 average. The data for each day period were then spatially averaged by a Laplacian diffusive filter to remove small-scale features due to isolated cloud fluctuations. Because the composite for the late stage of the surge is contributed to only by the prolonged events and because of the generally weaker signal-to-noise ratio during the late stage of the surge, the reliability of the results is expected to diminish as the lag time increases (see Section 4).

3. Results

a. Mean conditions

Fig. 2 shows the mean level of convective activity ($\bar{\alpha}$) over all the surge periods (shaded region in Fig. 1). As is apparent in Fig. 1, cold surges occurred almost continuously over the entire period so that the distribution shown in Fig. 2 was almost identical to the two-month mean. In a scale from -1 to $+1$, $\bar{\alpha}$ indicates conditions ranging from clear sky to highly organized convection. The positive value of $\bar{\alpha}$ over

the entire region indicates that the sky was, on the average, cloudy everywhere during this period. Strong convective activity is found over two broad regions: one centered over Borneo and the Java Sea and the other covering New Guinea and the equatorial western Pacific up to 165°E , with two local maxima located on opposite sides of the central New Guinea mountain range. It is important to note that although two broad maxima appear on the mean maps, it is not necessarily to be construed that they appeared simultaneously at any given time. From inspection of the daily satellite pictures and the analyses shown later, it was found that the distribution of convective activity within these preferred regions appeared to be inversely related.

b. Cold surge response

Fig. 3 shows a composite map of the anomalous convection α' ($=\alpha - \bar{\alpha}$) in a chronological sequence starting from Day 0. The main features of these maps are:

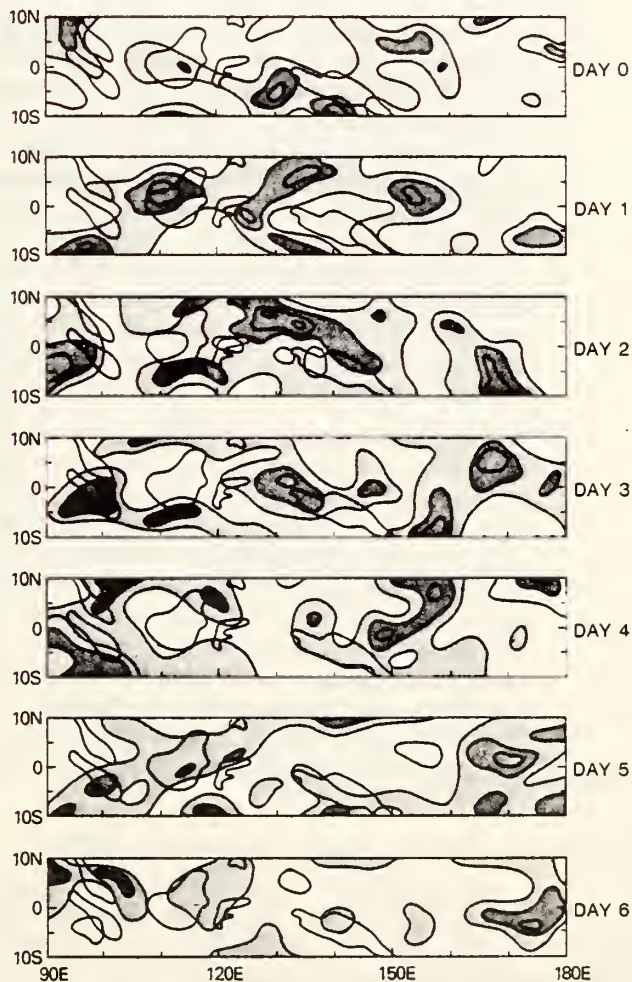


FIG. 3. Composite sequence of the anomalous convection α' ($=\alpha - \bar{\alpha}$) during a typical monsoon surge event. Contours are in units of 0.1 with positive values shaded.

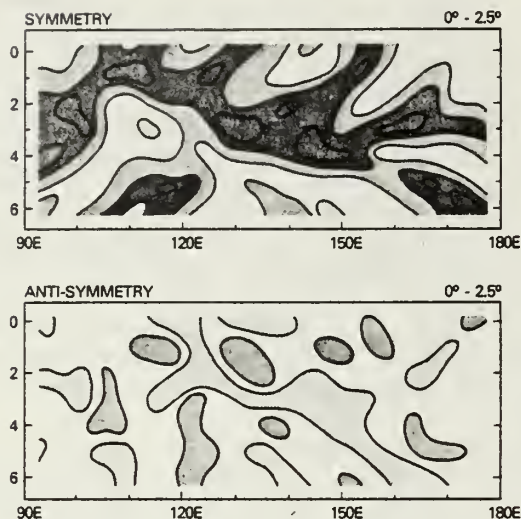


FIG. 4a. Composite time-longitude section of the symmetric and antisymmetric components of α' for the latitude band $0-2.5^\circ$.

1) Starting at Day 1 into the surge period, the level of convection in the area between $105-140^\circ\text{E}$ and $5^\circ\text{S}-5^\circ\text{N}$ is enhanced; in particular, the convection over Borneo shows strong development.

2) Contemporaneous with the increased Borneo convection at Day 1, convection over northern New Guinea appears to be much weakened; this situation is reversed on Days 2 and 4.

3) At later stages of the surge, the major convective activity appears to separate from the source region described in 1), becoming more developed in the vicinity and westward of peninsular Malaysia and in the eastern regions near the date line.

In general, as shown in Fig. 3, the variation in convective activity which is associated with upward motion and hence divergence/convergence of the large scale flow, is rather complex. Individual cloud clusters appear to amplify and decay as the centers of the convective pattern move away from the source region between $105-140^\circ\text{E}$ and $5^\circ\text{S}-5^\circ\text{N}$. Conceivably, in the patterns shown, both eastward and westward propagating components as well as temporal vacillation of stationary components can be present. However, it is not at once apparent without further analyses how each of these components contributes to the overall pattern.

c. Symmetric and antisymmetric modes

To assess the relative roles of the various propagating components, we divided the above data into a symmetric (α^+) part and an antisymmetric (α^-) part with respect to the equator:

$$\left. \begin{aligned} \alpha^+ &= \alpha'_N + \alpha'_S \\ \alpha^- &= \alpha'_N - \alpha'_S \end{aligned} \right\}, \quad (1)$$

where the subscripts N and S denote respectively lat-

itudes in the Northern and Southern Hemispheres, equidistant from the equator. The effectiveness of such decomposition for wind data in separating eastward and westward traveling tropical disturbances have been demonstrated by Yanai and Murakami (1970) and Zangvil and Yanai (1980). Since α can be regarded as an indicator of the divergence/convergence associated with large-scale disturbances, it was felt that the same procedure applied to our data will also be useful for identifying tropical disturbances in terms of basic equatorial wave modes (Matsuno, 1966). Figs. 4a-d show the composite time-longitude sections of the symmetric and antisymmetric components for different latitude bands. The most prominent feature that emerges is the existence, in the symmetric component near the equator (Fig. 4a), of both eastward and westward propagating components away from the Borneo source region at Day 1 of the surge. The average speed of the eastward movement is $\sim 10 \text{ m s}^{-1}$ and that of the westward component $\sim 5 \text{ m s}^{-1}$. It is also seen from Fig. 4a that the eastward propagating cloud clusters appear to intensify when they encounter westward moving disturbances from the region near New Guinea and the equatorial western Pacific. Near the equator, the antisymmetric component also shows an eastward movement with speed 8 m s^{-1} but its amplitude, in contrast to the symmetric mode, is much smaller. At the $2.5-5^\circ$ latitude zone (Fig. 4b), the symmetric mode tends to be somewhat stationary, although some eastward moving component can be detected at later stages. Westward propagation in the antisymmetric components at these latitudes, though not very well defined, can also be discerned. However, the significance in this component, as shown later, is very low. Further away from the equator (Figs. 4c, d) the westward propagating tendencies of both the symmetric and antisymmetric

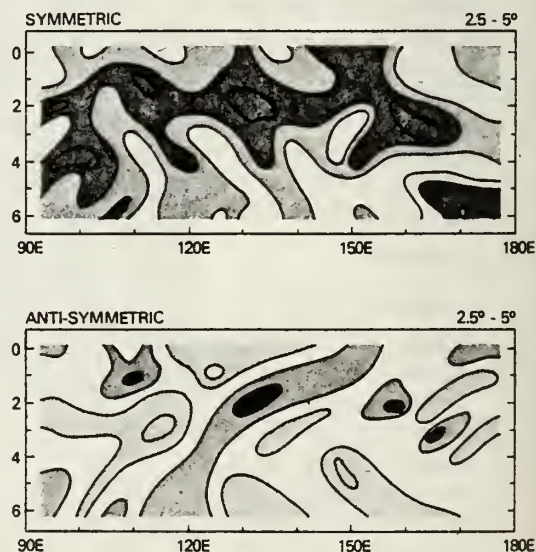


FIG. 4b. As in Fig. 4a, except for the latitude band $2.5-5^\circ$.

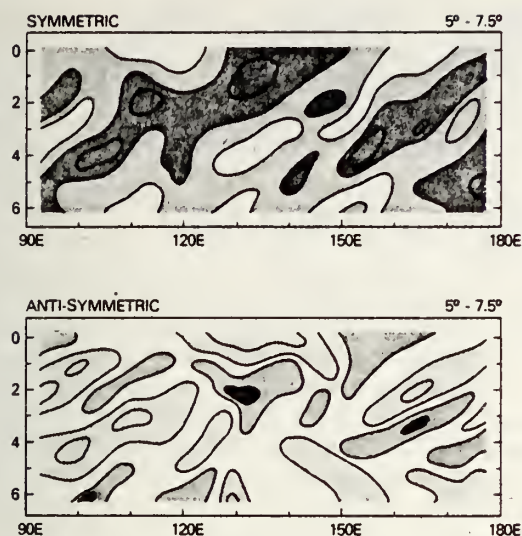


FIG. 4c. As in Fig. 4a, except for the latitude band 5–7.5°.

modes are increasingly obvious. The speeds are estimated at 8 m s^{-1} for the symmetric and antisymmetric modes, respectively. The westward propagating disturbances found at the higher latitude bands appear to originate from the western Pacific as rather periodic wave disturbances with periods of 4–5 days. The convective activities associated with these disturbances are also seen to be somewhat enhanced as they traverse the monsoon maritime continental regions between 105 and 140°E.

The contribution by the symmetric and antisymmetric components to the overall level of convection within a 10° latitude belt bounded by 90 and 180°E are shown in Fig. 5 together with the total area-averaged contribution within the chosen region. A value of 100 in the brightness data shown will correspond to $\alpha = 1$ for all the grid squares within the latitude band shown. It is not difficult to see that the sym-

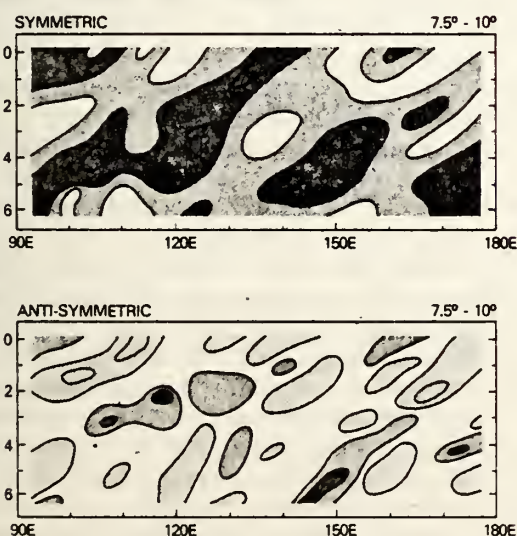


FIG. 4d. As in Fig. 4a, except for the latitude band 7.5–10°.

metric components contribute by far the major share to the amplitude of the observed convection. There is a rather dramatic increase in the overall level of convective activity within the entire region represented by a near-doubling of total cloud brightness during the surge period compared with that at the start (Day 0). The variations within each latitude band appear more complex. For the equatorial band 0–2.5°, the most intense convection is reached at Day 3, although the immediate response to the surge as shown earlier is found at Day 1 near the longitude of western Borneo. The delayed response is a result of the re-intensification of the eastward moving cloud cluster as it encounters westward moving disturbances between 125 to 150°E (Fig. 4a). The maxima for the 2.5–5° band and the first peak for the 5–7.5° band, both at Day 2, are related to westward propagating Rossby-wave-type response directly induced by the cold surge. The second peak for the 5–7.5° band at Day 4 and the delayed maximum at Day 5 for the 7.5–10° band is probably related to intensi-

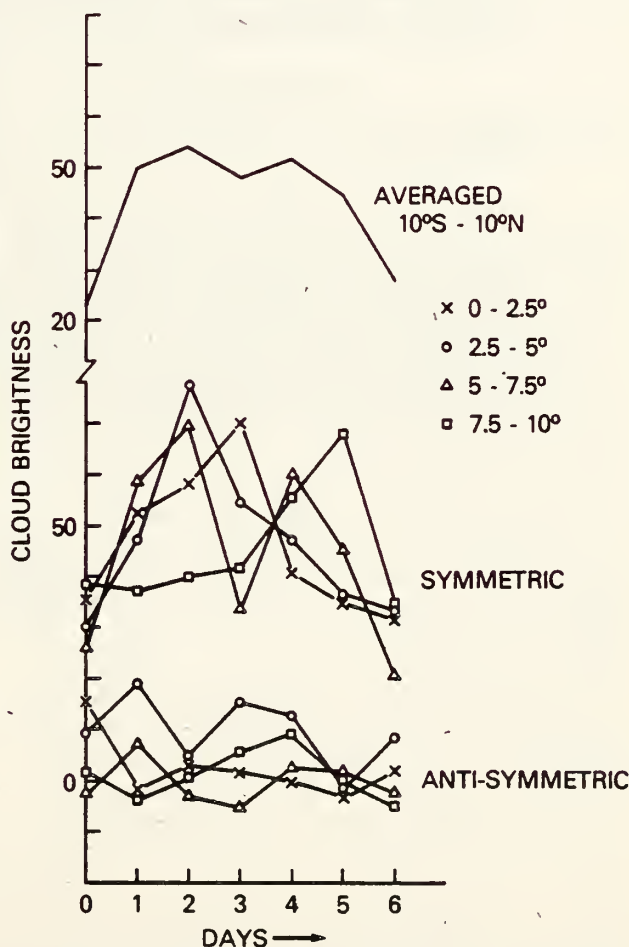


FIG. 5. Variation of total area-averaged cloud brightness within the region bounded by 10°N–10°S and 90–180°E together with contributions by latitude of the symmetric and antisymmetric components. A numerical value of 100 in the brightness scale shown corresponds to $\alpha = 1$ in all grid squares within the latitude band shown.



FIG. 6. Averaged signal-to-noise ratio distribution over Days 0-7. Shaded areas denote values of $S \geq 1$, indicating more reliable composite values.

fication by the prolonged cold surges of easterly waves originating from the western Pacific as they traverse the winter monsoon region.

4. Statistical significance

Since the foregoing results are based on a small sample of data, the statistical significance of our composites is not expected to be very high. To ensure that these results are nevertheless meaningful, a number of tests were made to evaluate the reliability of our procedures.

The significance of the composites was determined by computing the signal-to-noise ratio (S) for each grid-point and each category Day N ($N = 0-6$) as

$$S_N = \frac{|\alpha'_N|}{\sigma(\alpha' - \alpha'_N)}, \quad (3)$$

where

$$\sigma(\alpha' - \alpha'_N) = \left(\frac{1}{J_N - 1} \sum (\alpha' - \alpha'_N)^2 \right)^{1/2} \quad (4)$$

is the standard deviation of the Day- N anomalous convection (α') with respect to the category mean (α'_N). Here, J_N is the number of samples in the Day N composite. As an overall measure of the reliability of the composite over the entire period, the mean of

S_N was obtained by averaging for $N = 0$ to 6. The computed result for the mean signal-to-noise ratio shown in Fig. 6, with areas exceeding 1 (shaded) indicating more reliable composite values. It can be seen that there are considerable geographical variations in the significance of the composites. In general, two broad areas, one over Borneo and Malaysia and one over New Guinea show acceptable significance ($S \geq 1$). Whereas, eastward of 160°E over a large area in the western Pacific and the oceanic area between 120°E and 140°E , the ratio falls below 1.

Fig. 7 shows the spatially averaged values of S over selected regions as a function of the category days N . Each region consists of a $10^\circ \times 10^\circ$ square domain centered over Borneo, New Guinea and the equatorial western Pacific near the dateline. It is not difficult to observe that while the overall significance obtained by averaging all the grid points falls below the $S = 1$ level by Day 4, those over Borneo and New Guinea remain above the significance level up to Day 6 and Day 5, respectively, and that over the western Pacific is always below the $S = 1$ level. Thus, the regional variations in significance appear to depend on the distance away from the Borneo source region and are also a strong function of the local topography. The low signal-to-noise ratio eastward of 160°E also suggests that any signal in the convection that is related to the cold surge is probably too weak or absent over the western Pacific, where strong variability is likely to be dominated by convective activity not necessarily correlated with the cold surges over southeast Asia. Interestingly, the inverse relationship between the convection over Borneo and New Guinea noted in the previous section is also evident in the corresponding time series.

Another important feature exhibited by all four curves in Fig. 7 is the apparent decrease in the significance of the composite as the category day increases. At a first glance, this would not be surprising, because the direct influence, if any, of the northeasterly cold surge on equatorial convection is expected to be strongest near the time of the local maximum northeasterly wind intrusion during the onset stage of the cold surge. As the lag time increases, transient features not related to the cold surge may become important and eventually wipe out the initial signal. However, this interpretation may not be entirely satisfactory because the significance of the composite after Day 4 is also affected by the increased sampling error due to the smaller size of the sample used.

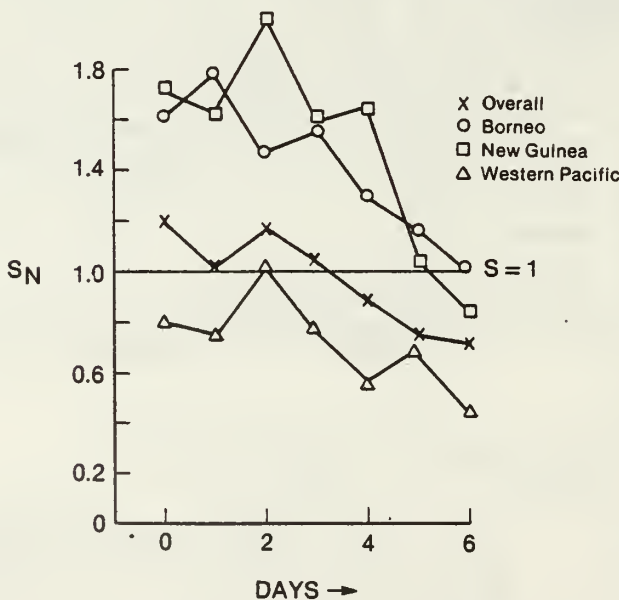


FIG. 7. Averaged signal-to-noise ratio (S_N) as a function of category date number over selected geographical areas.

Similar procedures were applied to the symmetric and antisymmetric component of the anomalous convection. Fig. 8 shows the decomposition of the signal-to-noise ratio by latitude for each component. The significance of the symmetric component is well above the acceptable level throughout the entire period, while that of the antisymmetric component is only marginal, with the largest relative signal ($S \approx 1.2$) occurring at the latitude bands $0-2.5^\circ$ and $7.5-10^\circ$ at Day 2-3. The modal decomposition therefore separates out the "signal" from the "noise" with strong signal only in the symmetric mode. This result is also consistent with the much larger amplitude in the symmetric compared to antisymmetric component as noted earlier. Our results should therefore be emphasized on the symmetric components. In summary, it can be concluded that the composites used in this study are reasonably adequate for describing the gross features of the response of low-latitude convection to northeasterly cold surges, especially the meridionally symmetric component of the response.

5. Interpretations

In a series of recent theoretical studies related to this work, Lim and Chang (1981) and Lau and Lim (1982) showed that equatorial disturbances can be triggered by adjustments of the various wave modes to large initial imbalances produced by forcing remote from the equator. Among the mixture of waves generated, only the gravest of the Rossby, Kelvin and mixed modes have significant amplitudes at the equator. In view of their studies, we venture the following rather speculative interpretation of our results. The eastward-moving pattern confined between $0-2.5^\circ$ observed in our convective estimates, suggests very strongly the presence of a Kelvin-type response. The phase speed of 10 m s^{-1} agrees well with the preliminary findings of Williams (1979) using WINTER-MONEX data. The westward moving component away from the Borneo source region is probably linked to the gravest symmetric Rossby wave ($n = 1$). This wave moves much slower (5 m s^{-1}) than its eastward counterpart. (Theoretically the inviscid large-scale $n = 1$ Rossby wave moves with a speed approximately one-third that of the Kelvin wave.) Away from the equator, the westward moving symmetric components are likely to be related to higher-order Rossby modes which have their origins in the western Pacific. In the antisymmetric mode, only the eastward propagating signal near the equator is statistically significant. They can likely be identified with mixed Rossby-gravity ($n = 0$) wave types. Their slower propagating speed of 8 m s^{-1} compared with that of the Kelvin wave (10 m s^{-1}) is also consistent with that predicted by equatorial wave theory (Matsuno, 1966). An interesting feature in the time-latitude sections shown is the predominantly larger amplitude of the symmetric compared with that of the antisymmetric

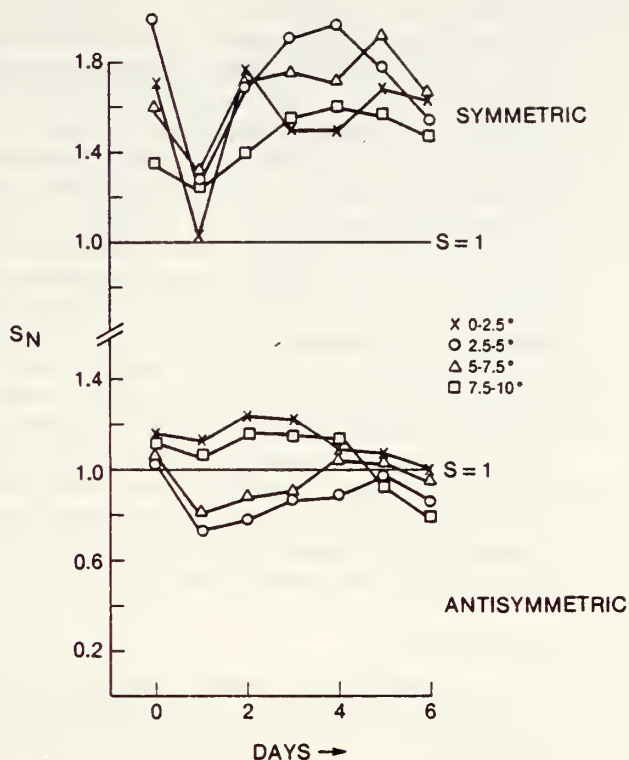


FIG. 8. As in Fig. 7, except for the symmetric and antisymmetric modes averaged over latitude bands.

component, especially near the equator, where our significance tests showed the composites are reasonably reliable. Such dominance implies that the direct source of these disturbances must also be somewhat symmetric with respect to the equator (Lau and Lim, 1982). The analyses therefore suggest that these waves are generated from enhanced heat sources concentrated near the equator. The mechanism(s) which lead to the enhancement of equatorial convection by low-level monsoon surges are not very well understood. Lau and Lim (1982) suggested that they may be related to the changes in low-level convergence/divergence during the initial adjustment of the large-scale wind field to the monsoon air burst off the southeast China coast. The increased latent heat released then sets off travelling waves away from the source region. The Kelvin wave excited interacts strongly with easterly waves originating from the western Pacific, resulting in an overall increase of convective activities in the equatorial belt between 110 and 180°E . While a strong equatorial heat source is implied by the predominantly symmetric response near the equator, the presence, on the other hand, at the equator of non-vanishing antisymmetric modes which have maximum convergence away from the equator cannot be due to symmetric heat sources. This suggests two possibilities: 1) the antisymmetric modes arise locally from slightly asymmetric distribution of the heat sources and 2) the mechanism of equatorial wave generation by remote lateral forcing (Lim and Chang,

1981) may be responsible for their existence. However, the determination of the relative importance of these two effects is not possible from this study.

While the preceding interpretation may be criticized as being founded on a seemingly tenuous theoretical basis arising from linear barotropic systems, the problem, however, can be somewhat alleviated by the fact that in an equatorial β -plane each free mode of a baroclinic system has the same horizontal structure as a barotropic system with different equivalent depths (Matsuno, 1966). Further, the presence of friction (Chang, 1977) also tends to favor large vertical scales for equatorially trapped waves and hence more closely resemble a barotropic system. The effects of vertical wind shear and nonlinearity could, of course, further complicate our interpretations. Thus our results and interpretations should only be viewed as a first step toward the understanding of a potentially more complex phenomenon.

6. Conclusion

From analyses of routinely available satellite images over a two-month period (December–January) in 1974–75, we have shown that convection in the equatorial regions was enhanced following northeasterly cold surge onsets. East–west propagating disturbances were generated near the source region over Borneo. The eastward travelling disturbances interacted strongly with westward propagating disturbances originating from the western Pacific. The statistical significance analysis showed that the signature of the northeasterly surge in equatorial convection was a strong function of the local topography and tended to be less obvious away from the source region and for an increasing lag time. When the convection associated with these disturbances was decomposed into symmetric and antisymmetric components, the signal appeared to be strong only in the symmetric modes, while the antisymmetric modes remained obscured, due to their relative low signal-to-noise ratios. Further, the strong equatorially trapped character of these eastward (westward) moving disturbances suggested the possibility of Kelvin (low-order Rossby) mode responses.

Due to the limited scope of the present work, the conclusions we reached are tentative at best. Obviously, further studies are needed to substantiate our results. Yet this study demonstrates the feasibility of isolating the effect of low-level monsoon surges on equatorial convection from a rather complex ensemble of interacting components while at the same time allowing plausible physical interpretations. The insight gained from this work will hopefully be useful in further pursuit of dynamical interpretation of large-scale monsoon related phenomena using FGGE/MONEX data.

Acknowledgments. Part of this work was done while the author was at the Naval Postgraduate

School. The author wishes to thank Drs. C. P. Chang and H. Lim for helpful discussions that motivated this study. This work was partly supported by the National Science Foundation, Division of Atmospheric Sciences, Global Atmospheric Research Program under Grant ATM80-13153 and Climate Dynamics Section under Grant ATM79-24010.

REFERENCES

- Chang, C. P., 1970: Westward propagating cloud patterns in the tropical Pacific as seen from time-composite satellite photographs. *J. Atmos. Sci.*, **27**, 133–138.
- , 1977: Viscous internal gravity waves and low-frequency oscillations in the tropics. *J. Atmos. Sci.*, **34**, 901–910.
- , J. Erickson and K. M. Lau, 1979: Northeasterly cold surges and near-equatorial disturbances over the winter MONEX area during December 1974. Part I: Synoptic aspect. *Mon. Wea. Rev.*, **107**, 812–829.
- , and K. M. Lau, 1980: Northeasterly cold surges and near-equatorial disturbances over the winter MONEX area during December 1974. Part II: Planetary-scale aspects. *Mon. Wea. Rev.*, **108**, 298–312.
- Gruber, A., 1974: The wavenumber-frequency spectra of satellite measured brightness in the tropics. *J. Atmos. Sci.*, **31**, 1675–1680.
- Houze, R. A., S. G. Geotis, F. D. Marks and A. K. West, 1981: Winter monsoon convection in the vicinity of N. Borneo. Part I: Structure of the clouds and precipitation. *Mon. Wea. Rev.*, **109**, 1595–1614.
- Johnson, R. H., and D. L. Priegnitz, 1981: Winter monsoon convection in the vicinity of N. Borneo. Part II: Effects of large-scale fields. *Mon. Wea. Rev.*, **109**, 1615–1628.
- Lau, K. M., and H. Lim, 1982: Large-scale winter monsoon circulation as a response of the tropical atmosphere to time-dependent forcing submitted to. *Mon. Wea. Rev.*
- Lim, H., and C. P. Chang, 1981: A theory on mid-latitude forcing of tropical motions during winter monsoons. *J. Atmos. Sci.*, **38**, 2377–2392.
- Matsuno, T., 1966: Quasi-geostrophic motions in the equatorial area. *J. Meteor. Soc. Japan*, **44**, 25–41.
- Murakami, T., 1980a: Temporal variations of satellite-observed outgoing longwave radiation over the winter monsoon region. Part I: Long-period (15–30 day) oscillations. *Mon. Wea. Rev.*, **108**, 408–426.
- , 1980b: Temporal variations of satellite-observed outgoing longwave radiation over the winter monsoon region. Part II: Short-period (4–6 day) oscillations. *Mon. Wea. Rev.*, **108**, 427–444.
- , and F. P. Ho, 1972: Spectrum analysis of cloudiness over the northern Pacific. *J. Meteor. Soc. Japan*, **50**, 285–300.
- Payne, S. W., and M. M. McGarry, 1977: The relationship of satellite inferred convective activity to easterly waves over west Africa and the adjacent ocean during Phase IV of GATE. *Mon. Wea. Rev.*, **105**, 413–420.
- Wallace, J. M., and L. A. Chang, 1972: On the application of satellite data on cloud brightness to the study of tropical wave disturbances. *J. Atmos. Sci.*, **29**, 1400–1402.
- Williams, M., 1979: Interhemispheric interaction during winter MONEX. Report of the Sixth Planning Meeting for the Monsoon Experiment, GARP Special Rep., **34**, WMO, 16 pp.
- Yanai, M., and M. Murakami, 1970: Spectrum analysis of symmetric and antisymmetric equatorial waves. *J. Meteor. Soc. Japan*, **48**, 331–347.
- Zangvil, A., 1975: Temporal and spatial behavior of large-scale disturbance of tropical cloudiness deduced from satellite brightness data. *Mon. Wea. Rev.*, **103**, 904–920.
- , and M. Yanai, 1980: Upper tropospheric waves in the tropics. Part I: Dynamical analysis in the wavenumber-frequency domain. *J. Atmos. Sci.*, **37**, 283–298.

stream. No large-scale circulation and stress changes are included. This analysis was extended to effects of rotation via the equator (Hanson, 1983). The two components of the upper ocean heat content, η , are considered separately. The thermodynamic must also be included in the use the sea-air heat flux depends on η on the heat content. The continuous dynamic equations are coupled to the momentum rate. In the momentum the pressure terms (η , and η), describe both the perturbation mixed layer and the SST. Thus, the upper ocean heat depends both on the surface layer and the SST.

The problem can be formulated in terms of a beta-plane theory, but only for a baroclinic mode, when the equivalent is defined as a (complex) function of the associated with the air-sea heat exchange. Interesting results emerge. First, the upwind propagating wave speeds are retarded by the heat exchange as described previously (Figure 1). The lowest order Rossby waves of the baroclinic mode associated with the mean surface wind, when added to the mean surface wind, exhibit phase speeds which are first baroclinic mode speeds of 10 m s^{-1} . This unexpected and gratifying suggests that the westward propaga-

tion of SST anomalies documented by Rasmusson and Carpenter (1982) may be associated with diabatically forced mixed layer changes, and not only with thermocline oscillations as implied by the first mode models which do not consider the SST explicitly. A further result of the analysis is that the group speeds associated with energy propagation are even more enhanced.

This short note is descriptive rather than analytic; mathematical details may be found in Kraus and Hanson (1983) and Hanson (1983). Our purpose here is to underscore the need for measuring the upper ocean thermal structure, which shows both SST and mixed layer depth, in order to understand the evolution of tropical Pacific SST anomalies.

References

- Busalacchi, A. J. and J. J. O'Brien (1980) The seasonal variability in a model of the tropical Pacific. *Journal of Physical Oceanography*, 10, 1929-1951.
- Hanson, H. P. (1983) Equatorial waves in the presence of sea-air heat exchange. *Journal of Physical Oceanography*, submitted.
- Hoskins, B. J. and D. J. Karoly (1981) The steady linear response of a spherical atmosphere to thermal and orographic forcing. *Journal of the Atmospheric Sciences*, 38, 1241-1259.
- Kraus, E. B. and H. P. Hanson (1983) Air-sea

interaction as a propagator of equatorial ocean surface temperature anomalies. *Journal of Physical Oceanography*, 13, in press.

- McCreary, J. P. (1981) A linear stratified ocean model of the Equatorial Undercurrent. *Philosophical Transactions of the Royal Society of London*, A298, 603-635.
- Moore, D. W. and S. G. H. Philander (1977) Modeling of the tropical oceanic circulation. In: *The Sea, Ideas and Observations on Progress in the Study of the Seas*, 6, E. D. Goldberg, I. N. McCave, J. J. O'Brien and J. H. Steele, editors, Wiley-Interscience, New York, 319-361.
- Rasmusson, E. M. and T. H. Carpenter (1982) Variations in tropical sea-surface temperature and wind fields associated with the Southern Oscillation/El Niño. *Monthly Weather Review*, 110, 354-384.
- Webster, P. J. (1981) Mechanisms determining the atmospheric response to sea surface temperature anomalies. *Journal of the Atmospheric Sciences*, 38, 554-571.

Howard P. Hanson
Eric B. Kraus
Cooperative Institute for Research in
Environmental Sciences
University of Colorado
Campus Box 449
Boulder, CO 80309

Model of Atmosphere-Ocean Coupling in El Niño

It has been suggested that the El Niño can be viewed as the normal mode response of the system to changes in the surface wind field following a prolonged period of unusually strong trades (Wyrtki, 1971). This concept has been verified to some extent by observational and numerical studies (e.g., Hurlburt *et al.*, 1976). In addition to the oceanic features, an El Niño event involves changes in the atmosphere, presumably the redistribution of ocean heat and the atmospheric response to El Niño is a modification of the normal Walker circulation (and hence the distribution of rainfall in the tropics) as well as possible teleconnections to middle latitudes (Rasmusson and Carpenter, 1982). In the equatorial wind field, the ocean response, the system is coupled, making causal relationships complex. This note describes a dynamical model, very simple, but fully coupled to the atmosphere-ocean system. Some experiments are described, which use the model to gain some physical insight into

the mechanisms which determine the atmospheric and oceanic aspects of El Niño and how they interact with each other.

The model describes the first internal mode of the atmosphere and ocean using the shallow water equations. The equations are linearized about a motionless basic state in the ocean and a geostrophically balanced state of solid zonal rotation in the atmosphere. The atmospheric equations are solved globally; the oceanic equations are solved in a closed rectangular basin extending from 150°E to 80°W and from 15°S to 15°N, representing the equatorial Pacific Ocean.

The oceanic momentum equations include terms which represent the surface wind stress. The atmospheric continuity equation includes a source term which represents heating in the atmosphere. These terms control the interaction between the atmosphere and the ocean. In this respect the coupling is conceptually the same as that employed by Lau (1981). The specification and interpretation of the forcing terms is different, however.

The wind stress terms are specified conventionally:

$$F_x = \frac{\rho_a C_D V^* (U + u_1)}{\rho_0 (H + h_0)}$$

$$\text{and } F_y = \frac{\rho_a C_D V^* v_1}{\rho_0 (H + h_0)}$$

where h_0 is the ocean mixed layer depth anomaly, H is the mean mixed layer depth, U is the mean zonal wind, and u_1 and v_1 are the components of the atmospheric wind perturbation at the surface. ρ_a is the air density, ρ_0 is the water density, V^* is a typical low level wind speed and C_D is the drag coefficient.

The nature of the heating term, Q , is central to the operation of the model. It completes the feedback loop and determines how the ocean drives the atmosphere. Conceptually, Q may be thought of as a product of two parts, Q_a , which depends on the state of the atmosphere, and Q_o , which depends on the state of the ocean. Q_a reflects the large scale stability and vertical motion field of the atmosphere. It is undoubtedly important, but is treated as a constant here for simplicity. Q_o depends mostly on the sea surface temperature (SST) which in turn is controlled by such physical

mechanisms as horizontal advection, vertical advection (upwelling), mixing, air-sea exchange, and net radiation.

The effect of upwelling on SST may be (very roughly) parameterized in terms of h_m , the mixed layer depth anomaly, so that $Q_n = \alpha h_m$. Thus, with a shallow mixed layer ($h_m < 0$) we expect upwelling from below the thermocline and therefore low SST. Conversely, a deep mixed layer corresponds to higher SST. This is the approach taken by Lau (1981, 1982) and McCreary (1982) who used ocean models very similar to this, but prescribed the state of the atmosphere (specifically, the surface wind stress) in terms of h_m . In the present model, the predicted distribution of h_m is used to force the atmosphere explicitly, rather than to choose between two predetermined atmospheric states.

The modeling approach is similar to that of several other El Niño studies (Hurlburt *et al.*, 1976). The ocean was initialized at rest and the atmosphere was initialized with solid easterly zonal rotation with magnitude 0.5 m s^{-1} at the equator. (The value of 0.5 m s^{-1} was chosen to be consistent with the magnitude of the first empirical orthogonal function of the interannual trade wind variation determined by Barnett (1977)). The coupled system achieved a quasi-steady state after about 200 days of integration. At day 240 the solid zonal rotation was turned off and the model was allowed to relax. Figure 1 shows the time-longitude series for the ocean mixed layer depth anomaly, h_m , and vertical motions in the atmosphere, w_a . As expected, the SST (proportional to h_m) fell in the eastern Pacific Ocean during the spin up time and rose following the relaxation of the strong trades. However, this event cannot qualify as an El Niño because the SST anomaly remained negative everywhere east of 125°W even as the system reestablished a quasi-steady state about one year after the relaxation of the trades. The atmospheric re-

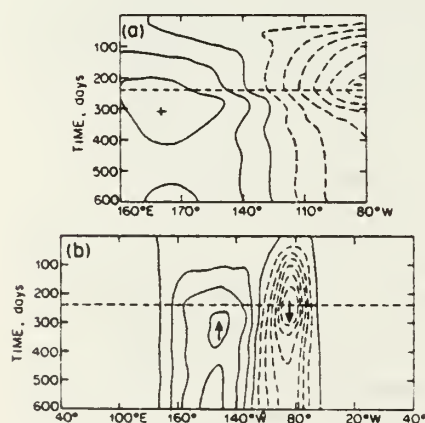


FIGURE 1 (Rennick)

Time-longitude cross sections of (a) mixed layer depth anomaly and (b) vertical motion anomaly at the equator with atmospheric heating proportional to mixed layer anomaly. Negative anomalies are dashed. Units are arbitrary.

sponse of the model, as characterized by w_a , is also unrepresentative of El Niño observations. At all times there is upward motion at about 170°W and more intense downward motion near 90°W . The intensity of this circulation wanes as the system relaxes, but there is no eastward shift of the axis of upward motion. Thus it is apparent that a simple linear coupling between mixed layer depth and atmospheric heating is not capable of producing an El Niño-like response within the context of this simple model.

In order to generate an El Niño-like response, the assumption that SST is proportional to h_m was abandoned. Instead, the SST was computed using a simple advective equation

$$\frac{\partial(\overline{SST})}{\partial t} = -u_0 \frac{\partial(\overline{SST})}{\partial x} - E(\overline{SST})$$

where $\partial(\overline{SST})/\partial x$ is a prescribed gradient of SST across the ocean basin and u_0 is the perturbation zonal current in the mixed layer. $\partial(\overline{SST})/\partial x$ was taken to be uniform, corresponding to a 10°K temperature difference across the entire ocean basin. E is an exchange coefficient with a time scale $E^{-1} \approx 80$ days. With this system, the ocean currents are determined by shallow water equation dynamics. These currents subsequently determine the SST distribution through zonal advection.

The results of this model are shown in Figure 2. The model was spun up for 120 days and then allowed to relax. Examination of the results shows that during the spin up stage the h_m anomaly was positive in the western part of the ocean and negative in the east, as in the previous case. However, the equatorial currents associated with the oceanic Kelvin wave during spin up produced a weak negative SST anomaly across the entire ocean basin. In the atmosphere there was a broad region of anomalous descent over the ocean basin. This was accompanied by enhanced surface easterlies so that the SST-driven atmospheric circulation tended to reinforce the surface wind stress which generated the SST anomaly in the first place. Conditions at day 120 roughly correspond to the pre-El Niño conditions reported by Rasmusson and Carpenter (1982). Following the relaxation of the zonal wind forcing, the equatorial ocean current and therefore SST advection changed sign in the eastern part of the ocean, resulting in a region of positive SST anomaly which spread westward with time. This positive SST anomaly led to enhanced convection over the ocean accompanied by anomalous surface westerlies from 125°W across the dateline to 125°E and anomalous surface easterlies elsewhere. This weakened Walker circulation is consistent with observations of the atmosphere during El Niño events. The peak of the model El Niño was reached at about day 300, or about 5 months after the first

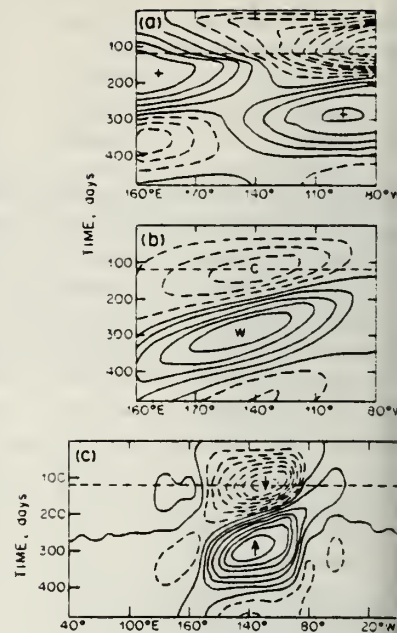


FIGURE 2 (Rennick)

Time-longitude cross sections of (a) mixed layer depth anomaly, (b) SST anomaly and (c) vertical motion anomaly at the equator with atmospheric heating proportional to SST anomaly.

appearance of a positive SST anomaly at the eastern boundary of the ocean.

At about day 300, weak westward currents appeared in the eastern Pacific Ocean signalling the end of increasing SST in that region, and a decrease in atmospheric convection. The SST at 80°W returned to normal about 6 months after the first appearance of a warm anomaly there. About 2-3 months later the SST in the central Pacific also returned to normal. The atmosphere responded to the return to normal forcing by relaxing toward the zero anomaly field itself.

Based on these results it would appear that the SST field is largely controlled by the progression of eastward propagating Kelvin waves and westward propagating Rossby waves through advection. The SST field determined in this way acts as a heat source for the atmosphere. The resulting atmospheric circulation then modifies the ocean forcing through the surface wind stress.

To determine the importance of this feedback, the model was run with

$$F_v = \frac{\rho_a C_D V^* U}{\rho_0 (H + h_0)} \text{ and } F_s =$$

Thus, during the spin up, the ocean was subject to a zonal stress due to the solid zonal rotation of the atmosphere. At day 120 the zonal rotation was removed and thereafter the state of the ocean was determined by internal dynamics alone. There was no external forcing. Comparison with the fully interactive model shows that the results are qualitatively similar but with two important differences. The magnitudes of the anomaly fields are greatly reduced and the time scales are about 10% longer.

active case. This is consistent with the feedback. The induced atmospheric circulation reinforces the easterly wind driving the spin up, intensifying the Kelvin wave. During the relaxation phase, the atmospheric anomaly over most of the eastern Pacific, again providing positive feedback to the ocean currents, strengthening the easterly wind, prolonging the time during which the wind acts on the mean SST gradient to produce atmospheric forcing.

The model results clearly do not reproduce the entire scenario of an El Niño event. They do provide a convenient framework for a mechanistic understanding of the event. The westward progression of the SST anomaly from the coast of South America to the central Pacific is reproduced as the general response of the Walker circulation. It should be noted that the model does not have a natural internal oscillation. The event is triggered by an external forcing of the trades (presumably by mid-latitude events). The most notable

shortcoming of the model is its failure to reproduce the exact structure of the SST anomaly pattern and its evolution with time. Neither the initial positive anomaly near the dateline nor the local maximum anomaly near the South American coast during the peak period of the event is present in the model results. However, it is speculated that further refinement of the SST equation (and inclusion of Q_a) may lead to better simulation of these features while at the same time contributing to our understanding of the physical mechanisms which produce them.

References

- Barnett, T. P. (1977) An attempt to verify some theories of El Niño. *Journal of Physical Oceanography*, 7, 633-647.
- Hurlburt, H. E., J. C. Kindle and J. J. O'Brien (1976) A numerical simulation of the onset of El Niño. *Journal of Physical Oceanography*, 6, 621-631.
- Lau, K. M. (1981) Oscillations in a simple equatorial climate system. *Journal of Atmospheric Sciences*, 38, 248-261.

- Lau, K. M. (1982) A simple model of atmosphere-ocean interaction during El Niño Southern Oscillation. *Tropical Ocean-Atmosphere Newsletter*, No. 13, 1-2.
- McCreary, J. P. (1982) A linear model of tropical ocean-atmosphere coupling. *Tropical Ocean-Atmosphere Newsletter*, No. 9, 6-7.
- Rasmusson, E. M. and T. M. Carpenter (1982) Variations in tropical sea surface temperature and surface wind fields associated with the Southern Oscillation/El Niño. *Monthly Weather Review*, 110, 354-384.
- Wyrtki, K. (1975) El Niño—the dynamic response of the equatorial Pacific Ocean to atmospheric forcing. *Journal of Physical Oceanography*, 5, 572-584.

Mary Alice Rennick
Department of Meteorology
Naval Postgraduate School
Monterey, CA 93940

Reflection of Equatorial Waves from Oceanic Boundaries

In the last several years, theoretically equatorial wave motions have been described (e.g., Wunsch and Gill, 1976). Depending on frequency and wave type, the energy of equatorial waves can travel eastward or westward. Eventually the waves strike oceanic boundaries and reflect. Recently results along the coasts of North and South America (e.g., Smith, 1978; Enfield and Le 1980; Chelton, 1980) and in the eastern Pacific (Picaut, 1982) suggest that the oceanic variability along these boundaries is of equatorial origin.

To emphasize the importance of equatorial waves, fundamental questions remain unanswered. For example, when an equatorial wave of frequency ω and eastward group velocity c strikes an eastern oceanic boundary, what fraction of the energy of the incoming wave is reflected poleward along the boundary as Kelvin waves?

Previous descriptions of various equatorial waves striking meridional eastern and western boundaries are given elsewhere (e.g., Picaut, 1982). As an example, energy flux reflection coefficients for an equatorial Kelvin wave striking an eastern meridional boundary are plotted as a function of frequency (Figure 1). Frequency has been non-dimensionalized by $\sqrt{\beta c}$, where c is the long wave speed associated with the n th meridional mode and β is the northward gradient of the Coriolis parameter. Note the general trend of zero reflectivity (total absorption

as poleward propagating Kelvin waves) for the range $(1 - 1/\sqrt{2}) < \omega < (1 + 1/\sqrt{2})$ where no westward group velocity equatorial waves exist. As ω decreases from $(1 - 1/\sqrt{2})$ toward zero, more westward propagating equatorial planetary waves become available for reflection and the reflectivity monotonically increases. The monotonic increase is sharpest when low-numbered odd equatorial planetary wave modes (1, 3, 5) become available for reflection. This is not surprising since these wave modes have the same symmetry and similar scales north and south of the equator.

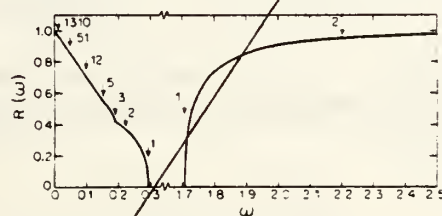


FIGURE 1 (Clarke)

The energy flux reflection coefficient of an equatorial Kelvin wave reflecting from an eastern meridional boundary. The graphs intersect the ω axis at $\omega = (1 - 1/\sqrt{2})$ and $\omega = (1 + 1/\sqrt{2})$, the frequencies corresponding to the highest frequency for equatorial planetary wave modes and the lowest frequency for inertia gravity wave modes. For $(1 - 1/\sqrt{2}) < \omega < (1 + 1/\sqrt{2})$, no waves with westward group velocity away from the boundary exist and $R(\omega) = 0$. For ease of plotting, the ω axis is broken between $\omega \approx 0.3$ and $\omega \approx 1.7$. The arrows and associated numbers point to the frequency when that number mode (planetary or inertia gravity) becomes available for reflection ($\omega = ((m+1)/2)^2 - (m/2)^2$ or $((m+1)/2)^2 + (m/2)^2$, respectively).

for the eastward current velocity as the eastward current velocity for the incoming Kelvin wave. The result

$$\lim_{\omega \rightarrow 0} R(\omega) = 1$$

indicated in Figure 1 is due to the absence of poleward propagating Kelvin waves on a β -plane at the low frequency limit.

When $\omega < (1 + 1/\sqrt{2})$, Figure 1 shows that $R(\omega)$ also increases monotonically with ω , a sharp increase occurring at $\omega = (1 + 1/\sqrt{2})$ when the first meridional mode equatorial inertia gravity wave becomes available for reflection. In fact, Figure 1 shows that almost total reflection is possible with just this $m = 1$ mode. The result

$$\lim_{\omega \rightarrow \infty} R(\omega) = 1$$

suggested by the curves in Figure 1, is due to the physical fact that at high frequencies, the incoming wave is negligibly affected by rotation and is totally reflected as an internal gravity wave. This internal gravity wave is actually the $m = 1$ mode, since at large ω the $m = 1$ mode has the same eastward current velocity structure as the incoming equatorial Kelvin wave.

In addition to energy flux reflection estimates, analytic theory can be used to estimate currents and pressure fields near non-meridional eastern oceanic boundaries. If there is effectively no wind forcing near the boundary,

Short-Term Climate Variability and Atmospheric Teleconnections from Satellite-Observed Outgoing Longwave Radiation. Part I: Simultaneous Relationships

KA-MING LAU

Goddard Laboratory for Atmospheric Sciences, NASA/Goddard Space Flight Center, Greenbelt, MD 20771

PAUL H. CHAN

Applied Research Corporation, Landover, MD 20785 and Goddard Laboratory for Atmospheric Sciences, NASA/Goddard Space Flight Center, Greenbelt, MD 20771

(Manuscript received 2 November 1982, in final form 6 May 1983)

ABSTRACT

Satellite-inferred short-term climate variability and atmospheric teleconnections are studied using seven years (1974–81) of Outgoing Longwave Radiation (OLR) data from NOAA polar orbiters. This study utilizes composite, partition-of-variance and multiple correlation techniques to investigate the simultaneous relationship in OLR fluctuation between remotely separated regions of the globe.

Results show that two dominant modes of variation are present in the monthly anomalous OLR time series fluctuation in the tropics. They are 1) variations of 2–3 month time scale associated with quasi-stationary fluctuation in the Walker Circulation and 2) an abrupt shift in the mean level of fluctuation related to the Southern Oscillation. The distribution of diabatic heat sources and sinks appears to exhibit a dipole-like oscillation that alternates between dry and wet periods over the equatorial central Pacific region and the maritime continent of Indonesia. The wet period is characterized by strong convection over the equatorial central Pacific, an eastward migration of the South Pacific convergence zone, and an equatorial migration of the ITCZ over the central and eastern Pacific, resulting in considerable shrinkage of the eastern Pacific dry zone. The dry period corresponds to intense convection over the maritime continent and an extensive eastern Pacific dry zone. While one major transition from dry to wet conditions is believed to occur from March 1976 to December 1977 associated with the 1975–76 El Niño, minor transitions between the two periods also occur frequently in the time scale of 2–3 months.

The major significant teleconnections using the equatorial central Pacific OLR fluctuation as reference are (identified by key geographical areas, with the sense of the correlation denoted by the signs in parentheses):

	(+)	(–)
Tropics:	equatorial central Pacific East Africa	maritime continent Australia northeast Brazil
Extratropics:	western North Atlantic Siberia	Hawaii South Pacific dry zone

It is suggested that the dry period over the equatorial central Pacific corresponds dynamically to stronger zonal teleconnections by equatorially trapped Kelvin and low-order Rossby-type response, and the wet periods, to stronger downstream meridional teleconnections characteristic of external higher-order Rossby-wave response to tropical diabatic forcing.

1. Introduction

Numerous recent studies have suggested the importance of the tropics in determining, at least in part, the severity of the northern winter in midlatitudes (e.g., van Loon and Madden, 1981; van Loon and Rogers, 1981; and others). In particular, the unusually severe winter of 1976–77 over the east coast of the United States was found to coincide with an extreme phase of the Southern Oscillation (SO) (Namias, 1978; Bar-

nett, 1981). Teleconnections in geopotential height fields between the tropical and the midlatitude atmosphere, which appears to be most pronounced during certain phases of the SO, has been demonstrated both empirically (Horel and Wallace, 1981) and theoretically (Webster, 1982; Hoskins and Karoly, 1981).

While individual “abnormal weather” (e.g., severe storms, blocking, intense cold polar outbreaks, etc.) occurs in the time scale of days to weeks, the variability in their frequency of occurrence, preferred locations

and tendency to interact with tropical systems appear to depend strongly on the prevailing planetary-scale circulation. These observations lead to the interesting hypothesis that quasi-stationary atmospheric anomalies such as those associated with teleconnections, would interact and thus cause changes in the statistics of the high-frequency fluctuation associated with weather over different parts of the globe. The study of the low-frequency variability associated with atmospheric teleconnections is therefore an important attribute to the understanding of long-range weather predictions.

The use of only geopotential fluctuation to describe teleconnection patterns often suffers from the relatively small signal in its response near the source region in the tropics for a given tropical diabatic forcing. This feature, coupled with the generally less reliable quality of geopotential analysis in the tropics, makes the use of satellite data both an attractive alternative and a complementary means to study climate teleconnections involving both the tropics and the midlatitudes. Furthermore, the sensitivity of the Outgoing Longwave Radiation (OLR) at the top of the atmosphere to small changes in convective cloudiness provides a good estimate of relative changes in the distribution of heat sources and sinks in the tropical atmosphere.

Satellite-derived earth radiation budgets have been used to study large-scale circulation changes in the tropical atmosphere. For example, Winston and Krueger (1977) used satellite radiance data to study tropical radiative heat source and sink distributions during the summer monsoon. Murakami (1980a,b) inferred changes in the winter monsoon circulation from analysis of OLR. More recently, the availability of satellite data of extended periods over several years offers, for the first time, opportunities to study interannual variability of the tropical circulation via satellite observations. Heddinghaus and Krueger (1981) showed that annual and interannual changes in OLR is related to the variation of the same time scale in the large-scale tropical circulation. Liebmann and Hartmann (1982) demonstrated that the evolution of OLR anomalies is closely tied to sea surface temperature anomalies (SSTA) associated with SO.

In this series of papers, we focus our attention on the low-frequency variability of OLR fluctuations, their possible correlations over different parts of the globe and their relationships with teleconnections obtained from other meteorological parameters, e.g., geopotential and temperatures fields. In Part I, simultaneous relationships with respect to the SO signal and the reference OLR fluctuation over the equatorial central Pacific are investigated. The relative importance of the SO signal over preferred regions will be emphasized. In Part II, using lag cross-correlation statistics, possible lagged relationships between the tropics and midlatitudes and their relationships with SO will be studied. A major problem encountered in an analysis of the

type described here is the limitation on the number of independent events due to the short length of the record compared to the climatic time scale in question. Therefore, we highlight only features which are consistent with our present knowledge of the dynamics of the system. We also explore features which may not meet rigorous statistical significance tests, but yet are either expected *a priori* from independent observations or predicted from dynamical theories.

Sections 2 and 3 describe respectively, the data and the general approach used in this study. The relevance of selected OLR indices to other climate indices is discussed in Section 4. Sections 5–8 are devoted strictly to description of observations using the various methods. The dynamical interpretation and inference of the results appear in Section 9. Conclusions and some considerations on short-term climate predictability are presented in the last section.

2. Data

The data used in this study are OLR from NOAA polar orbiting satellites digitized on a global grid of $2.5^\circ \times 2.5^\circ$ during an approximately seven-year period (June 1974–May 1981) with a gap of ten months from March to December 1978. Details concerning this data set were described in Gruber and Winston (1978). The equatorial crossing time for the sun-synchronous orbiter during different periods are summarized in the following:

Periods	Satellite	Equatorial crossing time
June 1974–February 1978	NOAA-4	0900–2100
January 1979–February 1980	TIROS-N	0300–1500
February 1980–May 1981	NOAA-6	0730–1930

The effect of the different equatorial crossing times shows up in large shifts in the individual nighttime and daytime observations during the above periods. This undesirable effect is somewhat allayed by the use of daily averaged data which effectively filter the diurnal variation. Since we concentrate on only the monthly and yearly time scales, the above sampling problem is not expected to seriously affect our results.

For this study, monthly mean OLR are used. The monthly climatology of OLR is obtained for each calendar month by averaging the corresponding daily values over the seven-year period. Monthly deviations at each grid point are then obtained by subtracting the monthly climatology. These deviations form the basis of our analyses. Hereafter, unless otherwise specified, all data referred to are for the monthly deviation field. Possible trends due to instrument bias, which might affect an analysis, are tested by computing the global annual average values for individual years and are

found to be negligible compared to the variability of the monthly anomalies.

3. Analysis technique

a. Composite methods

In this method, an index relating to the fluctuation of OLR over a selected region or in the time variation for a particular pattern (for example, principal components of selected eigenvector from empirical orthogonal function analysis) will be chosen to form a base time series. OLR values and a derived rainfall index (see Section 5) at all grid points are then composited according to the so-called "superposed-epoch method", where data during the same epochs determined from the base time series are averaged to form a mean for that epoch. In the present study, due to the relatively small size of our data with respect to the interannual variations, we decided to group the data into only two epochs corresponding to the months when the base time series attains its local maxima and minima. An anomaly pattern is obtained by taking the differences at each grid point between the means of the two epochs. This procedure tends to yield and maximize the amplitude of the contemporaneous teleconnections with the base fluctuation.

b. Partition of variance

The presence of a 10-month gap in the OLR data precludes the use of conventional spectral analysis to determine the time scale of the fluctuations. Nevertheless, as shown in the next section, the time series at some grid points are found to exhibit two distinct modes of variation—one related to a 2–3 month oscillation in tropical cloudiness and one related to the SO. A temporal variation relating to the latter is constructed at each grid point from the data. The relative variance contributed by the two modes can then be evaluated. The spatial pattern of the variance distribution yields valuable information on the preferred region of each mode of the fluctuation. The partition of variance into seasonal contributions, e.g., winter and summer, also sheds light on the relative amplitude of the SO signal in the two seasons. The method is akin to the poor man's spectral analysis methods (Lorenz, 1979) but is much simpler to apply and appears to be most appropriate when used in the present context.

c. Multiple correlation

Multiple-correlation statistics based on reference time series at selected stations or grid points have been used (Wallace and Gutzler, 1981) to study atmospheric teleconnections. In this paper, one-point multiple-correlation patterns are constructed by choosing as reference, the average OLR over several grid points taken at a nodal point of the teleconnection patterns revealed

by the above two techniques. A simple test is then devised to focus on only statistically significant correlations, taking into account the autocorrelation in each time series.

4. Regional climate indices

A number of recent studies (Horel and Wallace, 1981; Liebmann and Hartmann, 1982) suggested that convection over the equatorial central Pacific bears a close relationship with SSTA over the tropical Pacific during SO and provides a crucial link between local and remote atmospheric response to SSTA. In this section, we shall briefly explore and review such relationships using the OLR data and other related climate indices.

Figures 1a and 1b show the area-averaged OLR time variation over two key regions, one over the equatorial

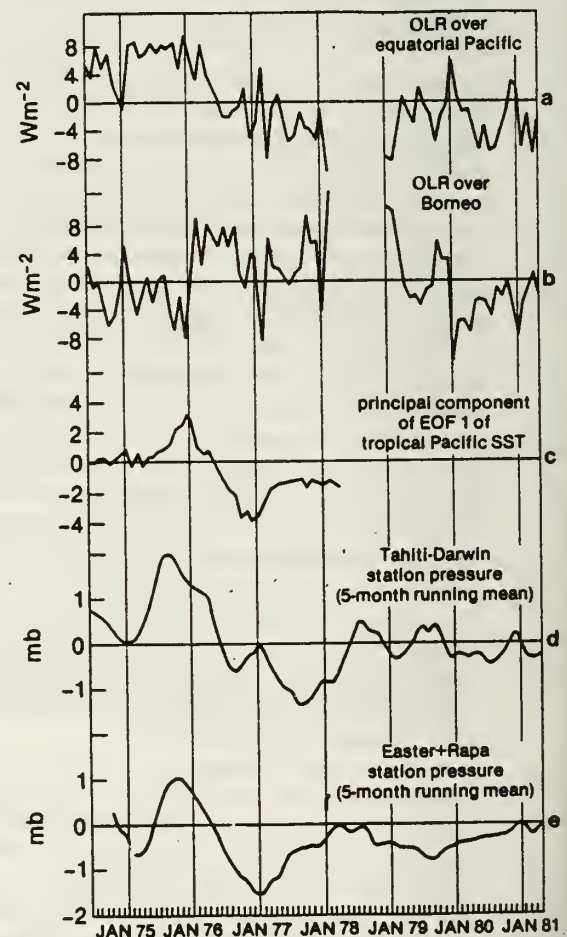


FIG. 1. Regional climate indices represented by area-averaged OLR over (a) the equatorial central Pacific (10°N – 20°S , 150°E – 150°W); (b) the maritime continent (5°N – 10°S , 100° – 120°E); (c) principal component of first empirical orthogonal eigenvector for tropical SSTA adopted from Weare *et al.*, 1976; (d) 5-month running mean of station surface pressure difference between Darwin and Tahiti; and (e) 5-month running mean of station surface mean pressure between Rapa and Easter Islands.

central Pacific (10°N–20°S, 150°E–150°W) and one over the maritime continent of Borneo and Indonesia (5–10°S, 100–120°E). Over the central Pacific, the time series show both strong fluctuation in the 2–3 month time scale and a clear interannual variation represented by a sudden shift from a predominantly positive to a negative level of fluctuation starting from the spring of 1976. The direction of the shift indicates a change from a less convective (dry) condition to a more convective (wet) condition associated with deep cumulus cloud types. A similar shift also occurs in early 1976 in OLR over the maritime continent but with opposite sign to that over the central Pacific. Here, the relative amplitude of the interannual variation is also considerably smaller than that over the equatorial central Pacific when compared with their respective monthly variability. The inverse relationship between the two time series in the monthly oscillation is a remarkable indication of a strong Walker-type circulation connecting the two regions.

Three indices associated with the SO are also included for comparison in Fig. 1. These indices are principal component of the first eigenvector of SSTA over the tropical Pacific adopted from the Weare *et al.* (1976), 5-month averages of station pressure difference between Darwin and Tahiti and mean pressure at Easter Islands and Rapa. The pressure indices (Figs. 1d and 1e) show the same large change at the latter part of 1975, 2–3 months prior to the major shift in OLR over the central Pacific and the maritime continent. An interesting observation as seen from these time series is that the OLR indices indicate a sudden change to anomalous dry (wet) conditions over the central Pacific (maritime continent) during January 1975–January 1976 about 9–12 months before the SSTA and the pressure indices attain their respective maxima. This precursory signal for El Niño, indicated by the antecedent OLR variation suggests the presence of an enhanced Pacific Walker circulation most likely related to a pre-El Niño increase in surface easterlies over the western Pacific (Wyrski, 1975).

From the above analysis, we can argue that the sudden shift in the level of fluctuations in the OLR time series over specific regions in the tropics possesses an interannual signal associated with the SO. Because this variation occurs in specific areas and with different modes of change and, moreover, because the occurrence of the shift is not concurrent with the time when NOAA switched satellites, we feel that it is probably safe to assume that the SO signal in the OLR indices is real and significant over and above any inherent bias in the data due to differences in instrumentation.

5. Composite fields

a. Analysis procedure

In this section, we use the central Pacific time series (Fig. 1a) as the basis of our composite analysis. To

examine the spatial distribution and possible teleconnection associated with the extremes of the index during different seasons, we define our winter season as from October to the following March and the summer season as from April to September. Within each season the data are grouped into two categories according to whether the base index shows an extreme positive or negative deviation. The selection of extreme events is based on the following objective criterion.

From the area-averaged daily fluctuations over the equatorial central Pacific, a theoretical noise level is calculated according to the formula (Madden, 1976)

$$\sigma_T^2 = \frac{\sigma_d^2}{T} \left[1 + 2 \sum_{j=1}^{T-1} \left(1 - \frac{j}{T} \right) R_j \right], \quad (1)$$

where σ_d^2 is the variance of the daily data and R_j , the autocorrelation of the daily data at the j th-day lag. The expected variance σ_T^2 of the time-average of length T (~ 30 days), which is due solely to the finite size of the sample, is a measure of the natural variability or noise inherent in the time series of monthly means.

Months are considered to be extreme only if the corresponding peaks in the base index exceed the $2\sigma_T$ value calculated from (1). The same criterion is applied to the winter and summer periods with the corresponding variances and autocorrelations. Thus, four patterns denoted respectively by DW (dry winter), WW (wet winter), DS (dry summer) and WS (wet summer) obtained by averaging the monthly data at each grid point within each category, emerge from the above procedure. The months which comprise the two categories for winter and summer are shown in Table 1. Anomaly patterns obtained by taking the difference of the dry and the wet categories will be shown.

The significance of the difference of the mean of the two categories is estimated by the following simple statistical test. Based on the null hypothesis that the two means are equal, the ratio

TABLE 1. Tabulation showing months of extreme events that comprise the different composite categories. See text for explanation of symbols.

Winter		Summer	
DW	October 1974 January, February, March, December 1975 March 1976 February 1977 January 1980	DS	June, August 1974 May, June, July, August 1975
WW	December 1976 March, December 1977 February 1978 February, October 1979 February, March 1981	WS	July, August 1977 June 1979 June, August 1980

$$t = \frac{\bar{X}_1 - \bar{X}_2}{\left[\frac{N_1 \bar{S}_1^2 + N_2 \bar{S}_2^2}{N_1 + N_2 - 2} \left(\frac{1}{N_1} + \frac{1}{N_2} \right) \right]^{1/2}} \quad (2)$$

is distributed as a t -distribution (Panofsky and Brier, 1968) where N_j is the number of independent observation of the j th category, \bar{X}_j and S_j are the respective observed mean and variance within each category and are given by

$$\bar{X}_j = \frac{1}{n_j} \sum_{i=1}^{n_j} X_{jn},$$

$$S_j = \left[\frac{\sum_{i=1}^{n_j} (X_{jn} - \bar{X}_j)^2}{n_j - 1} \right]^{1/2}, \quad (3)$$

where n_j is the actual number of cases comprising the j th category.

We use for the two seasons ($j = 1, 2$):

$$\begin{aligned} \text{winter: } & N_1 = 6, \quad N_2 = 7 \\ \text{summer: } & N_1 = 2, \quad N_2 = 3 \end{aligned}$$

The numbers are chosen on the crude assumptions that events separated by more than 6 months are considered independent.

b. Winter patterns

Figure 2a shows the global pattern of the difference DW - WW. Grid points in which the difference of the means exceeds the 90 and 95% confidence limits according to (2) are marked by numerals 1 and 2,

respectively, in Fig. 2b. The most outstanding significant features in the composites are as follows:

- A huge area of positive anomaly (enhanced convection during WW) is found over the central equatorial Pacific extending southeastward into the Southern Hemisphere midlatitudes. A large area with negative OLR anomaly (reduced convection during WW) is also found with centers over the maritime continent and southeast Australia. This dipole-like pattern implies a strong reverse Walker circulation in the anomalous sense, with rising motion over the central Pacific and subsidence over the negative anomaly centers.

- Alternate positive and negative centers emanate from the central Pacific convective source region, over Hawaii, across central America and the southeast United States to the Atlantic seaboard. This pattern is reminiscent of the wave train description of the Pacific-North American teleconnection in geopotential described by Wallace and Gutzler (1981), except that the global OLR depicts more clearly the pattern in the tropics. The teleconnections within the extratropics can be seen more clearly when the normalized variations are considered (see Section 7).

- The satellite inferred convective activity over Brazil extending across the Atlantic into East Africa also appears to vary inversely with that over the equatorial central Pacific. This negative anomaly over the equatorial Atlantic coupled with two regions of positive anomalies on both sides of the equator indicate that the Atlantic ITCZ is suppressed during WW while flanked on both sides by enhanced convection. The influence of this enhanced convection appears also to

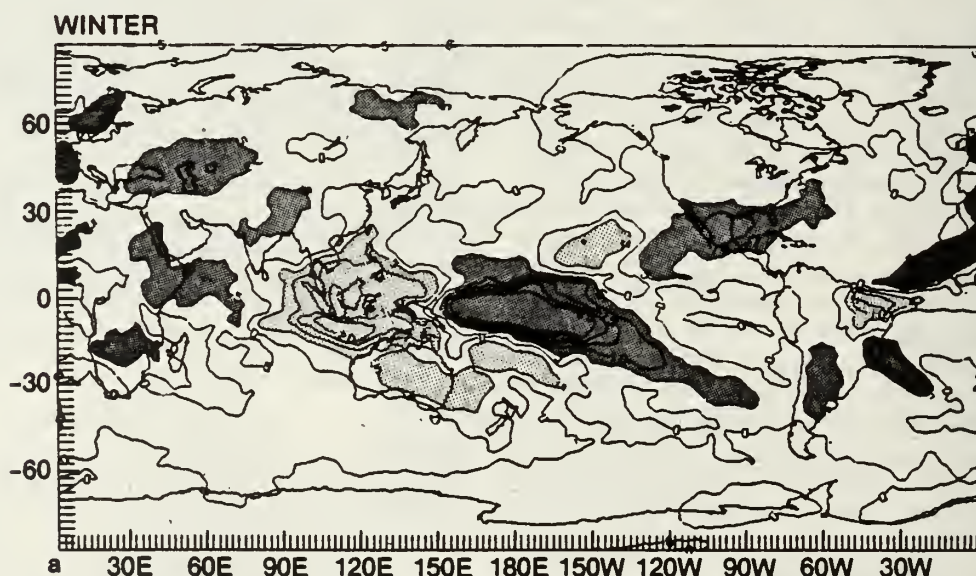


FIG. 2a. Teleconnection pattern of the difference of the composites for the dry and wet periods during winter (DW - WW as defined in the text) using the OLR variation over equatorial central Pacific as reference. Contour interval is 5 W m^{-2} . Positive values in excess of 5 W m^{-2} are stippled dark. Negative values less than -5 W m^{-2} are stippled light.

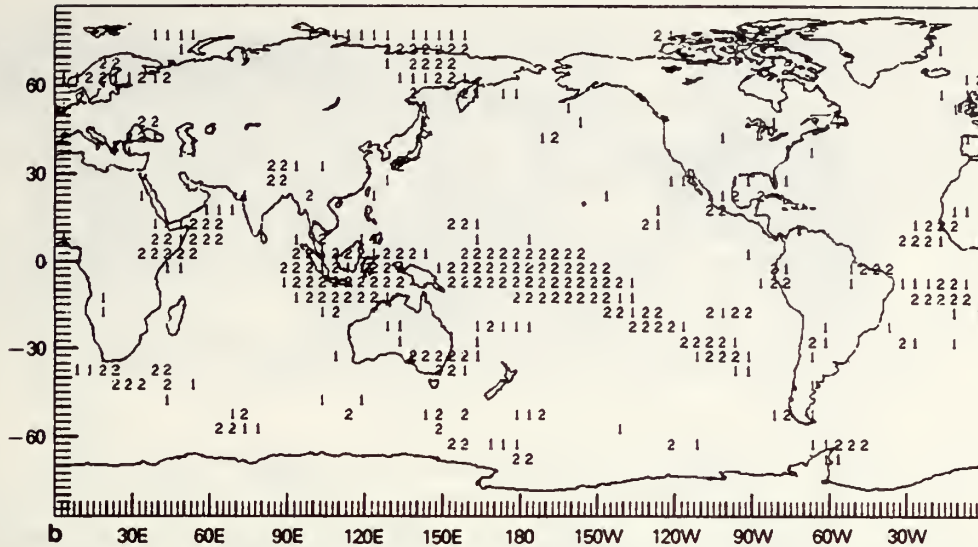


FIG. 2b. Statistical significance of the composite in Fig. 2a. Numerals 1 and 2 mark grid points in which the difference of the means exceeds the 90 and 95% confidence limits, respectively. Blanks represent regions where the significance is below the 90% level.

extend downstream into western Europe and the western South Atlantic.

- Elsewhere, significant teleconnection patterns are found over the Arabian Sea, the Himalayas and Siberia.

c. Summer patterns

Figures 3a and 3b show the pattern of DS - WS and the associated significant levels. The following features are noteworthy:

- The local influence of the central Pacific convection remains rather extensive although the amplitude is weaker than its counterpart.
- The downstream influence over North America and the southeast Pacific is greatly diminished.
- Strong negative anomalies are found over the East China Sea and India suggesting reduced convection or a weaker summer monsoon during the wet seasons of the equatorial central Pacific. However, due to the small number of independent cases comprising the composite, this feature does not meet the 90% significance test.

Overall, the summer teleconnection is much less organized than that of the winter, suggesting a possible reduced teleconnectivity of the atmosphere in the summer and therefore weaker remote response with respect to the central Pacific heat source variation. Also, the small degree of freedom in the sample could have contributed to uncertainties in the results.

6. Satellite-derived rainfall

In this section, we derive a new statistic regarding the frequency of occurrence of highly convective clouds

(HCC). The rationale for such an exercise is twofold. First, we wish to obtain an empirical relationship between OLR or its derived statistics and the rainfall rate. Because the frequency of HCC is associated with only a portion of the spectrum of clouds contributing to the total OLR, it will be interesting to compare the spatial distribution of this quantity in light of the teleconnection discussed earlier where the entire spectrum of cloud is included. Second, because it is often difficult to distinguish changes due to high cloud from those due to low cloud or the surface, the frequency statistics will isolate the effect of only deep cumulus clouds, thus enabling a better delineation of changes in features such as the ITCZ and the areal extent of convective cloud clusters during the wet and dry epochs.

To obtain the frequency distribution of HCC, we follow Kilonsky and Ramage (1976). The daily data are used to keep count of the total number of days within a given month at each grid point in which the daily-averaged OLR value falls below a threshold value. The threshold criterion is interpreted to mean that the cloud associated with deep convection has reached a certain fixed height in the upper troposphere. This procedure yields, for each month over the seven-year period, a frequency count N_c in number of days per month. Different values of the threshold are tried and the results are not very sensitive to the exact value of the threshold used, provided it is within the 230–250 $W m^{-2}$ range. In the results that follow, the threshold used is set at 240 $W m^{-2}$. An empirical relationship between N_c and the rainfall rate over the open ocean is derived in the Appendix where the frequency count method used here is shown to agree fairly well with other more sophisticated methods for rainfall estimation from space (e.g., Rao *et al.*, 1976). Henceforth,

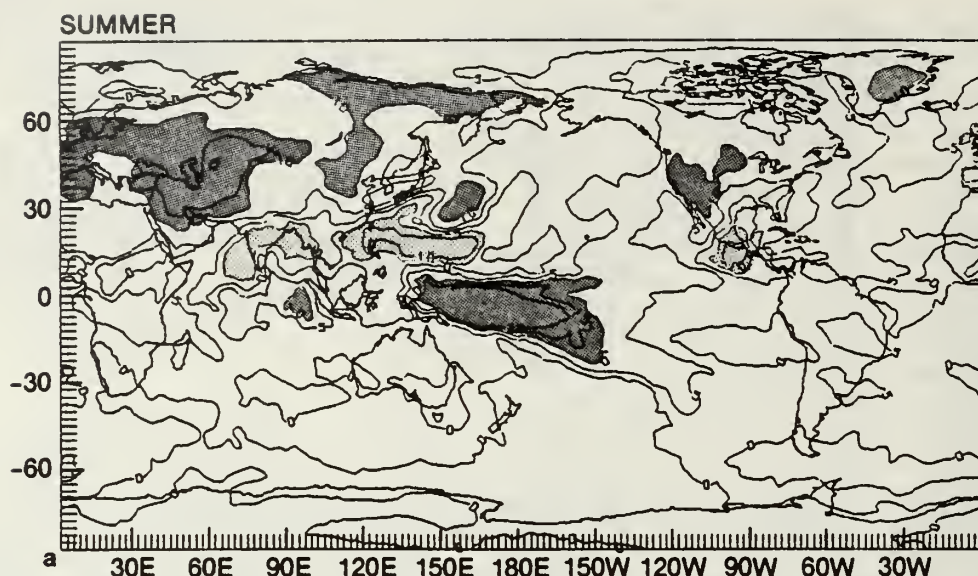


FIG. 3a. As in Fig. 2a but for the summer pattern DS - WS, as defined in the text.

the term rainfall and the N_c distribution will be considered synonymous.

Using the same procedure as in the preceding section, we arrive at composite rainfall patterns for the different categories. In order to better delineate the actual rainfall pattern, we include the mean seasonal field in the figures shown in the following. Due to the possible ambiguity in interpretation of N_c at high latitudes and over continental land masses, only the global band between 30°N and 30°S is shown.

Figs. 4a and 4b shows the N_c distribution during DW and WW, respectively. A striking feature in these distributions is the clear demarcation between the wet and the dry zones. This compares well with other an-

alyzed rainfall maps over the tropics (Rao *et al.*, 1976). Important features in these maps are as follows:

- There is an eastward shift of the major rain area from southern Indonesia and New Guinea in DW to the equatorial central Pacific in WW.
- During WW, there is a shrinkage of the eastern Pacific dry zone (roughly demarked by the $N_c = 3$ contour) accompanied by the eastward shift of a rainband extending from the central Pacific southeastward toward the midlatitudes of the Southern Hemisphere.
- The northeastward extension of a rainband from the central Pacific towards Central America is obvious during WW. A major difference between the rainfall

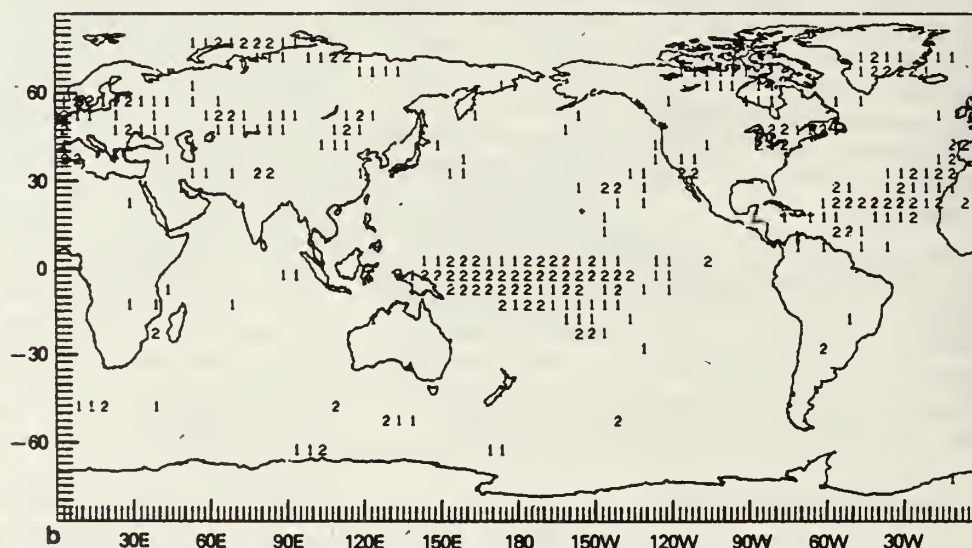


FIG. 3b. As in Fig. 2b, but for the summer pattern, DS - WS.

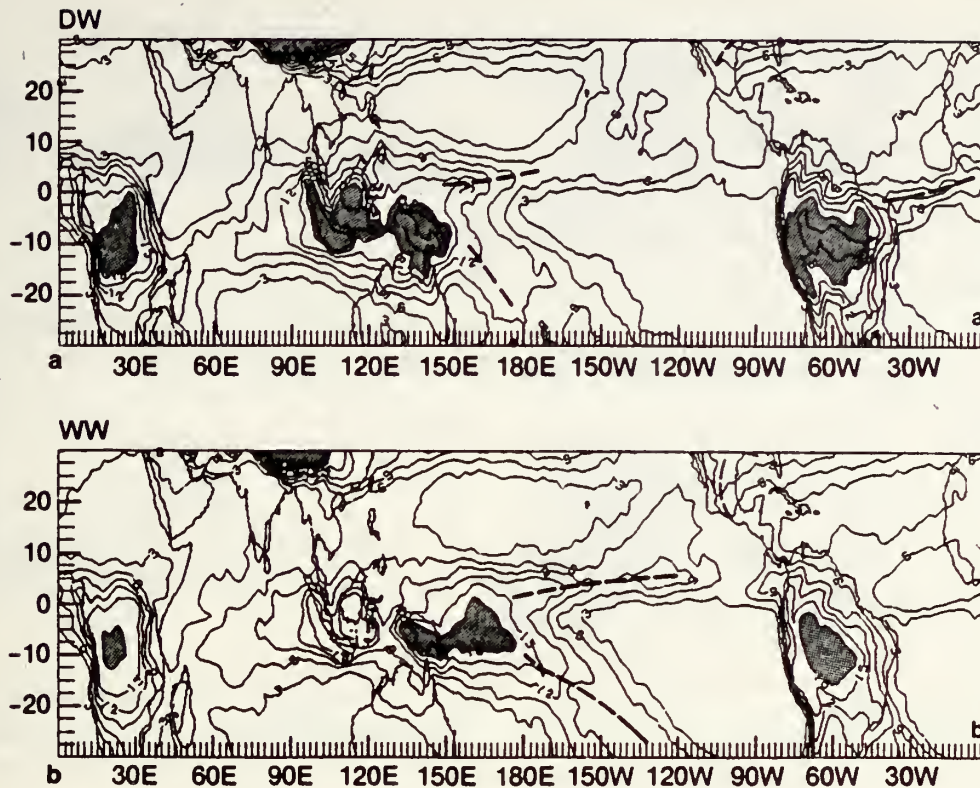


FIG. 4. Satellite-derived rainfall distribution over the tropics during (a) DW and (b) WW with the major precipitation centers shaded. Units in number of days. For explanation and conversion to rainfall rates, see text and Appendix.

and the OLR distribution is the absence of any rainfall activity in the dry zones showing that HCC is rarely found in this area during both periods. It also implies that the OLR variation in the dry zones in the previous composites is likely to be due to low cloud fluctuations or SST variations.

The following features are obvious in the summer rainfall patterns (Fig. 5a,b):

- The major rainband associated with the South Pacific Convergence Zone curves eastward and northward with enhanced rainfall over New Guinea during WS.
- Rainfall over the east Pacific ITCZ is strongly reduced during WS.
- There appears to be a reduction of precipitation over western India and Tibet associated with a weakening of the summer monsoon during WS. These results are consistent with those obtained from Section 5c.

To show the overall change in convective activity during the different periods, an index of convective activity (I_c) for each major heat source is defined by

$$I_c = \sum_{N_c > N_o} N_c(x, y). \quad (4)$$

For each diabatic heat source region, the summation

is over the local grid points where $N_c > N_o (=15)$, i.e., only over grid points in which at least half of the total number of days in a given month are covered by deep convection. While interpreting convective activity in terms of I_c , it should be borne in mind that the interpretation is most uncertain for the convective heat source over Tibet where signals from deep convection are contaminated with those from the snow-covered land surface. Table 2 shows the index I_c over the different source regions during different periods including the percentage changes going from the dry to the wet periods. Evident from Table 2 are the large changes of the opposite sign in the heat sources adjacent to the equatorial central Pacific, indicating fluctuations in the Walker-type circulation from the dry to the wet periods. Most important is the $\sim 12\%$ reduction (shown in the last column of the table) of overall convective activity going from the dry to the wet periods in both winter and summer. This suggests that the enhanced convection over the central Pacific during the wet periods is a result of the redistribution of total convection in the tropics. The total convective activities over all the convective centers may be even stronger in the dry than in the wet period.

7. Partition of variance

In the preceding analyses, we alluded that the SO signal is present in the OLR times series to various

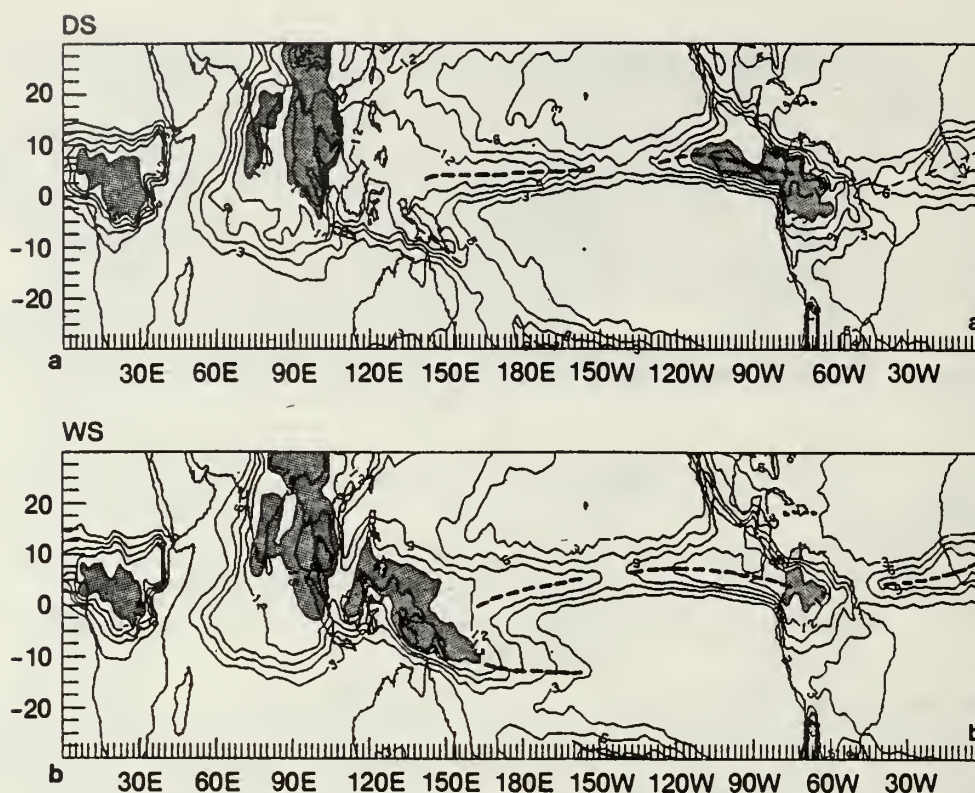


FIG. 5. As in Fig. 4, but for DS and WS.

degrees depending on the geographical location. It is therefore desirable to separate this signal from the "noise" due to other scales (e.g., the monthly scales) and that due to natural variability. With only one SO occurrence during our data period, the question that is most relevant to ask is: Does the OLR reflect any real changes in global climate before and after the SO? The statistical significance of such changes however, cannot be established until more SO events are considered. With satellite data this is impossible at present.

Consider a typical OLR time series $X(t)$ with observed variance $\text{Var}(X)$. Suppose at $t > t_c$, there is a sudden shift to a different level of fluctuation. We can define an SO signal by the function $X_{\text{SO}}(t)$ (see Fig. 6) as

$$X_{\text{SO}}(t) = \begin{cases} \frac{1}{t_c} \int_0^{t_c} X(t) dt, & t < t_c \\ \frac{1}{T - t_c} \int_{t_c}^T X(t) dt, & t \geq t_c. \end{cases} \quad (5)$$

Strictly speaking, the choice of t_c should be a function of the geographic location. However, since the SO phenomenon is global in extent and we are concerned only with simultaneous teleconnections in this part of the study, the use of a uniform t_c everywhere will not cause any serious problems. In the following results, t_c is set to be July 1976. Of course, one could have constructed a somewhat different, perhaps more precise functional form different from (5) to represent the

TABLE 2. Convection activity (I_c) of the major heat sources in the tropics during WW, DW, WS and DS and the percentage change ΔI_c going from the dry to wet periods in winter and summer. Only the relative magnitude of I_c is meaningful.

Winter	South Africa	Tibet-India	Maritime continent	Equatorial central Pacific	Northern South America	Total
I_c (WW)	169	162	112	263	175	881
I_c (DW)	176	171	234	164	252	997
ΔI_c (%)	-4	-5	-52	60	-30	-12
Summer	Central Africa	India-Indochina	Equatorial central Pacific	East Pacific ITCZ	Total	
I_c (WS)	109	334	140	68	651	
I_c (DS)	103	440	69	131	743	
ΔI_c (%)	6	-24	102	-48	-12	

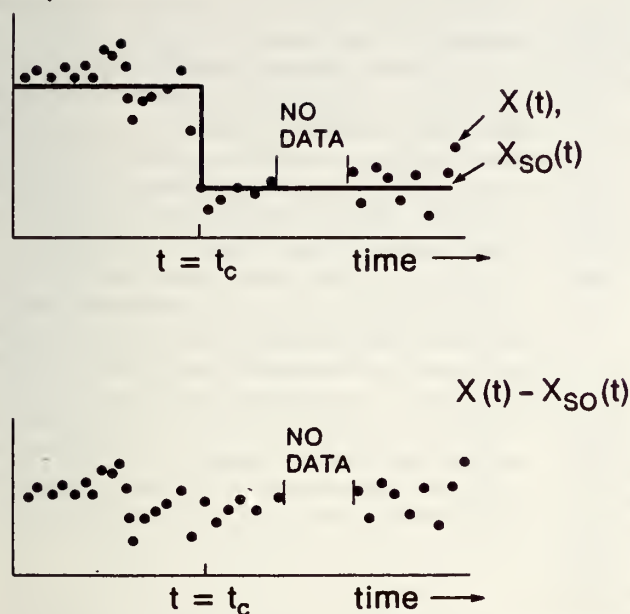


FIG. 6. Schematics showing the construction and the effect of removing the Southern Oscillation Signal (SOS) from the original OLR time series.

Southern Oscillation variation. But, bearing in mind that only one El Niño occurred during the data period, the results on this part can be considered as only a case study, at best. We therefore choose the simplest possible form, as in (5). Having defined the SO signal, the remaining variance $\text{Var}(X - X_{SO})$, after the SO signal has been subtracted, can be calculated. The ratio SOS (Southern Oscillation Signal) is defined by

$$\text{SOS} = 1 - \frac{\sigma^2(X - X_{SO})}{\sigma^2(X)}, \quad (6)$$

and gives the relative contribution of the total variance by the SO.

Figure 7 shows the distribution of SOS, with the numerals denoting in tenths the relative amount of

the SO-contributed variance and the blank regions denoting relative variance less than 10%. The strongest SO signal can be seen to appear over the equatorial central Pacific, providing further justification for our choice of reference for the composite. The most pronounced feature is an area of high SOS extending from the equatorial central Pacific in a fork-shaped pattern into the southern United States, Mexico and South America. The resemblance of the SO signal to the wintertime teleconnection pattern shown earlier is striking, but much less so with the summertime composite. This implies that the SO-related teleconnection is likely to be more active during winter. The strong teleconnection regions appear to coincide with the extent of the climatological subtropical westerly jet streams eastward and poleward of the tropical heat source region suggesting some downstream propagating effect from the source region in the tropics.

Next, we use the above method to estimate the relative amplitude of the SO-contributed variance in the base time series for the composites shown in Section 5. Here, the SO signal consists of a step function having a pre-El Niño ($t < t_c$) value of $+6 \text{ W m}^{-2}$ and a value of -3 W m^{-2} afterward. The difference of -9 units is statistically significant at the 95% level using (2). Table 3 shows the breakdown of the contributed variance for the various categories including the percentage of the total explained variance.

It can be seen that the combined DW and WW variance explains $\sim 45\%$ and that the combined DS and WS $\sim 26\%$ of the total variance with the remaining 29% accounted for by other signals not simultaneously correlated with the equatorial central Pacific fluctuations, including those associated with “natural variability”. With the SO signal removed, the variance drops to 16% for the winter and 3% for the summer. The variance contributed by SO is obtained by subtracting the second column from the first and is displayed in the third column—29% and 23%, respectively, for the winter and the summer. These contributions, when compared with the percentage variance

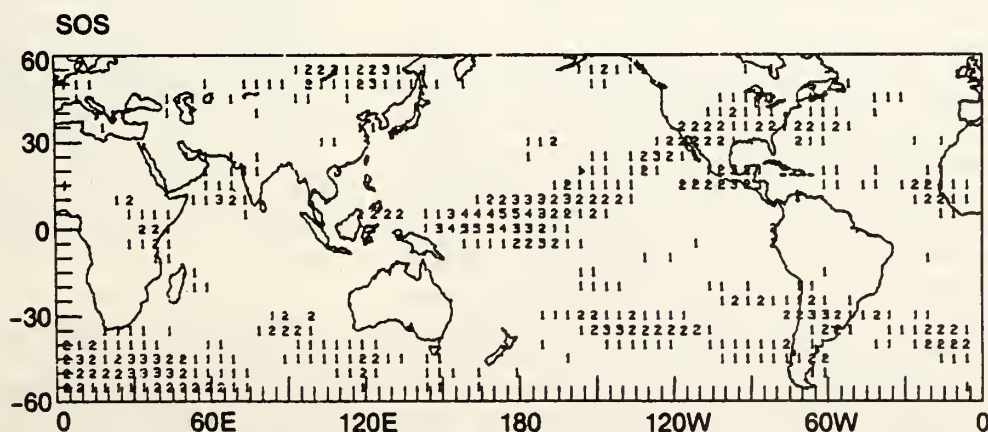


FIG. 7. Spatial distribution of the Southern Oscillation signal (SOS). Numerals denote in tenths the relative amount of the SO-contributed relative variance with blank regions denoting SOS less than 0.1.

TABLE 3. Partition of variance for the base time series in Fig. 1a by the four categories in the composite: $\text{Var}(X)$, $\text{Var}(X - X_{\text{SO}})$ and $\text{Var}(X_{\text{SO}})$ denote the contributed variance with and without the SO signal and that due to SO respectively. The number in parentheses shows the percentage of total variance as explained by the composites. Units are in $(\text{W m}^{-2})^2$.

	$\text{Var}(X)$	$\text{Var}(X - X_{\text{SO}})$	$\text{Var}(X_{\text{SO}})$
DW	427 (24)	157 (9)	270 (15)
WW	369 (21)	123 (7)	245 (14)
DS	334 (19)	17 (1)	317 (18)
WS	126 (7)	34 (2)	92 (5)
Total	1256 (71)	331 (19)	924 (52)

explained by the respective monthly variations, imply that during the northern winter, the OLR fluctuation over the central Pacific possesses a strong SO character as well as substantial variation in the 2–3 month time scale. Whereas, in the summer, the variation appears to be most predominant in the SO scale. Yet, the teleconnections shown appear to be more significant in the winter than the summer in spite of the relatively large local signal over the central Pacific. This would mean that the teleconnectivity of the northern summer hemisphere must be strongly reduced from that in winter. This point will be further discussed in Section 9.

8. Zero-lag correlations

The foregoing methods of analysis involve samplings from a preselected data subset and, in the case of the partition-of-variance method, require some prior information concerning the phenomenon that we intend to study. An alternative approach which does not require preselection is the use of correlation coefficients r_{XY} between two time series X_n , Y_n computed by the standard formula

$$r_{XY} = \frac{\frac{1}{N} \sum_1^N (X_n - \bar{X})(Y_n - \bar{Y})}{\left[\left(\frac{\sum_1^N (X_n - \bar{X})^2}{N-1} \right) \left(\frac{\sum_1^N (Y_n - \bar{Y})^2}{N-1} \right) \right]^{1/2}}. \quad (7)$$

Because the entire time series is now used, the additional information concerning, for example, the seasonality of the relationship, is lost in such a method. Yet, the increase in the effective number of independent observations and, therefore, the reduced sampling error, is a distinct advantage over and a complement to the other methods. Further, because the correlations are computed using normalized time series, the undesirable effect of the large difference in variance between the tropics and the higher latitudes in contaminating teleconnection signals between the two regions is taken into account by effectively providing a signal-to-noise estimate of any such relationships.

A problem that arises in the use of the correlation coefficient is the presence of autocorrelations for each

individual time series, which yield nonzero correlation coefficients even if the time series are completely independent. This is especially serious when the time series involved possess widely different autocorrelation time scales. A combined autocorrelation time must be established because for an event to be independent, the sampling time must be longer than the combined autocorrelation time scale. Although the problem can easily be solved in general by cross-spectrum analysis, the presence of a large data gap and the short length of the record forbid such an approach. Therefore, an alternative method has to be used to estimate the statistical significance of the correlation coefficients. A theoretical standard deviation for the correlation coefficient can be computed by using the more general formula by Jenkins and Watt (1968) to yield the following approximate expression for the standard deviation of the covariance for two independent first order Markov processes (see Part II, Appendix):

$$\text{SD}(c_{XY}) = \sigma_o \left(\frac{2}{N \{1 - \exp[-(\lambda_X + \lambda_Y)]\}} \right)^{1/2}, \quad (8)$$

where N is the total number of observations, σ_o the observed standard deviation from the OLR monthly time series and λ_X^{-1} , λ_Y^{-1} the e -folding time in months of the autocorrelation functions for the two time series determined by fitting a first order Markov process to the estimated autocorrelation function (see also Part II). In the following, the correlation is considered significant provided $|r_{XY}| > 2\text{SD}(c_{XY})/\sigma_o$, which corresponds approximately to the 95% significance level. In this paper, only the results for zero-lag correlations are presented. The lagged relationships, together with further analyses, will be discussed in Part II of this paper.

Figure 8 shows the significant correlation of the OLR time series at all grid points with respect to the area-

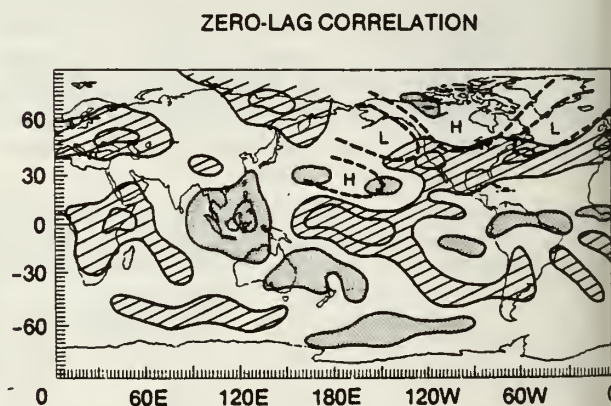


FIG. 8. Zero-lag correlation of OLR time series with respect to the area-averaged OLR fluctuation over the equatorial central Pacific (as in Fig. 1). Contour intervals are in units of 0.3. The lowest absolute value of the contours shown is 0.3, which is significant at the 95% level. Positive and negative values are denoted by cross-hatching and stippling, respectively. Dashed lines show the geopotential anomaly adopted from Horel and Wallace (1981).

averaged OLR fluctuation centered over the equatorial central Pacific shown in Fig. 1a. There is a remarkable similarity between the zero-lag correlation pattern with the DW - WW composite, especially in the tropics (Fig. 2). Again, this shows that the teleconnection patterns are strongest during the northern winter. The position of the extremes in the Pacific-North American branch of the correlation pattern compares well with the geopotential wave train description (dashed lines in Fig. 8) of a similar pattern by Horel and Wallace (1981). The overall pattern suggests that the Pacific-North American teleconnection is just a branch of an even wider global teleconnection complex involving the tropics and the midlatitudes of the two hemispheres. In the tropics, connecting with the Pacific-North America pattern is the positive and negative centers which can be taken as the fluctuation in the rising and the descending branches of the Walker circulation. In the Southern Hemisphere, a similar but less distinct wave train can also be discerned from the equatorial central Pacific across the southeast Pacific and central South America to the southwest Atlantic.

A broad area over northern Asia and Europe is also found to be significantly correlated with the central Pacific variation. Coupled with the negative correlation over the maritime continent, this pattern suggests a linkage between the northern Euro-Asian region and the maritime continent by some kind of large-scale thermally direct meridional circulation.

It is interesting to note that the zero-lag pattern (Fig. 8) and the wintertime composite (Fig. 2) both bear a strong resemblance to the nonseasonal eigenvector of Heddighaus and Krueger (1981) using only the first four years (1974-77) of the same data set. The principal component of their eigenvector also shows monthly and interannual variations similar to those of the reference time series in Fig. 1a. These observations suggest that the source of this global teleconnection pattern is most likely in the convection over the equatorial central Pacific.

9. Summary and interpretations

In this section, we summarize the significant results obtained from this study and highlight those which require more detailed discussion and interpretations:

1) *The OLR data show two basic modes of fluctuation, i.e., a short-term oscillation with a 2-3 month time scale and an abrupt shift of the level of oscillation associated with the Southern Oscillation; the relative importance of each depends strongly on the geographic location.*

The partition-of-variance method illustrates clearly the inherent spatial filtering effect of the atmosphere in exhibiting the SO signature in the OLR variation over only preferred regions. It is interesting to note that the regions of low SO amplitude (denoted by blanks in Fig. 7) correspond to the three climatological

tropical heat source regions: the vast land mass of Euro-Asia and the midlatitude storm tracks of the Pacific and Atlantic. These results are not too surprising because the larger daily variability of OLR in these meteorologically more "active" regions is expected to yield higher monthly variability compared with that due to SO. In contrast, over the vast oceanic regions of the central Pacific, away from the major land masses, the influence of SSTA is more strongly felt so that statistical probability of the formation of strong convection tends to vary with the time scale pertaining to the much longer oceanic or SO time scale.

While we have established the significance of the SO signal in the OLR data, the importance of the oscillations in the 2-3 month time scale should not be overlooked as they also contribute to the teleconnection pattern shown. Here, we note several past investigations which also provided evidences for oscillations of similar time scales in the tropical large-scale circulation. Madden and Julian (1971, 1972) found a 40-50 day oscillation in the zonal wind over the central Pacific. Using cloud motion vectors from geostationary satellites, Maruyama (1981) noted the presence of a standing wave oscillation of a 2-3 month period in the zonal wind component over the western and central Pacific. Since there have not been any similar observations in the meridional component of the wind, such oscillations are likely to be associated with the low-frequency fluctuations in the Walker circulation. The study of Maruyama (1981), in particular, supports our finding regarding the inverse phase relationship between the convection over the equatorial central Pacific and that over the maritime continent.

2) *As inferred from the OLR fluctuations and the derived rainfall patterns, there are strong atmospheric teleconnections both within and between the tropics and the middle latitudes.*

The OLR teleconnections discussed above reveal an oscillation of the tropical planetary-scale circulation between two extreme climate states. The two states correspond to abnormally dry and wet periods, respectively, over the equatorial central Pacific. A switch from the dry to wet state occurred in the spring of 1976. The phase of the event indicates that the shift is associated with the appearance of strong SSTA over the central Pacific. To a lesser extent, the central Pacific convection also appears to flip-flop between the two states in the 2-3 month time scale. During WW over equatorial central Pacific, the tropical atmosphere is characterized by reduced precipitation over the main tropical heat source areas, implying a weakened Walker circulation (see Table 3). The same period sees enhanced precipitation over preferred locations downstream and poleward of the source region.

Viewed in terms of the dynamical response of the atmosphere to tropical forcing, the WW period corresponds to (i) reduced equatorially trapped response associated with the Kelvin and the gravest Rossby modes and (ii) enhanced meridional propagating re-

sponse associated with higher order global Rossby modes. We shall refer to the equatorially trapped and the global Rossby modes as the nonradiating and radiating modes, respectively, in terms of their dynamical characteristics. The difference in characteristics is not unexpected in view of the recent theories on Rossby wave propagation on the sphere (e.g., Hoskins and Karoly, 1981; Webster, 1982). During WW, when the major anomalous convection (departure from the monthly mean) is over the equatorial central Pacific, part of the forcing falls under the influence of the upper-level westerlies over the tropical eastern Pacific. The strong subtropical jet streams poleward and downstream of the forcing region will, according to the theory, provide strong ducting of low-latitude anomalies into the extratropics. Whereas, during DW, the main heat source is over the maritime continent which is permanently capped by weak upper-level easterlies. Such configuration inhibits meridional propagation but favors equatorially trapped response associated with the Walker circulation (Lau and Lim, 1982).

A more recent study by Lau and Lim (1984) shows that for transient response, radiating modes can also be excited from easterly regime in the presence of westerly shear and that nonlinear effect can modify an initially easterly regime to allow for radiating response. Thus the conditions described above for nonradiating modes is strictly for steady-state linear response.

3) *The teleconnectivity of the atmosphere depends strongly on the season.*

As we have shown in Section 5, the summer teleconnection patterns are much weaker and less organized than the winter patterns. This may be true for

two reasons. First, so far we have concentrated on only atmospheric response to anomalous tropical forcings. During summer, the actual convection over the central Pacific is much reduced, as most of the diabatic heating is concentrated over Indochina and the Tibetan Plateau. As a result, the atmosphere over the central Pacific is inherently less unstable due to the reduced low-level moisture convergence. The ability of a SSTA to induce strong atmospheric response is greatly hampered. Therefore, the lack of teleconnection in summer may be due locally to the reduced efficiency of the atmosphere to produce a strong heat source from a given SSTA. Second, even if a heat source is generated, there is a lack of efficient mechanism for meridional propagation because the subtropical westerlies are located much further poleward and often the tropical eastern Pacific is affected by upper level easterlies during summer (Sadler, 1975).

A schematic summarizing the above discussions and showing different convective patterns and the most probable upper-level zonal wind distribution is shown in Fig. 9.

10. Conclusions

This study utilizes composite, partition-of-variance and multiple-correlation techniques to infer short-term climate fluctuation and atmospheric teleconnections from seven years of OLR data. A new statistic derived from the OLR data is also used to infer monthly rainfall distribution over the tropical oceans. The most important findings of this study are as follows:

1) During the period 1974–81, two dominant modes of oscillation are exhibited by the OLR fluctuation

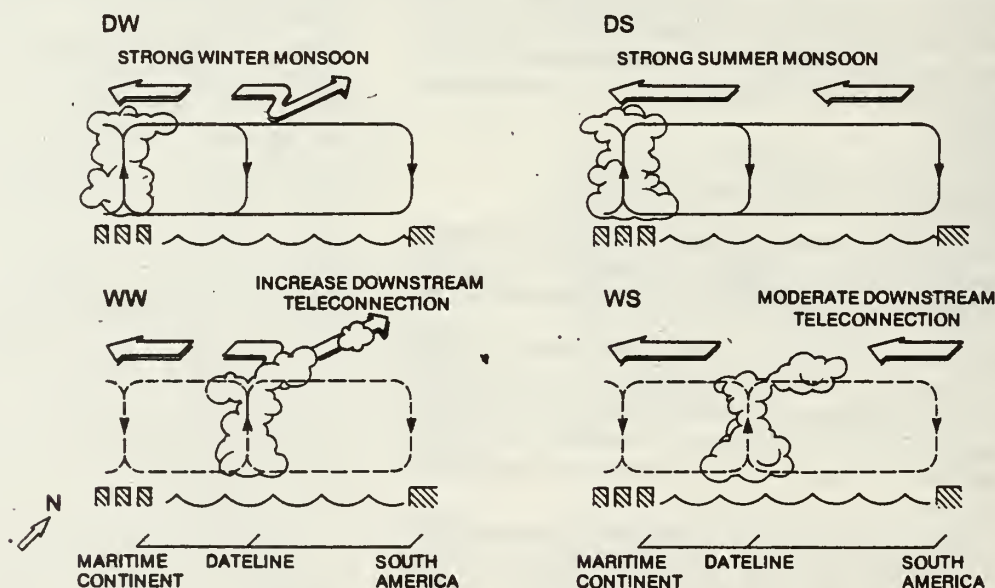


FIG. 9. Schematics summarizing the different anomalous convective patterns and most probable upper-level zonal wind distribution. The dotted lines for the WW and WS periods denote relatively weak Walker circulation compared with the DW and DS periods respectively. The degree of tropics-midlatitude coupling is proportional to the extent of the cloud bands extending from the tropics to midlatitudes.

over many regions in the tropics. They are interpreted here as the 2–3 month quasi-stationary fluctuation in the Walker circulation and a rather abrupt global change related to SO. The relative magnitude of the two modes of oscillation varies strongly but coherently over different areas.

2) The variation of diabatic heat sources and sinks over the tropical Pacific exhibits a spatially dipole-like vacillation between dry and wet conditions over the equatorial central Pacific. This vacillation is similar to the transition between two stable climatic states in the 2–7 year time scale of El Niño/Southern Oscillation suggested by Wyrski (1982). Our results show that the transition between the two states can also occur in a time scale of 2–3 months, independent of the SO. The dry periods correspond to stronger zonal teleconnections and the wet periods, stronger downstream meridional teleconnections.

3) During the wet periods, anomalously dry conditions prevail over the maritime continent. The South Pacific convergence zone migrates eastward and the ITCZ over the central and eastern Pacific moves closer to the equator resulting in a shrinkage of the extent of the eastern Pacific dry zone. In the dry periods, the major convection is found over the maritime continent and the east Pacific dry zone is extensive with its western edge extending westward of the dateline. These results are consistent with the findings of earlier studies (e.g., Liebmann and Hartmann, 1982; Rasmusson and Carpenter, 1982).

4) The SO signature as identified by the OLR teleconnections is most pronounced during winter and over specific geographic locations. The extratropical portion of the teleconnection pattern arising from the tropical source region may be related to the extent of the northern winter subtropical jet streams downstream and poleward of the source region.

5) The major significant teleconnection patterns identified by geographic regions are:

	(+)	(-)
Tropics:	equatorial central Pacific East Africa	maritime continent Australia northeast Brazil
Extra-tropics:	western North Atlantic Siberia	Hawaii South Pacific dry zone

The teleconnection pattern is also represented schematically in Fig. 10 with the positive (negative) sign denoting variations having the same (opposite) sense to that over the equatorial central Pacific.

There also appears to be significant correlation of OLR variation at high latitudes over Eurasia with that over the equatorial central Pacific. However due to the uncertainty in the interpretation of OLR fluctuation and the lack of *a priori* notion of the expected teleconnection patterns at these latitudes, the existence of such high-latitude teleconnections and its physical interpretation will have to be substantiated by further studies.

It should be noted that the teleconnections discussed in this paper are all with respect to the equatorial central Pacific OLR variations. It is likely that other patterns would also arise using similar techniques but based on a different reference location. By far, the teleconnections discussed in this paper is the most extensive compared with several others using different reference areas (see Part II).

An important implication that emerges from this study is the relevance of atmospheric teleconnections

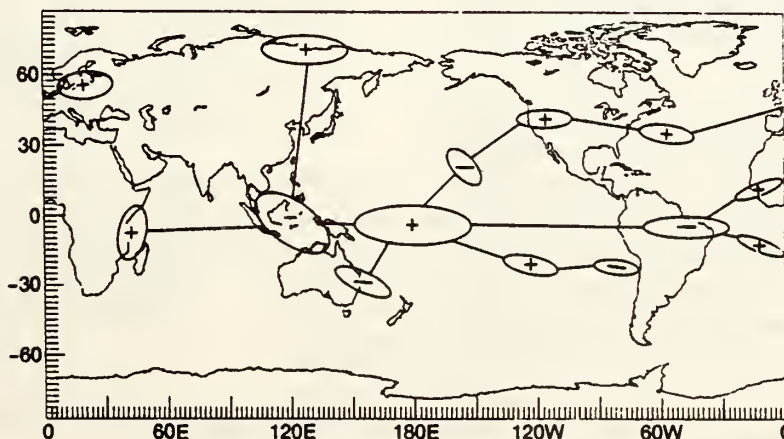


FIG. 10. Schematic showing the key regions in the global teleconnection pattern arising from OLR fluctuation in the equatorial central Pacific. The relative size and orientation represents the approximate magnitude and spatial distribution of the local correlation patterns. Signs of the correlations are also indicated.

using satellite-observed radiation parameters in long-range predictions. As we have seen, the OLR variation in the tropics is closely related to cloud and precipitation. In the extratropical oceans, signatures of wave disturbances are clearly imprinted in OLR visible radiations. Over continental regions OLR-inferred cloudiness is related to meteorological quantities such as surface temperature, relative humidity and wind (Fromm *et al.*, 1982; Short and Wallace, 1980). Thus a wide range of climate parameters, relating to both the dynamical and thermodynamical properties of the atmosphere and the ocean, can be deduced from satellite-derived radiation measurements.

In this paper, we have shown that convection over the equatorial central Pacific and the associated teleconnections tend to vary with a 2–3 month time scale as well as with the interannual time scale. Therefore, the spatial and temporal distributions of these teleconnection patterns enable the seasonal or interannual prediction of time-averaged atmospheric conditions over areas far removed from the source region by closely monitoring variations over the source region. More interestingly, this study shows that the predictability, for example, of extratropical rainfall, will be a function of both the geographic location and the season. To actually assess the potential of long-term prediction using satellite observations, the knowledge of the lagged relationships between teleconnections and the reference variation is essential. This research has been conducted and is reported in a companion paper (Lau and Chan, 1983).

Acknowledgments. The authors wish to thank Mr. D. A. Short for stimulating discussions and for his effort in compiling an atlas for the OLR monthly anomalies which provided much insight in our preliminary analyses. One of the authors (KML) would like to acknowledge support for travel and discussions with faculty members of the Department of Meteorology, Naval Postgraduate School, under Contract NA82AAG02003 of the National Oceanic and Atmospheric Administration and Grant 79-240101 of the National Science Foundation, both to the Naval Postgraduate School.

APPENDIX

Empirical Relationship between N_c and Tropical Rainfall Rate

The frequency count N_c of the total number of days in a given month in which the grid-point daily OLR value falls below a given threshold provides a new statistic which can be related to the rainfall rate over the open tropical oceans. Since there are no compatible rainfall records over the whole tropical ocean for the entire data period, we use the satellite derived rainfall rates by Rao *et al.* (1976) as a basis for our estimate. These rainfall rates were derived for all the tropical oceans based on the relationship between Electrical

Scanning Microwave Radiometer (ESMR) and precipitation rate (Wilheit *et al.*, 1976). It should be pointed out that the relationship derived below is not aimed at a new technique for rainfall estimation from space, but only at demonstrating that a physical meaning can be attached to the frequency statistics N_c as has been assumed in the text.

To obtain approximately independent estimates of rainfall rate over the overlapping periods of the Rao *et al.* rainfall chart and the OLR data (May 1974–February 1975), we calculate the area-averaged rates over a $20^\circ \times 20^\circ$ grid over the tropical oceans. Extra caution has been taken to avoid regions where questionable data are known to be present in the compiled charts. Because the linear scale of the averaging area is larger than twice the estimated autocorrelation of daily OLR fluctuation (Cahalan *et al.*, 1982), each estimate can be considered approximately independent. A total of 320 “independent” pair of estimates are made of N_c and the Rao *et al.* rainfall rates over the tropical Pacific, Atlantic and Indian Oceans for the overlapping data period. The two estimates are plotted on a scattered diagram (Fig. A1). A regression relationship between the rainfall rate R and N_c ,

$$R = 0.5 + 66.7N_c, \quad (\text{A1})$$

is constructed.

An analysis of variance table for testing the significance of the slope of the regression is set up. The F test of the relationship in (A1) is found to be highly significant. The 99% limit for 1 and 318 degrees of freedom is 6.76 (see Panofsky and Brier, 1968) com-

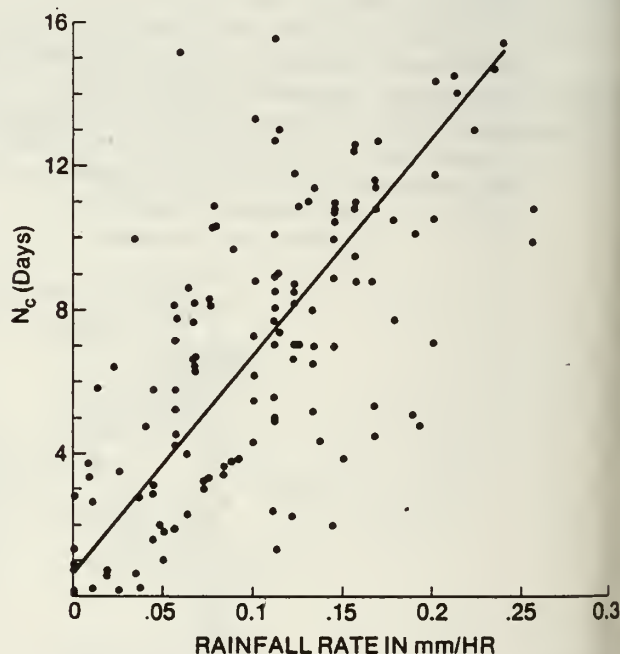


FIG. A1. Scatter diagram and regression line for the N_c -distribution (see text for explanation) and the rainfall rate derived from Rao *et al.* (1976).

pared with the observed F of 37.20. The large amount of scatter in the result may be due partly to the different sampling times for the two satellite estimates. The result shows that the rainfall estimates used here are at least compatible with the more sophisticated methods which Rao *et al.* used. However, the method is of questionable applicability when used over a continental region because of the relatively large OLR fluctuation due to, for example, moisture and surface temperature changes not correlated with convective cloudiness fluctuation. Therefore, although we use the term rainfall rates and N_c distribution interchangeably in the text, extreme caution has to be exercised when extending the above interpretation to over continental regions.

REFERENCES

- Barnett, T. P., 1981: Statistical prediction of North American temperature from Pacific predictors. *Mon. Wea. Rev.*, **109**, 1021–1041.
- Cahalan, R. F., D. A. Short and G. R. North, 1982: Cloud fluctuation statistics. *Mon. Wea. Rev.*, **110**, 26–43.
- Fromm, M. D., L. M. Penn, J. J. Cahir and H. A. Panosky, 1982: Statistical estimates of monthly mean and interannual changes of radiation fluxes at the top of the atmosphere. *J. Atmos. Sci.*, **39**, 1545–1554.
- Gruber, A., and J. S. Winston, 1978: Earth-atmosphere radiative heating based on NOAA scanning radiometer measurements. *Bull. Amer. Meteor. Soc.*, **59**, 1570–1573.
- Heddinghaus, T. R., and A. F. Krueger, 1981: Annual and interannual variations in outgoing longwave radiation over the tropics. *Mon. Wea. Rev.*, **109**, 1208–1218.
- Horel, J. D., and J. M. Wallace, 1981: Planetary-scale atmospheric phenomena associated with the Southern Oscillation. *Mon. Wea. Rev.*, **109**, 813–829.
- Hoskins, B. J., and D. J. Karoly, 1981: The steady state linear response of a spherical atmosphere to thermal and orographic forcing. *J. Atmos. Sci.*, **38**, 1179–1196.
- Jenkins, G. M., and D. G. Watts, 1968: *Spectral Analysis and its Applications*. Holden-Day, 525 pp.
- Kilonsky, B. J., and C. S. Ramage, 1976: A technique for estimating tropical open-ocean rainfall from satellite observations. *J. Appl. Meteor.*, **15**, 972–975.
- Lau, K.-M., and H. Lim, 1982: Thermally driven motions in an equatorial β -plane: Hadley and Walker circulations during the winter monsoon. *Mon. Wea. Rev.*, **110**, 336–353.
- , and P. H. Chan, 1983: Short-term climate variability and atmospheric teleconnection from satellite observed outgoing longwave radiation. Part II: Lagged correlations. *J. Atmos. Sci.*, **40**, 2751–2767.
- , and —, 1984: On the dynamics of equatorial forcing of climate teleconnections. *J. Atmos. Sci.*, **41**, (in press).
- Liebmann, B., and D. L. Hartmann, 1982: Interannual variation of outgoing IR associated with tropical circulation changes during 1974–78. *J. Atmos. Sci.*, **39**, 1153–1162.
- Lorenz, E. N., 1979: Forced and free variations of weather and climate. *J. Atmos. Sci.*, **36**, 1367–1376.
- Madden, R. A., 1976: Estimate of natural variability of time-averaged sea-level pressure. *Mon. Wea. Rev.*, **104**, 942–952.
- , and P. R. Julian, 1971: Detection of a 40–50 day oscillation in the zonal wind in the tropical Pacific. *J. Atmos. Sci.*, **28**, 702–708.
- , —, 1972: Description of global-scale circulation cells in the tropics with a 40–50 day period. *J. Atmos. Sci.*, **29**, 1109–1123.
- Maruyama, T., 1981: Upper troposphere zonal wind oscillation with a 30–50 day period over the equatorial western Pacific observed in cloud movement vectors. *J. Meteor. Soc. Japan*, **60**, 172–181.
- Murakami, T., 1980a: Temporal variations of satellite-observed outgoing longwave radiation over the winter monsoon region. Part I: Long period (15–30) oscillations. *Mon. Wea. Rev.*, **108**, 408–426.
- , 1980b: Temporal variations of satellite-observed outgoing longwave radiation over the winter monsoon region. Part II: Short period (4–6 day) oscillations. *Mon. Wea. Rev.*, **108**, 427–444.
- Namias, J., 1978: Multiple causes of the North American abnormal winter of 1976–77. *Mon. Wea. Rev.*, **106**, 279–295.
- Panofsky, H. A., and G. W. Brier, 1968: *Some Application of Statistics to Meteorology*. The Pennsylvania State University Press, 244 pp.
- Rao, M. S. V., V. Abbott III and J. S. Theon, 1976: Satellite-derived global oceanic rainfall atlas. NASA SP-410, Goddard Space Flight Center, Greenbelt, MD, 31 pp.
- Rasmusson, E., and T. Carpenter, 1982: Variation in tropical sea surface temperature and surface wind fields associated with the Southern Oscillation/El Niño. *Mon. Wea. Rev.*, **110**, 354–384.
- Sadler, J. C., 1975: The upper tropospheric circulation over the global tropics, UHMET 75-05, Dept. Meteor., University of Hawaii, Honolulu, 35 pp.
- Short, D. A., and J. M. Wallace, 1980: Satellite-inferred morning-to-evening cloudiness changes. *Mon. Wea. Rev.*, **108**, 1160–1169.
- van Loon, H., and R. Madden, 1981: The Southern Oscillation. Part I: Global associations with pressure and temperature in northern winter. *Mon. Wea. Rev.*, **109**, 1150–1162.
- , and J. C. Rogers, 1981: The Southern Oscillation. Part II: Associations with changes in the middle troposphere in the northern winter. *Mon. Wea. Rev.*, **109**, 1163–1168.
- Wallace, J. M., and D. S. Gutzler, 1981: Teleconnections in the geopotential height field during the Northern Hemisphere winter. *Mon. Wea. Rev.*, **109**, 784–812.
- Weare, B. C., A. R. Navato and R. E. Newell, 1976: Empirical orthogonal analysis of Pacific sea surface temperature anomalies. *J. Phys. Oceanogr.*, **6**, 671–678.
- Webster, P. J., 1982: Seasonality in the local and remote atmospheric response to sea surface temperature anomalies. *J. Atmos. Sci.*, **39**, 41–52.
- Wilheit, T. T., M. S. V. Rao; T. C. Chang, E. B. Rodgers and J. S. Theon, 1976: A satellite technique for quantitative mapping rainfall rate over the oceans. *J. Appl. Meteor.*, **16**, 551–560.
- Winston, J. S., and A. F. Krueger, 1977: Diagnosis of the satellite-observed radiative heating in relation to the summer monsoon. *Pure Appl. Geophys.*, **115**, 1131–1144.
- Wyrtki, K., 1975: El Niño: The dynamic response of the equatorial Pacific ocean to atmospheric forcing. *J. Phys. Oceanogr.*, **5**, 572–584.
- , 1982: The Southern Oscillation, ocean-atmosphere interaction and El Niño. *J. Mar. Tech. Soc.*, **16**, 3–10.

Short-Term Climate Variability and Atmospheric Teleconnections from Satellite-Observed Outgoing Longwave Radiation. Part II: Lagged Correlations

KA-MING LAU

Goddard Laboratory for Atmospheric Sciences, NASA/Goddard Space Flight Center, Greenbelt, MD 20771

PAUL H. CHAN

Applied Research Corporation, Landover, MD 20785 and Goddard Laboratory for Atmospheric Sciences, NASA/Goddard Space Flight Center, Greenbelt, MD 20771

(Manuscript received 2 November 1982, in final form 6 May 1983)

ABSTRACT

As a sequel to Part I of this study, lagged relationships in atmospheric teleconnections associated with outgoing longwave radiation (OLR) are investigated using Lagged Cross Correlations (LCC). The feasibility of extratropical seasonal-to-interannual predictions using satellite-derived observation is also quantitatively assessed. It is found that the global influence of teleconnectivity of the atmosphere is strongest for diabatic forcing located near the equatorial central Pacific, but much reduced for forcings over the maritime continent and to the east of the dateline. The LCC patterns show that at zero-lag, the OLR fluctuation over the equatorial central Pacific is associated with simultaneous excitation of quasi-stationary waves in the tropics. These tropics-tropics teleconnections eventually (in about 5 months) transform into tropics-midlatitude and midlatitude-midlatitude teleconnections associated with possible excitation of extratropical quasi-stationary waves in both hemispheres.

Analysis of the LCC pattern with the Southern Oscillation (SO) signal removed shows that during 1974–81, both the SO signal and the variability in the 2–3 month time scale contribute substantially to the observed LCC patterns. The presence of a convective heat source in the equatorial central Pacific is found to be important in forcing the tropics-midlatitude and the midlatitude-midlatitude teleconnections, which appear also to be phase-locked with the normal seasonal cycle. A mechanism is proposed to explain the observed lagged relationships. This mechanism is consistent with both internal atmospheric dynamics related to the seasonal cycle and with external influences such as sea surface temperature anomalies associated with the El Niño/Southern Oscillation.

Initial assessment of the predictability of regional climate using satellite-derived atmospheric teleconnection shows that about 30–40% of the wintertime OLR variance over the southeastern United States is accounted for by a 5-month antecedent OLR variation over the equatorial central Pacific. Because of the close relation between OLR variation and synoptic disturbances, the satellite-derived teleconnections described in Part I and Part II of this study can be used to identified regions with potentially higher seasonal-to-interannual predictability.

1. Introduction

In Part I of this paper (Lau and Chan, 1983, hereafter referred to as Part I), it was shown that simultaneous relationships exist in the variation of monthly anomalous Outgoing Longwave Radiation (OLR) between the equatorial central Pacific and different regions of the globe. These relationships or teleconnections were shown to possess preferred temporal and spatial distributions. Specifically, the equatorial central Pacific, the maritime continent and vicinity, the Amazons, the Hawaiian Islands, the southeast United States and the southeast Pacific appear to occupy the key positions of one gigantic global teleconnection complex. Since OLR is a good measure of cloudiness which reflects atmospheric conditions ranging from tropical convection to extratropical wave disturbances and surface temperature fluctuations, the teleconnections in OLR thus can be translated into teleconnections in these

climate parameters. The large spatial scale and the long time scales (monthly and longer) in the variation of these teleconnections suggest the possibility of prediction of time-averaged atmospheric conditions over a given region from events in a remote but correlated region.

Before any attempt to utilize satellite-derived teleconnection for long-range forecasting, coherent phase relationships, if any, of the OLR variation over the key regions have to be known. For practical forecasting purposes using atmospheric teleconnection, the target region (predictant) must be given first, then a source region (predictor) identified, and finally the lag time over which the relationship is strongest must be determined. A method often used in this regard is the so-called Lagged-Cross Correlation (LCC) analysis.

Statistical relationships using LCC on various meteorological parameters have been studied by a number of investigators. Namias (1978, 1980), Barnett (1981)

and Barnett and Preisendorfer (1978) used several tropical and North Pacific parameters including sea surface temperature to predict surface temperature over the continental United States. Chiu and Lo (1979) demonstrated statistically significant relationships between the tropical Pacific sea surface temperature and Northern Hemisphere large-scale atmospheric circulation. Harnack (1979) used a set of predictors including a fall Southern Oscillation (SO) index to make a seasonal forecast of winter temperature over the continental United States. Douglas and Englehart (1981) showed that there is significant success in forecasting winter rainfall over the southeast United States by using equatorial central Pacific rainfall during autumn. In addition, Harnack and Broccoli (1979) showed that oceanic variables other than sea surface temperature can be used to forecast atmospheric changes on the seasonal time scale.

In spite of the numerous studies cited above, there has not been much systematic study using satellite-derived information to investigate global statistical and dynamical relationships in relation to long-range forecasting. This is the second in a series of papers to address the above problem. In this paper, we focus on the lagged relationships as revealed by the OLR monthly time series over different parts of the globe. The emphasis of this work, however, is not on developing specific techniques or statistical prediction models but rather on establishing significant lagged teleconnection between various remotely separated regions, thus identifying the more potentially predictable regions for long-range forecasting. The observed lagged correlation from satellite-derived OLR will be compared with other observed statistical relationships to check for any physical connections. An interpretation of the observed lagged correlation patterns will also be attempted in light of our *a priori* knowledge on the dynamics of climate teleconnections (e.g., Webster, 1981, 1982; Branstator, 1983; Lau and Lim, 1982, 1984). In view of the potential of satellite observations for long-range predictions, it is believed that such a combined statistical and dynamical approach is a logical step in the quest to advance our understanding of climate predictability and to improve our skill in long-range prediction.

Two aspects of the predictability problem will be addressed in this paper. First, we shall introduce the concept of the teleconnectivity of the atmosphere and show, by way of examples of LCC patterns based on different reference or source locations, its usefulness in providing guidance for potential source regions (or predictors) for long-range forecasting. In particular, the lagged teleconnections with respect to the equatorial central Pacific will be analyzed in detail to examine if they are consistent with the theoretical interpretation given in Part I. Second, the contribution from the Southern Oscillation and other time scales to the lagged relationships will be determined. Their implications

on studies of atmospheric response to imposed forcing using general circulation models (GCM) and on seasonal and interannual predictions will be discussed.

2. Data and analysis technique

The data used are monthly OLR from NOAA polar-orbiting satellite on a $2.5^\circ \times 2.5^\circ$ global grid. Details concerning this data set were described in Part I. For two given discrete time series X_n , Y_n , the LCC for lag τ is computed from the standard formula

$$r_{XY}(\tau) = \frac{c_{XY}(\tau)}{[c_{XX}(0)c_{YY}(0)]^{1/2}}, \quad (1)$$

where

$$c_{XY} = \frac{1}{N - |\tau|} \sum_{n=1}^{N-|\tau|} (X_n - \bar{X})(Y_{n+\tau} - \bar{Y}), \quad (2)$$

$$\bar{X} = \frac{1}{N} \sum_{n=1}^N X_n \quad \text{and} \quad \bar{Y} = \frac{1}{N} \sum_{n=1}^N Y_n. \quad (3)$$

Because of the generally non-zero and often widely different autocorrelations in the OLR time series between the tropics and higher latitudes and between the oceans and continents, large spurious LCC can arise even if the time series in question are not correlated. This often poses serious problems when using LCC to detect statistical relationships between two or more variables. A method is described in the Appendix to take into account the effect of autocorrelation on the statistical significance of LCC. The standard deviation (SD) of the lagged correlation coefficients between two independent first order Markov processes is estimated in the Appendix, where the following expression is derived;

$$SD[r_{XY}(\tau)] = \left[\frac{2}{(N - |\tau|)\{1 - \exp[-(\lambda_X + \lambda_Y)]\}} \right]^{1/2}. \quad (4)$$

Symbols used are defined in the Appendix. In all the results described in this paper, the LCC is considered significant provided $|r_{XY}(\tau)| > 2SD[r_{XY}(\tau)]$, which is approximately the 95% confidence level (c.l.). Since the LCC is calculated for only the data found outside the data gap, the effective number of data pairs is reduced as the lag increases because of the data gap. This has been taken into account in calculating the statistical significance.

3. Autocorrelation time scale

In order to use (4) to test the statistical significance of the LCC between the OLR time series at different grid points, the total number of independent events and therefore, the characteristic time between independent events has to be determined. The theoretical autocorrelation function of a first order Markov process is given by

$$A(\tau) = e^{-\lambda|\tau|} \quad (5)$$

The e -folding time scales $\tau_0 \equiv \lambda^{-1}$ of the monthly OLR time series at each grid point is determined by using (5) to give a best fit to the autocorrelation $r_{XY}(\tau)$ obtained from (1)–(3). Fig. 1 shows the discrete autocorrelation coefficient and the best-fit autocorrelation function from a first order Markov process over different locations. It can be seen that a first order Markov process is a fairly good approximation of the OLR time series. The spatial distribution of the characteristic time scale (τ_0) is shown in Fig. 2. Areas with time scales greater than or equal to 2 months include: the equatorial central, eastern and southeastern Pacific; the equatorial Atlantic off the coast of Brazil; the eastern North Pacific; the southeastern U.S.; western Africa and Eurasia. Broadly speaking, two physical factors could have contributed to the above distribution. First, there is the time scale related to the slow changes in the surface boundary conditions such as those due to sea surface temperature anomalies (SSTA). Second, part of the observed monthly variability could also arise from the non-zero autocorrelation in the daily data. The latter, which is independent of changes in external conditions in the monthly time scales, is often referred to in the literature by such names as “intrinsic variability”, “climate noise” and “sampling fluctuations” (Madden, 1976; Madden and Shea, 1978). The analysis of the separation of “signal” versus “noise” using both the daily and the monthly data will be the subject of another study.

For this presentation, it suffices to state only the following observations. From Part I of this study and other related work (e.g., Heddinhaus and Krueger, 1981), it is likely that the extensive area of large characteristic time scales in OLR over the tropical Pacific is related to local SSTA. Whereas, over the middle latitudes, we note that areas with small characteristic times are more or less coincident with wintertime storm tracks of both hemispheres (Lau, 1979; Trenberth, 1981) and that areas with large characteristic times are associated with regions of frequent observed blocking events over the eastern North Pacific and northern Eurasia. The longer characteristic time over specific regions in midlatitudes may therefore reflect the intrinsic higher autocorrelation in the daily variation associated with persistent atmospheric anomalies over these regions. However, the above explanation does not exclude the possibility of forced response to slow changes in remote and/or local surface boundary conditions in also partially contributing to the observed longer autocorrelation time scale. For example, over the Tibetan region, the long time scale may reflect locally the persistently snow-covered land surface.

4. Teleconnectivity

In Part I, we showed that for a given reference OLR variation, the teleconnection pattern of the atmosphere depends strongly on the seasons. Because long-term signals in OLR tend to be found only over preferred areas (see Part I), it is likely that the degree of remote

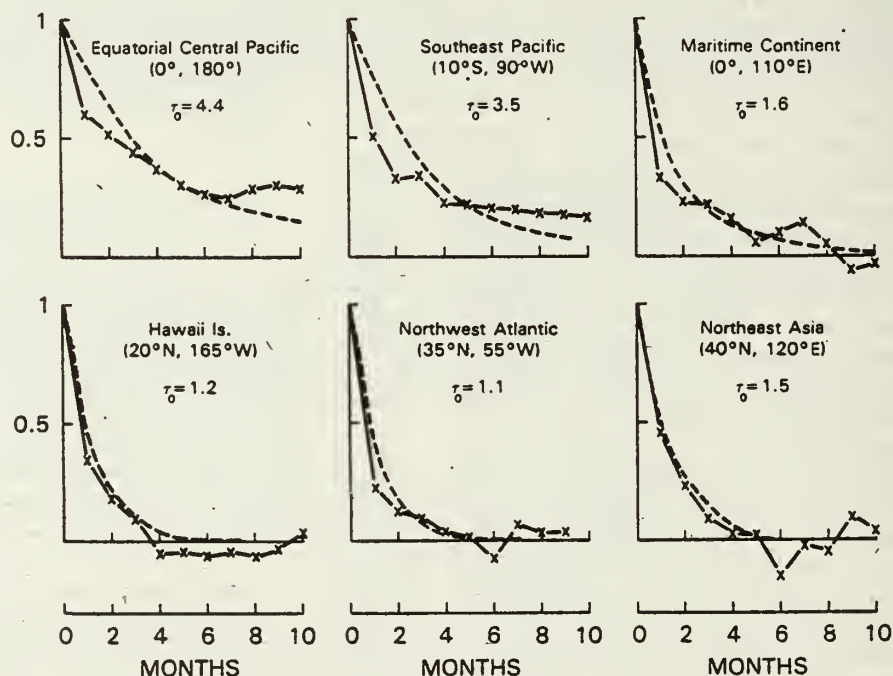


FIG. 1. Autocorrelation coefficient of OLR time series at selected locations. Also shown in dashed lines are the autocorrelation function of the best-fit first-order Markov process. The e -folding time scale τ_0 is in units of months.

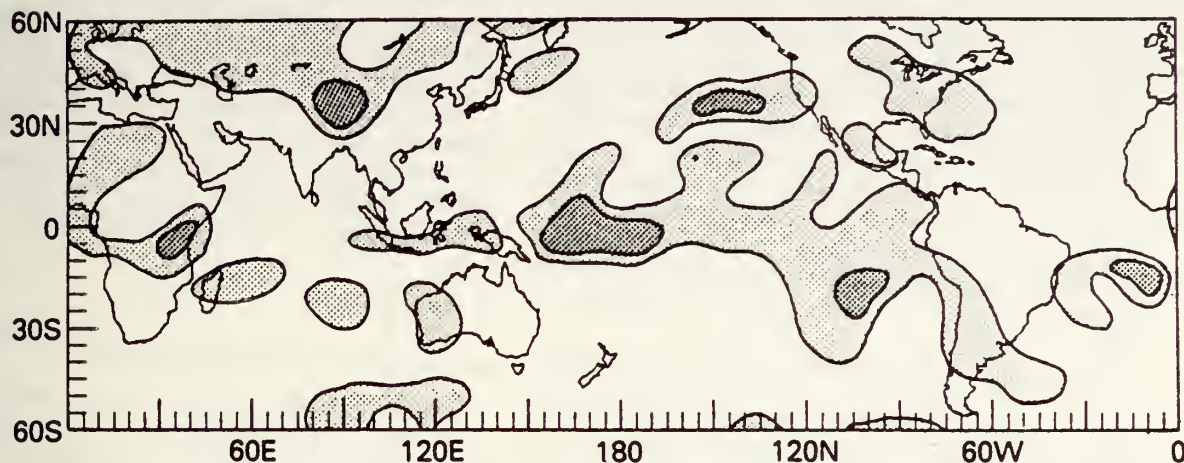


FIG. 2. Distribution of characteristic time scales in the monthly anomalous (monthly mean removed) OLR data. Contour interval is 2 months. Blank areas represent time scales <2 months and heavily shaded area, time scales over 4 months.

influence on the atmosphere as a whole (or teleconnectivity) by a given physical process is not only a function of the process itself, but also of the ambient state of the atmosphere. Therefore, when put in different large-scale environments, the same forcing could produce quite different local and remote responses.

To determine quantitatively the teleconnectivity of the atmosphere, we define for a given reference fluctuation X and lag time τ , teleconnectivity (Te) as

$$Te(X, \tau) = \frac{1}{N(X, \tau)} \sum_Y H(|r_{XY}(\tau)| - |\tilde{r}_{XY}(\tau)|) |r_{XY}(\tau)|, \quad (6)$$

with $\tilde{r}_{XY}(\tau) = 2SD(r_{XY}(\tau))$, where X and Y denote the reference and the correlated time series, respectively; $H(\alpha)$ is the Heaviside step function and $N(X, \tau)$, the total number of grid points between 60°N–60°S in which $|r_{XY}(\tau)| \geq \tilde{r}_{XY}(\tau)$.

Figure 3 shows Te of the atmosphere for reference variations based on a 9-point average on a $5^\circ \times 5^\circ$ grid of the monthly OLR values centered at 30° longitude intervals between 30° W and 60° E along the equator for lags $\tau = -5, 0$ and 5 months. The large zonal asymmetry in Te is striking. The largest value of Te for all lags is found for reference area near the dateline with much reduced Te away from it. At all locations, the teleconnectivity at nonzero lags is smaller

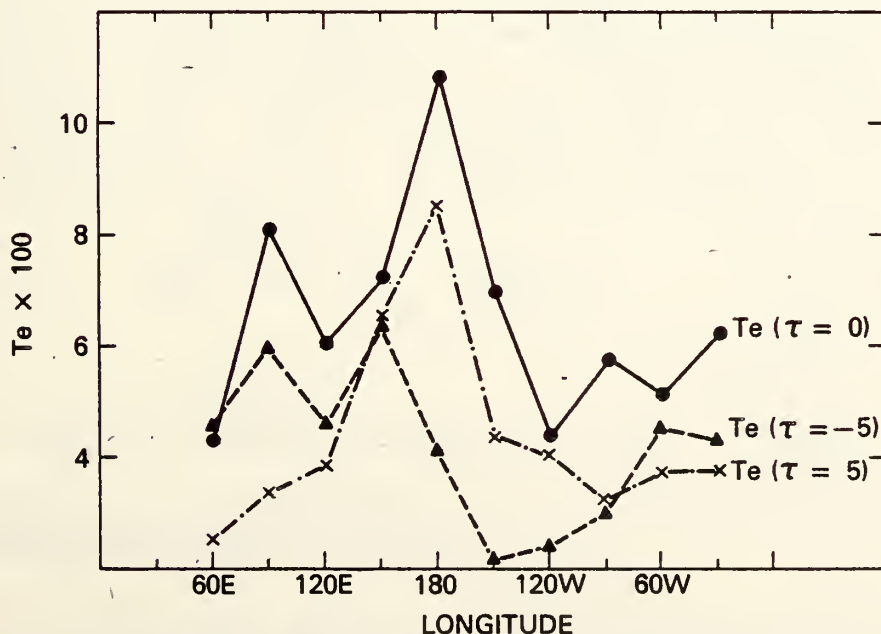


FIG. 3. Teleconnectivity (Te) as a function of the longitudinal location of the reference OLR time series, at lag $\tau = -5, 0$ and 5 months, respectively.

than that at zero lag. A secondary maximum is found for $Te(\tau = 0)$ at 90°E over the equatorial Indian Ocean. Intuitively, the higher teleconnectivity due to OLR fluctuation over the equatorial central Pacific and the lower values east of the dateline are expected because the former corresponds to a heat source region, while the latter corresponds to the equatorial dry zone where deep convection rarely occurs and the atmosphere is therefore, much less active energetically. The local minimum at 120°E , which corresponds to the strong convection over the maritime continent comes as a surprise as does the enhanced Te at 0° , 90°E which is not a convective heat source region. The implications of these zonally asymmetric features will be discussed later.

Figure 4 shows the teleconnectivity as a function of the lag time for three chosen reference locations, 180°E , 120°E and 90°E . The largest Te is found at $\tau = 0$ for all three locations. The most important difference between $Te(180^\circ\text{E})$ and $Te(90^\circ\text{E})$ is the oppositely skewed distribution about the corresponding Te at zero lag. At 180°E , predominantly higher Te is found at positive lags with a secondary maximum at 4–5 lags, while at 90°E , the secondary maximum is found at lag -2 and decreases rapidly at positive lags. At 120°E , Te is considerably lower than the other two at all lags. Viewed in terms of cause and effect, it would appear that the equatorial central Pacific is a potential source region producing remote atmospheric response elsewhere. On the other hand, the OLR variation over the equatorial Indian Ocean is likely a response to remote

changes in large-scale atmospheric conditions (to be identified in Section 5b). The diabatic heat source over the maritime continent is, however, much less effective in either influencing or being influenced by planetary-scale remote changes. These features agree with the dynamical interpretations of radiating (for heat sources in the central Pacific) and non-radiating (for heat source in the maritime continent) modes of atmospheric response to equatorial forcing discussed in Part I. The spatial distributions of the lagged teleconnection for 180°E and 90°E , including more detailed analyses, are presented in the next two sections.

5. LCC patterns

a. Central Pacific teleconnections

Figure 5 shows the LCC pattern using the 9-point OLR average centered at $(0^\circ, 180^\circ)$ as reference for lag = $-5, 0, +5$ months. Only patterns which are significant above the 95% confidence limit, as defined in Section 2, are shown. The zero-lag pattern which has been shown in Part I in smoothed contour is included here for completeness. The most important feature to note in these maps is the asymmetry in the $+5$ and -5 lag patterns with respect to the zero-lag pattern. By comparing the patterns at different lags, it can be seen that a rather persistent pattern consisting of positive correlations extending from the source southeast toward the southern tip of South America is present at all lags.

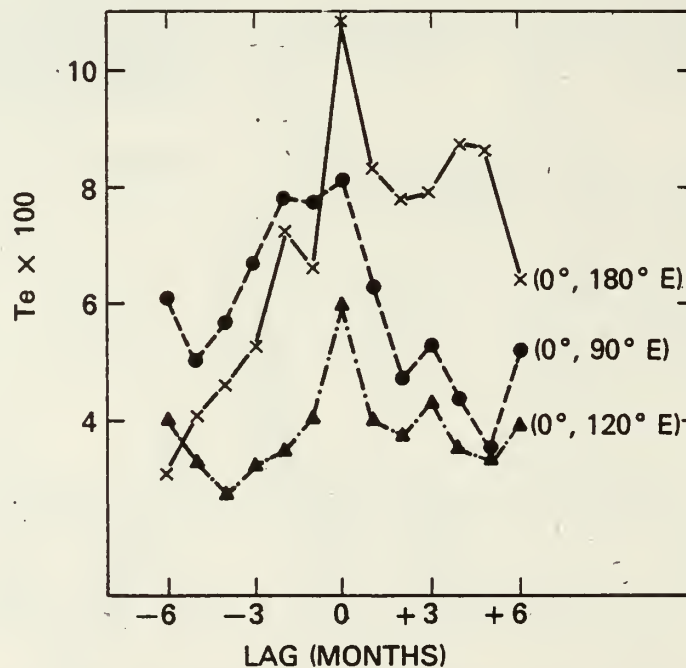


FIG. 4. Teleconnectivity (Te) as a function of lags for three different reference OLR fluctuations located at 0° , 180°E , 0° , 90°E and 0° , 120°E .

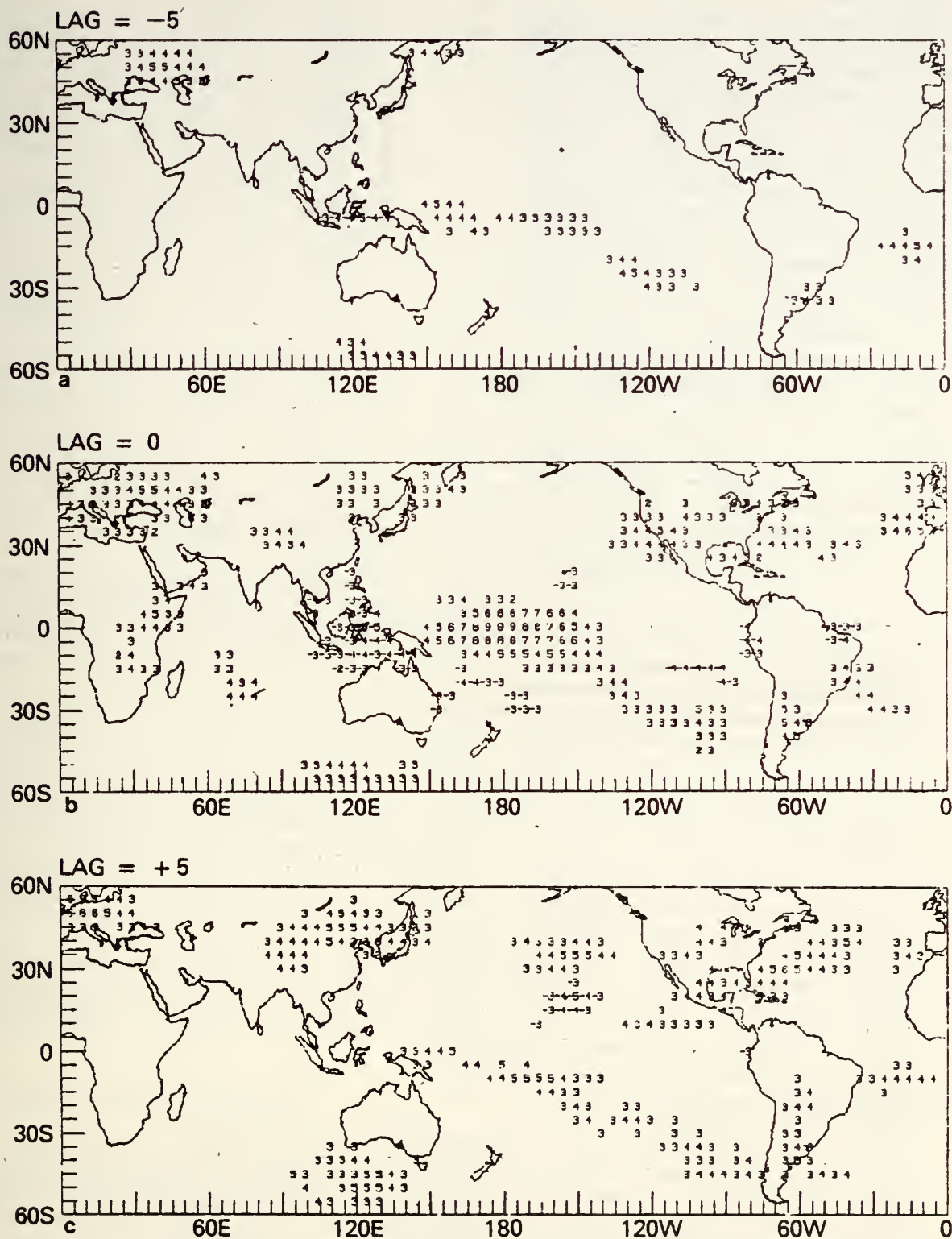


FIG. 5. Lag-cross-correlation (LCC) pattern of OLR for reference fluctuations over the equatorial central Pacific (0°, 180°) for lags: (a) -5 months, (b) 0 month and (c) +5 months. Numerals show in tenths the actual correlation coefficients. Only correlations which exceed the 95% significance level are shown.

While the tropics-tropics teleconnections are strongest at zero lag, the +5 month lag patterns are dominated by tropics-midlatitude coupling. Notably, the

subtropical portion of the Pacific-North America (PNA) pattern is strongly enhanced. The amplitude of the anomaly over Hawaii and those off the east coast

of the United States are stronger at +5 month lag than those found at zero-lag. A large area of positive correlation appears over the central North Pacific, East Asia and Europe at +5 month lag in consonance with the strongest correlation found over the Atlantic seaboard, suggesting some kind of planetary-scale wave (wavenumber 2–3) is being excited over the northern subtropics. In the Southern Hemisphere, a similar but weaker planetary wavenumber 2 structure is also noticeable at approximately 45°S. In contrast, at –5 month lag, the area of organized pattern, except near the reference location, is greatly diminished.

The notion of planetary wave response to equatorial forcing is further examined by decomposing the computed LCC into Fourier components in different latitude bands. Figs. 6a–6c shows the amplitudes of the LCC coefficients as a function of the lag time and wavenumber for three 10°-wide bands between 15°S and 30°N. The build-up of the tropical teleconnection is depicted clearly in the 15°S–0° and the 0–15°N bands by the gradual increase in the amplitude of wavenumber 2 from negative lags reaching maximum amplitude at zero lag over the two tropical bands. The wavenumber 2 distribution in the tropics corresponds to two strong heat sources, one over the equatorial central Pacific and one over eastern Africa. The amplitude of the strongest tropics–tropics teleconnection (Fig. 6a) appears to skew toward slightly smaller scales (larger wavenumber) and faster decay in the positive lag periods. Most interesting is the spatial-scale changes observed at the 15–30°N band (Fig. 6c). Here, the amplitude of the wavenumber 2–3 maximum at +(5–6) month lag is found after the tropics–tropics teleconnection has been greatly reduced (Fig. 6a). At lag +5, the teleconnection is dominated by high correlation over the western North Atlantic region extending into western Europe and East Asia and a secondary maximum over the central North Pacific (see Fig. 5).

The planetary wave feature in the LCC at +5 lag at 35°N is reconstructed by summing over the first six wavenumbers and its phase is compared with the climatological 500 mb January stationary geopotential wave at 40°N (cf Reiter and Westoff, 1981) in Fig. 7a. It can be seen that the regions of high correlation are located to the east of the 500 mb stationary trough and coincide with the winter storm tracks over the northern midlatitudes. In the Southern Hemisphere, a similar correspondence between the climatological 500 mb geopotential height field at 40°S with the LCC at 40°S is also noted (Fig. 7b).

The evolution of the teleconnection pattern suggests that, initially, the fluctuation of the OLR over the equatorial central Pacific is associated with simultaneous excitation of planetary waves in the tropics. The tropics–tropics teleconnection eventually (in about 4–6 months) transforms into tropics–midlatitude and midlatitude–midlatitude teleconnections associated with possible “resonant” excitation of the wintertime

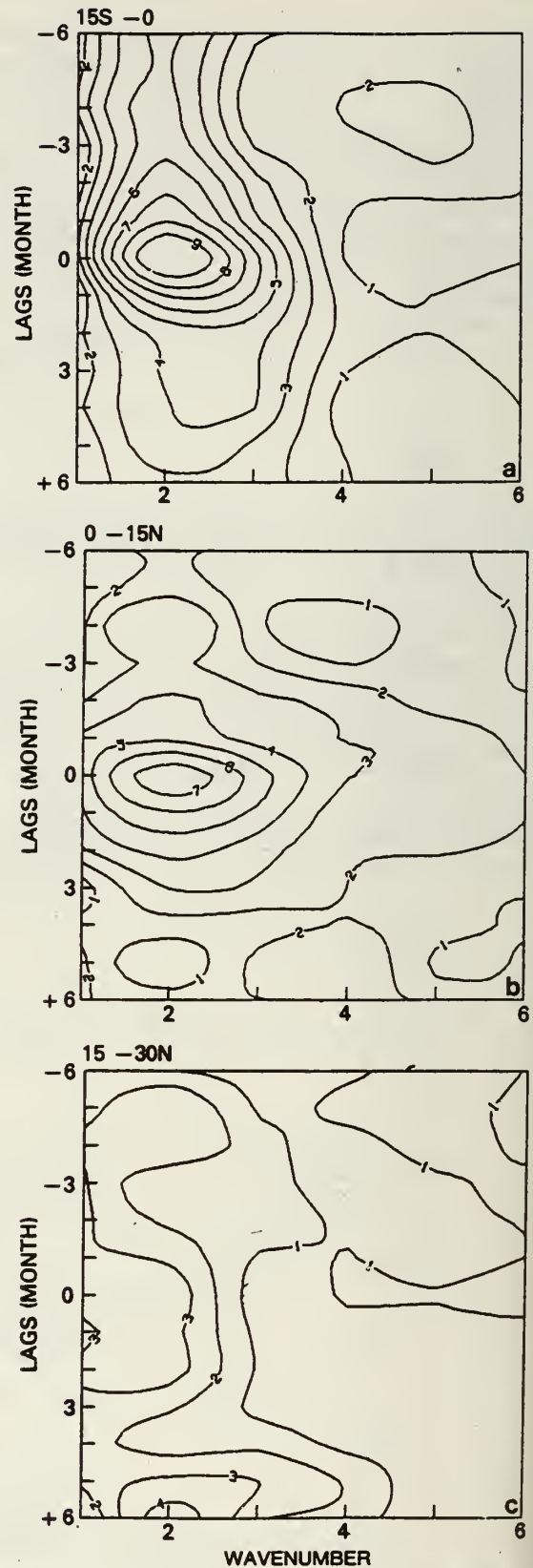


FIG. 6. Amplitudes of LCC based on equatorial central Pacific OLR variations as a function of lag and wavenumber: (a) 15°S–0° (b) 0–15°N and (c) 15–30°N. Units are arbitrary.

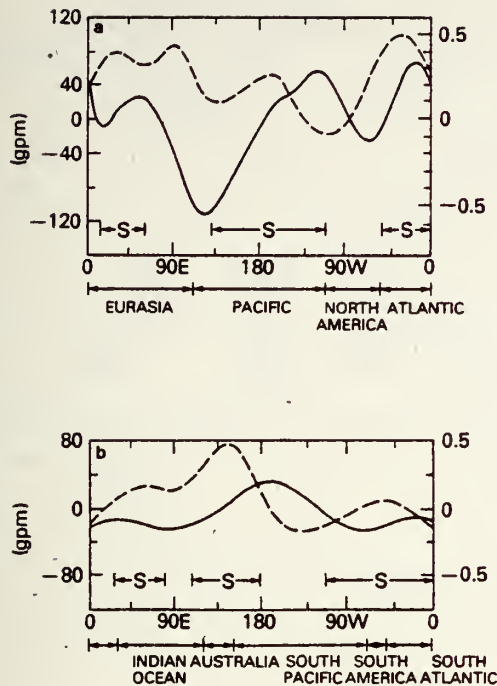


FIG. 7. Longitudinal distribution of northern winter quasi-stationary 500 mb geopotential (solid line) and wavenumber 1-6 reconstruction of correlation pattern at +5 month lag (dashed line) at (a) 35°N and (b) 40°S. Letter S denotes approximate location of storm tracks at the same latitudes.

extratropical quasi-stationary planetary waves in both hemispheres. Equivalently, the lagged relationships suggest that diabatic heat energy originally confined within the tropics is transported to the extratropics through planetary-scale wave interactions. Furthermore, the similarity of the LCC to the wintertime teleconnection found in Part I and other related work suggests that the downstream influence of the equatorial central Pacific convection on the extratropics must be phase-locked with the seasonal cycle and the lagged response at midlatitudes may involve the adjustment of the entire tropical and midlatitude ocean-atmosphere system to tropical forcings (e.g. Namais, 1978, 1980).

b. Indian Ocean teleconnections

The secondary maximum in teleconnectivity for reference OLR variation over the equatorial Indian Ocean (0°, 90°E) shown in Section 4 suggests some interesting features with regard to the spatial distribution of the corresponding LCC patterns. Because the OLR teleconnection based at 0°, 90°E for lags beyond +2 months is small and not very well organized, only maps at lags -2, 0 and +2 are shown (Fig. 8). At -2 lag, a broad region of strong positive correlation is found over subtropical Asia and the Middle East with a center over the Tibetan plateau. A plan-

etary-scale feature resembling a wavenumber 3 planetary wave can be seen at about 30°N. Over the Southern Hemisphere tropics, high correlations are found clustered around the Indian Ocean and eastern Africa, the central Pacific and central South America. A tendency for a stronger tropical teleconnection linking the reference region and the Caribbean Sea and vicinities is evident at zero-lag, when the strongest correlation near the reference region spreads over a large part of Australia. At +2 lag, the LCC is greatly diminished except near the source region. Some lingering remote correlations can still be discerned over the middle East.

The planetary feature formed by the LCC at 30°N at -2 lag is reconstructed as described in Section 5a and compared with the large-scale thickness between 850 and 300 mb at 30°N for the northern summer (cf White, 1982) in Fig. 9. The areas of high correlation generally agree with the two areas of large thickness, one over the Tibetan Plateau and one over the southern United States. The large correlation over Tibet at -2 lag suggests that the summer monsoon over India may have a strong lagged influence on the convective activities over the equatorial Indian Ocean.

6. SO contributions to LCC patterns

The variation of the LCC patterns as a function of lag time suggests that the crucial link between the tropics and the Northern Hemisphere midlatitudes lies in the so-called PNA pattern which is now known to be related at least partially to the SO (Horel and Wallace, 1981; also see Part I of this study). In this section, a more detailed analysis of the PNA and associated LCC patterns with respect to the SO is presented.

It was shown in Part I that the OLR time series over the equatorial central Pacific exhibits an abrupt shift in the mean level of fluctuation beginning about the spring of 1976 (Fig. 12a and also Fig. 1a of Part I). Because this shift agrees with almost all other conventional indices defining the El Niño/Southern Oscillation phenomena, it has been taken as a signal for the SO in this series of studies. Although one event (i.e., the El Niño of 1975-76) usually does not constitute very much statistical significance, it can still be used as a case study to provide important information.

As in Part I, we define the SO variation as

$$SO(x, y, t) = \begin{cases} \frac{1}{t_c} \int_0^{t_c} OLR(x, y, t) dt, & 0 < t < t_c \\ \frac{1}{T - t_c} \int_{t_c}^T OLR(x, y, t) dt, & t_c \leq t < T \end{cases} \quad (7)$$

where T is the total length of the data and t_c is taken to be the time corresponding to June 1976. The original monthly time series is then "detrended" by removing

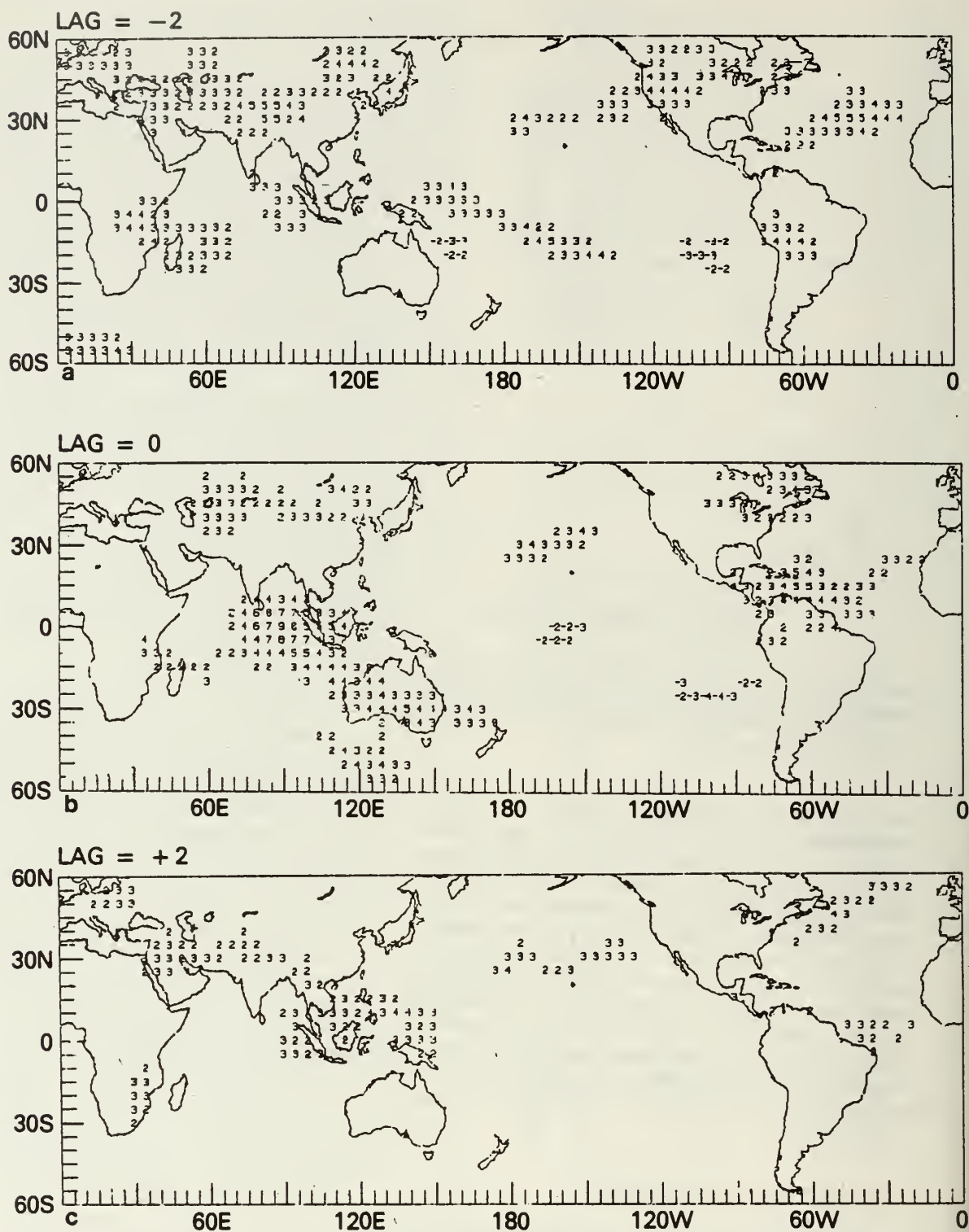


FIG. 8. As in Fig. 5 except for LCC pattern of OLR for reference fluctuations over the equatorial Indian Ocean (0°, 90°E) for lags: (a) -2 months, (b) 0 month (c) +2 months.

the SO signal at each grid point; the LCCs for different reference variations are computed using the detrended time series.

For the same reference locations as described in Section 4 it is found that, in general, the lagged correlations are reduced for all reference locations, esp

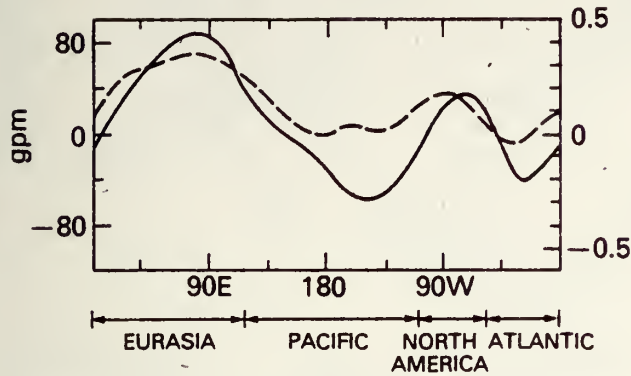


FIG. 9. Longitudinal distribution of thickness between 850 and 300 mb at 30°N for the northern summer (solid line) and wavenumber 1-6 reconstruction of LCC at -2 month lag at 30°N (dashed line).

cially at 180° where the most dramatic reductions are observed. In the following, we focus on the changes in the teleconnection pattern based at 180° due to the removal of the SO signal. The LCC at selected times for reference point at 90°E, based on the extended time series, is also included for comparison.

Figures 10a and 10b show the significant LCC ($\geq 95\%$ confidence limit) for zero and +5 month lags for basepoint at 180°. Compared with Figs. 5b and 5c, it can be seen that the area of significant correlations is greatly reduced with the SO signal removed. At zero-lag, a large part of the fork-shaped extension from the source region towards North America and South America vanishes, although some significant correlation can still be detected off the coast of Baja California. This feature shows that much of the downstream simultaneous correlation is due to the SO, in agreement with the conclusion reached in Part I using composite and partition-of-variance methods. Interestingly, the tropical east-west dipole pattern becomes stronger without the SO contribution. At +5 month lag, all the

tropical teleconnection becomes insignificant. Although, much less extensive, the midlatitude-midlatitude teleconnection remains noticeable over the western North Atlantic and East Asia suggesting that both the SO and the monthly fluctuation must have contributed significantly to the total maximum lagged correlation at +5 months.

The removal of the SO signal for the Indian Ocean teleconnection (Figs. 11a and 11b) also causes reduction in teleconnection (compare with Fig. 8). The basic patterns remain unchanged. At zero lag, a tropical dipole pattern similar to the one observed for the central Pacific (Fig. 10a) reappears, again showing that the dipole oscillation seems to be more prominent in the shorter time scales.

Focusing on the lagged relationships in the PNA pattern, we have constructed area-averaged time series based on an approximately 9-grid point mean over the key regions of the equatorial central Pacific, Hawaii and the western North Atlantic in Fig. 12. The time series of the latter two has been shifted backward in time by 5 months and that over Hawaii has been inverted to allow easier comparison. A large shift from a predominantly positive to a negative level of fluctuation occurs at approximately $t = t_c$ for all three time series. The close alignment of the time of major shift, after the central Hawaii and the Atlantic time series have been shifted, is consistent with the observations that a substantial part of the covariance at +5 month lag (with respect to the equatorial central Pacific) is due to the 5 month lag in the SO signal over these regions. The somewhat similar temporal and spatial distributions with respect to the key regions of the Northern Hemisphere midlatitude-midlatitude LCC patterns, with and without the SO signal, suggests that similar underlying physics are likely to cause the observed teleconnections. This point will be further discussed in Section 8.

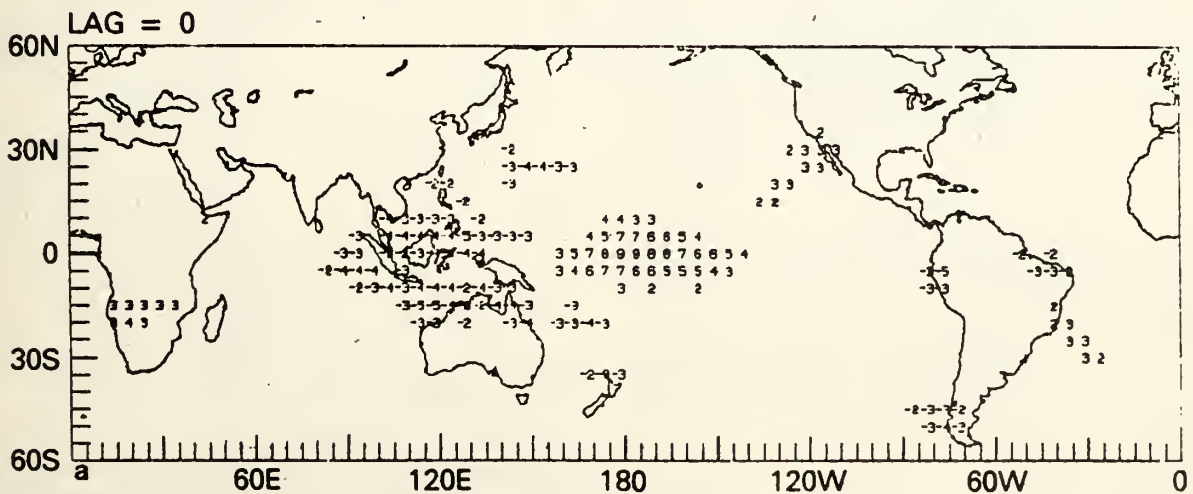


FIG. 10a. As in Fig. 5b, but with the SO signal removed.



FIG. 10b. As in Fig. 5c, but with the SO signal removed.

7. Predictability via OLR teleconnection

In this section, we present results of an analysis to assess the feasibility of monthly and seasonal predictions using one example of satellite-derived atmospheric teleconnection, i.e., the PNA pattern.

The ratio (α_{XY}) of the observed LCC at lag τ to the standard deviation which would be expected from two independent first-order Markov processes is given by

$$\alpha_{XY}(\tau) = \frac{r_{XY}(\tau)}{\left[\frac{2}{N_{XY}\{1 - \exp[-(\lambda_X + \lambda_Y)]\}} \right]^{1/2}} \quad (8)$$

is a measure of the signal-to-noise ratio of the time series $X(t)$ as explained by $Y(t)$. In (8), N_{XY} is the total number of data point pairs between the two series at lag τ . Other symbols are the same as used in (1). The predictability $P_{XY}(\tau)$ of $X(t)$ at lag time τ using $Y(t)$ is then defined as the normalized value of (8), i.e.,

$$P_{XY}(\tau) = \frac{r_{XY}(\tau)}{r_{YY}(0)} \left[\frac{N_{XY}\{1 - \exp[-(\lambda_X + \lambda_Y)]\}}{N_{YY}\{1 - \exp[-2\lambda_Y]\}} \right]^{1/2} \quad (9)$$

By definition, the predictability of a time series by itself at zero lag is then 1 (perfect prediction). It should be noted that the above definition of predictability crudely takes into account the effect of statistical sampling fluctuations due to the finite size of the data record.

The statistical significance of (9) can be estimated if we know the effective number of degree of freedom (NDOF) in the data. Using Davis' (1976) method of estimating NDOF, we have

$$\text{NDOF} = \frac{N_{XY}}{\sum_{k=-\infty}^{\infty} r_{XX}(k)r_{YY}(k)} \quad (10)$$

where N_{XY} is the number of pairs of observations and r_{XX} , r_{YY} are the discrete autocorrelation coefficients of $X(t)$ and $Y(t)$.



FIG. 11a. As in Fig. 8a, but with the SO signal removed.

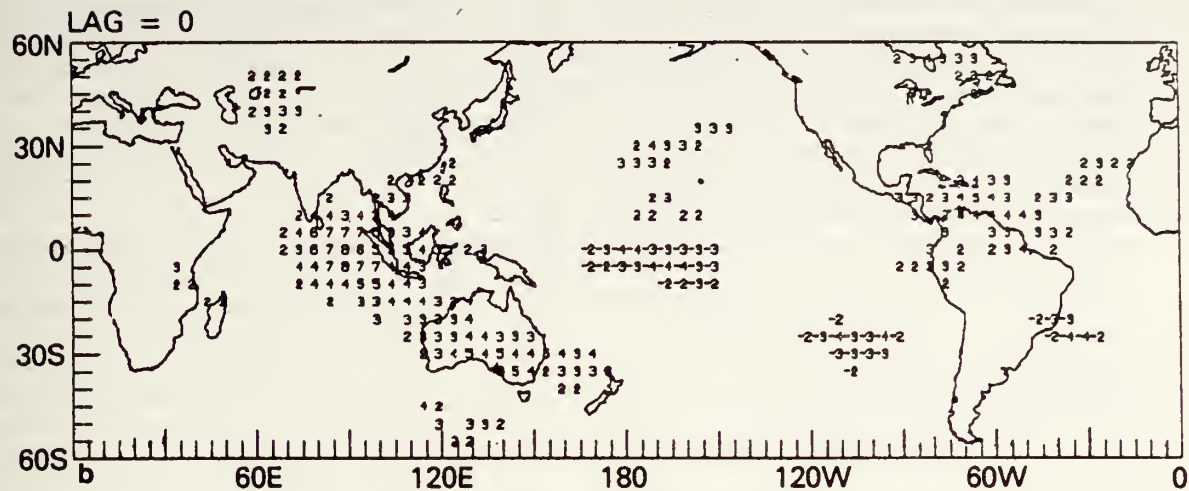


FIG. 11b. As in Fig. 8b but with the SO signal removed.

In the following, we shall focus on the three time series (shown in Fig. 12) over the key regions of the PNA pattern. Hereafter, the time series are referred to

as ECP (equatorial central Pacific), HA (Hawaii) and WNA (western North Atlantic). Table 1 shows the predictability of HA and WNA using ECP as predictor at 5-month lag and the zero-lag predictability of HA and WNA. The predictability of 0.49 at WNA (+5) by ECP (0) means that $\sim 25\%$ of the total variance at WNA is explained by the variation of ECP 5 months earlier. After the SO signal has been removed, the predictability of HA(+5) and WNA(+5) using ECP(0) falls below the significance level to 0.18 and 0.25, respectively. The zero-lag relationship between HA(+5) and WNA(+5) is also reduced from 0.39 to 0.21 indicating that the latter relationship is also stronger in the presence of SO.

As pointed out in Part I, with the seasonal cycles removed, the tropical atmosphere appears to exhibit a large-amplitude dipole-like oscillation between two states: one corresponding to the major convective heat source over the maritime continent with dry conditions over the equatorial central Pacific and one to the heat source over the equator near the dateline with dry conditions over the maritime continent. The wet and dry conditions are referred to only in a relative sense. Because the dynamical response of the atmosphere depends on the position of the tropical heat source with respect to the large-scale mean circulation, we

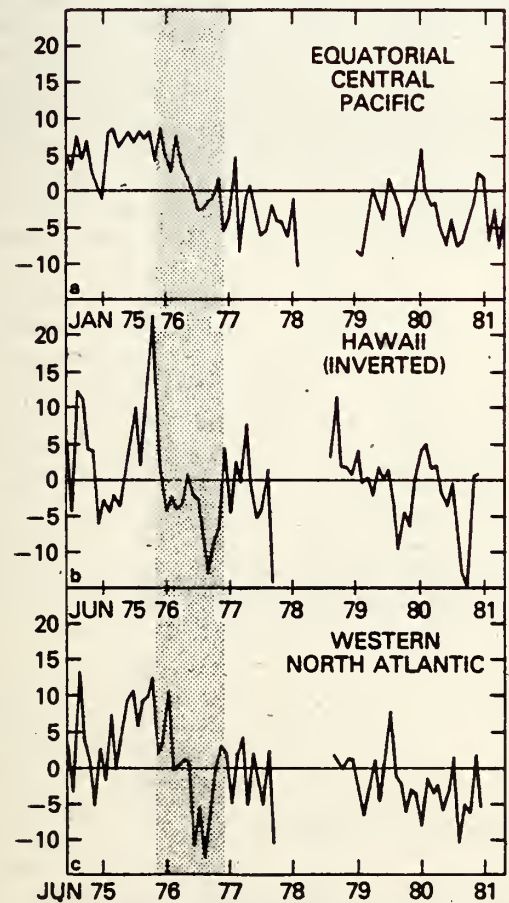


FIG. 12. Time series of monthly anomalous OLR over (a) the equatorial central Pacific, (b) Hawaii (inverted) and (c) western North Atlantic. Shaded areas denote the time of a major transition associated with SO. Time series in (b) and (c) have been shifted backward by 5 months.

TABLE 1. Predictability as defined in text over key regions of the Pacific-North America (PNA) teleconnection pattern. ECP, HA and WNA denote, respectively, the OLR time series over the equatorial central Pacific, Hawaii and the western North Atlantic. Numbers in parentheses denotes the lag in months. Numbers with asterisks denote predictability after SO signal has been removed. Values which are significant at the 95% level are underlined.

	ECP(0)	HA(+5)	-WNA(+5)
ECP(0)	1	<u>0.34</u>	<u>0.49</u>
HA(+5)	0.18*	1	<u>0.39</u>
WNA(+5)	0.25*	0.21*	1

might expect some differences in the predictability over the same regions before and after the 1975–76 El Niño. This feature is best seen in the general increase in predictability from the pre- to the post-El Niño period (Table 2) indicating that a stronger, or more frequently occurring, diabatic heat source over the equatorial central Pacific can lead to stronger influence on atmospheric conditions over Hawaii and the western North Atlantic. However, in Table 2, the simultaneous relationship between HA and WNA remains strong in the two periods. If we were to assume that the SO signal is caused by external changes such as SSTA, the relationship between HA and WNA, in addition to being influenced by the SO, must also arise from dynamics internal to the atmospheric system, e.g., blocking and multiple equilibria (Charney and DeVore, 1979).

Finally, the key time series are stratified into winter and summer seasons according to the actual calendar months (October–March for winter and April–September for summer) for HA and WNA (Table 3). The 5-month lag brings the late summer or fall variation of ECP to correlate with that for the winter months of HA and WNA. The dramatic increase in the wintertime predictability suggests that the remote lagged relationship in the PNA is prominent only in the winter half of the year. The null relationship between HA and WNA in summer is a result of the shift of the seasonal planetary-scale waves showing that Hawaii and the western North Atlantic no longer occupy key positions in the northern summer stationary wave pattern.

8. Dynamical interpretations and discussions

From the point of view of atmospheric dynamics, the results of the foregoing analyses regarding the lagged relationship are intriguing. From other related work (e.g., Horel and Wallace, 1981; Wallace and Gutzler, 1981), teleconnection patterns such as the PNA are known to possess a near-barotropic structure. Dynamical theories (e.g., Lim and Chang, 1983) suggested that these barotropic structures are likely to be forced by diabatic heat sources in the tropics. Depending on the mean flow, the response consists of 1) laterally propagating Rossby-type radiating modes for forcings embedded or partially embedded in westerly mean winds whose speed is within the range of the free Rossby wave phase speed and 2) Kelvin-Rossby nonradiating modes for forcings in other mean winds. However, all the responses involve either external or internal wave

TABLE 3. As in Table 1, except predictability estimate is for northern winter (without asterisks) and northern summer (with asterisks).

	ECP(0)	HA(+5)	WNA(+5)
ECP(0)	1	<u>0.58</u>	<u>0.64</u>
HA(+5)	0.19*	1	<u>0.51</u>
WNA(+5)	0.2*	0.0*	1

modes with large equivalent depths which have large phase speeds. Responses by these modes are expected to be established within a matter of days after the forcing sets in. Therefore, while our observed strong tropics–tropics teleconnection at zero-lag can be explained in terms of the nonradiating modes and the tropics–midlatitude teleconnections in terms of the radiating modes, the time (~ 2 seasons) in which these patterns are established in relation to the equatorial central Pacific convection is vastly different from that predicted from the above theories.

The clue to this apparent discrepancy is likely to lie in the observation that the tropics–midlatitude teleconnections are only prominent during the northern winter, thus suggesting that these quasi-stationary anomalies are phase-locked with, and perhaps represent merely the amplifications of, the seasonal cycle. In this view, the tropics–midlatitude link is only manifested as part of a global-scale adjustment to the tropical forcing which is strongly tied in with the seasonal migration of the upper-level easterly and westerly wind belt. The downstream meridional propagating tropical anomalies and eventually the “resonant” excitation of planetary stationary waves are favored by the upper-level westerly flow with strong westerly wind shear over the tropical eastern Pacific during northern winter (Lau and Lim, 1984). Namias (1978, 1980) pointed out that several planetary-scale anomalous features, such as the equatorward migration of the jet stream and the deepening of the Aleutian low and blocking ridge over the central North Pacific, all occurred in the fall season preceding severe winter conditions over North America. He also hypothesized that the phase relationship has to do with some subtle air–sea interaction mechanisms involving the interaction between the blocking ridge and the SSTA over the North Pacific. The lagged relationship revealed by the OLR teleconnection here appears to be consistent with the above hypotheses.

It is important to note that our results show that the PNA and associated teleconnection pattern can occur also in the 2–3 month time scale predominantly during winter, independent of long-term anomalies such as the SO. The SO, on the other hand, merely enhances the intensity and possibly alters the mean positions of the major anomaly centers. This suggests that the same underlying physical processes are likely to be responsible for the observed patterns in both the monthly and the SO time scales. We suggest that the migration of the winter convective heat source from

TABLE 2. As in Table 1 except predictability estimate is for post-El Niño (without asterisks) and for pre-El Niño (with asterisks) periods.

	ECP(0)	HA(+5)	WNA(+5)
ECP(0)	1	0.24	<u>0.29</u>
HA(+5)	0.16*	1	<u>0.36</u>
WNA(+5)	0.20*	<u>0.32*</u>	1

the maritime continent to the central Pacific, may have played at least a partial role in forcing the observed PNA and other associated teleconnection patterns. On a seasonal time scale, the monsoon heat source migrates from northern India in the summer to the maritime continent in October. The winter monsoon heat source subsequently moves to the vicinity of the dateline during late winter when convection over Africa and Brazil is also strongest, forming an intense wavenumber 3 heating pattern in the tropics (Fig. 13). The winter following an El Niño, anomalous strong convection is found over the Pacific (Horel and Wallace, 1981), thus stretching the seasonal extent of the winter convection to east of the dateline. Both the normal late wintertime and the post-El Niño conditions correspond to the wet winter (WW) condition (Part I), in which downstream meridional propagating response is favored. Because the normal winter convection does extend close to the region of upper-level westerly flow over the eastern Pacific (Fig. 13), the effect of downstream propagation, albeit weaker when compared with that due to SO, is also felt over North America. This probably accounts for the non-vanishing significant correlation even after the SO signal has been removed. The above interpretations are also consistent with the recent theory of Webster and Holton (1982), who used the distribution of upper-level zonal winds to explain interhemispheric interactions.

At this juncture, it is interesting to bring to attention the study of Lau (1981) who showed that the PNA pattern is present in the results of a 15-year GCM experiment with prescribed annual SST variation. He pointed out that the PNA may be an intrinsic mode

of the atmospheric circulation independent of external forcings such as SST anomalies. Our results on the simultaneous and lagged relationship support such a view. Here we have further identified a forcing mechanism, i.e., the eastward migration of the winter monsoon diabatic heat source, which is consistent both with internal dynamics relating to the seasonal cycle, and the external influence of SSTA associated with the El Niño/Southern Oscillation.

9. Conclusions and remarks

Based on seven years of global OLR data, lagged relationships and the role of the El Niño/Southern Oscillation in satellite-derived atmosphere teleconnections are investigated using multiple correlations. A plausible mechanism leading to the observed lagged relationships in the teleconnection pattern is proposed. The feasibility of extratropical long-range prediction using tropical parameters derived from satellites is also quantitatively assessed. The most important findings are as follows:

- 1) The degree of remote influence or teleconnectivity of the atmosphere by a given forcing depends strongly on the geographical location of the source region. Along the equatorial band, teleconnectivity is highest for convection near the dateline but much reduced for convection over the maritime continent and to the east of the dateline. A secondary maximum in teleconnectivity is found for sources near 0° , 90°E . These observations are compatible with theoretical predictions of remote versus local response of the atmosphere to tropical heating.

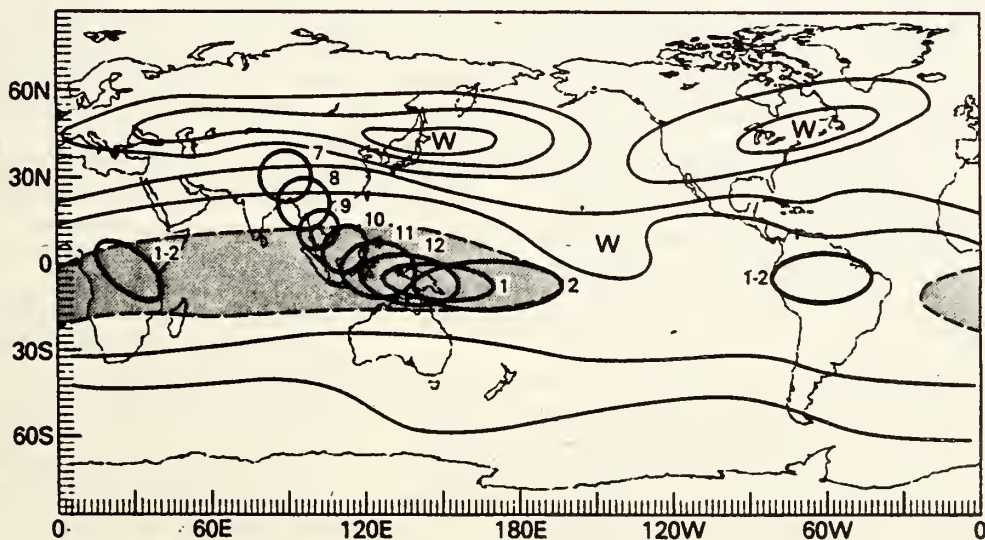


FIG. 13. Seasonal migration of the monsoon diabatic heat sources during the latter half of the year (July–February, denoted by matching numerals). The extent of the diabatic heat sources is determined from the areas with OLR values $< 225 \text{ W m}^{-2}$ from the monthly OLR climatology, and is approximately proportional to the size and orientation of the schematic drawings. Climatological 200 mb zonal wind during northern winter is also included. Easterly wind region is shaded and western maximum are denoted by letter W.

2) The LCC pattern based on dateline convection indicates at zero-lag a strong tropics-tropics teleconnection complex linking the equatorial central Pacific (+), the maritime continent (-), Australia (-), the Amazon Basin (-), South Africa (+), Hawaii (-) and the southeastern United States (+), with the sign denoting the sign of the correlation. As the positive lag increases, the tropics-tropics teleconnection gives way to stronger tropics-midlatitude and midlatitude-midlatitude teleconnections. As a $\sim +5$ month lag, central Pacific leading, the teleconnection consists of the following key regions: Hawaii (-), western North Atlantic (-), central North Pacific (+), East Asia (+) and western Europe (+).

3) The midlatitude LCC pattern bears coherent phase with climatological quasi-stationary waves. For the central Pacific teleconnections, the high-correlation areas coincide with storm tracks during northern winter. A similar planetary-scale correspondence is also found in the southern midlatitudes. These features suggest possible excitation and amplification of midlatitude stationary waves by diabatic heating near the equatorial central Pacific.

4) Lagged relationships between convection over the Indian Ocean (0° , 90°E) and those over Tibet and the areas near the Caribbean Sea reveal a maximum correlation at 2-month lag (Indian Ocean lagging), suggesting that a substantial portion of the convective activities over the equatorial Indian Ocean is likely to be a response to planetary wave forcing set up by the summer monsoon.

5) Analysis of the LCC pattern with the SO removed showed that both the SO and 2-3 month time scales contribute to similar lagged correlations in the PNA and associated teleconnections. It was argued that the presence of strong convective activity over the equatorial central Pacific due to 1) the seasonal migration of the winter monsoon convective heat source from the maritime continent to the vicinity of the dateline and 2) the occurrence of positive SSTA over the central Pacific during El Niño, is responsible for the observed similar tropics-midlatitude teleconnections but with different time scales. The large cross correlation at lag times of up to 2 seasons between the tropical forcing and extratropical response is probably associated with the seasonal adjustment time of the entire ocean-atmosphere system in concert with the time scale of the tropical forcing.

6) Predictability of OLR fluctuation over the southeastern United States is higher during the post-El Niño (1977-81) than the pre-El Niño period (1974-76). Much enhanced (reduced) predictability is indicated over Hawaii and the southeastern United States during winter (summer) using equatorial central Pacific as a predictor.

Our study also appears to be relevant to studies of atmospheric response to SSTA via GCM experiments

(e.g., Rowntree, 1972; Julian and Chervin, 1978; Shukla, 1975; and others). The results on the variation of atmospheric teleconnectivity as functions of the location of the source region and the time of the year suggest that such experiments should be performed systematically with imposed SSTA at different locations with respect to the large-scale circulation and in different seasons. Further, the highly significant inverse relationship between convection over the maritime continent and the equatorial central Pacific suggests that a diabatic heat sink over the maritime continent would perhaps generate similar downstream effects as a heat source over the equatorial central Pacific. This view is supported by the recent GCM experiments (e.g., Shukla and Wallace, 1983). Thus, depending on the sign of the forcing, the maritime continent can also be a potential source region. This nonlinear relationship between the forcing and the response has been demonstrated in a recent study by Simmons *et al.* (1983) and Lau and Lim (1984).

Studies of sensitivity of the atmosphere to imposed diabatic heating have, so far, concentrated on the steady-state response. In most cases, the near-barotropic remote response to tropical forcing, except for transients, becomes established in time scales of days. In order to study the possible lag time in the tropical-midlatitude teleconnection, our results suggest that the GCMs have first to reproduce "realistic" stationary waves and that anomaly experiments would be run with full annual cycles. Because the effect of the ocean is likely to be involved in such low-frequency variability, the simulation and full understanding of the lagged relationship in teleconnection must await the successes of ocean-atmosphere coupled models.

Finally, our initial assessment of the predictability of regional climate fluctuation using satellite-observed teleconnection is encouraging. Although only ~ 30 -40% of the wintertime variance over the southeastern United States is accounted for by the variation over the equatorial central Pacific, it is likely that increased predictability can be expected for other carefully chosen target regions using one or more potential predictors. The satellite-observed teleconnections identified by this series have provided guidelines for the choice of target regions with potentially higher seasonal or interannual predictability. The need now is for the development of statistical-dynamical prediction models which would optimize regional predictability using satellite-derived information in conjunction with other conventional approaches.

Acknowledgments. The authors wish to thank Mr. D. A. Short and Drs. J. Shukla and G. R. North for discussions. One of the authors (KML) also acknowledges support for travel and discussion with faculty members of the Department of Meteorology, Naval Postgraduate School under Contract NA82AAG02003 of the National Oceanic and Atmospheric Adminis-

trative and Grant ATM79-240101 of the National Science Foundation both to the Naval Postgraduate School.

APPENDIX

Covariance of Sample Cross-Covariance Function (SCCF)

An estimator (or SCCF) of the cross covariance of two discrete processes $X(t)$, $Y(t)$ at time lag T is given by

$$c_{XY}(\tau) = \frac{1}{N - |\tau|} \sum_{k=1}^{N-|\tau|} (X_k - \bar{X})(Y_{k+\tau} - \bar{Y}), \quad (\text{A1})$$

where

$$\bar{X} = \frac{1}{N} \sum_{k=1}^N X_k, \quad (\text{A2})$$

$$\bar{Y} = \frac{1}{N} \sum_{k=1}^N Y_k. \quad (\text{A3})$$

Because neighboring values in the individual time series are usually highly correlated, the SCCF (A1) for different lag time is also correlated. The covariance between the SCCF's $c_{XY}(\tau_1)$ and $c_{XY}(\tau_2)$ is given approximately by Bartlett's formula (Jenkins and Watts, 1968)

$$\begin{aligned} \text{Cov}[c_{XY}(\tau_1), c_{XY}(\tau_2)] \\ = \frac{1}{N_{XY}} \sum_{k=-\infty}^{\infty} (\gamma_{XX}(k)\gamma_{YY}(k + \tau_1 - \tau_2) \\ + \gamma_{XY}(k + \tau_1)\gamma_{YX}(k - \tau_2)), \quad (\text{A4}) \end{aligned}$$

where γ_{XX} , γ_{YY} , γ_{XY} and γ_{YX} are the autocovariance and the cross-covariance functions of the two time series respectively. Thus N_{XY} is the effective number of data pairs of $X(t)$ and $Y(t)$ at lags τ_1 and τ_2 , respectively.

Suppose the two processes are uncorrelated, i.e., $\gamma_{XY} = \gamma_{YX} = 0$; then (A4) reduces to

$$\begin{aligned} \text{Cov}[c_{XY}(\tau_1), c_{XY}(\tau_2)] \\ = \frac{1}{N_{XY}} \sum_{k=-\infty}^{\infty} \gamma_{XX}(k)\gamma_{YY}(k + \tau_1 - \tau_2). \quad (\text{A5}) \end{aligned}$$

For two first-order autoregressive (Markov) processes, the autocorrelation functions are given by

$$\left. \begin{aligned} \gamma_{XX}(\tau) &= \sigma_X^2 e^{-\lambda_X |\tau|} \\ \gamma_{YY}(\tau) &= \sigma_Y^2 e^{-\lambda_Y |\tau|} \end{aligned} \right\}, \quad (\text{A6})$$

where σ_X^2 and σ_Y^2 are the variance of $X(t)$ and $Y(t)$, respectively.

Substituting (A6) into (A5) with $\tau_1 = \tau_2 = \tau$ and $N_{XY} = N - |\tau|$ yields

$$\begin{aligned} \text{Cov}[c_{XY}(\tau), c_{XY}(\tau)] &= \frac{1}{N - |\tau|} \sum_{k=-\infty}^{+\infty} \sigma_X^2 \sigma_Y^2 e^{-(\lambda_X + \lambda_Y)|k|} \\ &= \frac{2\sigma_X^2 \sigma_Y^2}{N - |\tau|} \left[\frac{1}{1 - \exp[-(\lambda_X + \lambda_Y)]} \right]. \quad (\text{A7}) \end{aligned}$$

The standard deviation of the cross correlation at lag between two uncorrelated Markov process is given by

$$\begin{aligned} \text{SD}[r_{XY}(\tau)] &= \left[\frac{\text{Cov}[c_{XY}(\tau), c_{XY}(\tau)]}{\sigma_X^2 \sigma_Y^2} \right]^{1/2} \\ &= \left[\frac{2}{(N - |\tau|)\{1 - \exp[-(\lambda_X + \lambda_Y)]\}} \right]^{1/2}. \quad (\text{A8}) \end{aligned}$$

REFERENCES

- Barnett, T. P., 1981: Statistical prediction of North American air temperature from Pacific predictors. *Mon. Wea. Rev.*, **109**, 1021-1041.
- , and R. W. Preisendorfer, 1978: Multifield analog prediction of short-term climatic fluctuations using a climate state vector. *J. Atmos. Sci.*, **35**, 1771-1787.
- Branstator, G., 1983: Horizontal energy propagation in a barotropic atmosphere with meridional and zonal structure. *J. Atmos. Sci.*, **40**, 1689-1708.
- Charney, J. G., and J. G. DeVore, 1979: Multiple flow equilibria in the atmosphere and blocking. *J. Atmos. Sci.*, **36**, 1205-1216.
- Chiu, W. C., and A. Lo, 1979: A preliminary study of the possible statistical relationship between the tropical Pacific sea surface temperature and the atmospheric circulation. *Mon. Wea. Rev.*, **107**, 18-25.
- Davis, R. E., 1976: Predictability of sea surface temperature and sea-level pressure anomalies over the North Pacific Ocean. *J. Phys. Oceanogr.*, **6**, 249-266.
- Douglas, A. V., and P. J. Englehart, 1981: On a statistical relationship between autumnal rainfall in the central equatorial Pacific and subsequent winter precipitation in Florida. *Mon. Wea. Rev.*, **109**, 2377-2382.
- Harnack, R. P., 1979: A further assessment of winter temperature predictions using objective methods. *Mon. Wea. Rev.*, **107**, 250-267.
- , and A. J. Broccoli, 1979: Associations between sea surface temperature gradient and overlying mid-tropospheric circulation in the North Pacific region. *J. Phys. Oceanogr.*, **9**, 1232-1242.
- Heddinghaus, T. R., and A. F. Krueger, 1981: Annual and interannual variations in outgoing longwave radiation over the tropics. *Mon. Wea. Rev.*, **109**, 1208-1218.
- Horel, J. D., and J. M. Wallace, 1981: Planetary-scale atmospheric phenomena associated with the Southern Oscillation. *Mon. Wea. Rev.*, **109**, 813-829.
- Hoskins, B. J., and D. J. Karoly, 1981: The steady linear response of a special atmosphere to thermal and orographic forcing. *J. Atmos. Sci.*, **38**, 1179-1196.
- Jenkins, G. M., and D. G. Watts, 1968: *Spectral Analysis and its Applications*. Holden-Day, 525 pp.
- Julian, P. R., and R. M. Chervin, 1978: A study of the Southern Oscillation and the Walker circulation. *Mon. Wea. Rev.*, **106**, 1433-1451.
- Lau, K.-M., and H. Lim, 1982: Thermally driven motions in an equatorial β -plane: Hadley and Walker circulations during the winter monsoon. *Mon. Wea. Rev.*, **110**, 336-353.
- , and P. H. Chan, 1983: Short-term climate variability and atmospheric teleconnection from satellite-observed longwave

- radiation. Part I: Simultaneous relationships. *J. Atmos. Sci.*, **40**, 2735-2750.
- , and H. Lim, 1984: On the dynamics of equatorial forcing of climate teleconnections. *J. Atmos. Sci.*, **41**, (in press).
- Lau, N.-C., 1979: The observed structure of tropospheric stationary waves and the local balances of vorticity and heat. *J. Atmos. Sci.*, **36**, 996-1016.
- , 1981: A diagnostic study of recurrent meteorological anomalies appearing in a 15-year simulation with a GFDL general circulation model. *Mon. Wea. Rev.*, **109**, 2287-2311.
- Lim, H., and C.-P. Chang, 1983: Dynamics of teleconnections and Walker circulations forced by equatorial heating. *J. Atmos. Sci.*, **40**, 1897-1915.
- Madden, R. A., 1976: Estimates of natural variability of time-averaged sea-level pressure. *Mon. Wea. Rev.*, **104**, 942-952.
- , and D. J. Shea, 1978: Estimates of the natural variability of time-averaged temperature over the United States. *Mon. Wea. Rev.*, **106**, 1695-1703.
- Namias, J., 1978: Multiple causes of the North America abnormal winter of 1976-77. *Mon. Wea. Rev.*, **106**, 279-295.
- , 1980: Causes of some extreme Northern Hemisphere climate anomalies from summer 1978 through the subsequent winter. *Mon. Wea. Rev.*, **108**, 1333-1346.
- Reiter, E., and D. Westhoff, 1981: A planetary-wave climatology. *J. Atmos. Sci.*, **38**, 732-750.
- Rowntree, P. R., 1972: The influence of tropical east Pacific Ocean temperature on the atmosphere. *Quart. J. Roy. Meteor. Soc.*, **98**, 290-321.
- Shukla, J., 1975: Effect of Arabian sea-surface temperature anomaly on the Indian summer monsoon: A numerical experiment with the GFDL model. *J. Atmos. Sci.*, **32**, 503-511.
- , and J. M. Wallace, 1983: Numerical simulation of the atmospheric response to equatorial sea surface temperature anomalies. *J. Atmos. Sci.*, **40**, 1613-1630.
- Simmons, A. J., J. M. Wallace and G. W. Branstator, 1983: Barotropic wave propagation and instability, and atmosphere teleconnection patterns. *J. Atmos. Sci.*, **40**, 1363-1392.
- Trenberth, K., 1981: Observed Southern Hemisphere eddy statistics at 500 mb: Frequency and spatial dependence. *J. Atmos. Sci.*, **38**, 2585-2605.
- Wallace, J. M., and D. S. Gutzler, 1981: Teleconnections in the geopotential height field during the Northern Hemisphere winter. *Mon. Wea. Rev.*, **109**, 784-812.
- Webster, P. J., 1981: Mechanisms determining the atmospheric response to sea surface temperature anomalies. *J. Atmos. Sci.*, **38**, 554-571.
- , 1982: Seasonality in the local and remote atmospheric response to sea surface temperature anomalies. *J. Atmos. Sci.*, **39**, 41-52.
- , and J. R. Holton, 1982: Cross-equatorial response to middle-latitude forcing in a zonally varying basic state. *J. Atmos. Sci.*, **39**, 722-733.
- White, G., 1982: An observational study of the Northern Hemisphere extratropical summertime general circulation. *J. Atmos. Sci.*, **39**, 24-40.

Analous Diabatic Heating and Large-Scale Circulation e Tropics During the 1976-77 and 1982-83 ENSOs

El Niño Southern Oscillation phenomenon is closely related to analous changes in tropical convection the Pacific. In this note we compare the temporal and spatial changes in heating patterns in relation to the circulation during the ENSOs of 1976-77 and 1982-83. Figure 1 shows the time-longitude section along the equator of monthly outgoing longwave radiation between 5°S and 5°N, 60°E and 60°W from May 1974 to May 1983. With negative (positive) anomalies reflecting decrease (increase) in convective cloudiness and diabatic heating, it can be seen that before the 1976-77 event the equatorial central convection (ECPC) had been strongly suppressed for at least a two-year period prior to May 1975. Coupled with the enhanced convection over the Indonesian maritime continent, the diabatic heating formed a dipole pattern whose sign would imply an anomalous surface easterlies over the western Pacific, what appeared to be a precursor phase before the 1976-77 ENSO. It is interesting to note that this dipole-like pattern continued to recur with alternating polarity at a shorter time interval (order of 2-3 years) throughout the entire period. The largest fluctuation is most noticeable during the 1976-77 episode, the entire pattern did not settle down to the enhanced dipole characteristic of ENSO until the 1977-78 (no data are available from December 1978). The period 1979-1981 showed frequent alternation of the polarity of the dipole oscillation. The presence of a similar pattern in the 1982-83 event was, however, not apparent. Following a brief reversal in late 1981, the ECPC exploded into a deep convective system with corresponding reduction in convective activity over the maritime continent during the winter of 1982-83. (The blank data area during December of 1982-83 is due to a bad reception from the National Climate Service). There was also a distinctive eastward migration of the dipole anomaly towards the eastern Pacific. This migration was less obvious during the 1976-77 ENSO. The ECPC of 1982-83 was located much further east

than during the 1976-77 event. This is by far the most extreme eastward position ever reached by the ECPC, compared to those deduced from the low level wind convergence in the composite of Rasmusson and Carpenter (1982) for past ENSOs since 1950.

The different polarity of the dipole fluctuation shown in the OLR pattern has been suggested by Lau and Chan (1983 a, b) as representing oscillations between two stable climatic states in the tropical ocean-atmo-

sphere system. The ENSO events are large-amplitude realizations of one of these states. We are now hypothesizing that instability inherent in the large scale ocean-atmosphere system seasonally varying mean condition (e.g., trade wind, sea surface temperature, etc.), together with some short-term stochastic forcings, provide both the setup and triggering mechanism(s) to produce ENSO-like "catastrophic" events.

To compare the changes in the tropical scale circulation during the 1976-77 and 1982-83 events, the wintertime anomalies of 200 mb velocity potential and streamfunction were computed for each period, respectively. Figures 2 A, B, and C show the seasonal anomaly of the streamfunction before, during, and after the 1976-77 ENSO, with the anomalous OLR pattern superimposed. Not shown, but noted here, is that changes in the velocity potential field over the equatorial central Pacific and the maritime continent are in accord with the reversal of the dipole-like anomalous heating during this period. Changes in the velocity potential also reflect large fluctuation of the Walker-type circulation all the way around the globe. In the streamfunction maps, the Pacific North American (PNA) pattern was most noticeable during 1976-77. A deep low over the eastern coast of the United States, which corresponds to the easternmost node of the PNA, was found both in 1976-77 and 1977-78, with the former more intensely developed. However, the ECPC did not become fully developed until 1977-78. The tropical anomalies, i.e., upper anticyclonic (cyclonic) circulations forced by heat source (sink), were well developed during the 1975-76 winter, with the flow corresponding to a heat sink or reduction in condensational heating over the equatorial Pacific. This pattern is in agreement with that predicted by simple theory of heat induced motions near the equator (Lau and Lim, 1982; Lim and Chang, 1983). During and after the 1976-77 ENSO, this characteristic tropical signature was also observed but to a much lesser extent. The same sequence of maps (Figures 2 D, E, and F) show a distinctly different temporal evolution of events for the 1982-83 ENSO. The reversal of the dipole-like pattern in the velocity potential (not

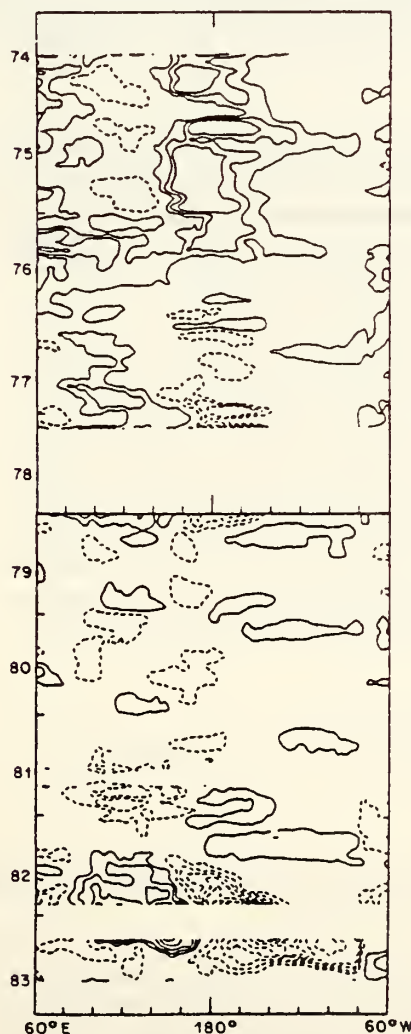


FIGURE 1 (Lau et al.)

Time-longitude section of monthly anomaly of outgoing longwave radiation from 1974 to 1983. Negative anomalies are dashed. Contour interval is 7 W m⁻². Only contours with absolute deviation greater than 7 W m⁻² are shown.

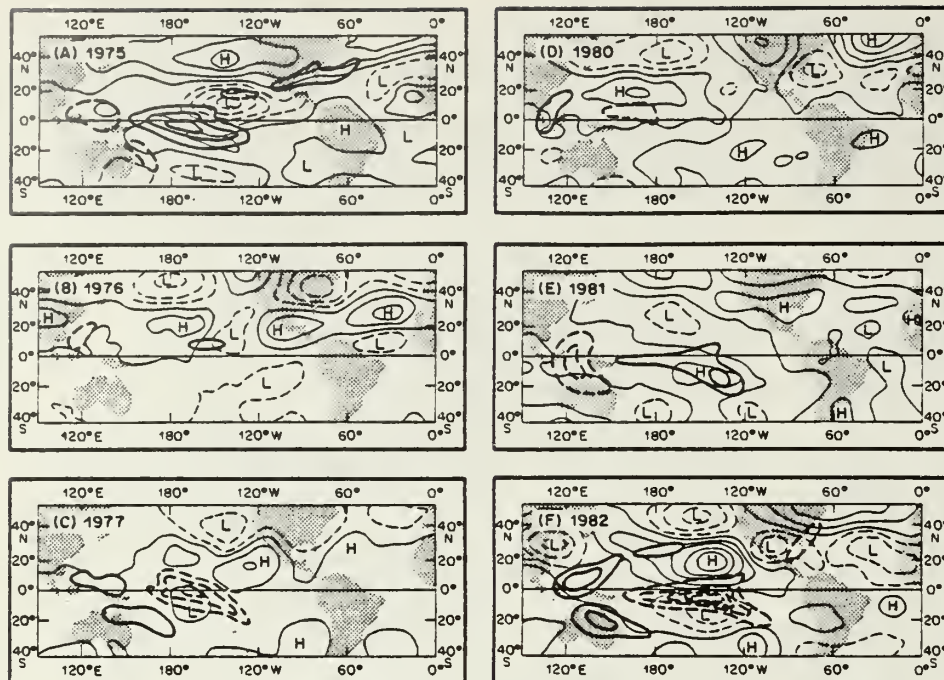


FIGURE 2 (Lau et al.)

Seasonal anomaly of 200 mb streamfunction for the winter (December, January, February) if (A) 1975-76, (B) 1976-77, (C) 1977-78, (D) 1980-81, (E) 1981-82, and (F) 1982-83. Contour interval is $5 \times 10^6 \text{ m}^2 \text{ s}^{-1}$. Seasonal anomaly of outgoing longwave radiation with absolute deviation greater than 10 W m^{-2} is shown by heavy solid (dashed) lines corresponding to reduced (enhanced) convective activity. Contour interval is 10 W m^{-2} .

shown) and in the heating field occurred within a one-year period, with not much buildup during the 1980 winter. The PNA pattern was not very well defined, but the anticyclones on both sides of the equator caused by the low-latitude heat source were very well developed during 1982-83 compared with that during 1976-77.

While the study of Horel and Wallace (1981) suggested a close relationship between the PNA and tropical heating, the above results indicate that in individual events, the two phenomena may not be in phase nor necessarily related by the simple relationship as suggested. The phase relationship described above suggests that atmospheric teleconnection between the tropics and the middle latitudes may also be strongly influenced by other processes such as normal mode instability (Simmons et al., 1983), nonlinear interactions (Lau and Lim, 1983) and factors not directly related to the ECPC. During the 1982-83 epi-

sode, it is likely that such forcings became dominant, so that the PNA signature was not particularly well observed. Our study also suggests that while there are certain basic characteristics shared by all ENSOs, e.g., sea surface temperature anomalies, dipole-like diabatic heating anomaly in the tropics, Walker circulation changes, etc., each individual ENSO is quite different, especially in terms of teleconnection with the midlatitudes. The temporal and spatial variation of the diabatic heating for the two ENSOs discussed here appeared to deviate substantially from the composite picture presented by Rasmusson and Carpenter (1982). A unified view (if there is any) of ENSO calls for a more profound understanding of the phenomenon beyond what can be gained from case-by-case studies.

References

Horel, J. D. and J. M. Wallace (1981) Plane-

tary scale atmospheric phenomena associated with the Southern Oscillation. *Monthly Weather Review*, 109, 813-829.

Lau, K. M. and P. H. Chan (1983a) Short-term climate variability and atmospheric teleconnection from satellite observations of outgoing longwave radiation. I: Simultaneous relationships. *Journal of the Atmospheric Sciences*, in press.

Lau, K. M. and P. H. Chan (1983b) Short-term climate variability and atmospheric teleconnection from satellite observations of outgoing longwave radiation. II: Lag correlations. *Journal of the Atmospheric Sciences*, in press.

Lau, K. M. and H. Lim (1982) Thermally driven motions in an equatorial β -plane Hadley and Walker circulation during the winter monsoon. *Monthly Weather Review*, 110, 336-353.

Lau, K. M. and H. Lim (1983) On the dynamics of equatorial forcing of climate teleconnections. *Journal of the Atmospheric Sciences*, in press.

Lim, H. and C. P. Chang (1983) Dynamical teleconnection and Walker circulation forced by equatorial heating. *Journal of the Atmospheric Sciences*, 40, 915-931.

Rasmusson, E. M. and T. H. Carpenter (1982) Variations in tropical sea surface temperature and surface wind field associated with the El Niño Southern Oscillation. *Monthly Weather Review*, 110, 354-382.

Simmons, A. J., J. M. Wallace, and C. W. Branstator (1983) Barotropic wave propagation and instability and atmospheric teleconnection patterns. *Journal of the Atmospheric Sciences*, 40, 1363-1392.

Ka-Min Lau
Goddard Laboratory
for Atmospheric Sciences
NASA/Goddard Space Flight Center
Greenbelt, MD 20771

James S. Boyle
Chih-Pei Chang
Department of Meteorology
Naval Postgraduate School
Monterey, CA 94064

The Costa Rica Dome During the Onset of the 1982-83 El Niño

The Costa Rica Dome is an area of upwelling, 200 to 400 km in diameter, located in the eastern tropical Pacific Ocean between 5-12°N and 84-92°W. In this region the thermocline often reaches to within 10-15 m of the surface, forming a domelike structure.

In February and June 1979, November 1981, and July-August 1982, vertical profiles of temperature and salinity were recorded with

a CTD in the Costa Rica Dome area. This note shows that the relative changes observed in the Costa Rica Dome in July-August 1982 were larger than the seasonal variations inferred from our previous measurements. This is interpreted as an indication of the effect of the 1982-83 equatorial Pacific warm anomaly (see TO-AN Nos. 16 and 21) in the tropical eastern Pacific as early as the end of July.

The July-August 1982 data showed a substantial increase in the volume of water with temperatures above 15°C in the periphery of the dome. By comparison with observations made in the summer of 1979, the dome, which was much better defined in 1982, was weakened by a cyclonic warm current transported northward from 3°N and then turned west at about 11°N. Data from the summer

DISTRIBUTION LIST

	No. Copies
1. Defense Technical Information Center Cameron Station Alexandria, Virginia 22314	2
2. Library, Code 0142 Naval Postgraduate School Monterey, California 93943	2
3. Department of Meteorology Library Code 63, Naval Postgraduate School Monterey, California 93943	1
4. Climate Dynamics Research Program National Science Foundation Washington, D.C. 20550	2
5. Professor C.-P. Chang, Code 63Cp Naval Postgraduate School Monterey, California 93943	2
6. Dr. K. M. Lau Goddard Space Flight Center Climate and Radiation Branch NASA, Code 915 Greenbelt, Maryland 20771	2

DUDLEY KNOX LIBRARY



3 2768 00330044 3